UNIVERSITY OF SOUTHAMPTON

Detailed Investigation of Loss Prediction Of An Axial Compressor Cascade At Off-Design Conditions In The Presence Of Incident Free-Stream Disturbances Using Large Eddy Simulations

by

John Leggett

A thesis submitted in fulfillment for the
degree of Doctor of Philosophy

in the
Faculty of Engineering and the Environment
Aerodynamics and Flight Mechanics

April 28, 2018

UNIVERSITY OF SOUTHAMPTON

ABSTRACT

FACULTY OF ENGINEERING AND THE ENVIRONMENT
AERODYNAMICS AND FLIGHT MECHANICS

Doctor of Philosophy

by John Leggett

The prediction of an axial compressor's loss early on in the design phase is a valuable and important part of the design process. The work presented here focuses on assessing the accuracy of current prediction methods, Reynolds Averaged Navier Stokes (RANS), compared with highly accurate Large Eddy Simulations (LES). The simulations were performed at the challenging running conditions of engine relevant Mach (0.67) and Reynolds (300,000) numbers. The work looks at the effects of off-design incidence and the influence of different free-stream disturbances on loss prediction.

From the highly accurate datasets produced by the LES the work is able to show how loss attribution varies under different conditions, and goes on to compare how well RANS captures these changes. It was found that overall loss trends are captured well by RANS but substantial differences exist when comparing individual loss sources, which are shown to vary significantly under different running conditions.

The investigation into loss attribution is performed using the *Denton* (1993) loss breakdown as well as a novel application of the *Miller* (2013) mechanical work potential. In addition to the discovery of the variation in the sources of loss, the comparison between the loss analyses highlighted some of the limitations of the Denton loss breakdown, which was shown to have increasing error under large off-design incidence or in the presence of discrete disturbances.

From the comparison of the loss breakdown analyses and LES and RANS flow field results, new insight into the characteristics, limitations and short comings of current modeling techniques have been found. The variation in the sources of loss under different running conditions was also discovered.

Contents

List of Figures

List of Tables

Nomenclature

Acronyms

CFD	Computational Fluid Dynamics
LES	Large Eddy Simulations
RANS	Reynolds Averaged Navier-Stokes

Greek Symbols

α	Angle of attach/stagger angle
λ	Bulk viscosity or Characteristic wave speed
ξ	Computational domain coordinate
η	Computational domain coordinate
ρ	Density
δ^*	Displacement thickness
ω	Dissipation
μ	Dynamic viscosity
μ_t	Eddy viscosity
ϕ	Flow coefficient
γ	Isentropic exponent
ν	Kinematic viscosity
δ_{ij}	Kronecker delta
ω	Loss coefficient
ω_{m_f}	Mechanical work potential loss coefficient
θ	Momentum thickness
τ_{ij}	Shear strain
σ_{ij}	Strain tensor
Ω	Vorticity strain tensor
Ω	Vorticity

Roman Symbols

D	Bar diameter
w_{bar}	Bar pitch
U_b	Bulk velocity
U_c	Centreline velocity

$\mathcal{L}$	Characteristic wave amplitude
l	Chord
$\mathbf{m}$	Closed system form mechanical work potential
Cf	Coefficient of friction
Cp	Coefficient of pressure
Q	Conservative variables vector
x_i	Coordinate component
S	Curvilinear distance along surface
d	Distance from reference
h	Enthalpy
$\widetilde{u_i'' u_j''}$	Favre averaged turbulent fluctuations
u^*	Friction velocity
c_p	Heat capacity at const. pressure
q	Heat flux
e	Internal energy
$M_i sen$	Isentropic Mach number
J	Jacobian
k	Kinetic energy
DF_{loc}	Local diffusion factor
M	Mach number
$\dot{S}_{mf}$	Mechanical work potential source terms
M_i	Mixed out integral
$\mathbf{m_f}$	Open system form mechanical work potential
w	Pitch
Pr	Prandtl number
p	Pressure
S_{ij}	Rate of strain tensor
f_{red}	Reduced frequency
Re	Reynolds number
c	Speed of sound
St	Strouhal number
T	Temperature
t	Time
E	Total energy
C_{pb}	Trailing edge pressure ratio
t	Trailing edge thickness
e_i	Unit vector
u_i	Velocity component
U	Velocity

Subscripts Superscripts

e	Boundary layer edge value
D	Dead state pressure
$1, 2, 3$	Directional components
$\tilde{}$	Favre averaged
$''$	Favre fluctuation
∞	Free stream value
se	Isentropic expanded value
max	Maximum value
$\hat{}$	Metric multiplied
bar	Moving bar parameter
ps	Pressure surface
$-$	Spatial filtered
$'$	Spatial or time fluctuation
sgs	Sub-grid scale
ss	Suction surface
$\langle\rangle$	Time averaged
t	Total quantity
pb	Trailing edge base pressure

Acknowledgements

I would like to take this opportunity to thank the people who have supported and helped me during my Ph.D. Firstly I would like to thank my supervisors Edward Richardson and Richard Sandberg for their help and guidance, without which I would not be here completing my thesis. I would also like to thank Stephan Priebe, Aamir Shabbir and Vittorio Michelassi for their patience and advice during our countless meetings. I am exceeding grateful for your help.

I would especially like thank my house mates Alex and Max who were always keen to get involved in our many house shenanigans and listen to endless hours of discussion and complaining when things didn't go to plan. You have both made my time in Southampton a brighter and more fulfilling one.

A special thanks goes to Jacques and Javi and the other members of the Awesome PGR CC who went on countless cycling adventures with me and shared many a dis-heartening moment in the pouring rain or a moment of tranquil bliss at the top of a gruelling climb in the glorious sunshine. Thank you for your friendship, I will miss our time here greatly.

I would also be remiss if I forgot Emily, Florian, and the many others who have supported me from far or near over the last four years. You have made my life better.

Lastly of course my parents Sylvia and John (for all the stuff you know parents do. Wow, such parenting, much supportive).

And now, without further ado, one for the road?

Chapter 1

Introduction and Review

1.1 Introduction

The work presented in this thesis focuses on the prediction of axial compressor performance in aviation turbo jet engines. Axial compressors form an integral part of a turbo jet engine and play a substantial roll in determining the performance of the engine. The compressor requires work input meaning that any improvement in its' efficiency releases work that can be used to drive the plane forward. The efficiency of the whole engine is a measure of the usable power compared with the total power. Thus any improvements in the efficiency of the compressor reducing the power needed to drive it, i.e not usable power, results in an improvement in engine performance.

Axial compressors have lent themselves nicely to aviation applications as they display many of the attributes needed for a successful engine. A second set of compressors, mentioned here only for completeness, is the group of radial compressors. These tend to have opposing characteristics to axial compressors, although they are used in aviation for applications such as helicopters where space is limited. The two compressor designs are highlighted in fig. 1.1 showing a schematic of a single compressor stage and the relative air motions.

The main characteristics of interest for aviation engines are the pressure rise per stage and mass flow rate, which tend to be inversely proportionate highlighted in the differences between axial and radial compressors. It is shown that radial designs result in substantially higher pressure rises per stage but are limited in their mass flow rate, while the opposite is true for axial compressors, which show much lower pressure rises per stage but can have very high mass flow rates. It is possible to achieve higher mass flow rates with radial compressors but the compressor becomes prohibitively large for aviation use. The remainder of introduction and review will focus solely on axial compressors.

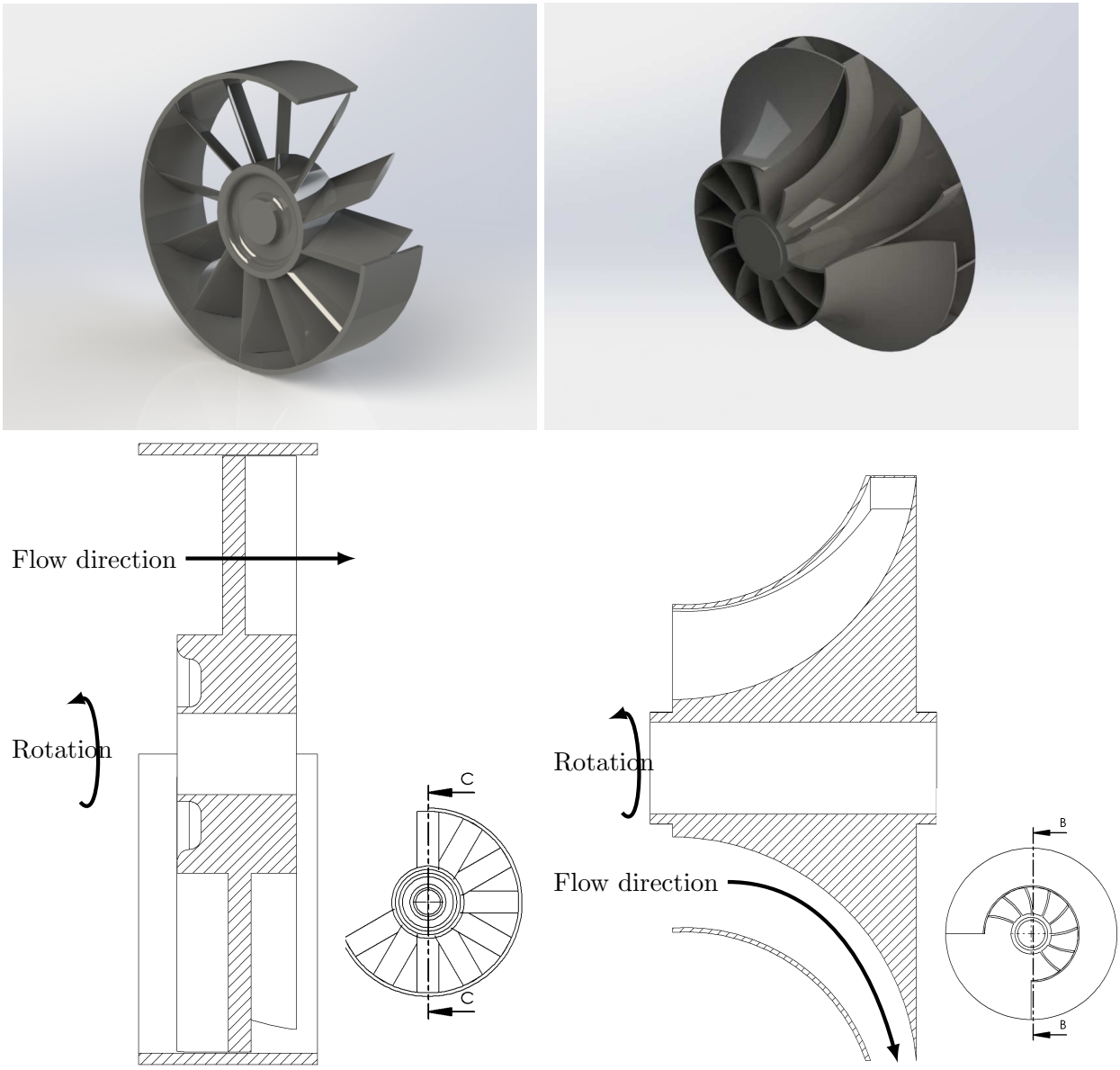

(a) Axial Compressor (b) Radial Compressor

Figure 1.1: Schematic representation of compressor types and air passage.

The design of axial compressors involves a complex set of parametric choices. There are a multitude of variables, each of which have an effect on the performance of the compressor. Despite such complexity, there have been marked improvements in efficiency in compressors over the years. For a full compressor spool for example parameters such as the meridional flow path can have drastic effects on performance. It is shown that if the radial distance to the mean blade span is increased longitudinally along the compressor, the aerodynamic challenges are eased. Further issues arise if the annulus areas are not adequately adjusted to account for the increased air density and reduced velocities. It is important to be aware of the effects of

such parameters when considering a full compressor though this is reliant on the performance of the individual stages. Stage performance is determined predominantly by the blade design and local flow which reduces the number of parameters involved but can have a cascade effect if designed poorly.

The trend in blade design over the years has seen a marked reduction in aspect ratio and an increase in the solidity (chord to pitch ratio) of the blades resulting in shorter deeper blades. Much of this trend has been driven by the improved compressor performance from increased solidity due to better end wall flow behaviour. This has also improved the compressor stall characteristics, while the low aspect ratios help to reduce the blade speeds, which can limit the operating range of the compressor due to transonic flow as well as cause mechanical problems with blade loading. The increase in solidity however, has reduce the efficiency at the design point due to the increased boundary layer length, though there is an improvement in the pressure rise. The effects of simple parameter variations, such as blade solidity, shows the importance of understanding the interaction of these parameters and ensuring that they are captured and accounted for during design.

With this in mind the work presented here focuses on a single compressor cascade stage and the effects variation in inflow incidence and free-stream flow conditions have on the stages' performance.

The work focuses more specifically on understanding how well performance is predicted when these variables are altered, using high fidelity simulations to improve our understanding of the performance of standard industrial methods. Furthermore the simulations, which are performed at engine relevant conditions, provide new insight into how the flow behaves as these parameters are varied as previous high fidelity numerical studies at engine relevant conditions are very limited.

1.2 Literature

1.2.1 Overview

The earliest investigations into compressor design and performance were all conducted experimentally. The restriction in computational power and lack of robust and accurate computational methods made any detailed investigations at running conditions infeasible. Today prototyping and physical testing remains a core element of compressor development but computational resources are rapidly improving opening up new possibilities. Replicating the true running conditions of modern compressors is challenging both for experimental and computational approaches as the running conditions of compressors become more extreme to improve energy efficiency. Because of this, many numerical studies are performed at lower Reynolds numbers or

Mach numbers to enable the study to be performed in acceptable time scales with reasonable cost.

The nature of the flow over a single compressor blade can be separated into three areas. The mid section of the blade, far from the casing and hub, the hub flow where the blade is attached and the tip flow where fluid can pass around the top of the blade. In the mid section the flow is often considered two dimensional, with negligible mean flow in the span-wise direction of the blade. However, as one moves toward either the hub or casing, the end wall boundary layers of the blade passage induce mean span-wise flows. These interactions result in complex three dimensional flows which can be classed as two further regions. Near the hub or blade attachment point, the interaction of the hub boundary layer and blade boundary layer results in root vortex interactions, while the flow near the tip of the blade shows various three dimensional flow structures due to the tip gap flows and casing boundary layer interactions. In addition to the basic flow structures of a single blade, incoming wakes from up stream blade rows interact with the blade boundary layer and end wall region which is a subject of great importance in modern multi stage compressors.

An overview of the work done on these different areas is presented next as well and insight into the areas necessary for this work, such as advances in numerical methods for simulating compressor cascade flows.

1.2.1.1 Blade mid section

Starting with the quasi two dimensional flow region in the mid section of the blade there has been considerable research done on understanding blade shapes and flow phenomena as this directly affects the loading a blade can achieve. It was predicted by *Cumpsty* (1989) that up to 40% of losses within a compressor are due to the development of the boundary layer and viscous shearing. For this reason it is beneficial to maintain a laminar boundary layer for as much of the blade surface as possible to limit losses. For this reason many early studies focused on boundary layer transition in compressors which have been reviewed by *Mayle* (1991) and *Walker* (1993).

In the book by *White* (1991) the process of natural transition on a flat plate is described, detailing the formation and breakdown of Tollmein-Schlichting (TS) waves rolling into hairpin vortices which eventually transition into a fully turbulent flow. These processes can also be seen in compressors with clean inflows as shown by *Hughes and Walker* (2001). It is generally suggested that the inflow can be considered clean when free-stream turbulence levels (Tu) are less than 0.5% of the free-stream velocity, (*Hodson and Howell*, 2005), which is rarely the case in compressors, suggesting other modes of transition are more likely.

Understanding the process of transition on a compressor blade is important if it is to be controlled and mitigated. The work by *Mayle* (1991) highlights two additional means of transition,

these being separated flow transition and bypass transition. It is suggested that bypass transition occurs when there is high intensity free-stream turbulence that excites the boundary layer instabilities, creating turbulent spots within the boundary layer. These turbulent spots then grow and coalesce into a fully turbulent boundary layer as they are transported down-stream, bypassing the natural progression highlighted by *White* (1991). The turbulence intensity necessary for bypass transition however is not clearly defined and depends on the blade profile and the flow conditions making it difficult to design around.

Separated flow transition often occurs when the boundary layer experiences a strong adverse pressure gradient as is often the case in compressors cascade down-stream of the peak suction. A separation bubble is formed where the flow reattaches to the surface, usually after undergoing transition of the free shear layer, though not always. The experimental study by *Schreiber et al.* (2002) on a controlled diffusion aerofoil at engine representative Reynolds numbers with varying free-stream turbulence showed that at lower turbulence levels ($Tu < 3\%$) transition occurred within the separation bubble with turbulent reattachment. Greater Tu levels showed the transition point move forward of the peak suction to give bypass transition. The earlier transition suppress the separation bubble but increases the turbulent wake loss. The presence of a separation bubble can greatly affect the loss of a compressor blade. Often separation bubbles are broadly categorised as "long" or "short" depending on the effect they have on the pressure distribution. Long separation bubbles have a marked influence on the pressure distribution over the whole blade and can dramatically increase the loss of a blade, while short bubbles show only local variation. Early work by *Roberts* (1975) showed that the length of a separation bubble was also a function of the turbulence intensity which effects the separated flow transition. Further studies such as that by *Zaki and Durbin* (2006) used computational techniques to look at these interactions. Zaki et al. used DNS to observe the influence of free-stream turbulence on the separation bubble at a Reynolds number of 138,000. The incompressible results they presented showed variation of the separation point due to the free-stream turbulence and a reduction in the separation bubble length for turbulence intensities of $\approx 3.5\%$ and higher.

Due to the nature of compressor blades, separation bubbles can also occur at the leading edge blend point where the leading edge radius blends into the larger curvature of the blade profile. This change in curvature often results in a peak in the pressure distribution as the flow is rapidly decelerated. If the deceleration is large, a separation bubble can occur. The nature of the leading edge separation bubble is described in the work done by *Walraevens and Cumpsty* (1995) who studied both elliptical and circular leading edges. It was shown that the leading edge shape can have notable changes on the boundary layer down-stream. The larger separation bubble caused by the circular leading edge produced a boundary layer momentum thickness 2-3 times larger.

Early studies of laminar boundary layer transition showed that most transition modes resulted in the formulation of turbulent spots. Work by *Emmons* (1951) and *Schubauer and Klebanoff*

(1955) provided the initial theory and quantitative data on turbulent spots and how they develop in a boundary layer. They showed turbulent spots to be roughly triangular in plan view propagating down-stream at a reduced velocity. *Schubauer and Klebanoff* (1955) showed that for zero pressure gradient flows, turbulent spots progress with leading and trailing edge velocities of 88% and 50% of the free stream velocity, growing in length. The turbulent spots also spread in the span-wise direction with a half-angle of approximately 11°. It was later shown by *Solomon et al.* (1996),*Gostelow et al.* (1996) and *D'Ovidio et al.* (2001) that the spreading angle and leading and trailing edge speeds are functions of local pressure gradients.

Further insight observed by *Schubauer and Klebanoff* (1955) was the presence of a calmed region following the passing turbulent spot. This calmed region was shown to travel at approximately 30% of free-stream velocity and resist transition and separation when exposed to external disturbances. The excitation of the boundary layer by external disturbances forming turbulent spots is a likely mode by which bypass transition occurs as the turbulent spots grow and finally merge.

1.2.1.2 End Wall and Tip-Gap Effects

The flow through the mid plane of a compressor passage is considered quasi two dimensional and does not take into consideration the 3D effects of the ends of the blade, be it the tip gap or the root mount point. However the end wall flows can be responsible for roughly half of the efficiency loss in a compressor (*Denton*, 1993) and are an area of great importance. The three-dimensionality found in an axial compressor is largely due to the root corner separation and the tip leakage flows, resulting in increased blockage that ultimately affects the flow distribution across the entire passage.

Investigations into these areas, such as those by *Joslyn and Dring* (1985) and *Dong et al.* (1987), have shown that large 3D separations exist on the suction surface of compressor blades near the end walls, driven by the cross-passage pressure gradient interacting with the lower momentum fluid in the end wall region. This cross-passage pressure gradient, driven by the relative velocity difference between the end wall and compressor row, tends to overturn the low momentum fluid which interacts with the blade boundary layer forming an area of separation.

The interaction of wakes and the end wall separation have also been studied. *Poensgen and Gallus* (1991b) and *Poensgen and Gallus* (1991a) experimentally investigated the influence of up-stream wakes in an annular compressor cascade at low speed using up-stream moving bars. It was found that the incident wakes could induce unsteady periodic motion in the hub end wall separation which varied the separation extent.

Work by *Bryce et al.* (1995), *Cherrett et al.* (1995a) and *Cherrett et al.* (1995b) also found similar periodic behaviour of the end wall separation in a high-speed transonic fan while *Suryavamshi*

et al. (1997) found the same phenomenon in a high speed multi-stage compressor. Blade incidence and Reynolds number are also known to influence the strength of the end wall separation. *Hobson et al.* (2001) performed an experimental analysis on a controlled diffusion stator blade at a Reynolds number of 640,000 with off-design angles of incidence. The results showed three-dimensional flow separation caused by end wall effects that appeared at approximately 80% of the chord and did not reattach. The effects of tip-gap width have been highlighted by *Peacock* (1982) who suggested that a 1% increase resulted in a 2% drop in efficiency, which is more important with modern low aspect ratio blades where the induced three-dimensionality affects more of the blade boundary layer.

The study of tip-gap effects, using linear cascades, has produced a good understanding of the general processes involved. *Storer and Cumpsty* (1991) showed that the mechanisms of tip-gap flow is primarily inviscid and is mostly controlled by the near region static pressure field. *Storer and Cumpsty* (1994) also showed that much of the loss from tip-gap flows was associated with the down-stream mixing of the tip vortices with the main flow field.

More recent experiments on low speed linear cascades by *Devenport et al.* (2004); *Wang and Devenport* (2004) detailed measurements made of the flow field with and without a moving end wall. The experiments were performed with varying tip-gap sizes of 0.83%,1.6% and 3.3% chord and found the moving wall smeared the tip vortex but did not show notable changes to mechanics of development.

Numerical simulations performed by *Valkov and Tan* (1999b) investigated the interaction of up-stream tip vortices with down-stream blades and found the interaction to have two effects. The interaction reduced the mixing loss of the tip vortex, but the interaction of the wake was also detrimental to the boundary layer losses of the down-stream blade. A more recent numerical study by *You et al.* (2007) using Large Eddy Simulations at a Reynolds number of 400,000 showed a more detailed analysis of the production of vorticity and turbulent kinetic for a linear cascade with a moving end wall. This was also compared with results for a similar experimental study by *Wang and Devenport* (2004) and showed good correlation.

1.2.1.3 Free-Stream Disturbances

The occurrence of free-stream disturbances in multi stage axial compressors is guaranteed for all but the first stage though this too is likely to experiences disturbances if inlet guide vanes are present. With this being the case it is necessary to understand how free-stream disturbances, especially incoming wakes, affect the boundary layer of down-stream blades. An overview of the interaction of passing wakes on a compressor boundary layers is given in fig. 1.2 taken from *Cumpsty et al.* (1995). Further down stream the wakes of the previous stages tend to mix and results in high levels of free-stream turbulence resulting in a combination of free-stream turbulence and discrete wakes

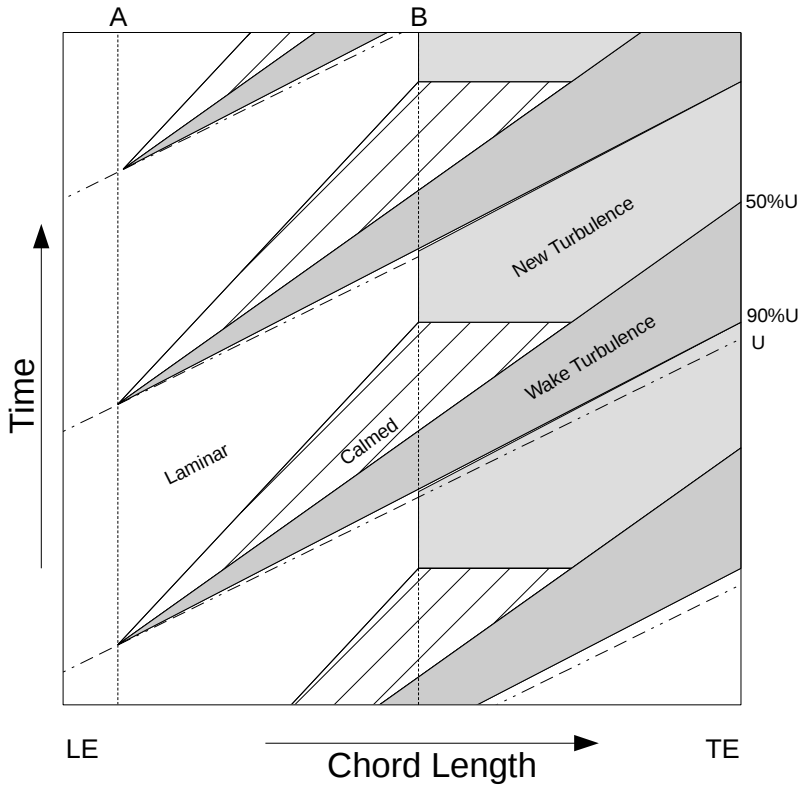

Figure 1.2: Overview of wake-induced transition of a compressor blade taken from the work by *Cumpsty et al.* (1995). Points 'A' and 'B' represent the onset of turbulence caused by the wake and natural transition respectively.

Although incoming wakes are potentially more disruptive to the boundary layer due to their periodic nature it is important to understand the effects of free-stream turbulence on the boundary layer as mentioned previously. The effects of free-stream turbulence on boundary layers has been investigated for quite some time, earlier works such as that done by *Abu-Ghannam and Shaw* (1980) looked at the effects free-stream turbulence and pressure gradients had on a non-separated boundary layer along a flat plate and derived correlations for the prediction of transition. These have since been used in numerical models such as that by *Drela* (1995) to help improve performance of numerical simulations and speed up design processes.

Work by *Hobson et al.* (1999) experimentally investigated the effects of free-stream turbulence at an intensity of 1.5% of the free-stream velocity and a Reynolds number of 700,000. *Hobson et al.* (1999) found that the free-stream turbulence interacted with the high shear of the boundary layer and free shear layer of the separation bubble resulting in transition. The extent of the interaction was also found to vary with a change of incidence and the resultant leading edge separation.

The first of a two part experimental study by *Dong and Cumpsty* (1990a), looked closely at the effects of free-stream disturbances on the boundary layer, considering incident wakes and

free-stream turbulence. The first part of the study considered free-stream turbulence of 6% intensity on transition at lower engine Reynolds numbers $\approx 400,000$. The study showed that with increased free-stream turbulence the normal laminar separation bubble found on the suction surface of the blade was suppressed and that there was also possible suppression of transition and laminarisation of the boundary layer along the pressure surface. This relaminarisation is not attributed to the free-stream turbulence but is likely due to the acceleration of the flow along the leading section of the pressure surface, the effects of which were studied by *Jones and Launder* (1972). The second part of the study by *Dong and Cumpsty* (1990b), looked at the effects of incident wakes on the transition and separation of the boundary layer of the cascade. It was found that the incoming wakes produced a turbulent spot within the boundary layer which elongated as it travelled down-stream. The turbulent spot was initiated at the leading edge and its presence had several effects on the boundary layer, in particular behind the turbulent spot the boundary layer seemed to return to laminar flow for a greater proportion of the blade chord compared to without incident wakes but eventually separating and becoming turbulent. The impinging wakes also suppressed the laminar separation bubble present in the first part of the study that were also suppressed by the increased free-stream turbulence.

Work by *Schreiber et al.* (2002) showed that high levels of free-stream turbulence ($Tu > 3\%$) had an amplifying effect on the surface roughness of a blade, causing transition earlier along the blade in the accelerated portion of the suction surface. Increasing the turbulence intensity further forced bypass transition near the leading edge at 7-10% of the chord. More recent experimental work by *Henderson and Walker* (2010) looked at controlled diffusion aerofoils at off-design incidence at a Reynolds number of 300,000 with incident wakes from up-stream moving bars. The investigation found that the local pressure peak caused by the leading edge blend point was receptive to wake induced transition.

Numerical investigations by *Iseler et al.* (2006) and *Zaki et al.* (2009) both look at the effects of incident wakes on the boundary layer. *Iseler et al.* (2006) looked at the numerical reproduction of experimental results to ascertain the effectiveness of Reynolds Averaged Navier-Stokes (RANS) based CFD in capturing incident wake effects. The results show good correlation with most quantities and modelled the effects of the fluctuations on the mean flow well, though there were some discrepancy with the prediction of turbulent transition and the extent of wake calmed regions which were overestimated. *Zaki et al.* (2009) performed an incompressible DNS of wake passing of a compressor blade at Reynolds 138,000. The simulations showed the suction surface boundary layer separated and rolled up due to Kelvin-Helmholtz instabilities forced by the passing wakes, while the pressure surface remain attached but underwent bypass transition. Further work by *Zaki et al.* (2010) detailed the interaction of free-stream turbulence on the transition methods seen in the boundary layer. The simulations were performed at a Reynolds number of 138,000 with turbulence intensities up to $\approx 6.5\%$ using an incompressible DNS code. They show an interesting interaction of multiple modes leading to transition depending on the turbulence level. At levels around 3% the flow remained laminar over the suction surface until

separation even though the presence of Klebanoff distortions could be detected. After separation the flow rapidly transitioned and reattached. Increasing the free-stream turbulence intensity resulted in bypass transition that occurred up-stream of the separation producing turbulent spots. The turbulent spots then suppressed separation as they passed and also produced a calmed region that delayed the re-establishment of the separation bubble.

The effects of incoming wakes on compressor performance at design conditions has recently been investigated by *Gourdain* (2015a,b). The work looks at the comparison of RANS and Large Eddy Simulations (LES) in predicting performance of stator rotor interaction and the performance limitations of both simulation methodologies. The results showed both RANS and LES predicted similar mean flow profiles but the lack of turbulent fluctuations present in the RANS simulations resulted in differences in the predicted transition point. These works show the benefits of LES simulations at engine Reynolds numbers in providing improved loss prediction and unsteady interactions between wakes and boundary layers. Furthermore they provide an initial outline for good practice of LES application for turbomachinery.

1.2.1.4 Compressor Performance

The desired outcome of much of the research work performed on axial compressors is to improve their performance. The design and development of modern compressors is a complex task, and today almost all of the development work on new compressors is done using CFD, especially RANS, which provides an efficient and effective way of optimising performance. Ultimately however the compressor must perform in the real world and the need for physical testing cannot be avoided though it can be reduced to a minimum.

The performance of a compressor over its entire operating range must be considered during its design as highlighted by the work done by *Steinert et al.* (1991). *Steinert et al.* (1991) performed a series of experimental tests at various angles of incidence over a range of Mach numbers to validate an optimised compressor profile. The profile was designed by combining boundary layer calculations with inverse and direct flow calculations allowing the expected velocity distributions at design incidence to be considered in the profile optimisation. A two part study by *Mo* (2000); *Mo et al.* (2000) shows a similar numerical optimisation of a compressor profile using numerical solvers to predict the compressor performance over the operating range prior to production. The second part of the study details the experimental and numerical analysis of the new blade profiles showing good loss agreement over a range of operating incidence and conditions. Studies by *Schreiber et al.* (2004); *Sonoda et al.* (2004) outlined the procedure of numerical optimisation of a low Reynolds number (130,000) compressor aerofoil profile. The studies employed two methodologies using evolutionary algorithms to improve the performance of the chosen profile. The resulting profiles from the study were tested both experimentally and numerical and it was

shown that improvements of up to 60% could be achieved over the base line controlled diffusion aerofoil profile.

1.2.2 Numerical Application

The use of computational fluid dynamics in researching turbomachinery has gained momentum over the years. With the advent of modern supercomputers capable of many teraflops operations it is now feasible to run engine relevant Reynolds number flows of relevant geometries. However, the accuracy of the CFD methodology employed is still somewhat limited. Currently the use of DNS is still too computationally expensive for compressor design condition, though application to the low pressure turbine is possible due to the lower operating Reynolds numbers. The application of Large Eddy Simulation is possible although still limited to limited number of runs and lower engine Reynolds numbers. LES provides an accurate intermediary compared with more wide spread application of RANS which provides the most cost effective form of CFD.

The applications of these CFD methodologies to turbomachinery is presented here highlighting the benefits of such research tools and the areas of caution. Starting with the application of DNS, although out of reach for the areas of interest here, it provides a clean overview of numerical simulations without the added complexity of a turbulence model.

DNS has been used to study the fundamental flow physics of many processes. It provides a highly accurate and complete view of a flow field down to the smallest length and time scales. It has been used to provide an understanding of processes such as boundary layer scaling (*Spalart*, 1988) and transition (*Wu et al.*, 1999), many of which are present in compressor cascades. A series of investigations performed at Reynolds number 138,000 on a V103 compressor cascade showed the effects of various flow phenomenon such as free-stream turbulence and incident wakes on the compressor cascade through the use of DNS (*Zaki et al.*, 2009, 2010; *Wissink et al.*, 2014).

The use of RANS modelling for turbomachinery is well established. RANS provides the most cost effective means of simulating the flow and many of the RANS models have been tuned to provide better accuracy for specific flows. However, the nature of RANS modelling means that no instantaneous flow features are simulated and only statistically averaged results are available, although RANS does provide a useful tool when looking at parameters such as blade loss where only averaged results are needed (*Chen et al.*, 1998). The prediction of unsteady phenomenon, such as wake interaction, have also been investigated with unsteady RANS. *Lardeau and Leschziner* (2004) perform a wake interaction of a turbine blade to highlight limitations of unsteady RANS in such cases. It was found that mesh resolution requirements were substantially increased when unsteady features were of interest, reducing unsteady RANS computational efficiency. It was also shown that unsteady RANS struggled with the different time scales of turbulent shedding of up-stream bars and the pitch-wise traversing period, resulting in poor turbulent energy prediction of the wakes. A study by *Iseler et al.* (2006) investigated wake

interaction on compressor blade using unsteady RANS and obtained similar results to Lardeau et al., highlighting the need for increased mesh resolution when looking at transient effects and a tendency for unsteady RANS to overestimate the coherence of unsteady structures, resulting in stronger interactions.

The use of LES in simulating turbomachinery flows has increased dramatically with the rapid development of high performance computers. LES provides an efficient means of investigating engine Reynolds number flows with reduced computational expense, compared to DNS, while still providing accurate results of unsteady phenomena and instantaneous flow features. With LES all the large scale motions are simulated while the fine scale dissipation is modelled reducing the need for DNS resolution meshes, as LES still models part of the flow the model choice is important as with RANS, both of which are reviewed in chapter 2.

With LES providing the added information of unsteady structures its application to turbomachinery flows is most appropriately applied to flows where unsteady phenomenon play an important role. *You et al.* (2007) looked at the effects of tip clearance on cascade losses using LES which provided an accurate means of tracing the trajectory and evolution of the tip clearance vortex as it was convected down-stream. The results showed improvements in predicting the decay and Reynolds stresses of the vortex over previous studies employing RANS methods. *McMullan and Page* (2010) used LES to predict compressor losses over a range of incidences at Reynolds number 700,000 and Mach 0.2. The results showed that LES predicted losses at off-design conditions reasonably well compared with experimental results, though the prediction was dependant on the slightly coarse wall mesh resolution and showed larger discrepancies at off-design incidences where turbulent breakdown occurs at the leading edge.

More recent studies by *Gourdain* (2013, 2015a) have focused on the comparison of LES and RANS and on good practice when using LES for turbomachinery applications. The first of these studies details the requirements of mesh resolution for wall resolved LES, and emphasises the need for mesh resolution to be adequate in the near wall region and not just at the wall, to properly resolve the flow. However the work also highlights that under-resolved LES compares very closely with resolved LES when predicting loss and efficiency. The second study highlights the difference seen in boundary layer development between RANS and LES showing the LES predicts unsteady effects of wake passing better though the time averaged results are very similar between RANS and LES at design conditions. *Medic et al.* (2016) investigated the performance of LES in capturing flow properties such as transition when compared with experimental data for a range of different profile shapes. The study showed LES performed well in capturing transition and boundary layer behaviour for the series of different aerofoils and suggest it may constitute a useful tool in the future for assessing loss of different designs.

Overall the use of LES in turbomachinery flows is proving useful in investigating unsteady effects that have previously been neglected in RANS studies. LES also provides a means of detailing the flow more precisely and improving the understanding of experimental investigations.

1.3 Summary

The literature shows a substantial amount or work has been done on understanding the fundamentals of flow dynamics surrounding a compressor. Improving our understanding of processes such as wake interaction and transition behaviour and the effects of blade shape and different operating conditions on performance. However, the majority of this work is experimental or if simulated, has been performed using either lower fidelity methods or at non-realistic engine Reynolds and Mach numbers. Recently there has been an increase in work moving toward simulations using both high fidelity methods and engine relevant Reynolds and Mach numbers. Though to date almost no high fidelity simulations have been performed at both engine relevant Mach and Reynold numbers. The few cases that have used high fidelity simulations tend to run at engine relevant Reynolds numbers but reduced Mach numbers. Furthermore the studies that have been performed at both engine relevant Reynolds number and Mach number focus on performance variations at design conditions.

As high fidelity simulations are still too expensive for commercial design, industry relies on RANS. However, with such a limited amount of high fidelity data available the possibility for optimisation of commercial RANS models is difficult, especially when relevant experimental set-ups are very costly to run. It is also well known that the performance of RANS deteriorates as the running conditions become more adverse, essentially RANS struggles when large scale turbulence occurs at the length scales RANS is trying to capture. To data no known detailed comparison of the performance of RANS under adverse running conditions, such as those found at off-design, with high fidelity simulations at engine relevant Reynolds and Mach numbers have been made. Which is what this work attempts to address, as a first step in further optimising RANS for off-design conditions.

Chapter 2

Formulation

2.1 Introduction

The study and examination of the fluid flows of interest performed here will be undertaken using computational fluid dynamics (CFD). The choice of CFD as the investigation tool, rather than an experimental analysis, is based on the complexities and extreme flow conditions found within a compressor cascade. CFD presents a much cheaper and more flexible means of studying the flow as small changes can be made to the investigation without expensive changes in experimental set-up. Further benefits of a numerical study are the knowledge of the complete flow field allowing accurate time averaged statistics of many quantities that could not be collected for the full flow field experimentally. Although CFD offers a cheaper means of investigating the flow compared with experimental set-ups, methods such as direct numerical simulation are still out of reach due to limited computational resource. For this reason the investigations will be performed using large eddy simulations which are less computational intensive but also provide a time accurate solution. Further simulations are also performed using Reynolds Averaged Navier-Stokes to investigate the effects of modelling on accuracy.

LES simulations are time resolved, unlike some other modelling techniques, which allow the evolution of turbulent structures, as they move though the flow domain, to be investigated giving greater detail and improving one's understanding of the physics involved. It is important to note that the use of LES introduce some limitations in accuracy of the numerical experiments. LES relies on a model to correctly capture the flow and in cases where the simulation is of complex untested geometries one must trust the CFD model to capture the flow correctly. This emphasises the importance of proper verification and the need to run test cases to ensure the solver behaves correctly.

In this chapter the governing equations will be outlined. Firstly the full Navier-Stokes equations will be given followed by the implementation of the RANS and LES models used, including the numerical set up of the solver. Followed by a lower Reynolds number verification case.

2.2 Governing Equations

The governing equations solved here are the full compressible LES equations including the energy equation which describe the motion of a compressible fluid. The LES equations are solved in conservative form written in terms of flux quantities to improve the numerics as well as capture any flow field discontinuities, such as shocks. The flux form of the equations allows the derivatives in each direction to be called fewer times per Runge-Kutta sub-step reducing the computational time and the number of stored arrays.

The full non-dimensional compressible Navier-Stokes equations are given first, the non-dimensionalisation can be found in appendix B.

The full Navier-Stokes equations are given as:

$$\frac{\partial \mathbf{Q}}{\partial t} + \frac{\partial \mathbf{F_1}}{\partial x} + \frac{\partial \mathbf{F_2}}{\partial y} + \frac{\partial \mathbf{F_3}}{\partial z} = \mathbf{S} \tag{2.1}$$

where

$$\mathbf{Q} = \begin{Bmatrix} \rho \\ \rho u_i \\ \rho E \end{Bmatrix} \tag{2.2}$$

$$\mathbf{F_k} = \begin{Bmatrix} \rho u_k \\ \rho u_i u_k + \delta_{ik} p - \sigma_{ik} \\ u_k(\rho E + p) - q_k - u_j \sigma_{kj} \end{Bmatrix} \tag{2.3}$$

$$\mathbf{S} = \begin{Bmatrix} 0 \\ \rho f_k \\ \rho(u_j f_j) \end{Bmatrix} \tag{2.4}$$

where f_k terms are body forcing terms such as gravitational or buoyancy forces. The stress tensor is defined as

$$\sigma_{ij} = 2\frac{\mu}{Re} S_{ij} + \delta_{ij} \lambda S_{kk} \tag{2.5}$$

where

$$S_{ij} = \frac{1}{2}\left(\frac{\partial u_i}{\partial x_j} + \frac{\partial u_j}{\partial x_i}\right),$$

and the bulk viscosity, λ, is approximated as $\lambda \approx -2/3\frac{\mu}{Re}$. Finally the heat flux is calculated based on a non-dimensional thermal diffusivity as

$$q_k = \frac{-\mu}{(\gamma-1)M^2 PrRe}\frac{\partial T}{\partial x_k}.$$

The equations are non-dimensionalised using the free-stream inflow fluid properties and it is assumed the fluid acts as a perfect gas allowing the pressure to be solved from the perfect gas law

$$p = \frac{\rho T}{\gamma M^2}$$

The total energy is given as

$$E = \frac{T}{(\gamma(\gamma-1)M^2)} + \frac{u_i u_i}{2}.$$

The simulations involve air over relatively small temperature and pressure ranges, the Prandtl number is assumed constant at $Pr = 0.72$, as is the isentropic exponent $\gamma = 1.4$. Finally the molecular viscosity is calculated using Sutherland's law (*White*, 1991), setting the Sutherland constant to 0.36867.

2.3 Implementation

The equations given above are in physical coordinates and are transformed to a uniform coordinate system first before being solved. The transformation in this case is restricted to two dimensions by using a Fourier expansion in the third dimension. This is possible as the simulations are periodic in the span-wise direction. This also allows the transformation to be simplified and improves the computational speed. The benefits of this transformation are realised by using a structured multiblock mesh in the plane and the afore mentioned Fourier expansion in the span-wise direction.

The transformed equations for two dimensions are given by the following:

$$\frac{\partial \widehat{\mathbf{Q}}}{\partial t} + \frac{\partial \widehat{\mathbf{F_1}}}{\partial \xi} + \frac{\partial \widehat{\mathbf{F_2}}}{\partial \eta} = 0 \tag{2.6}$$

where

$$\widehat{\mathbf{Q}} = \mathbf{JQ} \tag{2.7}$$

$$\widehat{\mathbf{F_1}} = \mathbf{JF_1}\frac{\partial \xi}{\partial x} + \mathbf{JF_2}\frac{\partial \xi}{\partial y} \tag{2.8}$$

$$\widehat{\mathbf{F_2}} = \mathbf{JF_1}\frac{\partial \eta}{\partial x} + \mathbf{JF_2}\frac{\partial \eta}{\partial y}, \tag{2.9}$$

$$\tag{2.10}$$

and the Jacobian is given as:

$$\mathbf{J} \equiv \begin{vmatrix} \dfrac{\partial x}{\partial \xi} & \dfrac{\partial y}{\partial \xi} \\ \dfrac{\partial x}{\partial \eta} & \dfrac{\partial y}{\partial \eta} \end{vmatrix} \tag{2.11}$$

Solving the equations in the computational domain ξ, η allows the discretisation stencils to be optimised by assuming a constant distance between nodes, which ensures high-order accurate derivatives during the computations. A more detailed break down of the equations used is given in appendix appendix A

2.4 Reynolds Averaged Navier-Stokes Equations

One of the first methods used to simplifying the Navier-Stokes equations is to time average. This results in a set of equations that govern the mean flow field and was first derived by *Reynolds* (1895) and as such the mean flow equations are now know as the Reynolds averaged Navier-Stokes equations. The derivation of these equations are based on separating the flow variables into a time mean quantity and a fluctuation quantity.

$$\phi(x, y, z, t) = \langle \phi(x, y, z) \rangle + \phi'(x, y, z, t),$$

where $\langle \phi \rangle$ represents a time average of the form

$$\langle \phi \rangle = \frac{1}{\Delta t} \int_{t_0}^{t_0 + \Delta t} \phi(t) dt,$$

and $'$ represents the fluctuating quantity, defined as

$$\phi' = \phi - \langle \phi \rangle.$$

The benefits of solving the time averaged equations is in the majority of cases they provide the averaged quantities we are most interested in directly. They are also substantially cheap in terms of computational cost compared to solving a time resolved simulation.

Time averaging the Navier-Stokes equations and substituting the Reynolds decomposition for the flow variables results in the RANS equations, as the equations are also compressible they are further simplified using Favre averaging, which is a density weighted average, defined as

$$\widetilde{\phi} = \frac{\langle \rho\phi \rangle}{\langle \rho \rangle}.$$

The non-dimensionalised RANS equations are give as;

$$\frac{\partial \langle \mathbf{Q} \rangle}{\partial t} + \frac{\partial \langle \mathbf{F_1} \rangle}{\partial x} + \frac{\partial \langle \mathbf{F_2} \rangle}{\partial y} + \frac{\partial \langle \mathbf{F_3} \rangle}{\partial z} = 0 \tag{2.12}$$

where

$$\langle \mathbf{Q} \rangle = \begin{Bmatrix} \langle \rho \rangle \\ \langle \rho \rangle \widetilde{u_i} \\ \langle \rho \rangle \widetilde{E} \end{Bmatrix} \tag{2.13}$$

$$\langle \mathbf{F_k} \rangle = \begin{Bmatrix} \langle \rho \rangle \widetilde{u_k} \\ \langle \rho \rangle \widetilde{u_i}\widetilde{u_k} + \langle \rho u_i'' u_k'' \rangle + \delta_{ik}\langle p \rangle - \widetilde{\sigma_{ik}} - \langle \sigma_{ik}'' \rangle \\ \widetilde{u_k}(\langle \rho \rangle \widetilde{E} + \langle p \rangle) + \frac{\langle \rho u_k'' T \rangle}{(\gamma(\gamma-1)M^2)} + \widetilde{u_k}\langle \rho u_k'' u_j'' \rangle + \frac{\langle \rho u_k'' u_i'' u_i'' \rangle}{2} - \frac{-\mu}{(\gamma-1)M^2 PrRe}\frac{\partial \widetilde{T}}{\partial x_k} \\ -\frac{-\mu}{(\gamma-1)M^2 PrRe}\frac{\partial \langle T'' \rangle}{\partial x_k} - \widetilde{u_k}\widetilde{\sigma_{jk}} - \langle u_k'' \rangle \widetilde{\sigma_{jk}} - \widetilde{u_k}\langle \sigma_{jk}'' \rangle - \langle u_k \sigma_{jk}'' \rangle \end{Bmatrix} \tag{2.14}$$

The result of time averaging the Navier-Stokes equations is a set of unknown terms known as Reynolds stresses. In order to solve the equations these terms must be modelled. The Reynolds stresses, representing the turbulent fluctuations are unknown and modelled, meaning that the resultant flow field depends largely on the performance of the model to accurately predict the effects the stresses have on the averaged flow field. This has resulted in a substantial amount of research into RANS models thought this will not be reviewed here. The text by *Wilcox* (2006) provides a good review of common models.

2.4.1 The Closure Problem

The terms containing Favre or Reynolds fluctuating variables are unclosed and need to be modelled. In formulating the RANS models some of the terms can be neglected due to scaling as they are negligibly small at high Reynolds numbers, such as terms containing σ_{ij}'' and $\langle T'' \rangle$, reducing the number of unknowns. The most common approach to the closure problem is to relate the Reynolds stress terms ($\rho u_i'' u_j''$) to the mean shear using the Boussinesq approximation. This approximations assumes a linear relationship between the Reynolds stress and the mean

shear and is given as

$$-\rho u_i'' u_j'' \approx 2\mu_t \left(\widetilde{S_{ij}} - \frac{1}{3}\frac{\partial \widetilde{u_k}}{\partial x_k}\delta_{ij} \right) - \frac{2}{3}\langle\rho\rangle k\delta_{ij}, \tag{2.15}$$

where μ_t is the eddy viscosity obtained from the chosen turbulence model. In the Boussinesq approximation the term containing k is often ignored, based on scaling.

There are several approaches to solving the closure problem, with the simplest being an algebraic model. Algebraic models use the flow variables only to derive an approximation for the eddy viscosity though they are often too simple for practical problems, and suffer from turbulent history effects, i.e they do not account for effects such as turbulent energy diffusion.

Increasing the complexity of the closure problem solution are one equation models. These models try to address some of the short comings of the algebraic models by solving a single transport equation, often the turbulent kinetic energy equation, to account for effects such as turbulent diffusion.

Increasingly complex linear models are the two equations models that solve transport equations for two flow variables, often the turbulent kinetic energy and the turbulent dissipation or specific dissipation. The two equation models are based on solving the Boussinesq approximation, which makes several simplifications and assumptions, making it easier to derive transport scalars. However, the Boussinesq approximation is often not properly valid in complex flows where the mean shear rates are not linearly related to the Reynolds stresses. Despite this, two equation models do perform well enough to be useful and form the basis for most commercial RANS solvers.

2.4.1.1 SST RANS Model

The RANS simulations used in this study were performed in house by General Electric and used the Shear Stress Transport model (*Menter*, 1994) implemented in the commercial software ANSYS CFX. The SST model is a two equation model that solves transport equations for the turbulent kinetic energy, k, and ω to model the eddy viscosity.

$$\frac{\partial(\rho k)}{\partial t} + \frac{\partial(\rho u_j k)}{\partial x_j} = \tau_{ij}\frac{\partial u_i}{\partial x_j} - \beta * \rho\omega k + \frac{\partial}{\partial x_j}\left[(\mu + \sigma_k\mu_t)\frac{\partial k}{\partial x_j}\right] \tag{2.16}$$

$$\frac{\partial(\rho\omega}{\partial t} + \frac{\partial(\rho u_j\omega)}{\partial x_j} = \frac{\gamma}{\nu_t}\tau_{ij}\frac{\partial u_i}{\partial x_j} - \beta\rho\omega^2 + \frac{\partial}{\partial x_j}\left[(\mu + \sigma_\omega\mu_t)\frac{\partial\omega}{\partial x_j}\right] + 2(1 - F_1)\frac{\rho\sigma_{\omega 2}}{\omega}\frac{\partial k}{\partial x_j}\frac{\partial\omega}{\partial x_j} \tag{2.17}$$

From these two equations the eddy viscosity is computed from

$$\mu_t = \frac{\rho a_1 k}{max(a_1\omega, \Omega F_2)}. \tag{2.18}$$

Additional functions are given as:

$$\begin{aligned} F_1 =& tanh(arg_1^4) \\ arg_1 =& min\left[max\left(\frac{\sqrt{k}}{\beta * \omega d}, \frac{500\nu}{d^2\omega}\right), \frac{4\rho\sigma_{\omega 2}k}{CD_{k\omega}d^2}\right] \\ CD_{k\omega} =& max\left(2\rho\sigma_{\omega 2}\frac{1}{\omega}\frac{\partial k}{\partial x_j}\frac{\partial \omega}{\partial x_j}, 1o^-20\right) \\ F_2 =& tanh(arg_2^2) \\ arg_2 =& max\left(2\frac{\sqrt{k}}{\beta * \omega d}, \frac{500\nu}{d^2\omega}\right) \end{aligned}$$

where d is the distance from the field point to the nearest wall and Ω is the vorticity magnitude.

The SST $k-\omega$ model is chosen here as it provides the best performance currently available in commercial RANS codes. The SST model is known to provide accurate simulation of flows with adverse pressure gradients and separations, and combines the stability of the $k-\epsilon$ in the free-stream avoiding the over-sensitivity associated with the standard $k-\omega$ model. Making it an ideal candidate for compressor cascade flows.

2.5 Large Eddy Simulations Navier-Stokes Equations

The large eddy simulations (LES) equations are formed in a similar manner to the RANS equation, except in this case the Navier-Stokes equations are spatially filtered not averaged in time. The process of spatially filtering the equations is done in a similar way, first by introducing a spatially filtered variable. The type of filter function used affects the resultant filtered equations, some of which are quite difficult to work with. For this reason the formulation of the LES equations usually uses homogeneous spatial filters. The filtering operation can be described as

$$\overline{\phi} = \int G(r,x)\phi(x-r,t)dr, \tag{2.19}$$

where the integration is performed over the entire domain, and the specified filter satisfies

$$\int G(r,x)dr = 1.$$

Applying this filtering to the flow variables results in a set of filtered flow quantities that can be decomposed in a similar manner as the time averaged quantities. This results in a fluctuating quantity of a filtered variable defined as

$$\phi' = \phi - \overline{\phi}. \tag{2.20}$$

Favre filtered quantities are also introduced for the derivation of the LES equations. In this case the Favre filtering is defined in the same manner but now with a spatially filtered density,

$$\widetilde{\phi} = \frac{\overline{\rho\phi}}{\overline{\rho}} \tag{2.21}$$

and similarly a Favre fluctuation

$$\phi'' = \phi - \widetilde{\phi}$$

The Navier-Stokes equations can then be reformed into the LES equations given as

$$\overline{\mathbf{Q}} = \begin{Bmatrix} \overline{\rho} \\ \overline{\rho}\widetilde{u_i} \\ \overline{\rho}\widetilde{E} + \frac{1}{2}\overline{\rho}\tau_{ii} \end{Bmatrix} \tag{2.22}$$

$$\overline{\mathbf{F_k}} = \begin{Bmatrix} \overline{\rho}\widetilde{u_k} \\ \overline{\rho}\widetilde{u_i}\widetilde{u_k} + \delta_{ik}\overline{p} - \widetilde{\sigma_{ik}} + \tau_{ik} \\ \widetilde{u_k}(\overline{\rho}\widetilde{E} + \overline{p}) - \widetilde{q_k} - \widetilde{u_j}\widetilde{\sigma_{kj}} + \frac{1}{2}\widetilde{u_k}\overline{\rho}\tau_{jj} \end{Bmatrix} \tag{2.23}$$

It is seen in eqs. (2.22) and (2.23) that an additional term $\frac{1}{2}\overline{\rho}\tau_{ii}$ is present for the energy time derivative, this term representing the energy of the residual filtered field, while two additional terms τ_{ik} and $\frac{1}{2}\widetilde{u_k}\overline{\rho}\tau_{ii}$ are present for the momentum and energy fluxes. These two terms represent the transport of the sub-grid scale momentum and energy respectively.

2.5.1 The Closure Problem

Spatially filtering the Navier-Stokes equations results in a set of unknown terms just as time averaging the Navier-Stokes equations does. In this case the terms are slightly different although the same problem arises, how to model or account for the unknown terms.

In LES the unknown residual stress tensor is closed by introducing the linear eddy-viscosity model

$$\tau_{sgs:ij} = -2\nu_{sgs}\widetilde{S_{ij}}, \tag{2.24}$$

where $\tau_{sgs:ij}$ is the residual stress tensor and ν_{sgs} is the eddy-viscosity. Secondly, using an analogy to the mixing length hypothesis the eddy-viscosity can be modelled as

$$\nu_{sgs} = (C_s\Delta)^2\left(2\widetilde{S_{ij}}\widetilde{S_{ij}}\right)^{\frac{1}{2}}, \tag{2.25}$$

where C_s is a constant and Δ is the filter width.

This model was first introduced by *Smagorinsky* (1963) but fails to appropriately damp the eddy viscosity in areas of pure shear such as the boundary layer, which introduces errors and must be corrected for with the use of wall damping functions.

However, this model does form the basis for many newer models where the mixing length analogy is used. For the simulations performed in the studies presented here the more common Wall adaptive Local Eddy viscosity (WALE) model is used and is described next.

2.5.1.1 The WALE Model

The WALE model, (*Nicoud and Ducros*, 1999), is the model that has been chosen for use in all the LES simulations performed here. The WALE model tries to address the main failings of the Smagorinsky model, which lie in the choice of invariant used to construct it. The Smagorinsky model is based on the second invariant of the velocity gradient tensor, which means the model does not take into account the rotational straining of the velocity when calculating the eddy viscosity. Furthermore the second invariant remains a similar order of magnitued near the wall even in laminar boundary layers meaning the eddy viscosity shows non-physical behaviour at the walls. The WALE model uses the traceless symmetric square of the velocity gradient tensor as a basis for the eddy viscosity. Letting $\widetilde{g}_{ij} = \frac{\partial \widetilde{u}_i}{\partial x_j}$ be the velocity gradient tensor then the proposed invariant tensor is given as

$$\mathcal{D}^d_{ij} = \frac{1}{2}\left(\widetilde{g}^2_{ij} + \widetilde{g}^2_{ij}\right) - \frac{1}{3}\delta_{ij}\widetilde{g}^2_{kk}, \tag{2.26}$$

where $\widetilde{g}^2_{ij} = \widetilde{g}_{ik}\widetilde{g}_{kj}$. By using the Cayley-Hamilton theorem of linear algebra and rewriting eq. (2.26) in terms of the symmetric and anti-symmetric parts of the velocity gradient tensor following relation can be formed

$$\mathcal{D}^d_{ij}\mathcal{D}^d_{ij} = \frac{1}{6}\left(S^2S^2 + \Omega^2\Omega^2\right) + \frac{2}{3}S^2\Omega^2 + 2IV_{S\Omega} \tag{2.27}$$

where

$$S^2 = \widetilde{S}_{ij}\widetilde{S}_{ij}, \quad \Omega^2 = \widetilde{\Omega}_{ij}\widetilde{\Omega}_{ij}, \quad IV_{S\Omega} = \widetilde{S}_{ik}\widetilde{S}_{kj}\widetilde{\Omega}_{jl}\widetilde{\Omega}_{li}.$$

Using the relationship given in eq. (2.27), a new model can be found by scaling the operator tensor correctly in order to get the correct behaviour for near wall flow as well as far field flow. The WALE model proposes the following for the eddy viscosity,

$$\nu_{sgs} = (C_w\Delta)^2\frac{(\mathcal{D}^d_{ij}\mathcal{D}^d_{ij})^{3/2}}{(\widetilde{S}_{ij}\widetilde{S}_{ij})^{5/2} + (\mathcal{D}^d_{ij}\mathcal{D}^d_{ij})^{5/4}}, \tag{2.28}$$

where Δ is a characteristic length of the grid cell size, defined here as $\Delta = \sqrt{dx^2 + dy^2 + dz^2}$. The constant C_w is set to 0.325 as suggested by *Nicoud and Ducros* (1999).

2.6 Numerical Implementation

The solver used in this investigation is the in-house code HiPSTAR , originally developed by Professor Richard Sandberg. The code solves the full compressible Navier-Stokes equations either directly using DNS or through LES. The code has previously been used to perform in-depth studies on compressible pipe flows (*Sandberg et al.*, 2012), supersonic wakes (*Sandberg*, 2012) and turbulent jets in coflow (*Sandberg et al.*, 2011). More recently work by *Sandberg et al.* (2015) used the code to simulate low pressure turbines.

The HiPSTAR code is a structured mesh solver optimised for aerodynamic and aeroacoustic problems. The code employs two forms of numerical methods firstly a finite difference method for the in plane discretisation, and a Fourier spectral method for the span-wise discretisation. The finite difference in plane use a 4^{th}-order five-point scheme, the boundaries are dealt with using the *Carpenter et al.* (1999) boundary stencils. The choice of a Fourier spectral method for the span-wise discretisation was made to reduce the computational expense of a full 3D finite difference scheme as well as improves numerical performance by reducing memory usage. The Fourier expansion in the third direction also allows the numerical scheme to be run as a 2D set-up by calculating only the zeroth mode of the Fourier expansion. This enables the simulation to be expanded into 3D simply by adding Fourier modes and a span-wise extent without reinitialising the simulation, which can be used to speed up flow transitions.

To improve stability the code utilizes skew-symmetric splitting of the non-linear terms (*Kennedy and Gruber*, 2008), and employs a sixth-order accurate standard difference filter, to damp numerical oscillations. Lastly the time integration of HiPSTAR uses a low-storage 4^{th}-order accurate five-step Runge-Kutta scheme by *Kennedy et al.* (2000) to avoid excessive memory usage.

The code is a structured mesh solver and uses multi-block meshes to accommodate complex geometries. In order to deal with metric discontinuities between blocks a characteristic interface condition is employed as detailed by *Kim and Lee* (2003).

Finally the HiPSTAR code offers the option to solve the equations using LES as well, using either the Smagorinsky model or the Wall Adapting Local-eddy Viscosity model (WALE) (*Nicoud and Ducros*, 1999).

2.7 Boundary Conditions

In order to complete the "set-up" appropriate boundary conditions are required to ensure that there are no unwanted reflections of acoustic waves or forcing of the flow in an unnatural way.

To help explain the boundary conditions employed fig. 2.1 shows an outline of a generic compressor cascade flow domain, detailing where certain boundary conditions are applied.

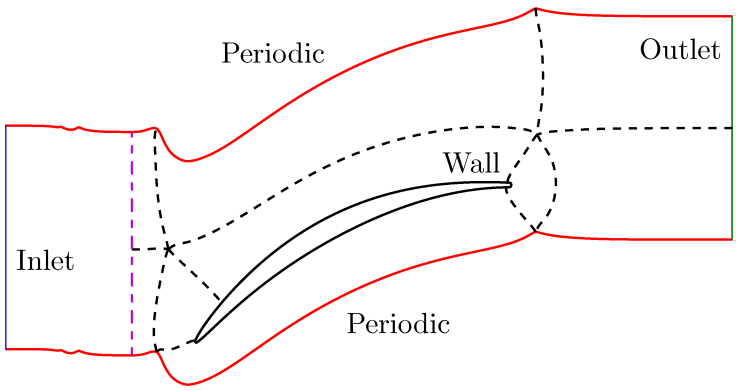

Figure 2.1: Flow domain of the compressor, showing the multiblock set-up and the boundaries.

2.7.1 Inlet Boundary

The inlet boundary conditions for the compressor cases are set as fixed with a prescribed inflow velocity triangle and density. Depending on the simulation interest free-stream turbulence may be superimposed on to the prescribed inflow. The artificial fluctuations are evaluated using the digital filter turbulence method by *Klein et al.* (2003) which produces fluctuations based on prescribed length scales and intensities. This method is shown to produce good homogeneous turbulence which develops quickly.

For the cases where no inflow turbulence is needed and a clean flow is desired, a sponge region is also added to the inflow. The sponge is achieved by a weighted ramping function between the calculated flow quantities and the prescribed inflow as

$$\phi = (1 - \omega)\phi_{inlet} + \omega\phi_{domain},$$

where ω is set by the user to achieve the desired level of damping.

2.7.2 Outlet Boundary

The outlet boundary is treated using the characteristic boundary condition described in *Sandberg and Sandham* (2006). This boundary treatment is performed by converting the Navier-Stokes equations into a 1D quasi wave equation normal to the boundary, neglecting the viscous terms, which is then solved to obtain the values of the variables at the boundary. The characteristic wave amplitudes of these equations are calculated and or set accordingly to ensuring the correct passage of information, in this case the non-reflective propagation of waves out of the flow domain. The transformation of the Navier-Stokes equations introduces some approximations as the viscous terms are neglected in the calculation of the characteristics, suggesting that all information is convected or travels at higher speeds than in the viscous case. However, this is

not always a valid assumption as viscous terms can be large in some cases. Such as in the wake region or in the boundary layers, where the viscous terms are more dominant, resulting in a potential error. A further issues is that the equations are derived from the linearized Navier-Stokes equations based on the assumption that perturbations are small, though this is not the case when turbulent structures pass.

The characteristic boundary conditions is prescribed as follows. The solution of the quasi 1D wave equations of the primitive variables, neglecting viscous terms and linearizing results in a set of characteristic velocities,

$$\lambda_1 = u_1 - c \tag{2.29}$$

$$\lambda_2 = \lambda_3 = \lambda_4 = u_1 \tag{2.30}$$

$$\lambda_5 = u_1 + c, \tag{2.31}$$

$$\tag{2.32}$$

where λ_1 and λ_5 correspond to the propagation of sound waves into and out of the domain, respectively, c is the speed of sound, and λ_2, λ_3 and λ_4 are the propagation of entropy waves and the convection of the pitchwise and span-wise velocities u_2, u_3.

By manipulating the wave equations accordingly, the time variation of the flow variables can be found in terms of the characteristic wave amplitudes, found from the wave equations. These are either calculated from within the domain or specified as a boundary condition to close the system. In this case the outlet boundary condition used here only has one unknown characteristic λ_1 which is the pressure wave moving into the domain. For the outlet boundary condition we wish to enforce an exit static pressure. If this is imposed explicitly it would result in reflected waves and domain disturbances. Ideally a completely non-reflective boundary would be best, which would be achieved by setting $\mathcal{L}_1$ to zero, where $\mathcal{L}_1$ is the characteristic wave amplitude for the pressure. However this is not a well posed problem and would allow the mean pressure of the system to drift. In order to avoid this $\mathcal{L}_1$ is manipulated in such a way as to drive the mean pressure toward the desired value. This is achieved by setting

$$\mathcal{L}_1 = K(p - p_{exit}),$$

where K is a constant to adjust the forcing appropriately. Once the pressure converges on the desired exit static pressure the value of $\mathcal{L}_1$ tends to zero which reduces the magnitude of any incoming waves, making the boundary less reflective.

2.7.3 Pitch wise Treatment

The pitchwise treatment of the flow domain is based on the periodicity of the problem. In a compressor it is assumed that each blade is identical allowing the flow domain to be broken down into simple periodic sections spanning between two adjacent blades or passages. The pitchwise boundaries are thus periodic and the boundaries are treated as if there was a neighbouring block equal to that on the opposite side of the simulated domain. Numerically this is done by passing the flow solution of the bottom boundary to the top boundary and vice versa using the characteristic interface conditions, as the two boundaries can be thought of as neighbouring blocks. This means that any information passed out of or into the bottom boundary is seen coming into or out of the top.

2.7.4 Span wise Treatment

Because the span-wise extent of the domain is performed using a Fourier spectral method there is no need to apply any span-wise boundary condition. This is implicitly done by the Fourier method which assumes that the domain is periodic in the span-wise extent. This in essence makes the span-wise domain infinitely long. However, the length of the periodic section or span-wise extent simulated does determine the maximum wave length that can exist in the span-wise fluctuations.

2.7.5 Blade wall Treatment

The blade wall is treated as a non-slip boundary whereby after every Runga-Kutta step the boundary points are updated by setting the velocities to zero at the wall. The wall is also treated as adiabatic in these simulations as there is limited information in the reference material to set the blade temperature accurately. This is achieved by calculating the temperature of the wall using the 4th order finite difference wall stencil and setting the wall temperature derivative to zero. The use of adiabatic conditions is also justified in the early stages of a compressor where no blade cooling is necessary as the temperature of the fluid is still relatively low.

2.7.6 Sliding Mesh Interface

For the addition of incoming wakes a further sliding internal boundary is required. The sliding interface is outlined by *Johnstone et al.* (2015). The sliding interface allows the introduction of a set of body fitted cylinders up-stream of the cascade, which can be translated in the pitchwise direction.

The sliding mesh method employs the same characteristic interface conditions used for inter-block communication to overcome mesh discontinuities and allows for easier and cheaper communication.

2.7.7 Flow Initialisation

It is found that due to the diffusive nature of the flow in a compressor, the simulations are very sensitive to the flow initialisation. It was found that depending on the accuracy of the flow initialisation, initially done with constant density and velocity magnitude, there existed quite strong pressure waves and shock waves which introduced restrictive time steps and numerical instabilities.

The most effective way was found to set the inlet values, as applied by the boundary condition, and vary the flow quantities isentropically to the prescribed exit Mach number. The exit Mach number is found by assuming a constant axial flow rate and calculating the exit static pressure as a variation in the flow momentum.

The initialisation routine can be better described as follows.

Working forward from the inlet, the pressure ratio can be estimated as follows,

$$\Delta p = \frac{1}{2}\Delta u_i u_i. \tag{2.33}$$

The change in velocity magnitude is estimated from the change in pitchwise velocity as the stream-wise velocity is assumed constant. This is done by assuming the flow exits the cascade at close to the metal angle of the blade. In reality the flow is not properly aligned so a slight variation of a few degrees is added, in this example $\approx 5°$.

$$\Delta u_y = u_{y:in} - u_{y:out} = u_{x:in}(sin(\theta) - tan(5)). \tag{2.34}$$

Finally the pressure ratio is estimated as:

$$\Delta p = 0.5\Delta {u_y}^2 \tag{2.35}$$

From this pressure ratio the exit Mach number can be estimated, starting with the inlet pressure, which in this case is calculated from the prescribed simulation Mach number and equation of state.

The inlet pressure ratio is found from the isentropic relationships,

$$\frac{p_t}{p_1} = \left(1 + \frac{\gamma - 1}{2}M^2\right)^{\frac{\gamma}{\gamma - 1}} \tag{2.36}$$

from this the exit pressure ratio is found using the estimated exit static pressure and inlet total pressure. Finally the exit Mach number can be calculated from the equation above.

$$M_{out} = \sqrt{\frac{\left[\left(\frac{p_t}{p_2}\right)^{\frac{\gamma-1}{\gamma}} - 1\right]}{\frac{\gamma-1}{2}}} \tag{2.37}$$

Once the exit Mach number is know, the flow is initialised by linearly varying the Mach number from the inlet to the exit. The flow variables are found using the isentropic relationships and total quantities calculated from the inlet conditions. The local velocity magnitude is calculated from the local Mach number and speed of sound and the stream wise and pitchwise components are calculated to align with the local camber.

2.8 Mesh generation

In all forms of numerical simulation, where the solution is found by disretising the domain of interest to solve the governing equations, an appropriate mesh is needed. Computational fluid dynamics is by no means an exception to this. The importance of appropriate mesh design is evident in the effects it can have on the solution. It is important that factors like mesh resolution, stretching and skewness are taken into consideration.

The meshes used for the LES simulations performed here have all been produced using an in-house code based on the work by *Gross and Fasel* (2008). The method solves a Poisson equation for the positions of the grid points and optimises the mesh in a manner to reduce curvature and smooth cell size variation.

The method starts by initialising a uniform mesh across each of the blocks in the flow domain. The mesh is then run allowing the internal points to move freely while fixing the inlet and outlet boundaries to moving in the pitchwise direction only. The blade points are found by ensuring that the first free point is normal to the blade surface. This is achieved by allowing the blade points to move along the line defining the boundary of the blade profile.

It was found that some trial and error was needed in order to optimise the block sizes to get appropriate block boundaries and mesh stretching. However the process is quite trivial requiring simple changes to the number of cells in the respective blocks and rerunning the mesh solver.

A view of the initialisation and final block boundaries is shown in fig. 2.2

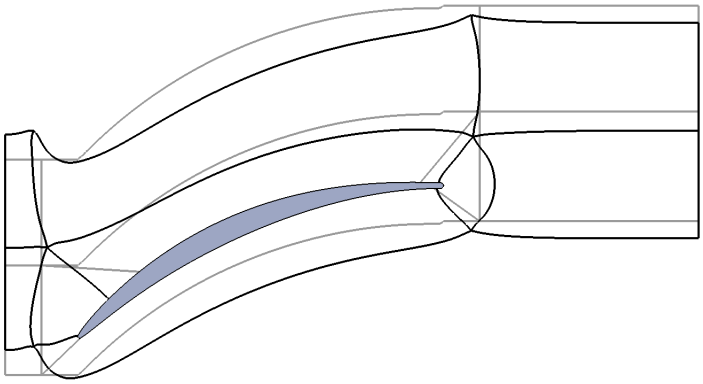

Figure 2.2: Initialisation (grey) and converged (black) block boundaries of Poisson mesh solver.

2.9 Post Processing Methods

Once the simulations have been performed an appropriate means of post processing is needed. In this section an overview of the main techniques used will be outlined.

2.9.1 Averaging Techniques

Turbulent flow is a statistically random phenomenon as such it is easiest to deal with averaged quantities which can be more easily compared. Furthermore, LESs provide time resolved solutions which must be averaged in order to look at mean quantities.

The averaging of the flow variables is performed during run time where an instantaneous snap shot of the various flow quantities and their properties needed for post processing are captured. For all the simulations performed here the snap shots were taken every 10 times steps in order to ensure the samples provide a good statistical average without unnecessarily long run times. The resultant averaged quantities are then post processed to produce all other statistical quantities of interest, such as Reynolds stress.

The period over which the statistical averages are collected was determined for each set of simulations by comparing various statistical intervals, to ensure that the flow is converged, and that no further statistical variation occurred from the addition of more samples.

2.9.1.1 Mixed Out Quantities

When looking at compressor performance, such as pressure losses, the results depend on how the averaged quantities are calculated. This can be done in several ways with the simplest being an area average, to obtain the averaged quantities at plane of interest. However, as the flow is

compressible a more accurate method is to calculate a density weighted average to account for changes in the density of the flow. Both methods will provide a reasonable comparison between different simulations but there are limitations with each and comparisons can be skewed if one of the simulations has a higher density variation, such as a compressor running at off-design conditions. The use of mass averaging does take this into account but it is also affected by the location at with the averaging is performed. To over come this the mixed out average is used to calculating averaged quantities, (*Prasad*, 2005).

The method is based on conserving mass, momentum and energy between two states such that the input state from the simulations matches a state where the flow properties are uniform. The mixed out average can be thought of as allowing the fluid to converge to a steady state conditions in a inviscid container without external heat flux.

Firstly the integral of the statistically averaged non-uniform state variables defined as:

$$\dot{M} = \int \widetilde{\rho}(\widetilde{u_i}n_i)dA \tag{2.38}$$

$$M_1 = \int \widetilde{\rho}(\widetilde{u_i}n_i)\widetilde{u_1}dA + \int \widetilde{p}(e_{x;i}n_i)dA \tag{2.39}$$

$$M_2 = \int \widetilde{\rho}(\widetilde{u_i}n_i)\widetilde{u_2}dA + \int \widetilde{p}(e_{y;i}n_i)dA \tag{2.40}$$

$$M_3 = \int \widetilde{\rho}(\widetilde{u_i}n_i)\widetilde{u_3}dA + \int \widetilde{p}(e_{z;i}n_i)dA \tag{2.41}$$

$$E = \frac{\gamma R}{(\gamma - 1)} \int \widetilde{p}(\widetilde{u_i}n_i)\widetilde{T}dA + \frac{1}{2}\int \widetilde{p}(\widetilde{u_i}n_i)\widetilde{u_j u_j}dA, \tag{2.42}$$

are calculated, where ($\sim$) are Favre averaged variables and e_1, e_2, e_3 are the unit vector in x,y,z directions respectively and n is the normal vector to the area surface. To formulate the mixed out quantities the integrated variables must satisfy the following.

$$\dot{M} = \overline{\rho u}A \tag{2.43}$$

$$M_1 = \dot{M}\overline{u_1} + \overline{p}A_1 \tag{2.44}$$

$$M_2 = \dot{M}\overline{u_2} + \overline{p}A_2 \tag{2.45}$$

$$M_3 = \dot{M}\overline{u_3} + \overline{p}A_3 \tag{2.46}$$

$$E = \frac{\dot{M}\gamma}{\gamma - 1}\frac{\overline{p}}{\overline{\rho}} + \frac{\dot{M}}{2}(\overline{u_i u_i}) \tag{2.47}$$

where (-) are the mixed out variables.

All the simulations performed here are span-wise averaged and periodic the M_3 values are zero and not needed. The variables A_1, A_2, A_3 are the area projection on the respective axes of the line that has been integrated over.

These equations can then be rearranged to calculate the mixed out values.

$$\left(E - \frac{\dot{M}\overline{u_1^2}}{2} + \frac{\dot{M}\overline{u_2^2}}{2}\right)\frac{\gamma - 1}{\overline{u_1}\gamma} = \overline{p} \tag{2.48}$$

Substituting for u_2

$$\left(E - \frac{\dot{M}\overline{u_1^2}}{2} + \frac{M_2^2}{2\dot{M}}\right)\frac{\gamma - 1}{\overline{u_1}\gamma} = \overline{p} \tag{2.49}$$

Now substituting pressure in the axial momentum equation and rearrange for u.

$$M_1 = \dot{M}\overline{u_1} + \left(E - \frac{\dot{M}\overline{u_1^2}}{2} + \frac{M_2^2}{2\dot{M}}\right)\frac{\gamma - 1}{\overline{u_1}\gamma} \tag{2.50}$$

$$0 = \dot{M}\overline{u_1}^2 + \frac{(\gamma - 1)}{\gamma}E - \frac{(\gamma - 1)}{\gamma}\frac{\dot{M}\overline{u_1^2}}{2} - \frac{(\gamma - 1)}{\gamma}\frac{M_2^2}{2\dot{M}} - M_1 u_1 \tag{2.51}$$

$$0 = \left(\dot{M} - \frac{\dot{M}}{2}\frac{(\gamma - 1)}{\gamma}\right)\overline{u_1}^2 - M_1 u_1 + \left(E - \frac{M_2^2}{2\dot{M}}\right)\frac{(\gamma - 1)}{\gamma} \tag{2.52}$$

$$A = \left(\dot{M} - \frac{\dot{M}}{2}\frac{(\gamma - 1)}{\gamma}\right) \tag{2.53}$$

$$B = -M_1 \tag{2.54}$$

$$C = \left(E - \frac{M_2^2}{2\dot{M}}\right)\frac{(\gamma - 1)}{\gamma}. \tag{2.55}$$

Finally, solve for $\overline{u_1}$, the negative root is chosen to solve for the subsonic flow condition.

$$\overline{u_1} = \frac{-B - \sqrt{B^2 - 4AC}}{2A} \tag{2.56}$$

From this all other variables can now be found using the integral values and eq. (2.47) to provide a fully averaged uniform state.

2.9.2 Denton Loss Breakdown

The loss breakdown analysis proposed by *Denton* (1993) is a means of associating loss with certain processes that occur over a compressor blade. The analysis is based on applying a control volume to the trailing edge of a cascade as outline in fig. 2.3, and applying the conservation of

mass and momentum. The derivation makes the assumption that the flows are uniform across the passage and wake, as a results of this a certain amount of care is needed when applying the analysis to ensure the appropriate averaging technique is used. The control volume, fig. 2.3, shows a blade row with a stagger angle α, a trailing edge thickness of t and pitch of w. In the analysis the combined boundary layer quantities, from both pressure and suction surfaces, are given as δ^* and θ for displacement and momentum thickness respectively. In the application of the analysis that follows later on the same naming convention is used though the symbols δ^* and θ are also used to mean the momentum and displacement values from just a single surface but clarification is given where needed. In the derivation Denton assumes the flow is incompressible, which will be done here. However, for its application in this work this assumption is overcome by using numerical integration to capture any density variation.

Applying the mass balance across the control volume results in the following equation

$$\dot{m} = \rho u_1 (w - t - \delta^*) = \rho u_2 w \frac{\cos(\alpha - \delta)}{\cos(\alpha)} \approx \rho u_2 w (1 + \delta \tan(\alpha)), \tag{2.57}$$

where the last term assumes δ (which is the deviation of the exit flow) is small.

The deviation angle can be found by applying the momentum equation in the y direction to give

$$\delta \approx \frac{(p_s - p_2) w^2 \tan(\alpha)}{\rho u_1^2 (w - t - \delta^*)^2}, \tag{2.58}$$

again, assuming that δ is small.

Finally applying the momentum equation in the x directions gives

$$\frac{p_{t1} - p_{t2}}{0.5 \rho u_1^2} = \frac{u_2^2}{u_1^2}(2\delta \tan\alpha + 1) - 1 + 2\left(\frac{t + \delta^* + \theta}{w}\right) - C_{pb}\frac{t}{w}, \tag{2.59}$$

where C_{pb} is the trailing edge pressure coefficient defined as

$$C_{pb} = \frac{p_b - p_{ref}}{0.5 \rho u_i u_i}. \tag{2.60}$$

This eq. (2.59), can then be solved using the continuity equation and simplified by assuming that δ is zero, justified on the grounds that this assumption makes the entropy production almost independent of blade trailing edge stagger. These assumptions lead to the approximation of loss as

$$\omega = \frac{C_{pb} t}{w} + \frac{2\theta}{w} + \left(\frac{\delta^* + t}{w}\right)^2 \tag{2.61}$$

The method of applying the Denton loss analysis to a compressor cascade is described in greater detail in the results chapters, such as defining a boundary layer limit in an internal flow. The general outcome of the analysis is to provide a breakdown of the loss generated over a blade,

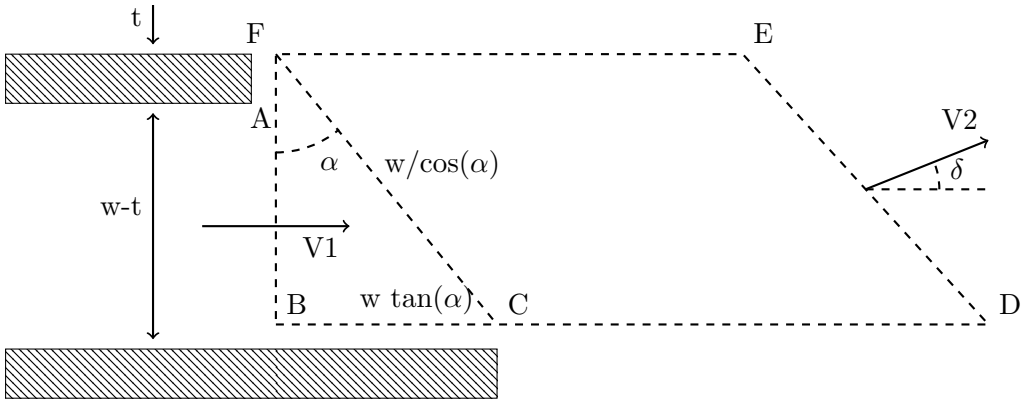

Figure 2.3: Control volume for Denton loss analysis. Control volume of interest is shown by the dashed line.

attributing the loss to three processes, a form factor loss, a momentum loss, and a displacement or blockage loss. These can thought of as the loss attributed to the pressure drop across the blade from leading edge to trailing edge due to its profile shape, a loss associated with the energy need to overcome viscous losses in the boundary layer and a loss associated with the increased work needed to drive the flow through a reduced passage are from boundary layer expansion.

2.9.3 Mechanical Work Potential

Extending the analysis performed by Denton, *Miller* (2013) proposed an analysis based on an exergy balance equation. The work tries to account for the effects of heat transfer and quantify the various viscous and thermal losses that occur. This is done by introducing a new quantity called mechanical work potential which measures the available work a fluid can do. By doing this the affects of viscosity or heating can be quantified by the changes in available work potential. Although the effects of thermal losses are not strongly applicable to most axial compressors, there is still thermal variation which can become relevant for a high pressure compressors when heating from viscous shearing can be notable.

The analysis focuses on introducing a new variable, the mechanical work potential, which is a measure of the useful work that can be extracted from a given fluid when exhausted isentropically to a given dead state pressure. The importance of this is that depending on the choice of the dead state pressure the relative losses of different stages in a turbo machine can be compared. This allows the loss for all the stages in a compressor to be compared if the dead state is chosen as atmospheric. This potentially shows where efforts to improve performance would results in the greatest pay-off.

The mechanical work potential is defined for a closed system as

$$\mathbf{m} = (e - e_{se}) + (\nu - \nu_{se}) + \frac{1}{2}u_i u_i, \tag{2.62}$$

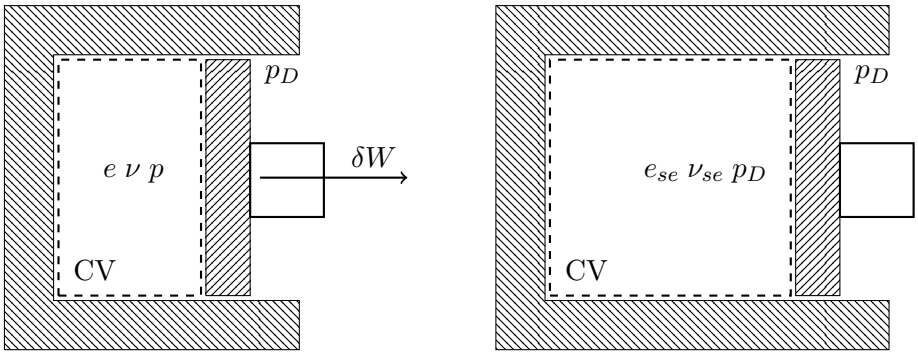

Figure 2.4: Isentropic expansion of a closed system cylinder to the dead state pressure, showing change in fluid variables.

and for an open system as

$$\mathbf{m_f} = \mathbf{m} + (p - p_D)\nu = (h - h_{se}) + \frac{1}{2}u_i u_i. \tag{2.63}$$

where the terms with subscript *se* are terms isentropically expanded to the dead state pressure p_D. For a perfect gas the mechanical work potential can be reposed as

$$\mathbf{m} = e\left(1 - \frac{T_{se}}{T}\right) + p_D(\nu - \nu_{se}) + \frac{1}{2}u_i u_i, \tag{2.64}$$

for a closed system and

$$\mathbf{m_f} = h\left(1 - \frac{T_{se}}{T}\right) + \frac{1}{2}u_i u_i \tag{2.65}$$

for an open system.

The closed system form $\mathbf{m}$ is associated with an isentropic expansion to the dead state pressure as illustrated in fig. 2.4. For the open system form of the mechanical work potential the addition of flow work allows it to be reformed in terms of enthalpy as shown by eq. (2.63)

The derivation of the balance equation is based on a control volume approach outlined in this case as a control volume encompassing the full blade, shown in fig. 2.5, but is not restricted to this volume.

Starting with the substantial derivative of the mechanical work potential,

$$\frac{\partial \rho \mathbf{m}}{\partial t} + \frac{\partial\left(\rho u_i \mathbf{m_f}\right)}{\partial x_i}, \tag{2.66}$$

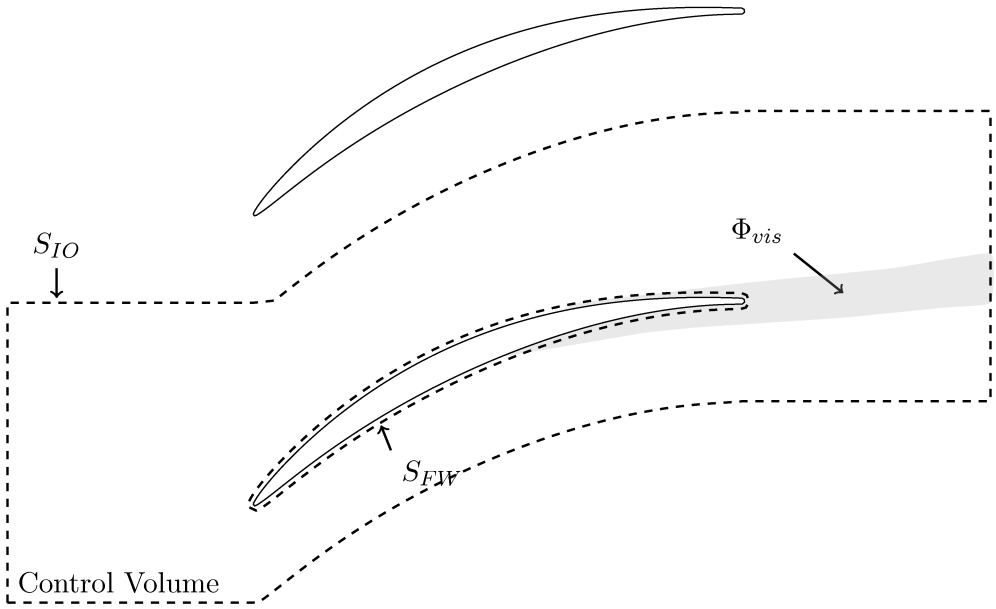

Figure 2.5: Control volume analysis for Miller mechanical work potential analysis. Control volume of interest is shown by the dashed line.

the local time rate of change and advection rate can be rewritten using the definition of the mechanical work potential and general vector identities giving

$$\begin{aligned}\frac{\partial \rho \mathbf{m}}{\partial t} + \frac{\partial \left(\rho u_i \mathbf{m_f}\right)}{\partial x_i} = &\left(1 - \frac{T_{se}}{T}\right)\left[\frac{\partial \rho e}{\partial t} + \frac{\partial \left(\rho u_i e\right)}{\partial x_i}\right] \\ &+ \left[\frac{\partial \left(\rho \frac{u_k u_k}{2}\right)}{\partial t} + \frac{\partial \left(\rho u_i \frac{u_k u_k}{2}\right)}{\partial x_i}\right] \\ &+ \frac{\partial \left(p_D u_i\right)}{\partial x_i} \\ &- \left(\frac{T_{se}}{T}\right) p \frac{\partial \left(u_i\right)}{\partial x_i}. \end{aligned} \tag{2.67}$$

Next Miller substituted the conservation equations for internal energy and kinetic energy from *Bird* (1957) and rearranged to give the equation for the mechanical work potential in differential form.

$$\begin{aligned}\frac{\partial \rho \mathbf{m}}{\partial t} + \frac{\partial \left(\rho u_i \mathbf{m_f}\right)}{\partial x_i} = &\left(1 - \frac{T_{se}}{T}\right)\left[-\frac{\partial \left(q_i\right)}{\partial x_i}\right] \\ &+ \frac{\partial \left(\tau_{ij} u_j\right)}{\partial x_i} \\ &- \left(\frac{T_{se}}{T}\right) \tau_{ij} \frac{\partial u_i}{\partial x_j} \end{aligned} \tag{2.68}$$

Noting that the heat flux term on the RHS can be rewritten in the form of a mechanical power associated with local heat transfer, and a change in mechanical work potential from internal

heat transfer across a local pressure gradient.

$$\left(1-\frac{T_{se}}{T}\right)\frac{\partial\left(q_i\right)}{\partial x_i}=\frac{\partial}{\partial x_i}\left[\left(1-\frac{T_{se}}{T}\right)q_i\right]-\left(\frac{T_{se}}{T}\right)\left(\frac{\gamma-1}{\gamma}\right)q_i\frac{1}{p}\frac{\partial p_i}{\partial x_i} \tag{2.69}$$

Substituting eq. (2.69) into the mechanical work potential conservation eq. (2.68), it can be rewritten and expanded using general vector identities to give the final form as:

$$\begin{aligned}\frac{d(\rho\mathbf{m})}{dt}+\frac{\partial\left(\rho u_i\mathbf{m_f}\right)}{\partial x_i}=&-\frac{\partial}{\partial x_i}\left[\left(1-\frac{T_{se}}{T}\right)q_i\right]\\&+\left(\frac{\gamma-1}{\gamma}\right)\frac{1}{p}\frac{\partial p}{\partial x_i}q_i\\&-(\tau_{ij}\frac{\partial}{\partial x_j})u_i\\&-\left(1-\frac{T_{se}}{T}\right)\left(\frac{\gamma-1}{\gamma}\right)\frac{1}{p}\frac{\partial p}{\partial x_i}q_i\\&+\left(1-\frac{T_{se}}{T}\right)(\tau_{ij}\frac{\partial}{\partial x_j})u_i\\&+\frac{\partial}{\partial x_j}\left[\overline{\overline{\tau}}_{ij}u_i\right]\end{aligned} \tag{2.70}$$

The mechanical work potential applied to compressors helps to improve our understanding of loss mechanisms. The mechanical work potential was originally derived for application to processes where the interest is in potential work extracted. However, the application of the mechanical work potential to compressors has a slightly different meaning. In a compressor the mechanical work potential provides a measure of the work potential lost during the compression process. In an isentropic compressor the mechanical work potential is conserved as it is changed from kinetic energy to internal energy. In a real process the change from kinetic energy produces heat through viscous dissipation which results in a loss of mechanical work potential. Although if the viscous heating occurs at higher pressures, relative to the reference state, it results in lower losses compared with viscous loss that takes place at a lower pressure. This is an important concept in the application of the mechanical work potential as is shows that losses for a later stage compressor are less detrimental when looking at the overall efficiency of the machine. This process allows some recovery of the viscous losses, depending on the compressor stage in question.

The terms of eq. (2.70) can be interpreted as a set of physical processes, with each term representing a certain phenomena. The various terms and their interpretation are outlined here.

Mechanical work from external heating

$$-\frac{\partial}{\partial x_i}\left[\left(1-\frac{T_{se}}{T}\right)q_i\right] \tag{2.71}$$

This term represent the change in mechanical work potential associated with external heat transfer to a local point. In this case it can be heat from outside the domain or from a different part of within the domain.

Thermal creation

$$\left(\frac{\gamma-1}{\gamma}\right)\frac{1}{p}\frac{\partial p}{\partial x_i}q_i \tag{2.72}$$

This term represents the creation of mechanical work potential from internal heat transfer across a local finite pressure gradients.

Viscous dissipation

$$-(\tau_{ij}\frac{\partial}{\partial x_j})u_i \tag{2.73}$$

This is the rate of viscous dissipations associated with the work done by shear forces in opposing fluid deformation. It is the rate of transfer of kinetic energy to internal energy.

Thermal recool

$$-\left(1-\frac{T_{se}}{T}\right)\left(\frac{\gamma-1}{\gamma}\right)\frac{1}{p}\frac{\partial p}{\partial x_i}q_i \tag{2.74}$$

This term represents the secondary effects thermal creation has on the fluid. In the thermal creation term mechanical work potential is changed based on heat transfer across a local finite pressure gradient. However the thermal recool is the effect the heat transfer has on the local point where the heat is being moved from and is determined by the local pressure. For example if heat is removed from a location where the pressure is higher than the reference then mechanical work potential is lost and visa versa.

Viscous reheat

$$\left(1-\frac{T_{se}}{T}\right)(\tau_{ij}\frac{\partial}{\partial x_j})u_i \tag{2.75}$$

Viscous reheat is similar to the process of thermal recool where secondary effects of one process produce changes in the mechanical work potential. The viscous reheat term captures the effects the viscous dissipations has on mechanical work potential related to the changes in internal energy. It is known that the effects of viscous dissipation result in a local heating as the kinetic energy of the fluid is changed to internal energy. If this local heating from the fluid shearing occurs at a higher pressure compared to the reference pressure then there is a local creation of mechanical work potential. This shows why dissipation at higher pressures within a compressor are less detrimental to the over all efficiency than dissipation at lower pressures.

Shear work

$$\frac{\partial}{\partial x_j}\left[\overline{\overline{\tau}}_{ij}u_i\right] \tag{2.76}$$

This term represents the shear work done on a local fluid element.

2.10 Low Reynolds Number Validation

2.10.1 Introduction

In order to verify the HiPSTAR code capabilities applied to compressor cascades, an initial study was performed. A low Reynolds number and low Mach number case was selected in order to gain insight into applying the code to more challenging cases while limiting the complexity and cost of the simulations as much as possible. The code has successfully been applied to low pressure turbines, *Sandberg et al.* (2015), but has not been used for the simulation of a compressor and although the set-up of the two cases is very similar, the flow dynamics can be quite different. Most notably the diffusive nature and adverse pressure gradient found in compressors can be quite challenging with regards to the stability of the simulation.

The paper by *Zaki et al.* (2010) was chosen for this initial test case as it is a low Reynolds number incompressible DNS simulation of a compressor cascade and provides comparable reference data which meets the desired criteria for the initial simulation. The paper investigates the effects of free-stream turbulence on transition though the interest here is only on replicating the results of a single case. The case chosen was the minimum turbulence intensity case.

Although the effects of free-stream turbulence are not investigated, the decision to include a nominal level of free-stream turbulence is based on two factors. Firstly it was deemed beneficial to verifying the code with a nominal level of free-stream turbulence as a certain level of free-stream turbulence will be present in any working compressor. Even the first stage will experience some free-stream turbulence due to up-stream fan blades in modern aero engines or purely from atmospheric fluctuations and inlet ducting. Secondly as the reference case was performed as an incompressible DNS the presence of acoustic fluctuations were neglected but these can have a notable effect on phenomena such as transition. Because of this it was deemed easier to compare cases where a known level of disturbance is applied rather than predict the effects of acoustic fluctuations on a clean flow field. that being said a further simulation without free-stream turbulence was also performed to verify the assumptions that compressibility in the current simulations resulted in different transitional behaviour.

2.10.2 Case Set-up

The simulations are performed on a NACA 65 aerofoil profile at a Reynolds number of 138,000, based on the inlet velocity and chord length, with an inflow turbulence intensity of 3.25% for the turbulent cases. The domain set-up is shown in fig. 2.6 with the nominal parameters outlined in table 2.1.

The simulations are performed using the WALE LES model. The domain extents are set to 0.5 chord up-stream of the leading edge, 1 chord down-stream of the trailing edge and 0.2 chord in the span. The boundary conditions applied to the domain are as follows. For the inflow a digital filter turbulence method was applied, superimposed onto a prescribed inflow velocity with fixed density. For the additional clean case the turbulence was replaced with a sponge applied at the inlet to reduce acoustic reflections. At the outflow only the static pressure is prescribed using a characteristic boundary condition treatment to reduce acoustic reflections and force the pressure to the desired value. In the span-wise and pitchwise directions periodic boundary conditions are applied while the blade boundary was set as non-slip and adiabatic.

The initial simulations done by *Zaki et al.* (2010) were incompressible while those performed here are compressible some additional complexity is introduced into the problem set-up. In order to try and replicate the flow conditions as accurately as possible, a low Mach number of 0.2 was chosen to limit any compressibility effects in matching the reference results.

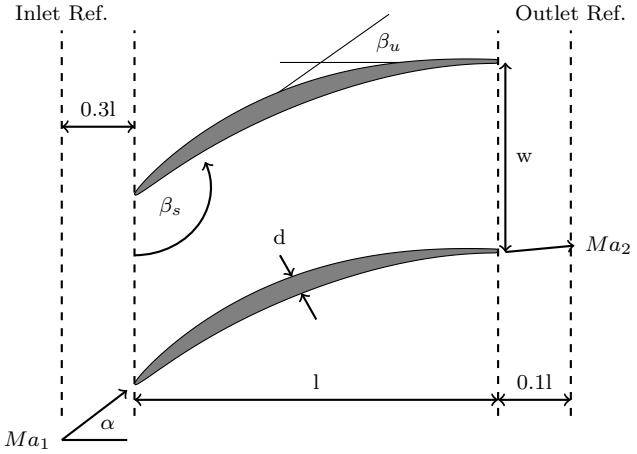

Figure 2.6: NACA 65 schematic showing general cascade geometry

Reference Conditions	
w/l = 0.59	$\beta_s = 112.5°$
$d_{max}/l = 0.0595$	$Re = 138\ 000$
$\beta_u = 48°$	α= 42°

Table 2.1: Nominal conditions for low Reynolds number verification simulation, taken from *Zaki et al.* (2010).

2.10.3 Simulation procedure

This case was chosen to verify the code applied to compressors and some details of the methods used to achieve good results are present here. It was found, as expected, that the pressure ratio setting affected the inflow angle. However no quick way of finding the required pressure ratio was found and it was necessary to let the flow developed and adjust it as necessary. Finding the pressure ratio setting is described in section 2.7.7 on initialisation to provided a good first estimate and reduced the fine tuning needed. The pressure ratio in the simulations is determined by altering the exit static pressure as the inlet static pressure is set by the chosen Mach number.

To start with the simulation is run for an initial period in 2D until the first transient stage has passed. The flow domain is then made three dimensional by extending it in the span-wise direction by adding modes to the Fourier decomposition. The higher modes are initialised with zeros and energy allowed to cascade into them as the simulation progresses. The simulation is then run through this second transient, as the three dimensional flow is established. Fine tuning of the exit static pressure is then done to obtain the correct flow angle at the reference plane as the flow develops. With the change to 3D, the inlet boundary condition is also changed to add the inlet turbulence generation, which helps accelerate the energy cascade to higher modes as at the inlet these modes are filled immediately.

Once the correct flow inlet angle was achieved, matching the value given in the reference paper, the blade loading was calculated and compared to ensure the values were correct. The final values of the case are shown in table 2.2 giving both the prescribed values and the final flow values. In the following figures detailing the comparison the cases are referred to as follows, for the coarse turbulent case (TuC), for the fine turbulent case (TuF) and for the fine clean case (T0F).

Property	Set Value	Case TuC coarse	Case TuF fine	Case T0F fine
Angle	42	42.0	42.0	42.0
U	1.0	1.0	1.0	1.0
Re	138,000	137,992	138,003	138,000
Mach	0.2	0.2	0.2	0.2
%Tu	3.23	2.8	2.9	0.0
%Tu LE	N/A	4.5	4.8	0.1

Table 2.2: Table showing flow condition for the *Zaki et al.* (2010) 3D Cascade verification. Table shows set and actual values for the simulations at a measurement plane 0.3 chord up-stream of the blade.

2.10.4 Mesh Quality

Before comparing the verification case with the reference an initial case was run with a coarse mesh. This first case forms a type of gird dependence study but was intentionally run in order to provide a bench mark to make a fine mesh with the required wall scaling. However, comparing these two cases provides a grid comparison, despite the scaling between them being quite large, that shows limited variation between the results. For the verification study two meshes have been produced, an initial mesh with 317,440 points in the plane and a second, which was used for the comparison runs, with 352,256 in the plane. The focus of the dependency study was to achieve the necessary wall normal resolution for the LES simulations. The free-stream in plane mesh quality for the remainder of the domain was left unchanged. The number of span-wise modes was also changed, from 64 to 96 to increase the span-wise wall resolution. Both meshes have the same domain sizes, as outline in the set-up, and span-wise extent of 0.2 chord. The final mesh count for the two meshes are $\sim$ 41 million and $\sim$ 68 million for the coarse and fine meshes respectively. The additional clean case was run using the fine mesh.

The comparison of the wall scaling for the two meshes is shown in fig. 2.7 where it can be seen that the wall scaling in the span-wise and wall normal show clear variation while the wall tangential scaling is very similar. The change in behaviour of the tangential wall scaling seen in the coarse mesh is due to a change in transition behaviour for the base mesh. The fine mesh shows a wall normal scaling of $y^+ \approx 2$ compared with $y^+ \approx 3$ for the base mesh. This value maybe considered too large for wall resolved LES, however for the higher Reynolds number cases that were planned for later studies the resolution would be limited to similar values due to computational expense, so it was desirable to verify the code under similar conditions. Furthermore it has been highlighted by *Gourdain* (2013) that the importance of the first cell resolution can be easily outweighed if the near wall mesh scaling is inadequate. For this reason it was decided that improving the near wall resolution at the expense of the first cell was more beneficial.

The fine mesh scaling was set using the coarse mesh to estimate the expected skin friction and setting the wall normal grid spacing appropriately. This first iteration was run for a short period,

≈ 3 flow through units to allow the flow to develop, and the wall resolution checked. The fine mesh was then iterated upon and the final mesh produced. The comparison with the clean case shows some minor difference to the fine case due to the changes in the flow due to the free-stream turbulence.

The energy spectrum for the two meshes at two points within the flow domain are shown in fig. 2.8. The points are chosen as one up-stream at the inlet reference plane and one down-stream at 1.4 chord from the leading edge. The energy spectrum comparison shows good correlation for high wave numbers and a clear cascade for all cases. This suggest the mesh resolution is adequate to ensure the spatial filtering cut off is within the inertial range and not affecting the large scale motions. The spectrum for the clean case is also included and shows quite a substantial difference, most notably a lack of any form of disturbance in the free-stream as expected. There is an interesting feature seen in all cases though, in the form of a peak seen at a wave number of ≈ 63 for the inlet point. This peak is associated with the natural shedding of the blade that causes global pressure fluctuations, highlighting the presence of disturbances in the free-stream even in the clean case.

The comparison of the blade loading for the two meshes is shown in fig. 2.9. It is seen here that the two meshes show reasonable comparison though the base mesh has slightly different transition characteristics. The base case predicts slightly earlier transition and suppresses the separation bubble as seen in the skin friction plot in fig. 2.10. Here the discrepancies are seen more clearly. On both the suction and pressure surfaces the main difference between the base mesh and fine mesh is the change in transition location. For the fine mesh both surfaces see a later transition compared with base mesh. The clean case supports the trends predicted by the fine turbulent case and shows even later transition, as well as clear separation on the suction surface in the skin friction figures.

———————-

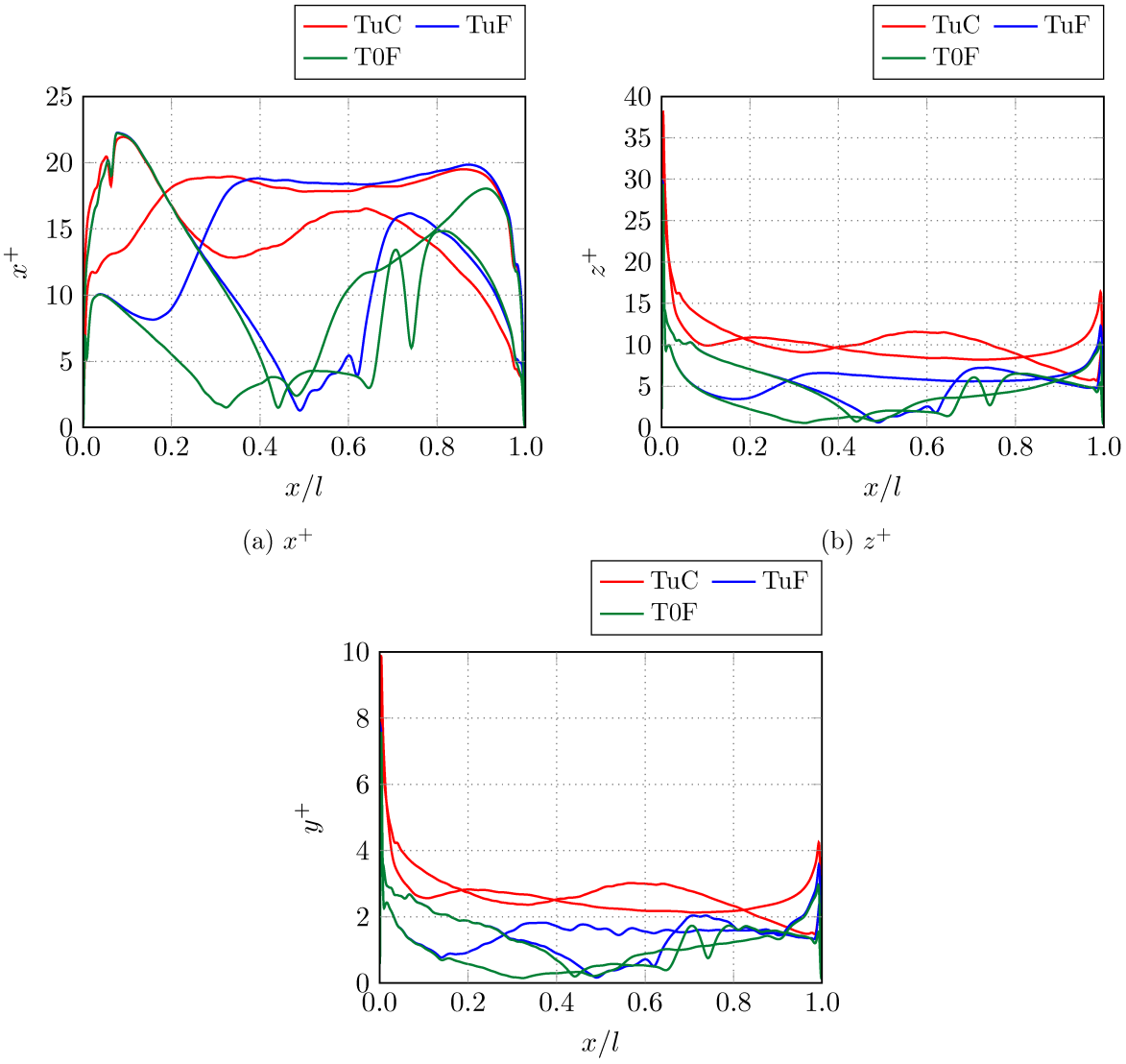

(a) x^+

(b) z^+

(c) y^+

Figure 2.7: Mesh verification plots for coarse and fine meshes for turbulent and clean cases for the NACA 65 3D cascade running at Reynolds number 138,000 and Mach 0.2. The variation seen in the x^+ plot for the coarse mesh is a result of the early onset of transition that results in this case.

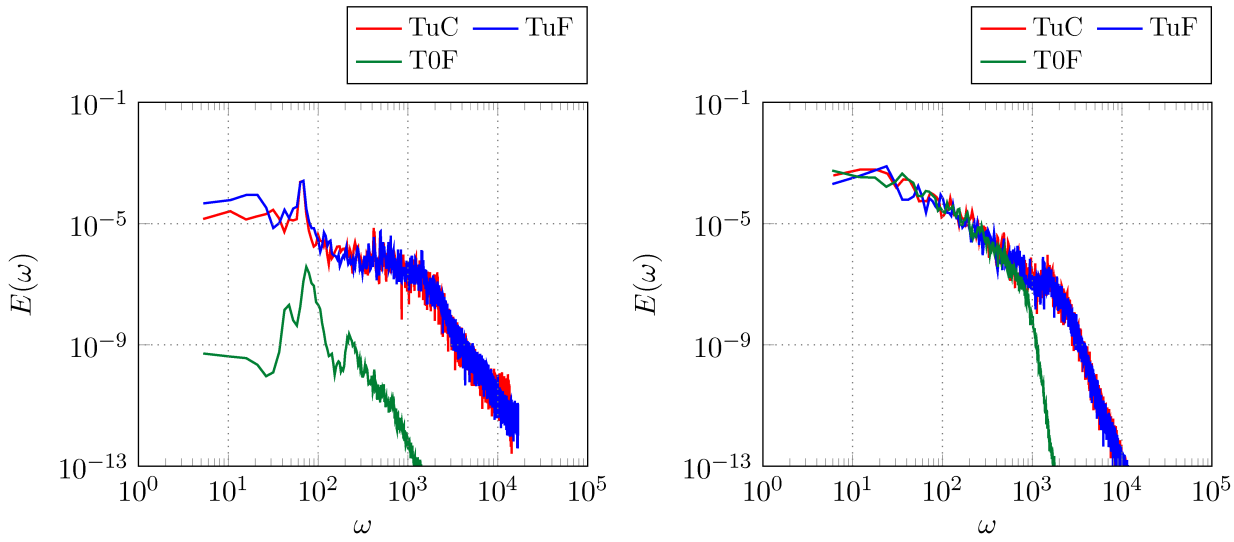

(a) Inlet (b) Outlet

Figure 2.8: Energy cascade for point (a) -0.3 chord up-stream and point (b) 1.4 chord down-stream for both fine and coarse meshes, plotted against wave number based on chord length.

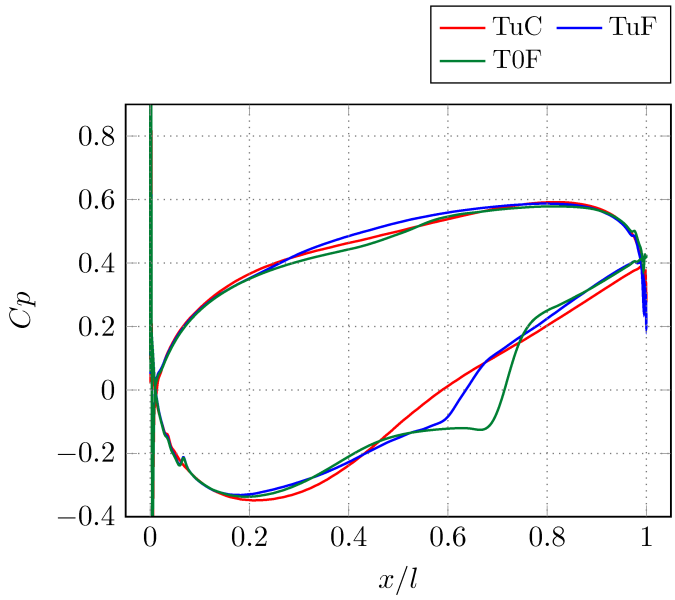

Figure 2.9: Coefficient of pressure for both fine and coarse meshes. Cases run at Reynolds number 138,000 and Mach 0.2.

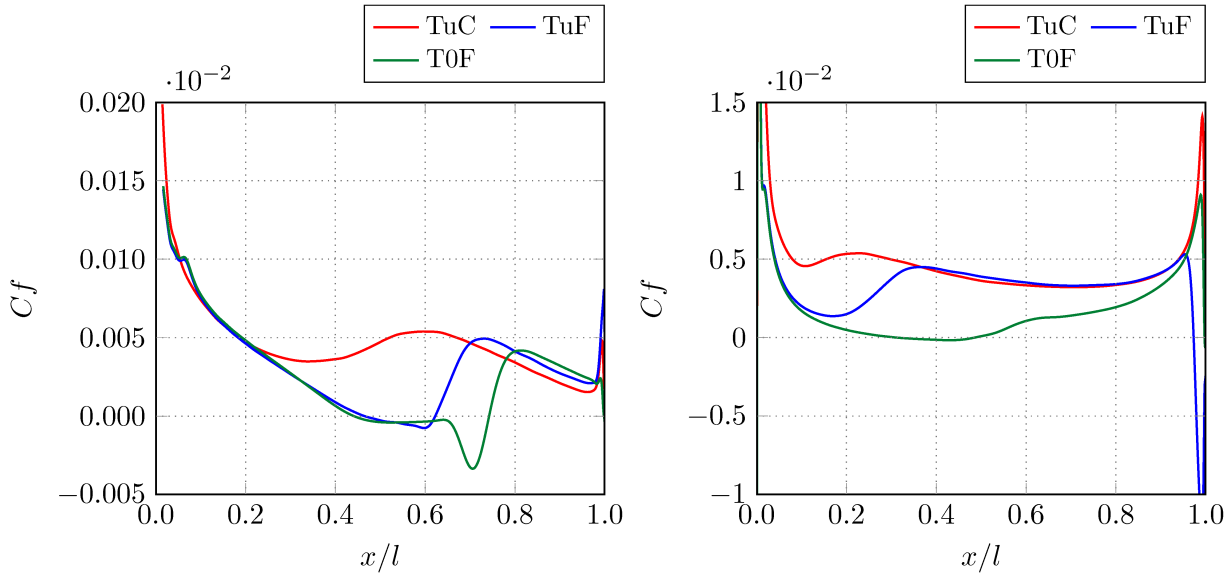

(a) Suction surface

(b) Pressure surface

Figure 2.10: Wall shear for both fine and coarse meshes for suction (a) and pressure surface (b).

2.10.5 Results Comparison

The comparison with the reference data was carried out on the fine mesh described in section 2.10.4 with 96 Fourier modes in the span-wise direction and a span-wise extent of 0.2 chord. The simulations were averaged for a total of 5 time periods once the steady state was reached to ensure the following statistical results were adequately converged and no further change in the statistical results was found.

2.10.5.1 Blade Surface Results

The pressure distribution over the blade is an effective way of comparing the simulations. It provides a means of measuring the direct effect the blade has on the flow and should therefore give almost identical statistical results for the same flow conditions. The coefficient of pressure distribution (Cp) for the TuF and T0F simulations are compared with the reference data from Zaki et al. in fig. 2.11. The comparison generally shows good agreement between the different cases. There are some difference seen between the respective cases which appears consistent for both the turbulent and clean flows. The main difference being slightly faster transition to turbulence of the LES for both the clean and turbulent cases compared with the Zaki et al. reference.

The same trend is highlighted in the friction coefficient (Cf) plot in figures fig. 2.12 and fig. 2.13. The Cf plots show a slight change in the length of separation on the suction surface between the reference data and the current simulations. With both cases showing the faster transition compared with the DNS. The comparison of the clean case is a little better than the turbulent case in this instance. With the clean case capturing the large separation and reversed flow regime. However, the LES does not capture the coherent structures that propagate down-stream in the DNS case.

For the pressure surface the comparison shows the same change with a slightly faster transition compared with the DNS data. Outside of the transition region the agreement between the LES and the reference data is good as is seen in the suction surface skin friction and Cp plots.

The variation between the reference data and LES is attributed to the compressibility of the LES simulations. The compressibility of the flow results in much higher disturbance levels in the domain due to the shedding and turbulent breakdown of the wake of the blade and despite the added stability of compressible flow forces earlier transition. The increased turbulence intensity is highlighted in table 2.2 where the turbulence intensity at the leading edge shows how the compressible fluctuations result in a measurable amount of turbulence even in the clean case.

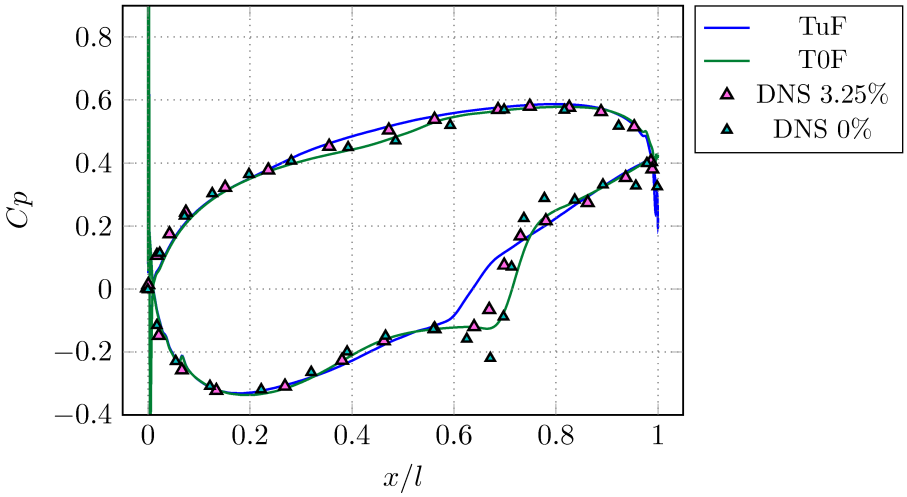

Figure 2.11: Coefficient of pressure distribution for fine 3D LES cases with and without 3.25% free-stream turbulence, with reference data from *Zaki et al.* (2010) for corresponding cases.

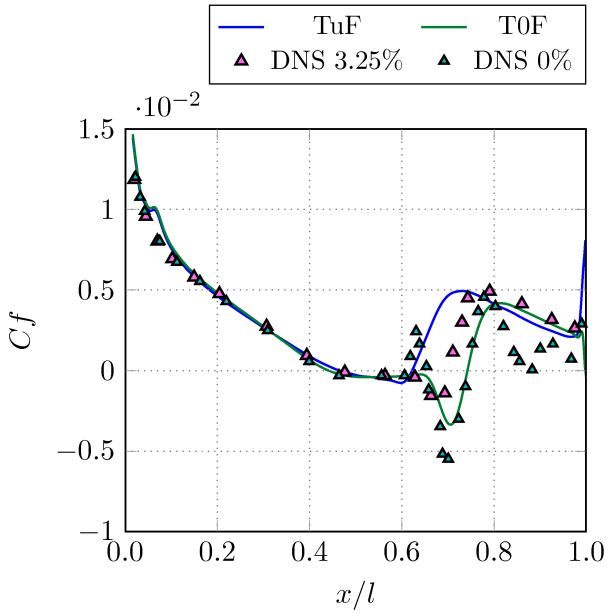

Figure 2.12: Suction surface coefficient of friction distribution for 3D LES cases with and without 3.25% free-stream turbulence, reference data from *Zaki et al.* (2010) for corresponding cases.

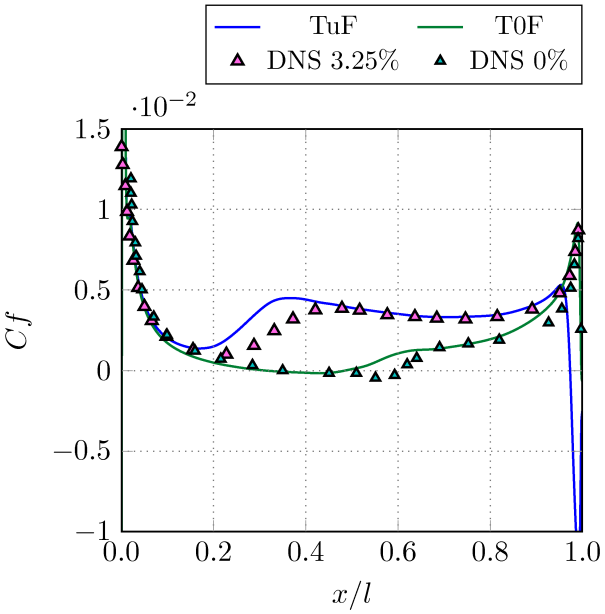

Figure 2.13: Pressure surface coefficient of friction distribution for 3D LES cases with and without 3.25% free-stream turbulence, reference data from *Zaki et al.* (2010) for corresponding cases.

2.10.5.2 Wall Tangent Profiles

The comparison of the wall tangent velocity profiles in fig. 2.14 between the DNS and LES results show very good comparison. It is seen that the LES predicts the wall tangent profiles up-stream of separation and transition well, further supporting the suggestion that it is the

compressible flow that is driving the slightly different transition behaviour. The comparison without turbulence is also included though there is almost negligible difference in the profiles for all but the last at $x/l = 0.4$ where the profile is slightly less full. The reference data for this profile has been included and shows good agreement with the clean LES case.

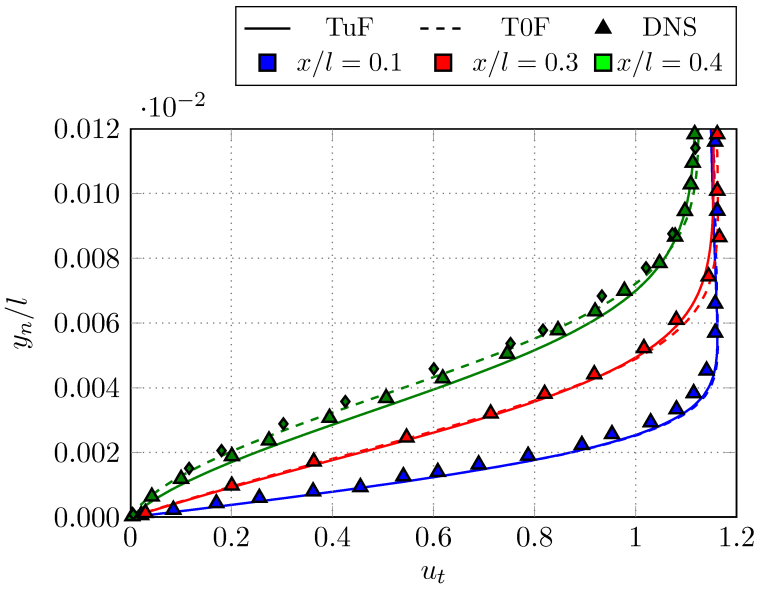

Figure 2.14: Suction surface wall tangential velocity profiles for 3D LES case with and without 3.25% free-stream turbulence and DNS reference case with 3.25% free-stream turbulence. Clean reference data for $x/l = 0.4$ included as diamonds.

2.10.6 Verification Results

The low Reynolds number verification study of the implemented LES against the case by *Zaki et al.* (2010) shows good agreement. Although there are some discrepancy with the slightly earlier transition for both suction and pressure surfaces. However, the variation in transitions is minor given the substantial change in flow dynamics brought about by the addition of compressibility. The addition of compressibility effects add further perturbations to the flow in the form of acoustic waves which results in greater forcing of the boundary layer instabilities. This is clearly shown in the suction surface skin friction plots where the separation and reversed flow are captured by the clean LES but the coherent structures do not persists as they do in the DNS. The added disturbances in the LES quickly cause transition of these structures. The increased turbulence is also highlighted in the final simulation conditions where the turbulence intensity at the leading edge shows an increase from that added at the inflow.

The comparison of the results also support the decision to focus on refining the near wall region in the LES mesh at the expense of a slightly coarser wall resolution by showing good agreement with the DNS without excessive computational expense.

Overall the verification gives confidence that the HiPSTAR code can capture compressor flows well. Unfortunately a one to one comparison could not be made due to the nature of the comparison between the LES and DNS and the introduction of compressibility. However, from the results obtained it is seen that the LES provides a very good match at a resolution substantially lower than that for DNS.

Chapter 3

Effects of Off-Design Incidence on Loss Prediction

3.1 Introduction

Historically the losses in a compressor have been separated into "profile loss", "end wall loss", "leakage loss" and "shock loss". Although this is known as a strong simplification, it still provides reasonable guidance when looking at loss breakdown. The relative importance of these losses may change along the speed-line, from design to off-design. Each of these areas when considered individually are governed by certain physical processes which can often be modelled more easily by removing the complex interactions between the different loss areas. In this chapter the focus is on computing and modelling the profile losses in a linear cascade at both design and off-design conditions. In the present set-up the losses are governed by only the boundary layer with no effects from the end wall or tip leakage flows. While this simplified quasi 2D view of a compressor stage only accounts for about a third of the total losses in a real stage, *Denton* (1993); *Steinert and Starken* (1996), the processes are not independent from each other and improvements in one may well show improvements with others.

Today the design of axial compressors is largely performed using cheaper and simpler correlations and mean line computations that are then further verified by Computational Fluid Dynamics (CFD) methods. The majority of which are performed using Reynolds Averaged Navier-Stokes (RANS). The use of CFD has improved iteration times of designs and afforded greater insight into potential compressor performance, reducing the need for experimental testing. With CFD being such a powerful design tool it is unlikely to be replaced in the future. However, there are limitations to current methods, most notably the loss of information and accuracy introduced by the modelling assumptions inherent in RANS models, which are not easily overcome without great computational expense and time. The assumptions made in RANS models can break down

in complex flow regions leading to inaccurate predictions. In axial compressors, complex flow phenomena of interest include up-stream wake blade interactions, free-stream turbulence and the limit of off-design conditions in the presence of strong adverse pressure gradients and flow reversal. Events such as stall and surge can render an engine inoperable or lead to mechanical failure. These conditions are often found at the limit of the operational envelope, and their accurate prediction is of paramount importance. While the move to more accurate CFD models or even Direct Numerical Simulation (DNS) to overcome the failings of RANS is certainly a desired one, for most routine CFD applications this is not feasible. Even with recent developments in high performance computing, many of the high fidelity CFD methods, most notably DNS are still confined to Reynolds numbers lower than those present in aircraft engine compressors, as well as to simplified geometries. However Large Eddy Simulation (LES) is feasible for limited numbers of runs at low engine Reynolds numbers.

A set of such simulations is performed for the work presented here with the prediction and breakdown of loss over a range of incidences being the main focus. It has been seen that RANS produces good results near to the design conditions and provides well resolved mean flow properties. However the performance of RANS at off-design incidences is limited. Much of the design work in industry is performed with correlations and optimized design tools, the poor performance of RANS at off-design running conditions means that validation of these tools and designs at later stages of the design process using RANS still has limited certainty. Improving these simulations using LES modelling and providing a greater understanding of loss prediction performance will aid in optimizing design correlations and loss prediction methods used in industry. Previous work on compressors at off-design conditions, specifically the effects of incidence on blade performance has been performed by *Steinert and Starken* (1996); *Evans et al.* (2010), which has provided good insight into the physics and complexities involved but such studies are largely limited to academic research. Making this information available to designers testing new designs is key to new advancements in working compressors. Of course this is a known problem and there has been an increase in interest of LES application to turbo machinery with work on secondary flows *You et al.* (2007); *Boudet et al.* (2007), heat transfer *Duchaine et al.* (2009); *Bhaskaran and Lele* (2010) and acoustics *Greschner and Thiele* (2011) all performed recently.

The comparison of LES and RANS in recent work by *Gourdain* (2015b) shows the performance of the two CFD methods at design conditions of rotor stator interactions. The literature highlights the benefits of using LES to improve our understanding when compared with RANS. More relevant to the current study are works on off-design conditions *McMullan and Page* (2012); *Hah* (2009), highlighting the importance of capturing unsteady phenomena such as stream-wise structures that can effect loss prediction at off-design conditions, and accurate shock boundary layer interactions in transonic compressors.

The remainder of this chapter outlines the cascade set-up and running conditions, followed by the numerical set-up and CFD methods employed. The comparison of the LES and RANS results is then shown and analysis of the loss production presented.

The application of the *Denton* (1993) analysis is also reviewed and a recommended practice for its application to compressors outlined. The Denton analysis is based on applying an energy, mass and momentum balance across a control volume spanning the blade passage, as outlined in chapter 2. The analysis is used to give a breakdown of loss production across the blade. The results of the Denton analysis between the LES and RANS are compared here and the differences in the relative processes that contribute to the total loss shown.

3.2 Numerical and Physical Case Set-up

The focus of this chapter is on assessing the performance of LES and RANS in simulating compressor cascade flows over a range of incidences. The simulations have been performed with a fixed amplitude of free-stream turbulence to compare with experimental data from *Leipold et al.* (2000), which also provides the nominal design incidence and working conditions. Prescribing a nominal level of free-stream turbulence is also done as a certain level of turbulence is always present in a working compressor.

The investigation focuses on the simulation of a NACA 65 profile at an axial chord Reynolds number of 300,000 based on the inflow free-stream parameters, and an inflow Mach number of 0.67. The set-up is shown in fig. 3.1 with the nominal set-up parameters given in table 3.1. For the current investigation a set of four incidence angles are studied, $\alpha = 37°$, $40°$, $44°$ and $49°$, all with a nominal free-stream turbulence level of $\sim 3\%$ measured at the blade inlet plane. The angles are defined here as the incidence of flow with reference to the horizontal or with reference to fig. 3.1 $\alpha = \beta_1$–$90°$. The mesh structure for the LES simulations is an H-grid with an embedded O-grid type mesh set-up as shown by dashed lines in fig. 3.2. For all the LES simulations the domain extends to 0.5 chord up-stream of the leading edge and 1 chord length down-stream of the trailing edge, with a span-wise extension of 0.2 chord length. The mesh contained 603,136 points in the plane with 128 modes in the span-wise extent, totalling 155,609,088 points for the full domain, giving a wall resolution of $\Delta x^+ \sim 15 - 20$, $\Delta y^+ \sim 1.5$ and $\Delta z^+ \sim 12 - 25$. The lowest resolution found near the leading edge suction surface near to the stagnation point. The boundary conditions, initially outlined in chapter 2 are also shown in fig. 3.2. Periodic boundaries are applied in both the pitchwise and span-wise directions, with a non-reflective zonal characteristic boundary for the exit. At the inflow, synthetic turbulence is superimposed onto a fixed mean velocity profile prescribed with constant density, the pressure being extrapolated from within the domain. A digital filter turbulence generation method *Klein et al.* (2003) is used to provide the synthetic turbulence at a prescribed intensity at the inlet. Finally a non-slip adiabatic boundary condition is applied to the blade wall. The synthetic

Reference Paper Conditions	
$Re = 300,000$	Mach $= 0.67$
$\alpha = 42°$	$\beta_s = 112.5°$
$w/l = 0.59$	$d_{max}/l = 0.0595$

Table 3.1: Nominal set-up parameters taken from Leipold et al.

turbulence length scales are set to 10% chord for the pitchwise and stream-wise directions and 5% chord for the span-wise direction. The length scales are limited by the domain extent and filter width. These lengths scales were chosen based on previous simulations to allow for adequate breakdown to homogeneous turbulent and to avoid excessive decay of the turbulence up-stream of the blade, as was seen to happen with initial LES simulations. Furthermore there is limited information on the turbulent length scale found in the experimental reference data leaving this a somewhat open question.

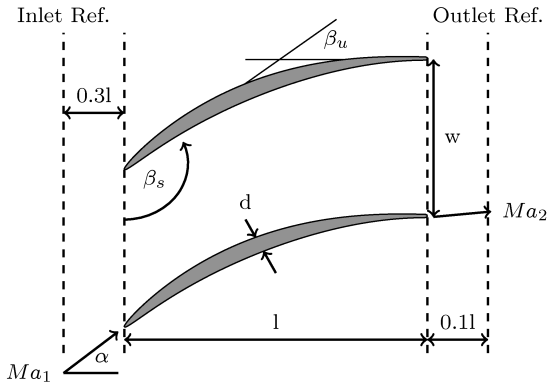

Figure 3.1: Schematic representation of linear compressor cascade NACA65 profile, based on outline in *Leipold et al.* (2000)

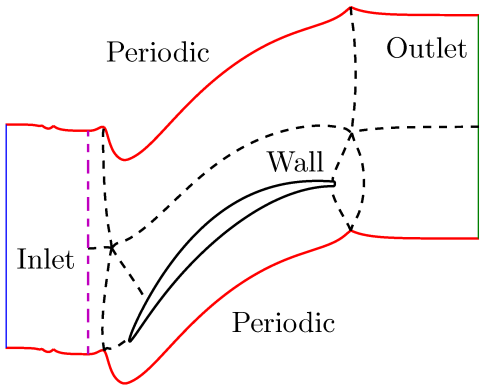

Figure 3.2: Boundary conditions and O-grid/H-grid layout

3.2.1 CFD Methods

The 2D RANS computations were run using ANSYS CFX and the SST turbulence model. For transition modelling, the two-equation $\gamma - Re_\theta$ model was used. In order to match the LES set-up, Sutherland's law, was used to calculated the dynamic viscosity in the RANS. The LES simulations were performed using the in-house compressible LES multi-block structured code, HiPSTAR, outlined in chapter 2.

3.2.2 Computational Expense

A short overview of the cost and performance of the LES simulations is given here. For the LES simulations the time step was set to 1×10^{-5} non-dimensional time units to satisfy the CFL criterion and approximately 4 blade passing time periods were required for convergence of basic statistical data. The simulations were performed on the UK national computer Archer and required 30 hours on 7,344 cores to run the 400,000 iterations needed. A further 3 blade passing time periods were required to establish the flow, which was initialized with the mean flow obtained from the RANS calculations.

3.3 Flow Field Analysis

The results analysis performed here focuses on understanding loss prediction. There are many different measures of cascade performance, each with their own merit. Of these different methods two are most popular. Energy loss coefficients, looking at loss in properties such as enthalpy, and the stagnation pressure loss coefficient which is has been the preferred method as it is easily measured in working machines. The stagnation pressure loss coefficient is used in this work and is defined here as $\omega = (P_{t1} - P_{t2})/(P_{t1} - p_1)$, where the subscript ,$t$, is a stagnation value. In calculating the stagnation pressure loss coefficient it is common practice to take mean values of two planes, one up-stream and one down-stream of the blade to calculate these losses. It is important to note, though, that this method looses all information about the origins of these losses, as well as assuming a certain level of homogeneity of the wake at the point where the mean quantities are calculated. Often the errors involved in this process are negligible but as compressors become more compact and blade to blade spacing reduces this may not always be the case. The mixed out mean values as defined by *Prasad* (2005) are used here for the pressure loss coefficient.

3.3.1 LES and RANS Comparison

Initial simulations of the case by *Leipold et al.* (2000) raised some questions as to the correct nominal incidence as first LES runs at the experimentally specified 42° incidence did not match the blade loading. In order to overcome this a RANS simulation was run using the operating conditions provided in the experimental paper by *Leipold et al.* (2000), which are an inlet Reynolds number of Re = 300,000 an inlet Mach number of M = 0.67, and an inlet flow angle of $\alpha = 42°$. Since the loading from RANS did not match the experimental loading at these operating conditions (see fig. 3.3), a series of RANS were performed to investigate the dependence of the loading on the operating conditions. A parametric study was performed, varying the following parameters in the RANS: the Reynolds number Re, the Mach number M, the inlet

Table 3.2: Final running conditions of LES and RANS simulations at off-design incidence.

LES Angle	36.99°	39.97°	44.09°	49.2°
Re	302K	302K	298K	289K
Mach	0.654	0.674	0.666	0.65
% Tu at LE	2.9	3.3	3.2	3.5
RANS Angle	37°	40°	44°	49.2°
Re	298K	313K	335K	309K
Mach	0.652	0.672	0.676	0.659
%Tu at LE	2.9	3.4	3.4	3.5

turbulence intensity and length scale, and the flow angle α. Three-dimensional effects and Axial Velocity Density Ratio could also be relevant. However, no information on these latter effects is available in the experimental paper and they were therefore not investigated in the RANS study. The loading is strongly affected by the inlet flow angle α (see fig. 3.3) as expected. A close match between the RANS loading and the experimental loading can be obtained by lowering the flow angle by 2°, from $\alpha = 42°$, which is the value provided by Leipold et al., to $\alpha = 40°$.

The RANS study thus suggests that the appropriate design operating conditions for this case are: Re = 300k, M = 0.67, and $\alpha = 40°$, these operating conditions were specified as the baseline conditions for the LES. Note that performing the parametric study using LES would have been prohibitively expensive and the operating conditions were therefore verified using RANS. It was later found that three dimensional effects were present in the experimental set-up by *Leipold et al.* (2000) as noted in a later study by *Iseler et al.* (2006) showing that end wall boundary layers were large in the experimental set-up, and likely have an effect on the mid span flow.

Following the nominal simulation a set of three other simulations at off-design incidence were performed from a low incidence of 37° to a high incidence of 49°. The final conditions of these simulations are given in table 3.2

3.3.1.1 Flow field contours

To introduce the results analysis instantaneous contours of the span-wise vorticity component of the LES cases are plotted in fig. 3.4 showing the turbulent inflow and wake paths for the four LES cases. The four vorticity contour plots help to clarify the physical processes present in the simulations and give an overview of the full flow domain. There are several things to note from fig. 3.4, firstly that there is no large separation for any of the cases on the suction surface. The suction surface over the incidence range shows laminar development up to the peak suction after which transition takes place either via a separation bubble at 37° and 40° or via bypass transition seen at 44°, to leading edge separation seen at 49° with turbulent reattachment, this is difficult to see in the vorticity contours and is taken from further analysis. Secondly over the

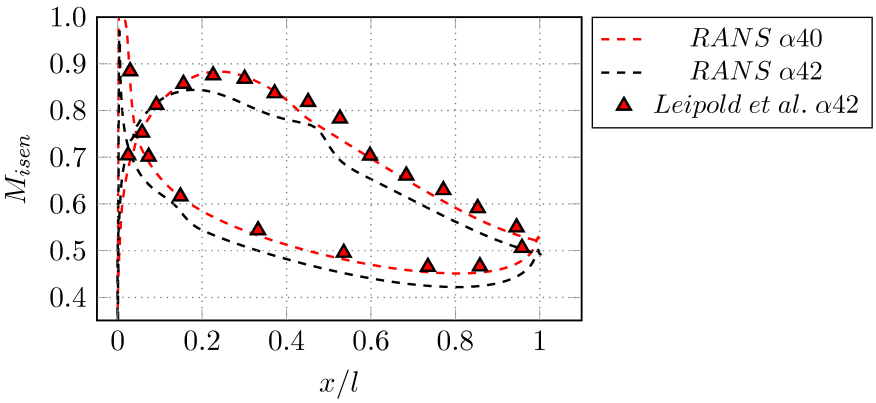

Figure 3.3: RANS loading at different inlet flow angles and comparison to the experimental loading of Leipold et al.

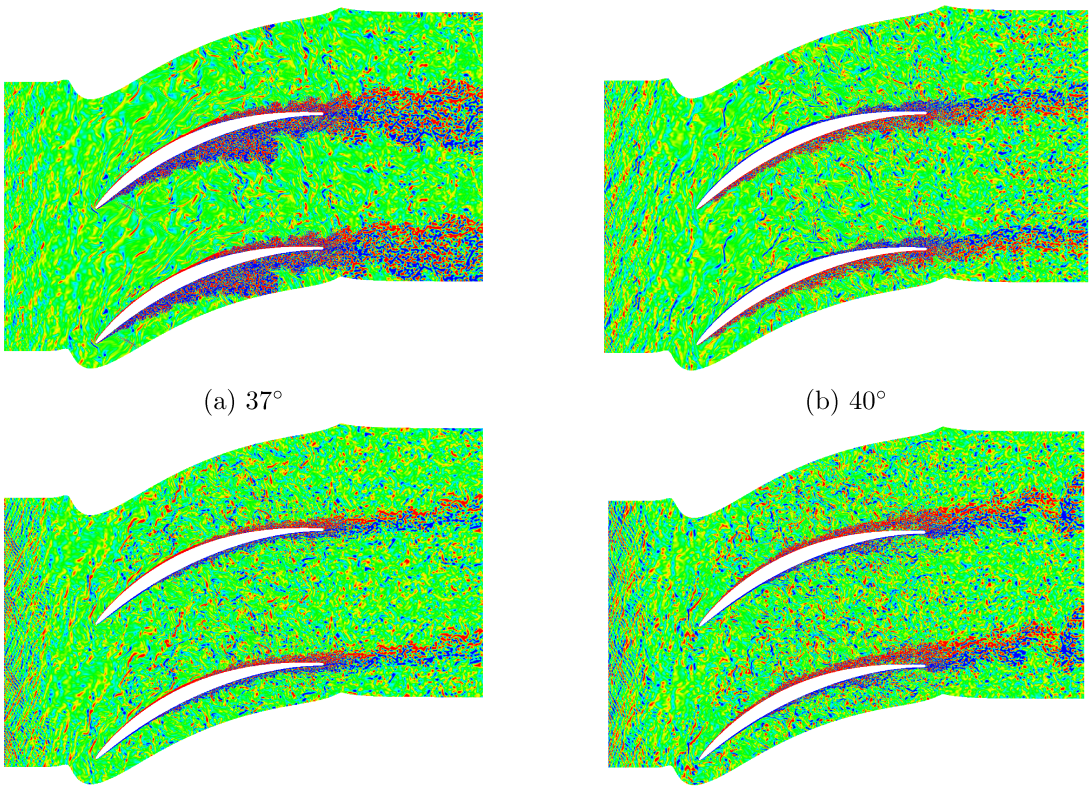

(a) 37°

(b) 40°

(c) 44°

(d) 49°

Figure 3.4: Instantaneous contours of the span-wise vorticity component for LES, vorticity contour limits [-10,10]

full incidence range chosen the pressure side undergoes transition early either via a small leading edge separation bubble at the lower incidences or via bypass transition in the 44° and 49° cases, resulting in a turbulent boundary layer for the majority of the pressure surface. However the variation in the flow structures changes quite dramatically from an attached turbulent boundary layer at 49° to substantial turbulent shedding at 37°. There is also some mild turbulent shedding

present in the 49° case, though this occurs at the trailing edge and appears to originate from the suction surface boundary layer.

To help further explain the trends seen in the loss prediction between the two methods the turbulent kinetic energy contour plots are shown in fig. 3.5. These plots provide an initial insight into the trends seen in the wall normal profiles (discussed later) over the full flow domain. It is clear in the 44° case that little loss is generated by the leading edge and that turbulent breakdown occurs further along the blade. This is captured in both the RANS and LES, although the LES predicts the turbulent break down sooner, producing a slightly wider wake at the trailing edge. The TKE contours of the suction surface for the 40° case also show a variation in maximum TKE seen between LES and RANS. Here the RANS shows a shift towards the trailing edge with a notable amount of TKE produced on the suction surface side compared to the LES. For the LES this peak production is nearer the centre of the blade. This shift in peak TKE production at the trailing edge is seen for all incidences, with the RANS showing a higher production from the suction surface than the LES which predicts a peak production nearer the centre of the blade. It is likely that this shift is due to the LES resolving the turbulent recirculation and shedding that occurs at the trailing edge, while the RANS is unable to capture these phenomena, predicting a steady shear layer.

The pressure surface shows similar trends between LES and RANS for the 44° and 40° cases, capturing very similar TKE contours apart from the slightly thicker boundary layer for the 40° case. However, for the 37° case there are a few differences. Firstly it is noted that the LES captures a weak shock at the pressure surface leading edge separation which is not seen in the RANS case. Secondly the RANS predicts a shift in the maximum TKE production away from the wall, which is observed in the wall shear stress plots, where a notable reduction is seen compared to the LES.

3.3.1.2 Profile loading

Looking next at the blade loading profiles given in fig. 3.6, we find reasonable comparison between RANS and LES for the 49°, 44° and 40° cases while at 37° there is more substantial variation between the profiles. Starting with the comparison of the loading at 40° with the experimental data, both the LES and RANS show reasonable correlation, with the LES matching the suction surface down-stream of $x/l = 0.6$ better than the RANS, though up-stream of transition the opposite is true with the LES predicting a higher loading than the RANS and experimental data. The pressure surface comparison shows good agreement with experimental data for both the RANS and LES down-stream of $x/l \approx 0.5$ though up-stream of this the LES shows a slight increase in the loading compared with the RANS and experimental results, which match well. Although it is noted that it is now known post simulation that three dimensional effects are present in the experimental reference data, which would result in an effective narrowing of the

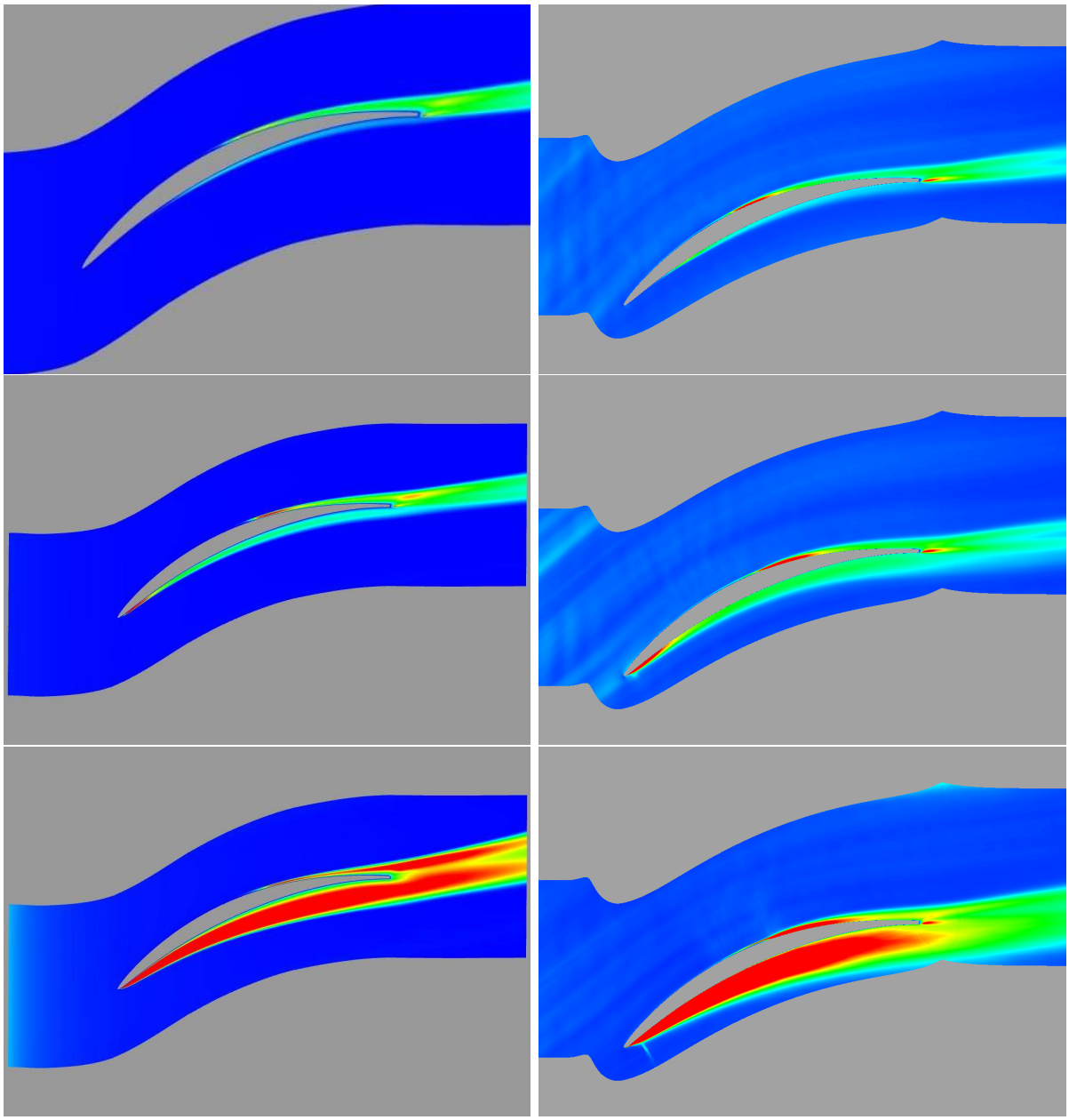

Figure 3.5: Time-averaged Turbulent Kinetic Energy (TKE) contours for RANS (left) and LES (right) at incidences 44°, 40° and 37° from top to bottom, respectively. Contour range [0, 0.02].

stream tube. Accelerating the flow resulting in the higher trailing edge Mach numbers seen in the experimental data.

This increased loading seen in the LES likely contributes to the faster transition (discussed in section 3.3.1.3) in the same case due to a stronger deceleration of the flow at separation, destabilizing the shear layer further. The performance of the off-design incidence at 37° shows the most variation, as expected, as these are the running conditions RANS finds most challenging. The first notable difference when examining the loading profiles in fig. 3.6 is the higher peak

suction loading seen in the LES. It is clear here that the LES predicts a higher acceleration of the flow up to peak suction, attributed here to the sharper change in the boundary layer on the suction surface where a clear separation is triggered by the weak shock created at the pressure surface leading edge, impinging on the suction surface. This more rapid change in the boundary layer produces the sharper changes seen in the loading.

It is noted that for the 37° case it was found that the Mach number could not be increased to the desired 0.67 at the inflow without chocking the flow. Instead the Mach number was increased as far as possible while maintaining an un-chocked condition and run at these conditions. Because the RANS struggled most with converging the flow the final conditions were set by the RANS which settled on an inlet Mach number of 0.65. The final running conditions of the LES for the range of incidences are given in Table 2, measured at a reference plane 0.3 chord lengths up-stream of the leading edge. It can be seen in the loading profile plots that the flow is locally supersonic over parts of the suction surface at 37°. For the LES case this covered a region from $x/l \approx 0.25$ to 0.45 while the RANS predicted a shorter supersonic region from $x/l \approx 0.25$ to 0.4. The pressure surface loading shows quite marked variation, notably the LES predicts a lower trailing edge isentropic Mach number which extends up-stream to $x/l \approx 0.2$. This is likely attributed to the weak shock system slowing the flow in the LES, supported by the larger supersonic region on the suction surface, and the resulting deceleration following this.

The trend of LES predicting a sharper deceleration and clearer separations is carried over into the 40° and 44° cases seen by the clear drop in the suction surface loading. RANS shows a slight change in loading for the 40° case but does not capture the effects of transition for the 44°. The pressure surface behavior for the two middle incidences are similarly captured by both LES and RANS with no notable differences.

The 49° case is well represented by RANS apart from the short leading edge separation on the suction surface, which is not shown in the RANS loading. The remainder of the loading is well matched.

3.3.1.3 Wall Shear

The wall shear stress plots shows some interesting variations between the RANS and LES simulations. The RANS suction surface wall shear stress shows reasonable comparison with the LES with both the magnitude of the wall shear stress and similar trends seen in both LES and RANS. However, the RANS does not capture the separation predicted by the LES at 37° and 40°. It also fails to predict the turbulent reattachment seen at 49°, instead predicting laminar reattachment followed by a transition. In all the cases RANS tends to recover the LES results after transition showing similar trends though there is a noticeable difference in magnitude. The transition trends on the suction surface show that the LES predicts a change in transition method from 37° to 49°; at 37° the flow has a clear separation bubble and turbulent reattachment, at 44° the LES

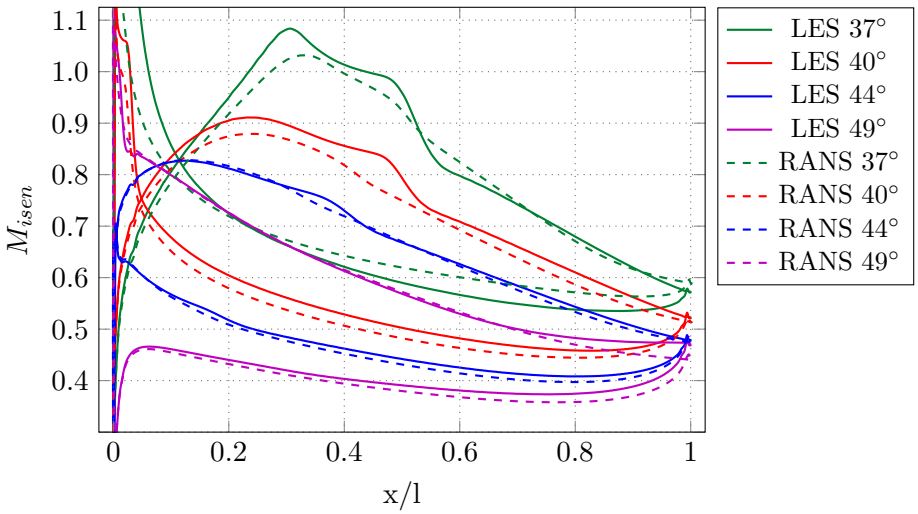

Figure 3.6: Isentropic Mach number loading of LES and RANS solutions at incidences 37°, 40°, 44° and 49°.

predicts transition without separation, most likely bypass transition forced by the free-stream turbulence, while at 49° there is a laminar separation bubble followed by bypass transition. The RANS on the other hand predicts bypass transition for all incidences.

The pressure surface predicts a higher time-averaged wall shear stress for all the LES cases compared with the RANS simulations. This higher wall stress seen in the LES is most notable for the largest negative incidence and is attributed to the RANS not capturing the regions between turbulent shedding where the boundary layer is attached. A similar process is suggested to occur for the nominal incidence case though the shedding under these conditions is reduced. A more unified trend for the transition method is seen on the pressure surface where the RANS and LES predict a separation bubble at 37° and 40° while at 44° and 49° the boundary layer transitions before separation and remains attached.

There are some oddities when examining the wall shear stress plots more closely, notably the apparent lower amplitude of wall shear stress predicted by the RANS whenever there is a turbulent boundary layer. This is clearest over the pressure surface where a turbulent boundary layer exists over most of the blade. It is suggested that the RANS prediction of a lower wall shear stress in turbulent regions is non-physical, which is supported by the close comparison between LES and RANS over the leading half of the suction surface where the flow is still laminar. The confusion associated with the lower values of wall shear stress predicted by the RANS is that the total losses are higher than those of the LES. This may be associated with the shear distribution over the boundary layer being shifted away from the wall as seen in the turbulent kinetic energy (TKE) distribution across the suction surface boundary layer shown later. This shift results in a stronger shear layer away from the wall, necessary to produce the same wake loss.

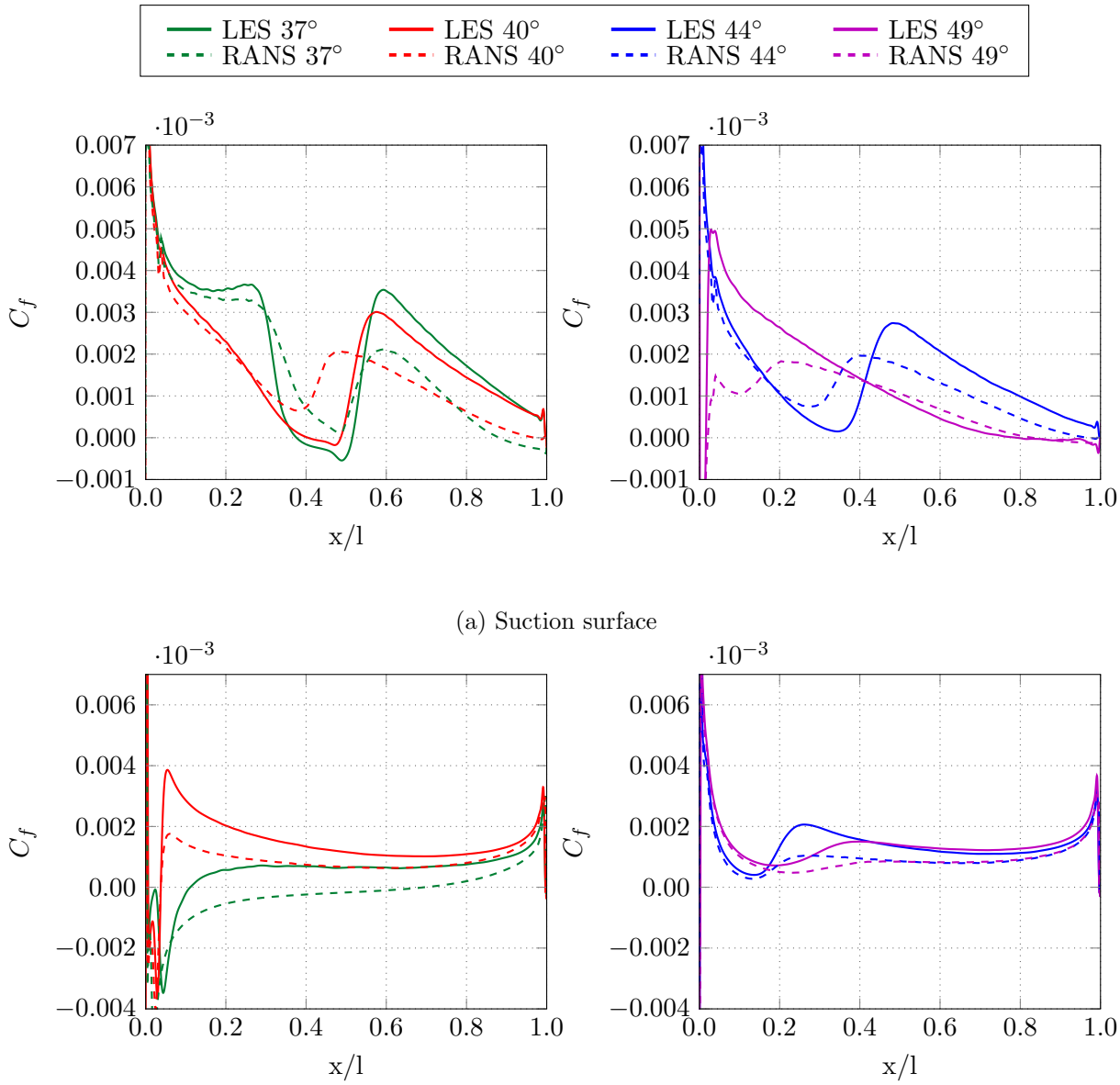

(a) Suction surface

(b) Pressure surface

Figure 3.7: Wall skin friction for LES and RANS solutions at incidences 37°, 40° and 44° with reference data from Leipold et al.

3.3.1.4 Wall tangential profiles

The wall normal boundary layer profiles for the tangential velocity component and the turbulent kinetic energy are shown in fig. 3.8a and fig. 3.8b. The figures show profiles on the suction surface boundary layer at several positions along the blade for all LES and RANS cases. These plots help to explain the variation seen in the wall shear profiles where a lower wall shear stress is seen in the RANS simulations for turbulent boundary layers. It is observed in the velocity profiles

that while the RANS and LES match in the free-stream the RANS has a velocity gradient profile that is highest near the centre of the boundary layer. This is in contrast to the LES which shows a high change in the velocity gradient nearer the wall and a much fuller velocity profiles as expected for a turbulent boundary layer. However the LES also tends to predict a thicker boundary layer, with the free-stream velocity reached further from the wall for all but the last position at $x/l = 0.99$ where the RANS shows a larger boundary layer influence into the free-stream. Apart from the 49° case where the LES predicts a separated boundary layer extending further in to the free-stream which the RANS does not capture.

The TKE plots show a similar trend where the position of maximum TKE moves outwards toward the free-stream for the RANS simulation, for all but the 49° case, suggesting the boundary layer is moving towards separation in the last profile at $x/l = 0.99$. This shift toward separation is captured in the velocity profiles at $x/l = 0.99$ where the near wall profile is almost stationary. However for the 49° case, where separation occurs in the LES, the TKE profiles captured in RANS show the opposite trend. With the maximum shear occurring nearer the wall. It is also seen that the RANS predicts a lower maximum TKE for all but the 37° case where the maximum value matches the LES in the last two profiles.

In general the velocity and TKE profiles between LES and RANS show reasonable correlation, showing similar trends with regards to changes in profile shape. However there are noticeable differences with magnitudes and the location of the maximums, suggesting that while the RANS model behaviour captures similar losses this is achieved with different near wall behaviour.

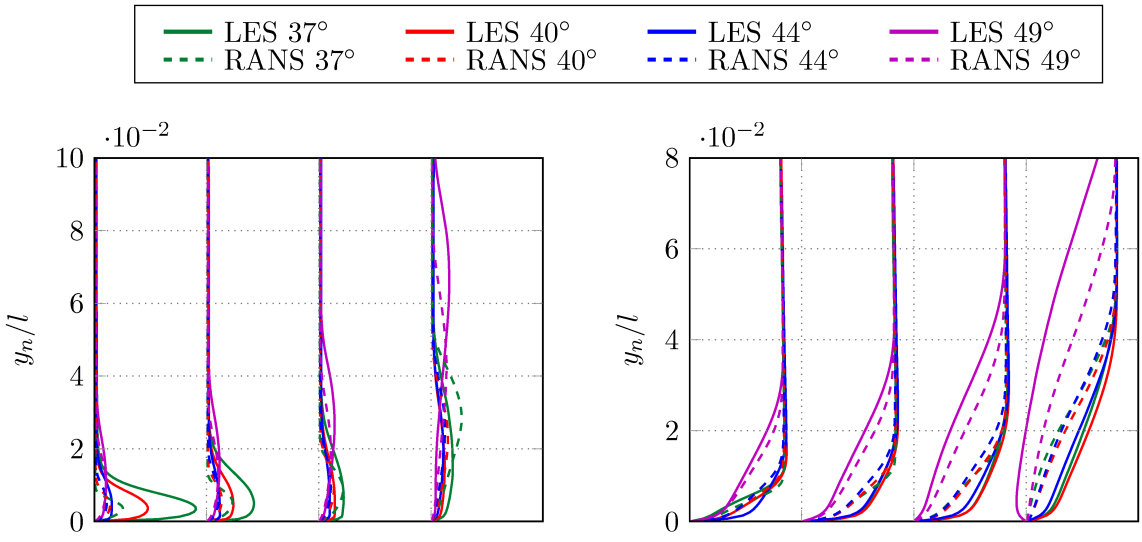

(a) Turbulent Kinetic Energy

(b) Tangential velocity

Figure 3.8: Comparison of LES and RANS wall tangential profiles on suction surface at streamwise positions, $x/l = 0.56$, $x/l = 0.64$, $x/l = 0.76$ and $x/l = 0.99$ from left to right respectively. Each profile is shifted by 0.08 for the TKE and 1.25 for the Tangential velocity.

3.3.2 Boundary Layer Quantities

The momentum thickness, displacement thickness and shape factor for the LES simulations are shown in fig. 3.9b, fig. 3.9a and fig. 3.10. The boundary layer properties help to explain the variation seen in the flow and clarify transition points. They also provide a measure of the differences seen in the boundary layer profiles.

The displacement thickness and momentum thickness are defined as follows.

$$\delta^* = \int_0^\infty \left(1 - \frac{\rho(y)u(y)}{\rho_\infty u_\infty}\right) dy$$

$$\theta = \int_0^\infty \frac{\rho(y)u(y)}{\rho_\infty u_\infty}\left(1 - \frac{u(y)}{u_\infty}\right) dy$$

where ρ_∞ and u_∞ are the values of the flow in the 'free-stream'.

The displacement thickness and momentum thickness help to quantify the effect the boundary layer has on the flow. The displacement thickness is useful to show an effective shape of the aerofoil if the fluid were inviscid. While the momentum thickness is used to show the reduction in momentum transport the blade has on the fluid if the fluid were again inviscid. The ratio of these two quantities is defined as the shape factor, given as

$$H = \frac{\delta^*}{\theta}$$

The shape factor helps to show the state of the boundary layer. Generally the higher the shape factor the less stable the boundary layer, and the closer to separation it is, or already separated.

The momentum and displacement thickness plots show that the flow on the suction surface (fig. 3.9a) undergoes a clear laminar turbulent transition. There is clear growth in the displacement thickness in the laminar region, followed by rapid growth at separation, then by the increased growth of the turbulent boundary layer. The separation is not captured in the momentum thickness as clearly, though the growth of the turbulent boundary layer is clear. The general trends of the suction surface are shared for all but the 49° case, where early transition occurs and the boundary layer shows steady growth up to separation near the trailing edge. This is shown by the drop in momentum thickness at trailing edge. The lower incidences show more clearly the laminar growth, transition and turbulent growth up to the trailing edge. The trends of the pressure surface (fig. 3.9b) are less clear. This is understandable as it has been shown that the pressure surface undergoes transition near the leading edge in all cases, with a leading edge separation in both the 37° and 40° cases and bypass transition in the 44° and 49° cases.

That being said the pressure surface boundary layer properties show a more interesting progression compared with the suction surface, which shows clear flow regimes typical of a boundary

layer in an adverse pressure gradient. It is interesting to see that both the momentum and displacement thickness for the pressure surface have a local maximum before reducing toward the trailing edge. It is suggested here that these changes are attributed to the inertia of the flow. After peak suction the turning of the blade is increased while the flow still has momentum in the pitchwise direction. This pitchwise momentum energises the pressure surface boundary layer. This can partially be seen in the recovery of the loading plots which show an increase in the isentropic Mach number of the pressure surface toward the trailing edge.

The shape factor for the pressure surface (fig. 3.10b) shows progression from a largely separated boundary layer to a turbulent boundary layer. *Spalart* (1988) shows a shape factor of ~ 1.3 describes a turbulent boundary layer on a flat plat. The suction surface shape factor (fig. 3.10a) shows a more typical laminar boundary layer shape factor,$H \approx 2.5$ for a Blasius boundary layer, followed by separation, shown by the rapid peak, and transition to a turbulent boundary layer. For the 49° case the boundary layer again separates as shown by the high shape factor at the trailing edge. The RANS also shows the increased shape factor for all cases, supported by the boundary layer profiles seen in fig. 3.8b, suggestive of separation or near separation.

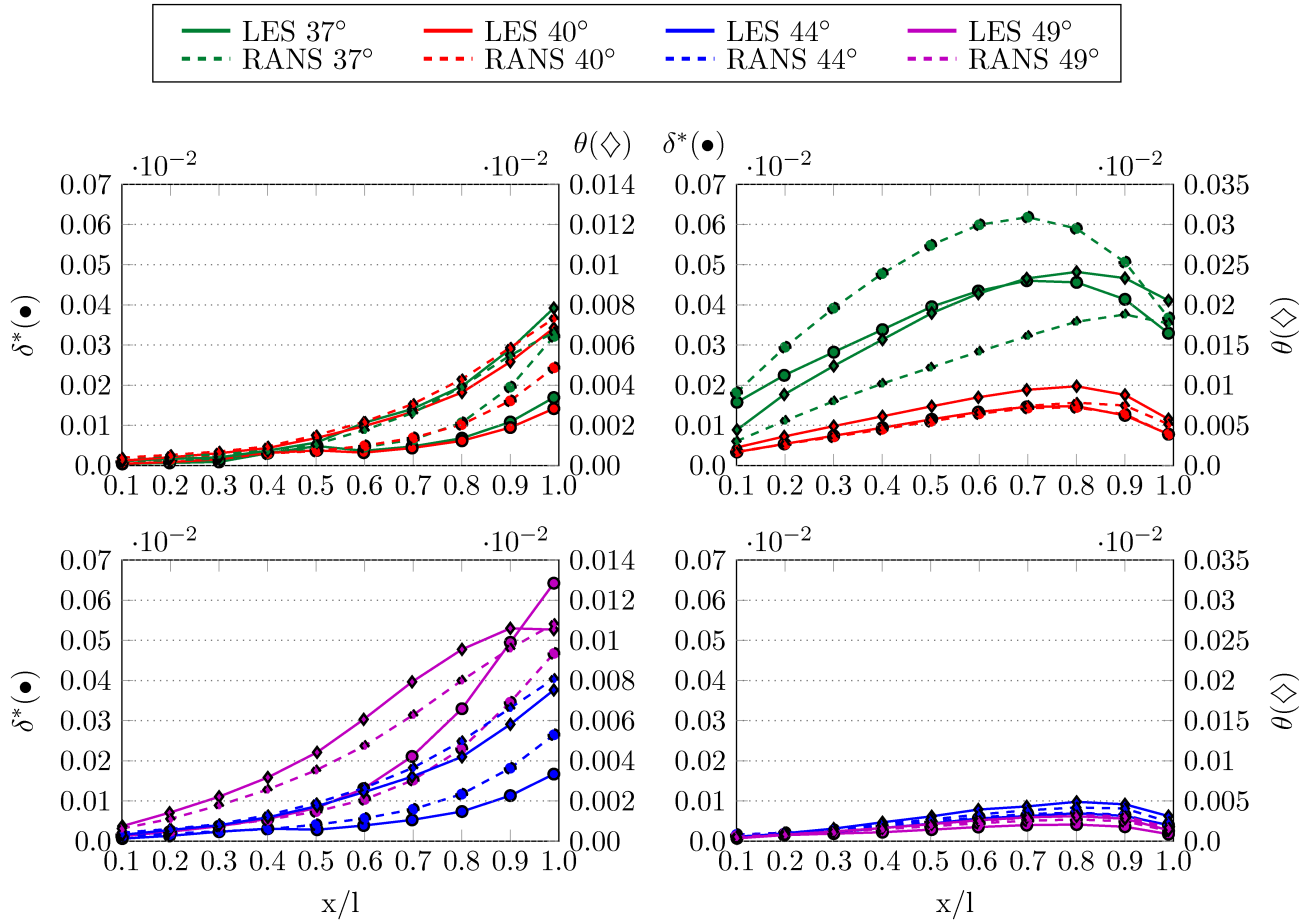

(a) Suction surface

(b) Pressure surface

Figure 3.9: Displacement, δ^*, and Momentum, θ, thickness for 37°, 40°, 44° and 49° for LES and RANS cases

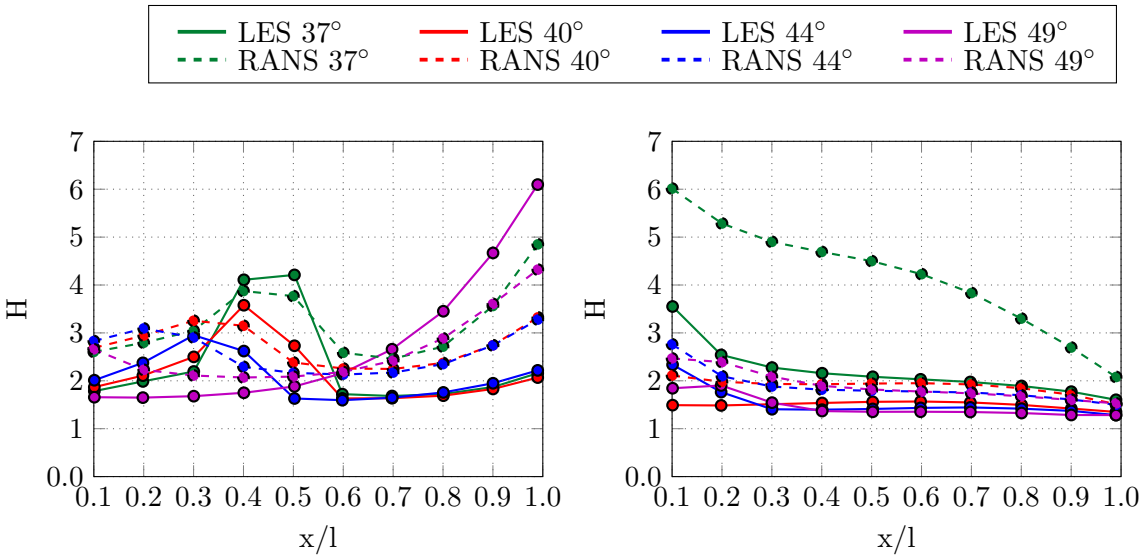

(a) Suction surface

(b) Pressure surface

Figure 3.10: Shape factor for 37°, 40°, 44° and 49° for LES and RANS cases

3.3.3 Wake Profiles

Figure 3.11 shows the normalised total pressure for wake profiles at 0.02 and 0.1 chord lengths down-stream of the trailing edge. Starting with the 44° case the progression and comparison is good, with the RANS matching the LES wake width well at both locations, though the RANS predicts a slightly higher peak deficit. For the 40° case the RANS wake shows a slightly narrower wake in comparison with the LES and again shows a higher peak deficit for both locations. The profile for the 37° case shows a substantially narrower wake for the RANS at both 0.02 and 0.1 chord lengths, but with similar wake spreading compared with the LES. The 37° case also shows a substantial shear layer at 0.02 chord lengths, that is not captured so clearly by RANS. In fact this shear layer exists for all cases in the LES results though the RANS results only show it at the limits of the incidence range. Finally the 49° cases shows a similar trend to the 37° case with greater wake spreading from the LES, this time predominantly from the suction surface, with a smaller pressure deficit. It is suggested that the difference in wake spreading between the LES and RANS simulations is due to the LES capturing coherent turbulent structures, such as the shedding seen from the leading edge, which is not captured in the RANS cases. This is supported in fig. 3.11 by noting that the majority of the increase in wake width for the LES results is attributed to the pressure side for the 37° case and the suction surface for the the 49° case. Furthermore it is seen in the comparison for the 37° case that the peak wake loss of the LES profile at 0.1 chord lengths down-stream is substantially lower than the RANS. Suggesting that the mixing out of the wake in the LES cases is more rapid compared with the RANS simulations.

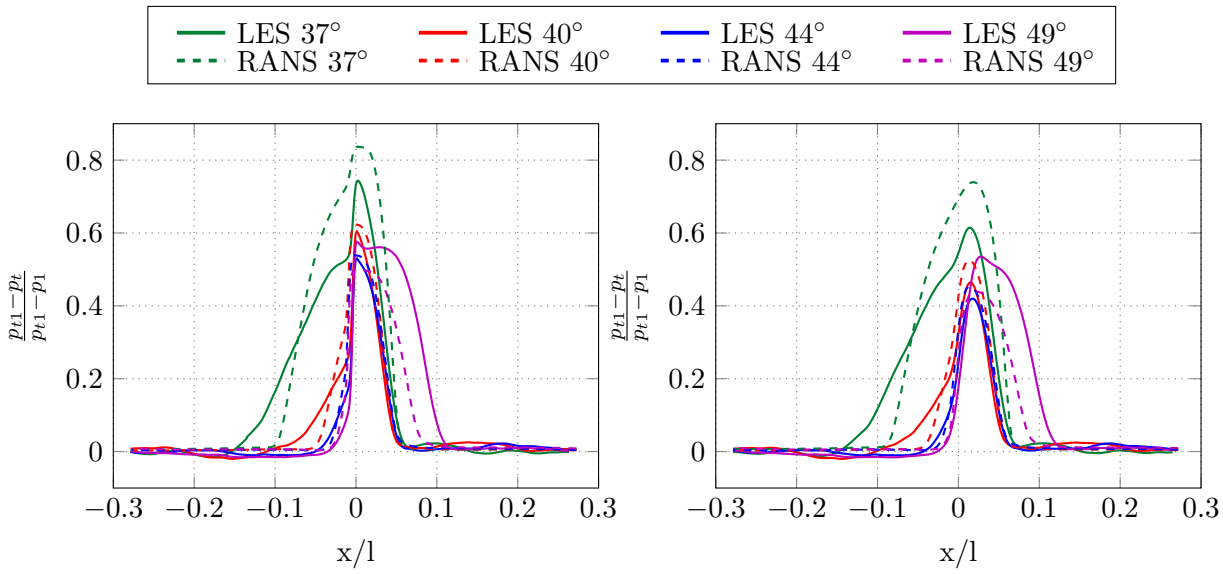

(a) 2% chord down-stream

(b) 10% chord down-stream

Figure 3.11: Total pressure $(p_{t1} - p_t)/(p_{t1} - p)$ wake profile 2% and 10% chord down-stream of trailing edge. Pressure surface is negative.

3.3.4 Flow Parameters

The variation over the incidence range of certain flow parameters are presented here. These quantities are presented for completeness and show the relative loading and flow state over the compressor cascade. The parameters are presented for both RANS and LES and the difference in the predicted flow highlighted.

3.3.4.1 Flow turning

The flow turning is defined as the difference between the inlet and outlet flow angle and is loosely related to the blade loading. The flow turning is shown in fig. 3.12 for both the RANS and LES. It can be seen that as the incidence is increased the flow turning increases. Showing the blade is moving toward a more highly loaded state. The reference case from *Leipold et al.* (2000) is also shown, and matches the turning from the LES at 40° well.

The difference between RANS and LES is quite substantial at the lowest incidence which reinforces the other results showing RANS poor performance at 37°. It is seen that the performance improves as the incidence increases although there is still a discrepancy of $\approx 0.5°$ at the design angle, which could have a compounding effect at design, resulting in poorer performance.

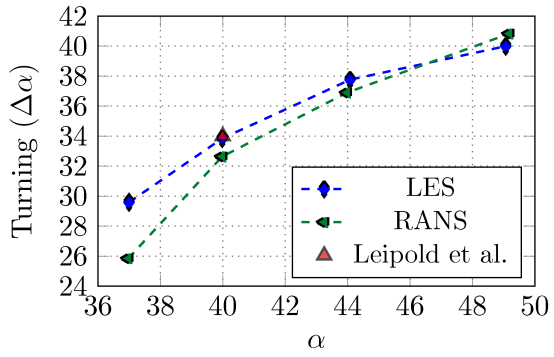

Figure 3.12: Flow turning for RANS and LES over incidence range given.

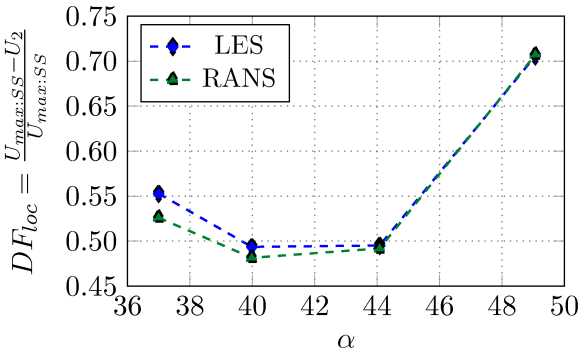

Figure 3.13: Lieblien diffusion factor showing relative blade loading for RANS and LES over incidence range given.

3.3.4.2 Blade loading

The blade loading is expressed here using the local diffusion factor introduced by *Seymour Lieblein and Broderick* (1953). This is a simple way of expressing the pressure diffusion of the suctions surface, which generally has a strong correlation with the loss and work a blade is doing

on the flow. The diffusion factor is defined as

$$DF_{loc} = \frac{U_{max:ss} - u_2}{U_{max:ss}}$$

where $U_{max:ss}$ is the maximum velocity on the suction surface.

The diffusion factor is shown in fig. 3.13 against incidence and shows the increase in loading for the off-design cases. The diffusion factor was originally designed to highlight loading at design conditions and is derived from the momentum thickness on the suction surface. If the diffusion factor is plotted against momentum thickness, fig. 3.14, or loss, fig. 3.15, it is seen that the relationship breaks down at low incidence. This is due to the large loss contribution from the pressure surface not captured by this simple metric. However for the positive incidence cases it is clear that blade is not lightly loaded reinforcing the relevance of the simulations compared with current real compressors.

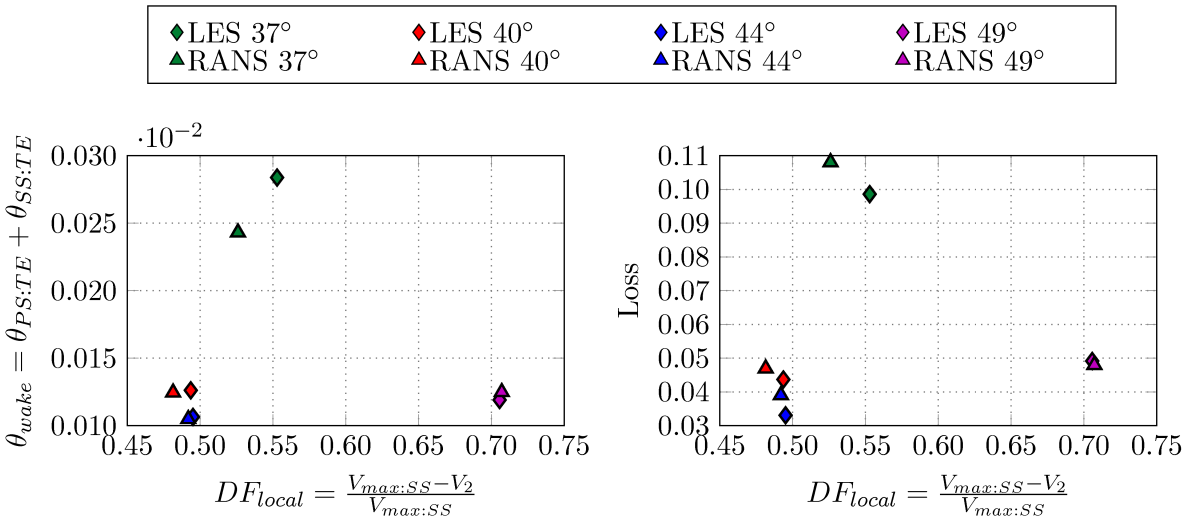

Figure 3.14: Momentum thickness against diffusion factor. Showing break down of correlation at low incidence.

Figure 3.15: Loss plotted against local diffusion factor. Highlighting the short coming in capturing loss from pressure surface at low incidence.

3.4 Loss Breakdown Analysis

To aid the understanding of compressor loss a breakdown of loss at the various incidences is found by applying the *Denton* (1993) analysis. The analysis is based on applying an energy, mass and momentum balance across a control volume spanning the blade passage at the trailing edge. Such analysis, while somewhat idealized, provides insight into the processes responsible for the generated losses. The Denton loss breakdown has been introduced in chapter 2 giving

its derivation. The result of the derivation is a simple way of associating loss with various flow properties. The analysis is achieved by applying the following equation:

$$\omega = -\frac{C_{pb}t}{w} + \frac{2\theta}{w} + \left(\frac{\delta^* + t}{w}\right)^2 \tag{3.1}$$

where C_{pb} is the base pressure coefficient, θ is the momentum thickness and δ^* is the displacement thickness for the trailing edge boundary layer. w and t are the pitch and trailing edge thickness respectively. The trailing edge base pressure coefficient is defined as

$$C_{pb} = \frac{p_b - p_2}{p_{t1} - p_1} \tag{3.2}$$

Looking at the loss breakdown equation in more detail it can be seen that the various terms account for different loss mechanisms. The first term of the equation is the base pressure loss due to the blunt trailing edge and resultant pressure difference across the blade, the second term is the momentum loss of the fluid from viscosity, and the final term is a blockage loss due to the boundary layer effectively narrowing the passage. Looking at each of these terms in turn allows some insight into where loss generation is highest. In compressors it is common that the momentum and displacement losses are greater than the base pressure losses as the boundary layers are often thicker than those for turbines. The diffusive nature of the flow also results in a low pressure difference across the blade.

An addition to the equation is also proposed by Denton to correct for cases where the boundary layers are separated at the trailing edge. In these case it is proposed that the base pressure loss be modified to act over a larger area $(t + \delta^*)$ including the contribution from the boundary layer displacement thickness as it becomes larger than the trailing edge. This addition being necessary for the 37° and 49° cases. The application of the Denton analysis raised some questions as to how best to define a boundary layer edge in a cascade flow. Initial work highlighted the sensitivity of the analysis as well as the effect of events such as the leading edge turbulent shedding observed in the current study at the lowest incidence. The definition of the boundary layer limit is investigated here using three possible definitions. Defining a limit in a wall bounded developing flow is difficult where the growth of the boundary layer directly affects the "free-stream" velocity which is often used as a limit for the boundary layer. In the derivation of the Denton analysis this problem is partly overcome by defining the inflow as uniform across the control volume spanning the throat at the trailing edge, though no detail as to what the boundary layer quantities are based on is given.

In this analysis three definitions for a boundary layer limit are proposed, a vorticity limit, a mid-channel velocity limit and a bulk or mixed-out velocity limit. The vorticity limit is defined such

that the edge of the boundary layer is found at the limit when the magnitude of the span-wise vorticity is less than a specified amount, i.e

$$U_e = U(y)|_{|\Omega(y)|==|\Omega_{ref}|} \tag{3.3}$$

The mid channel limit uses a "free-stream" velocity defined as the average velocity in the channel:

$$U_e = \frac{1}{h}\int_{y_1}^{y_2} U(y)dy, \tag{3.4}$$

$$h = y_2 - y_1 \tag{3.5}$$

where the limits are defined as

$$y_1 = y|_{U(y)=0.99U_{max}},\ y_{ps} \leq y \leq y_{pitch/2}$$

and

$$y_2 = y|_{U(y)=0.99U_{max}},\ y_{pitch/2} \leq y \leq y_{ss}$$

Finally the mixed out limit is again a "free-stream" velocity, however this time it is defined as a bulk velocity using the mixed out state. These three boundary layer limits are represented in fig. 3.16a and fig. 3.16b, showing the velocity profile across the blade passage at the trailing edge for the LES and RANS respectively. It is obvious from fig. 3.16 that the different definitions give quite varied limits, which translate into variations in the wake loss predictions from the Denton analysis.

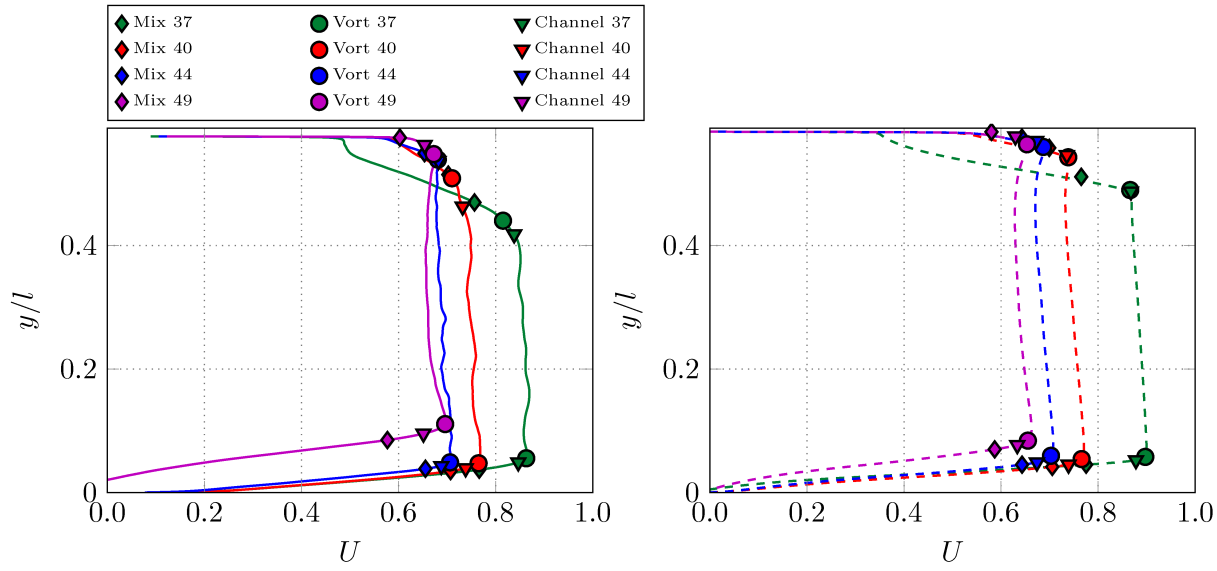

(a) LES (b) RANS

Figure 3.16: Trailing edge blade passage velocity profile for LES and RANS. Showing the limits for channel, vorticity and mixed out definitions.

3.4.1 Total Loss

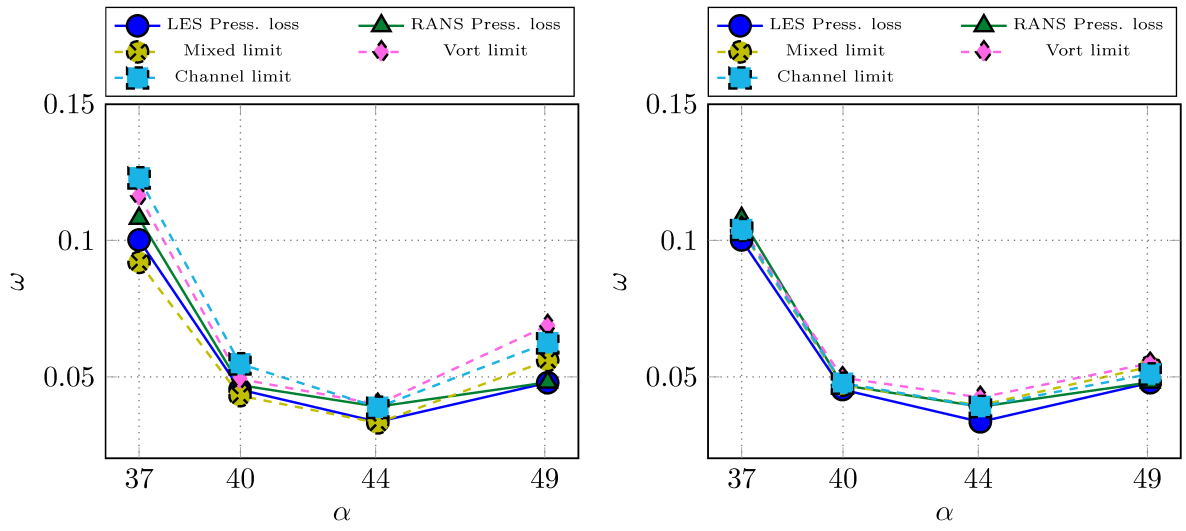

(a) LES (b) RANS

Figure 3.17: Total Loss coefficient for LES and RANS over incidence sweep 37° to 49°, including virtual point for reference data *Leipold et al.* (2000) to highlight the 2° change in incidence to match loading. Total Denton loss for, (a) LES breakdown, (b) RANS breakdown, for Channel Velocity limit, Vorticity limit and Mixed out limit.

The total pressure loss coefficients for the LES and RANS calculations are plotted in fig. 3.17, represented by the solid lines repeated in both figures (a) and (b). Here the total loss is calculated

from mixed out values for an up-stream plane at -0.3 chord from the leading edge and a down-stream plane at 0.1 chord from the trailing edge. The total loss calculated from the Denton analysis is also included in fig. 3.17 for the three boundary layer limit definitions. The total loss plot shows clearly the influence the definition of the boundary layer has on the analysis which will be discussed further. Firstly however the comparison of the total pressure loss coefficients between the LES, RANS and experimental data is reviewed.

The comparison of the LES and RANS results with the experimental data is difficult to do with certainty, as mentioned previously, as the experimental data is performed at a reported incidence of 42°; however it was found that in order to match the loading profile an incidence of 40° is required for the LES and RANS simulations. The exact cause of the difference is uncertain but it is very likely that this is due to three dimensional effects that were later shown to be present in the experimental set-up. Comparing the data that is available at the adjusted incidence of 40° where the loading profiles from RANS and LES match the experimental data, it can be seen that the LES matches the loss value reported in the experiments, while the RANS predict a slightly larger loss compared with the experimental data (which has been shifted by $-2°$ and is represented by the virtual point in fig. 3.17). This suggests that matching the loading (fig. 3.6) is sufficient in this case to compare with the experimental data. This is further supported by the good match in flow turning between the LES and the experiment seen in fig. 3.12. However, when comparing the loss it was also found that varying the mixed out measurement plane down-stream of the trailing edge showed minor variations in the loss prediction. Taking a measurement plane 0.4 chord down-stream improved the LES comparison with the experimental data giving a total loss of 0.043 compared with 0.045 in fig. 3.17. Again the exact measurement plan in the experimental set-up is not given so a completely accurate comparison cannot be made.

Looking in more detail at the loss predictions between the RANS and LES it is clear that the LES performs better at the nominal incidence of 40°, matching the experimental data well, while the RANS predicts slightly higher losses. At 44° the comparison is slightly worse with the LES predicting lower losses than the RANS although it is expected that the comparison improves as the boundary layers at this incidence are well behaved with no large separations as highlighted by the wall shear in fig. 3.7. It is suggested the cause of this discrepancies is the later transition of the boundary layer of the LES. Moving to the largest negative incidence at 37° the RANS again predicts a higher loss in comparison with the LES though this is expected with the know performance limitation of RANS with discreet unsteadiness. Interestingly the RANS matches the LES well at the largest positive incidence of 49° even though there is some shedding present in the LES results. It is likely the RANS performs well at this incidence as the flow is still reasonably well behaved here and represents likely running conditions of a compressor, which are the conditions RANS are tuned to.

The loss prediction for the RANS was limited to a maximum negative incidence of 37° as the simulations could not be converged for smaller angles. It is seen in fig. 3.4a that large turbulent

structures are shed from the pressure surface leading edge and it is likely that these are the cause of the RANS instabilities at even lower incidences. The trend in loss prediction seen in fig. 3.17 shows the LES loss coefficient increases at a slower rate compared with the RANS toward smaller incidences. It is likely that much of this difference in loss is attributed to the increased unsteadiness of the pressure surface, which is unlikely to be accurately captured in the RANS. These differences are highlighted in the loss breakdown analysis discussed in the next section.

Finally fig. 3.17 also highlights the sensitivities of the loss breakdown analysis. It is seen that the total loss is affected by the choice of boundary layer limit, where small changes in the predicted boundary layer edge varies the momentum and displacement thicknesses and hence the loss. This variation highlights some of the issues involved in applying this analysis to compressor cascades where the boundary layers tend to be thicker than those in turbines and influence the passage flow to a greater extent. From the analysis it has been suggested that using a mixed out velocity limit provides the most accurate and rigorous results. This is also in keeping with the derivation of the breakdown analysis, which assumed a uniform flow into the control volume.

3.4.2 Loss Breakdown

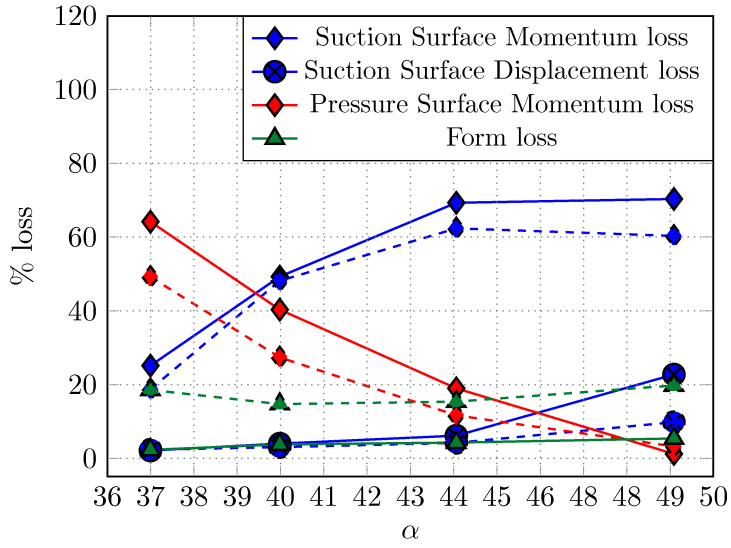

Figure 3.18: Percentage breakdown of Denton loss for significant terms on pressure and suction surfaces. For incidence sweep from 37° to 49°

The total loss predicted by the loss breakdown analysis for the RANS and LES results is presented in fig. 3.17 along side the total pressure loss. fig. 3.17a shows the total for the LES results while fig. 3.17b shows the RANS total loss breakdown. Comparing the total breakdown loss prediction with the total pressure loss in fig. 3.17 it is seen that each limit method produces slight different loss predictions. This is most notable in the LES results, partly due to the

limited statistic convergence meaning that the velocity profiles are not as smooth as the RANS but also due to the limit definition itself. For the LES results it is shown that both the channel velocity limit and vorticity limit definitions predict quite different results compared with the mixed out limit. With both showing higher losses compared with the total pressure loss for all incidences though notably worse at the limits of 37° and 49°. The variation seen in RANS is much smaller though again there is poorer prediction at the limits. For the RANS cases the prediction is similar between all three limit definitions although the vorticity limit is clearly the worst. The differences between the channel velocity and mixed out velocity limits are minimal, it also appears that the channel velocity limit is marginally better at the 49° case. However the difference is marginal and does not out weigh the improved performance in the LES case and more rigorous definition of the mixed out limit. The comparison of the total loss from the breakdown analysis highlights the difficulty of defining a boundary layer in a wall bounded internal flow over a curved surface. From the analysis performed here it is suggested that the mixed out limit be used to define the edge of the boundary layer in a compressor cascade. This method is easily applied and is without ambiguity. It is also in line with the derivation of the breakdown analysis, which assumes a uniform inlet into the control volume analysis.

The weighting of the various terms of the loss breakdown analysis are shown in fig. 3.18. It is seen that while the majority of the loss is associated with the boundary layer losses on the suction and pressure surfaces, the base pressure loss contribution is the largest variation seen between the LES and RANS predictions. It is seen that the RANS pressure loss prediction is 2-3 times larger than the LES for all cases. This notably lower base pressure, and the corresponding higher loss predicted by the RANS is associated with the much cleaner wake predicted by the RANS, which results in a lower relative back pressure. Although the difference in form loss between RANS and LES is substantial the form loss itself does not account for the variation in the total loss seen with incidence change.

The majority of the variation seen in the total loss is attributed to variation in the momentum and displacement loss from the suction and pressure surface boundary layers. It can be seen clearly in the percentage breakdown that the main contribution to loss shifts from the pressure surface to the suction surface as the incidence is increased. However it is interesting to see that the main contribution at low incidence is almost entirely momentum loss from both surfaces, while at positive incidence the pressure surface contributes very little loss, but the suction surface displacement loss becomes relevant. The higher contribution of displacement loss at positive incidences is more in-line with the loss breakdown trends seen for low pressure turbines outlined in the work by *Michelassi et al.* (2014). It is suggested that this increase in displacement loss is responsible for the over prediction in total loss calculated using the loss breakdown, as the loss prediction is very good at 44° where the loss is predominantly from momentum loss.

Looking in more detail at the change in incidence from 49° to 37°, there is a notable thickening of the boundary layer for the pressure surface at the trailing edge, seen in fig. 3.16. This

increased velocity deficit is mostly attributed to the boundary layer, though when viewing the instantaneous vorticity plots (fig. 3.4) it is seen that this may not be the case. At 37° the large turbulent structures shed from the leading edge do not always remain attached, making their inclusion as part of the boundary layer less clear. Although, they still contribute to loss. This variation in the pressure surface boundary layer is clearly captured in the loss breakdown with a clear almost linear variation in the pressure surface momentum loss. Rising to a maximum at 37°. However, the pressure surface displacement loss is negligible over the incidence range (as such is not included in fig. 3.18), as shown in the tabulated breakdown, table 3.3. The negligible displacement loss is attributed to the fact that these large turbulent structures at 37° do not remain attached and so can travel with the speed of the free-stream, and not affect blockage.

The suction surface on the other hand show similar changes as the pressure surface, with a steady thickening of the boundary layer as the incidence is increased to 49°. Resulting in similar changes to the momentum loss. However, at the most positive incidence the momentum loss plateaus which is attributed to the fact that the suction surface boundary layer is separated at the trailing edge for this incidence. The separation of the boundary layer is also responsible in part to the increase in displacement loss seen, as boundary layer is still coherent although separated, it has an effect of on the blockage of the passage. This is not the case for the pressure surface, where the turbulent boundary layer rolls up into semi coherent structures that can be convected much fast through the passage. This helps to explain the increase in displacement loss seen for the suction surface but not the pressure surface.

It is seen that the RANS in general predicts lower momentum and displacement losses compared with the LES, with the deficit accounted for by the form loss, to give a similar total loss. The general trends however are captured quite clearly, although there is a slight discrepancy at 49° where RANS does not predict as sharp a rise in displacement loss. Here we see that RANS shows only a slight rise in displacement loss from the suction surface though captures the same plateau of the suction momentum loss. The difference being made up by slightly higher loss from the pressure surface momentum and pressure loss terms.

In general the pressure loss is broadly unaffected by changes in incidence. However, increasing the incidence to more positive values does shows a slight increase in the pressure loss. The RANS in this case shows a greater change in pressure loss with a larger increase than that seen in the LES. However, the variation is still minimal compared with the other terms of the loss breakdown. It is suggested that the reason for the differences seen between the RANS and LES can be attributed to RANS predicting thinner boundary layers and deeper wake losses. Seen in the fig. 3.8b and fig. 3.11 for the suction surface boundary layer and wake profiles.

Table 3.3: Tabulated loss breakdown for incidences 37°, 40°, 44° and 49°. Showing loss contribution from suction and pressure surfaces for displacement, δ^*, and momentum, θ loss and form loss as well as percentage breakdown.

Case	37°			
	LES	LES%	RANS	RANS%
Ss δ^* loss	0.002	2.130	0.002	2.384
Ss θ loss	0.022	25.133	0.019	18.848
Ps δ^* loss	0.004	4.547	0.002	2.285
Ps θ loss	0.055	64.153	0.051	49.502
Cpb loss	0.002	2.325	0.019	18.032
Total	0.086	100.000	0.103	100.000
Case	40°			
	LES	LES%	RANS	RANS%
Ss δ^* loss	0.002	4.011	0.001	3.071
Ss θ loss	0.020	49.269	0.023	48.460
Ps δ^* loss	0.001	2.488	0.000	0.191
Ps θ loss	0.016	40.328	0.013	27.569
Cpb loss	0.002	3.792	0.007	14.155
Total	0.041	100.000	0.047	100.000
Case	44°			
	LES	LES%	RANS	RANS%
Ss δ^* loss	0.002	6.166	0.002	4.242
Ss θ loss	0.023	69.293	0.025	62.765
Ps δ^* loss	0.001	1.854	0.000	0.032
Ps θ loss	0.006	18.983	0.005	11.743
Cpb loss	0.001	4.296	0.006	14.836
Total	0.033	100.000	0.039	100.000
Case	49°			
	LES	LES%	RANS	RANS%
Ss δ^* loss	0.013	22.744	0.005	9.904
Ss θ loss	0.039	70.315	0.032	60.721
Ps δ^* loss	0.000	0.800	0.000	0.005
Ps θ loss	0.001	1.218	0.002	3.273
Cpb loss	0.003	5.396	0.010	19.222
Total	0.056	100.000	0.053	100.000

3.5 Conclusions

The results of this investigation into loss prediction of a compressor cascades at off-design conditions has further highlighted the need for accurate simulation methods. Starting with a review of the total loss and flow field comparison between the RANS and LES, the general differences in performance are minimal. However, there are some differences in the total losses and the flow field predictions which should be noted.

At the nominal incidence of 40° the predicted loss from the LES matched the corrected experimental data very well, with the RANS slightly over predicting it. At this incidence the suction surface shows laminar development, separation and turbulent reattachment for the LES with the RANS showing laminar development and bypass transition. The pressure surface in both cases shows a leading edge separation bubble with turbulent reattachment.

Increasing the incidence to 44° improves the boundary layer behavior with no separation occurring on either the pressure or suctions surfaces for both RANS and LES. Here it was seen that RANS and LES agreed well in the predicted blade loading and wall shear. However the total loss was higher in the RANS case associated with the more coherent wake and earlier boundary layer transition. Increasing the incidence further to 49° sees the difference between RANS and LES improve, with RANS predicting a total loss only fractionally higher than the LES. The loading is matched well although the skin friction and wall normal profiles show differences. Most notably the skin friction for the suction surface, where the RANS predicts relaminarisation before transitioning.

At the most negative incidence of 37° the predicted loss from the RANS is again slightly higher than the LES. However the variation in the profile loading and flow structure show quite substantial variations. With RANS failing to capture the separation on the suction surface and showing variations in wall tangential TKE and velocity profiles. The pressure surfaces also sees quite a large variation of the skin friction prediction, with RANS predicting a substantial separation from the leading edge up to approximately 60% chord. Suggesting the RANS is obtaining a reasonable result though not necessarily due to accurate representation of the flow features.

The investigation into loss breakdown analysis has provided further insight in the LES RANS comparison, as well as introducing some challenges. During the course of the investigation the application of the model has proved difficult and not entirely decisive. The most notable difficulty, which is addressed in this work, being the definition of a representative boundary layer edge in a wall bounded flow. Three approaches were posed based on various flow parameters, a channel velocity limit, a vorticity limit and a mixed out velocity limit. These three approaches have been applied to the simulations and the respective loss predictions compared. The results of the three approaches show reasonable qualitative comparison though there are large quantitative

variations between the approaches. Resulting in a miss match with the total loss calculations for some of the methods.

Of the three methods proposed the mixed out limit has shown to be the most consistent and is in keeping with the derivation of the method by Denton. It is suggested here that for compressor cascades the mixed out limit be used to determine a boundary layer edge for the calculation of predicted losses. Finally the merit of such a study is in showing to what extent certain processes are responsible for loss. The application of the loss breakdown analysis to the RANS and LES simulations has shown that the two CFD methods predict quite different weighting for the three terms of the Denton analysis. Such that even thought the total losses are similar the means by which these losses are produced differ.

For the suction surface both LES and RANS attribute most of the loss to the momentum term, though the RANS shows a slight reduction in momentum loss and a corresponding increase in form loss. It is also shown that the suction surface momentum loss is a relevant source of loss regardless of incidence, although at more positive incidences it plays a larger role. Displacement loss of the suction surface also becomes relevant at positive incidences while its contribution is almost negligible at negative incidence.

The pressure surface shows similar trends with almost all the loss being attributed to the momentum deficit. It is seen again that RANS predicts a lower momentum loss compared with LES. For the pressure surface the displacement losses are found to be negligible at all incidences. Even at 37° where it is expected that the large turbulent structures and thick boundary layer would result in a higher blockage and a corresponding increase in displacement loss. At this incidence it only accounts for $\approx 4\%$. Highlighting that fact the while a large turbulent boundary layer results in higher losses, most of the loss is associated with the production of these structures at the leading edge after which they are convected through the passage, as the boundary layer displacement loss that is expected is not seen in this case.

Finally RANS predicts that base pressure and form losses play a more substantial role compared with the LES, which is attributed to the more coherent wake predicted by RANS. Resulting in a lower relative trailing edge base pressure and increased form loss. This lower base pressure is likely in error highlighting a short fall of the RANS analysis in the presence of discrete unsteadiness. Overall the Denton loss breakdown analysis has provided some interesting insight into where the majority of loss is derived. While the comparison between LES and RANS has highlighted the limitation of RANS in predicting losses under off-design engine running conditions. Importantly it has shown that while RANS may predict representable total losses the means by which it arrives at these values is notably different from those predicted by LES, and care should be taken to ensure that one is aware of these trends in RANS.

Chapter 4

Loss Prediction and the Influence of Discrete Disturbances

4.1 Introduction

The pressure rise through a single axial-flow compressor stage is limited by the losses associated with the boundary layers. In order to achieve the overall pressure rise required for a modern gas turbine engine, it is necessary to employ a sequence of compressor stages, each with a relatively small pressure ratio. Therefore it is necessary to understand the interaction between stages including the effects of up-stream wakes on down-stream blades.

The presence of wakes in a compressor is an important source of unsteadiness in the blade rows down-stream and can have marked effects on performance. Their discrete nature results in an array of different flow regimes over the blades and various effects on the blade boundary layer development, depending on the phase of the passing wake. The interaction between an up-stream blade row and the one down-stream of it can be characterised with several parameters. The most relevant of which is the reduced frequency of the incident wakes ($f_{red} = (u_{y:bar}l)/w$). The reduce frequency determines the frequency with which wakes hit the leading edge of the down-stream blade. Work by *Schobeiri et al.* (2003) showed the effects of reduced frequency and how very high wake passing frequencies can imitate free-stream turbulence. This transition from discrete unsteadiness to broad band unsteadiness adds further complexity to understanding incident wakes as different flow regimes of the boundary layer are only prevalent for certain reduced frequencies.

The flow coefficient, $\phi = u_{y:bar}/u_x$, is a second parameter used to relate the relative convection speeds of the wakes, which determines the length of time a wake interacts with the blade boundary layer as well as the angle of incidence of the flow. Varying the flow coefficient results in a change in the contact area of the incident wake on the blade boundary layer. A higher incidence

or slower wake passing results in a stronger "negative jet" effect on the boundary layer, in a process outline by *Coull and Hodson* (2011) for turbines.

A review by *Cumpsty et al.* (1995) on the various regimes that are seen in the boundary layer of a compressor with incident wakes highlights the variety of different transition modes that exists in the presence of wakes. The fundamental effects of wakes on compressor boundary layers has been shown by *Halstead et al.* (1995). *Halstead et al.* (1995) report effects such as the early onset of transition, suppression of separation and existence of a calmed region following the wake passing. An experimental investigation by *Hilgenfeld and Pfitzner* (2004) looked at a V103 linear compressor cascade with different wake reduced frequencies, Hilgenfeld and Pfitsner's data series is used as an experimental reference for numerical comparison. The work was performed at a Mach number of 0.67 and Reynolds number 450,000 and are used in this research to provide the basic set-up for a computational investigation of the effects of incident wakes. The investigation also highlighted the interaction of free-stream turbulence and incident wakes, showing that the effects of wakes, even with low reduced frequencies was limited in the presence of high back ground turbulence.

Wissink et al. (2014) performed an incompressible DNS at Reynolds number 138,000 on the same V103 cascade and looked at the effects of wake turbulence intensity on a compressor boundary layer. In the study by *Zaki et al.* (2009), the wake disturbances were introduced as an inflow profile, based on a separate DNS of a moving bar by *Wissink and Rodi* (2008), allowing the intensity of the wakes to be varied. It was seen in the work that the weaker incident wakes did not have a marked effect on the suction surface separation, with the mean separation length only slightly altered. However, the stronger wakes did show a periodic suppression of the separation and a noticeable variation in the wall shear.

The use of LES in modelling the influence of wakes has been investigated by *Gourdain* (2015b) who ran a full stator-rotor stage at design conditions. The investigation focused on a comparison of unsteady RANS and LES and showed that LES improved predictions of unsteady effects. Such as tip leakage flows, compared with the RANS. However, the mean performance prediction was similar. Incident wakes at off-design conditions have also been investigated. *Hodson and Addison* (1989) showed the effects of wakes on turbine performance at off-design incidence and found the wakes had limited effect on the pressure surface but drove transition on the suction surface for the blade profile considered. Work on compressor performance has been done by *Henderson and Walker* (2010) who experimentally investigated wake effects at off-design incidences. The study found the existence of turbulent patches and calmed regions at all incidences although the variation in pressure gradient over the blade, as the incidence is changed, resulted in variation of intermittency of turbulent patches.

The study performed here investigates the effects that different types of free-stream disturbance have on loss at a positive off-design incidence. The types of disturbances are free-stream turbulence, turbulent wakes from moving bars and a reference case with no added disturbances. The

effects of different types of disturbance have been investigated before, as mentioned, though only focusing on the effects of varying the parameters of a single type, often at design conditions. Furthermore, the majority of previous work has been performed using RANS or experiments, with limited high fidelity LES studies performed. The investigation here performs a set of wall resolved LESs at engine Reynolds numbers and Mach numbers and at a positive off-design incidence. Providing highly accurate results and a comparison across different disturbance types rather than variations of a single type. The objectives originally set out to improve understand of how the type of free-stream disturbance affects loss but subsequently went on to also show what the effects to the instantaneous flow are as well.

4.2 Method

The moving bar simulations follow a similar method and set-up as used for the high Reynolds number cases with free-stream turbulence in chapter 3, with the exception that the free-stream turbulence is removed and moving wakes are introduced. The addition of the moving wakes requires a sliding mesh interface, that was introduced in chapter 2, in order to have the wakes traverse in a pitch-wise direction up-stream of the cascade. The wakes are produced by placing span-wise cylinders a given distance up-stream of the cascade.

The use of up-stream bars to produce incident wakes has been shown to provide an acceptable alternative to a full blade wake. It is well known that cylinder wakes produce vortex shedding, a phenomenon which is also found in the wakes of compressor blades. It is also known that the wakes of cylinders are symmetrical while those of compressors are not. However, it is suggested by *Dong and Cumpsty* (1990b) that this difference has little effect on the development and transition of the boundary layer which is mainly affected by the high levels of turbulence they contain.

The simulations are run first in 2D, as this was found to be the easiest and cheapest method of initialisation, then later extended to 3D with the addition of a span-wise extent and higher Fourier modes. The initialisation of the 2D simulation is performed using the same routine explained in section 2.7.7 with one addition: The inlet boundary conditions is now placed on a set of blocks that are moving relative to the cascade. Considering the frame of reference of the blades,it is necessary to subtract the block sliding velocity from the pitch-wise velocity of the inlet which is then later added by the relative motion of the sliding interface.

After extending the converged solution to 3D the simulations are run for a further ≈ 2 flow through times in order to allow the flow to transition and develop a statistically static state. The state of transition of the flow was determined by watching a rolling average of velocity at several monitor points within the domain. The flow was considered past the transient once the change in the rolling average of the flow variables was considered sufficiently small, $< 5\%$

of the mean. Following the transition period the simulations were then run for an additional time period in order to collect statistical data. The statistical convergence is based on the phase period of the moving bars as the phase locked statistics were collected by capturing an instantaneous snap shot of the flow at a given phase angle for each period. These snap shots were later averaged during post processing.

The bar period was divided into 18 phases and the simulations run for approximately 7.3 cascade flow through time units, giving a phase-locked average of 10 realisations per phase. Time-averaged statistics were also collected for the 7.3 flow through times, giving non-phase-locked averaged statistics of the flow domain.

4.3 Case Set-up

The use of moving bars to introduce the incident wakes was chosen in order to reduce computational expense, since the wakes are produced without the simulation of an up-stream blade row.

The moving bar study is performed on the same NACA 65 geometry used for the free-stream turbulence loss bucket investigation. The case is adapted to include up-stream moving bars and is based on the work by *Hilgenfeld and Pfitzner* (2004) who performed an experimental investigation on the effects of wake passing on compressor performance at design conditions at a Mach number of 0.67 and chord Reynolds number of 450,000 on the same NACA 65 cascade. The nominal parameters for this work however have been kept the same as the free-stream turbulence case in chapter 3, with the Reynolds number set to 300,000, and the Mach number set to 0.67. The incidence has been set to $\alpha = 44°$ in order to compare with the positive incidence off-design case. Here, α is again defined relative to the axial direction with reference to fig. 4.1. The interest here is on the effects the moving bars have on the cascade performance and on the comparison and quantification of loss.

Two moving bar cases have been run: one with three bar per blade pitch as a verification case to compare with the available data from *Hilgenfeld and Pfitzner* (2004), and a second case with one bar per blade pitch, a case more typical of practical turbo machines. Current compressors run with substantially higher reduced frequencies than performed in the reference case. The three bar case is not directly relevant to modern gas turbine machines. For this reason the three bar results are used primarily verification and not analysed further in the current chapter.

For the moving bar case the reduced frequency is based on the axial chord, l, and axial inlet velocity, u_x, and is set to 0.66 for the verification case and 1.9 for the comparison case. The flow coefficient, which relates the velocity of the bars to axial flow velocity is set to 7.704 for the verification case and 0.89 for the comparison case. By substituting the flow coefficient into the

reduced frequency equation, the reduced frequency can be given as

$$f_{red} = \frac{l}{w_{bar}\phi}, \tag{4.1}$$

where w_{bar} is the pitch of the bar. The simulations are run without free-stream turbulence so that the influence of the wakes can be considered in isolation from the effects of free-stream turbulence.

A schematic of the set-up is shown in fig. 4.1 with the nominal parameters in table 4.1. The moving bars are placed a distance $x/l = 0.38$ up-stream of the leading edge, with the flow domain extending to 0.6 chord lengths up-stream and one chord length down-stream of the blade. The span-wise extent is set to 0.2 chord lengths.

The implementation of the moving bars was developed through a separate bar-only investigation. Two methods were considered, both based on a sliding mesh interface, an approach in which the bars are placed in a region of mesh up-stream of the cascade. This mesh is then translated in the pitch-wise direction with the appropriate relative velocity. The first method considered is the Boundary Data Immersion Method (BDIM) of *Weymouth and Yue* (2011) which reduces the complexity of the mesh by allowing the use of a Cartesian mesh up-stream of the blade to accommodate the bars. The second method is the use of a body-fitted bar mesh which requires a more complex multi block set-up. The bar-only study is detailed further in next section.

The mesh around the blades remains the same as that used for the free-stream turbulence loss bucket simulations, which is an H-type mesh with an embedded O-type mesh around the blade. The total in plane mesh count for the blade is $603,136$ with a span-wise discretisation of 128 Fourier modes giving an effective cell count of $155,609,088$ for the blade domain. The wall resolution for the blade with this set-up is given as $\Delta x^+ \approx 15$, $\Delta y^+ \approx 1.5$ and $\Delta z^+ \approx 12 - 25$ (based on the free-stream turbulence loss bucket simulations). The lowest resolution is found near the leading edge suction surface for the 37° incidence case where the flow velocity is highest.

The boundary conditions for the simulations are as follows. The blade boundary is set as a non-slip adiabatic wall. The exit plane is treated with a non-reflective characteristic boundary condition prescribing an exit static pressure only. The inlet boundary conditions imposes a constant velocity and density. As no free-stream turbulence is injected in this case, a sponge is also applied to the inflow to reduce reflections. The pitch-wise and span-wise boundaries are periodic.

The boundary conditions for the moving bars are set as non-slip adiabatic. However for the initial bar-only study the boundary conditions for the bars was non-slip isothermal, with the temperature set to the reference temperature. The choice of isothermal bars, while not identical to the final coupled simulations the heat transfer was found to be negligible. It was found that

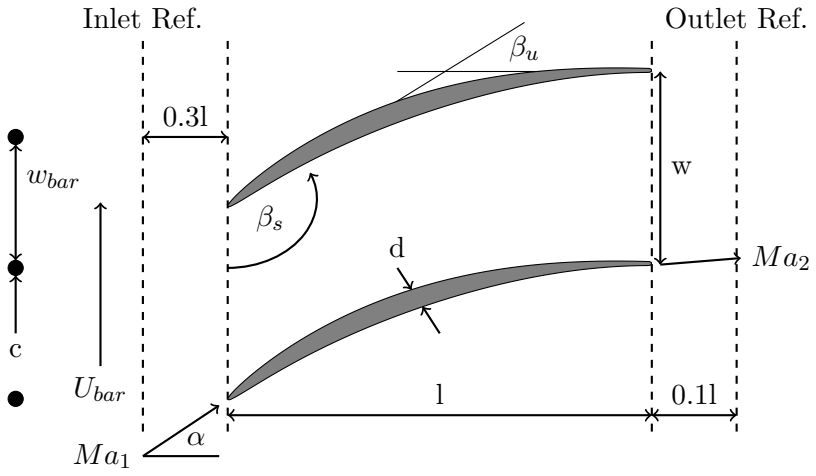

Figure 4.1: Schematic representation of cascade with up-stream moving bars.

Reference Paper Conditions	
$Re = 300,000$	Mach $= 0.67$
$\alpha = 44°$	$\beta_s = 112.5°$
$w/l = 0.59$	$w_{bar}/l = 0.197$
$d_{bar}/l = 0.0098$	$x_{bar}/l = 0.38$

Table 4.1: Full cascade parameters

the body-fitted mesh performed better and this was selected for the coupled simulations. The boundary condition of the bars for the full simulations was set to adiabatic.

The set-up for the base case without any form of free-stream disturbance is essentially identical as the set-up for the free-stream turbulence cases in chapter 3 aside from a change to the inlet boundary condition. For the base case the inlet boundary condition is set fixed velocity and density and a sponge employed as in the moving bar cases. No other changes to the domain or set-up were made.

4.4 Numerics

The simulations are performed using the in house code HiPSTAR and employ the WALE LES model implemented. The numerical set-up of the code is outlined in chapter 2. The WALE LES coefficient is set to 0.325 as suggested by *Nicoud and Ducros* (1999).

4.5 Bar Only Study

The objective of the bar study is to evaluating whether the body-fitted or immersed boundary method provides the best solution for a given computational cost. The two approaches have different advantages. The solution of the body-fitted mesh provides better boundary layer resolution for a given computation cost. The kernel interpolation region required by the immersed boundary methods are strongly mesh dependent and the mesh requirements can be substantial if fine flow details are needed. However the added complexity of the body-fitted curvilinear mesh introduces additional complexity in the multi block set-up which may require a larger mesh to ensure adequate resolution in the bar far field.

As the interest of this investigation is on the effects of incident wakes on the blade boundary layers resolving the near wake behaviour of the moving bars is not a priority. As such, the focus is on ensuring that the mean wake profiles and turbulent kinetic energy of the far wakes are adequately predicted. The study also investigates the effect of mesh resolution for the two methods, with two simulation performed for each.

The results of the simulations will be compared with the incompressible DNS simulations performed by *Wissink and Rodi* (2008). For the remainder of this work the immersed boundary cases will be referenced in tables and figures as BDIM , and the body-fitted cases are referenced by BDYF.

4.5.1 Case Set-up

The simulations are performed using the parameters given in the paper by *Wissink and Rodi* (2008). However, the simulations performed by Wissink and Rodi were incompressible while those performed here are compressible. In order to try and match the results as closely as possible the Mach number of the simulations will be set to 0.2 to reduce compressibility effects. The Reynolds number is set to 3,300, based on the cylinder diameter and free-stream velocity. This is closed to the expected Reynolds number of the bars in the full cascade simulation ($\approx 3,000$). The domain for the bar-only case is set to 10 diameters up-stream and 15 diameters down-stream with a span-wise extent of 4 diameters, as is set in the reference case. The pitch-wise extent is set to 20 diameters in the immersed boundary cases and ≈ 20 in the body-fitted case, again as prescribed by the reference. For the body-fitted case the pitch-wise extent is not constant. The variation in the pitch-wise extent of the body-fitted case is due to the in house mesh generation code which is designed to create periodic meshes for axial compressor blade cascades. In order to create a symmetric mesh with this method the top blocks of the H-grid mesh are copied below the bar, resulting in a #-grid mesh with embedded O-grid, and a slight variation in pitch-wise extent seen in fig. 4.2. It is argued that as the simulations are not periodic in the pitch-wise direction the non-uniform mesh boundary does not affect the solution as it is

Mesh	Cell Count
BDIM Base	49,601
BDIM Fine	102,017
BDYF Base	69,932
BDYF Fine	111,616

Table 4.2: Bar only mesh resolution for BDIM and Body fitted cases.

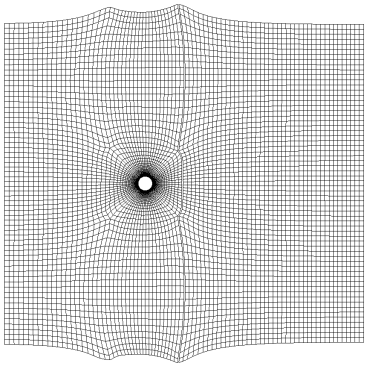

Figure 4.2: Mesh for the base body-fitted bar case showing every 3rd line

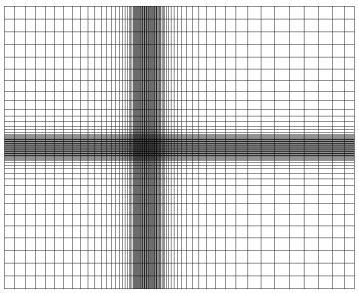

Figure 4.3: Mesh for the base BDIM case showing every 3rd line

a free-stream boundary. The body-fitted and BDIM meshes are shown in figures fig. 4.2 and fig. 4.3 respectively, showing the base case grid resolution and block structure. The mesh details of the four cases are given in table 4.2

For the bar-only simulations the inlet boundary condition is fixed with a sponge employed to reduce reflections, while the pitch-wise and outlet boundaries employ a non-reflective characteristic boundary condition, enforcing static pressure only. The span-wise boundaries are periodic and the bar is set as a non-slip isothermal wall in all cases.

4.5.2 Results

The statistical results for the bar cases are presented here and the final running conditions shown in table 4.3. The statistical results were collected for 100 flow through times.

The interest of the compressor simulations is on the interaction of the bar wakes on the blade boundary layer, for this reason only the far wakes of the bars need to be matched with the DNS reference. For the full cascade simulations the bars are placed a distance ≈ 40 diameters up-stream of the leading edge of the blade which means that the wake position being compared here at $x/D = 10$ is a still a substantial distance from the blade. However, it is reasoned that the wake is fully developed by this stage and representative of what is experience by the blade. Furthermore, in order to ensure that the wake continues to develop correctly the mesh size is kept as uniform as possible up to the leading edge of the compressor cascade.

	BDIM Base	BDIM Fine	BDYF Base	BDYF Fine
U_∞	0.96	0.96	0.98	0.98
Re	3194	3198	3249	3245
Mach	0.19	0.19	0.2	0.2
ρ	0.99	0.99	0.99	0.99

Table 4.3: Final converged conditions for bar-only cases.

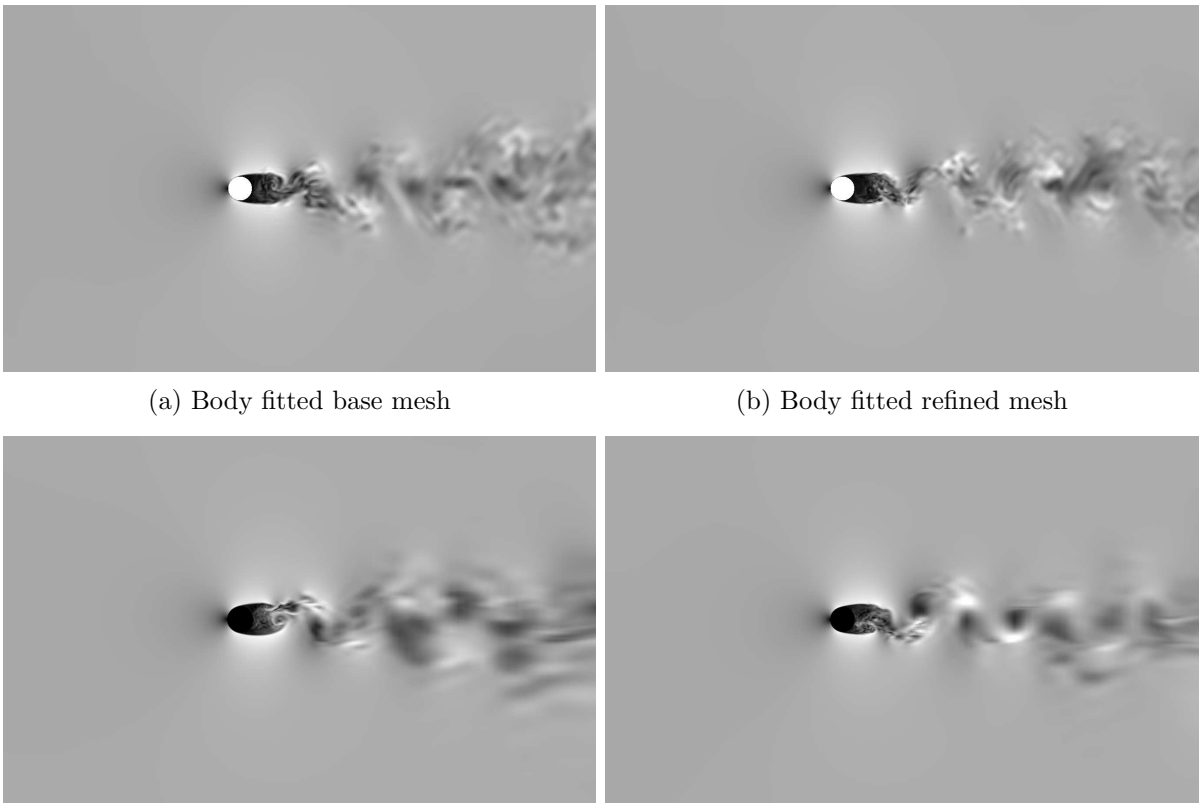

(a) Body fitted base mesh

(b) Body fitted refined mesh

(c) BDIM base mesh

(d) BDIM refined mesh

Figure 4.4: Contour plots of instantaneous velocity magnitude for both body-fitted and BDIM meshes.

A full-field view of the instantaneous velocity magnitude is shown in fig. 4.4 and a full-field view of the statistical results of velocity magnitude and TKE for the refined cases is presented in fig. 4.5. The instantaneous full-field plots highlight some of the differences of the two approaches. The most notable is the smearing of wake structures in the BDIM base case. This results from the mesh stretching necessary with this method in order to keep the total cell count down. However, the statistical results show this to have limited effect on the wake profiles. This smearing is still present in the refined BDIM case in fig. 4.4(d) although the structures remain a lot more coherent with the increased mesh resolution.

The stream-wise velocity profiles at several locations are presented in fig. 4.6 for both methods

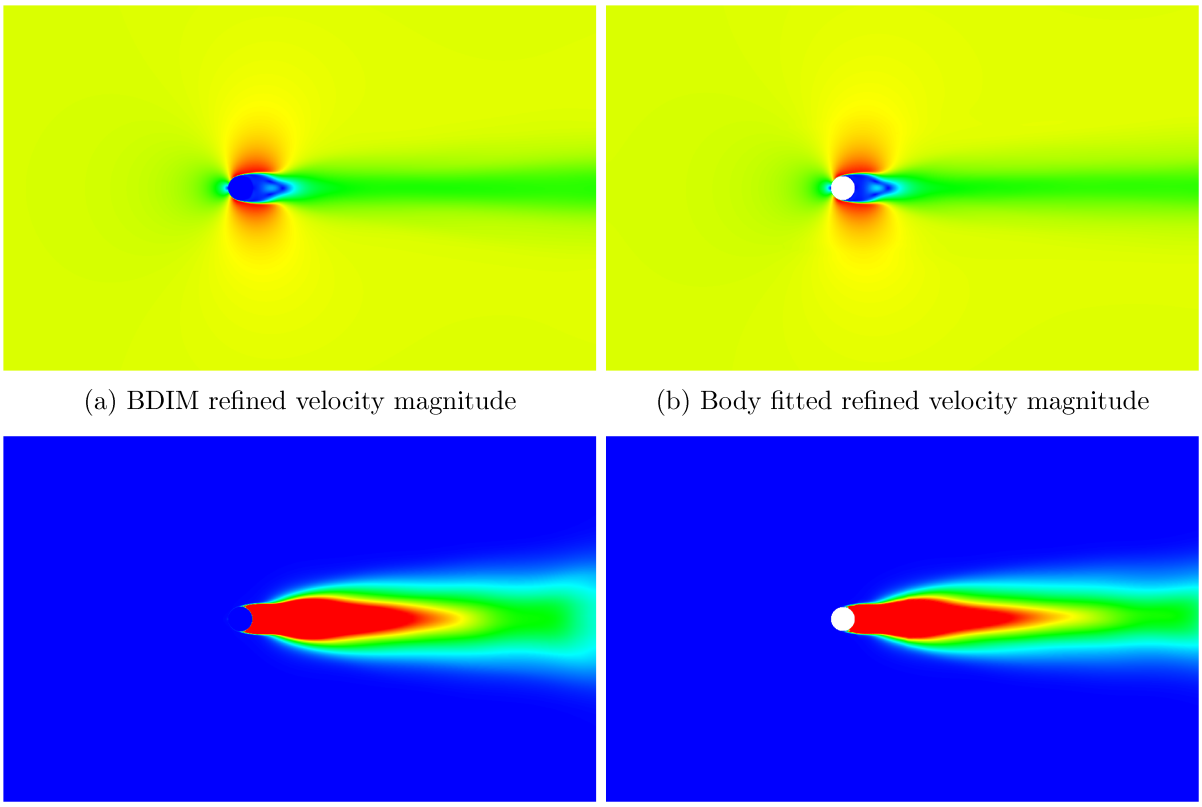

(a) BDIM refined velocity magnitude

(b) Body fitted refined velocity magnitude

(c) BDIM refined TKE

(d) Body fitted refined TKE

Figure 4.5: Contour plots of statistically averaged velocity magnitude (top) range [0;1.4] and TKE (bottom) range [0;0.5] for the refined BDIM and body-fitted meshes

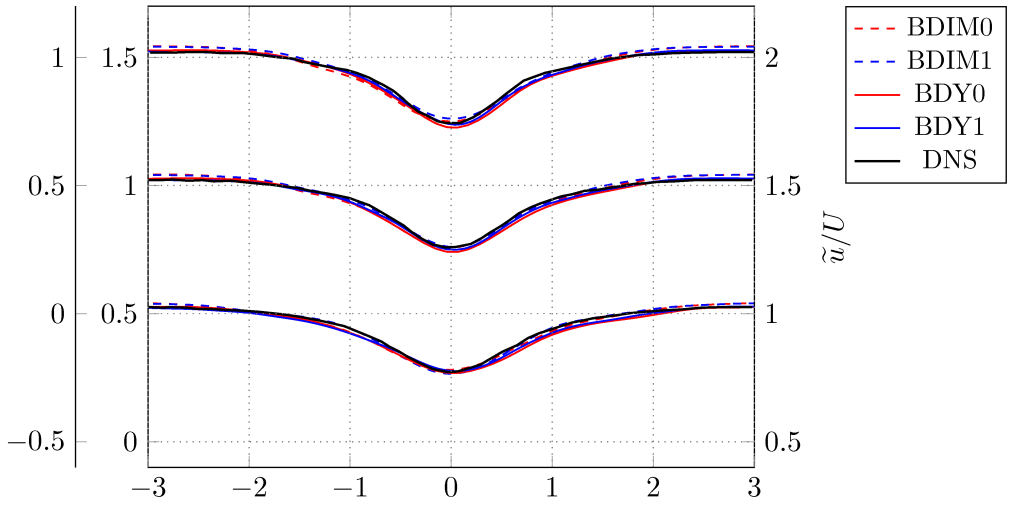

Figure 4.6: Stream wise velocity profiles, $\widetilde{u_x}/U_\infty$ at $x/D = 6$, $x/D = 7$ and $x/D = 10$ from top to bottom respectively with DNS reference data from *Wissink and Rodi* (2008).

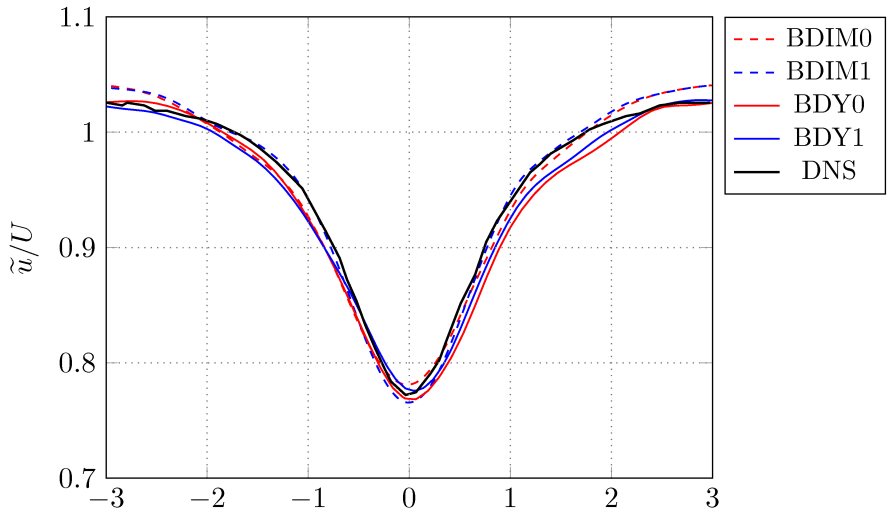

Figure 4.7: Stream wise velocity profiles $x/D = 10$ only highlighting difference with DNS reference data from *Wissink and Rodi* (2008).

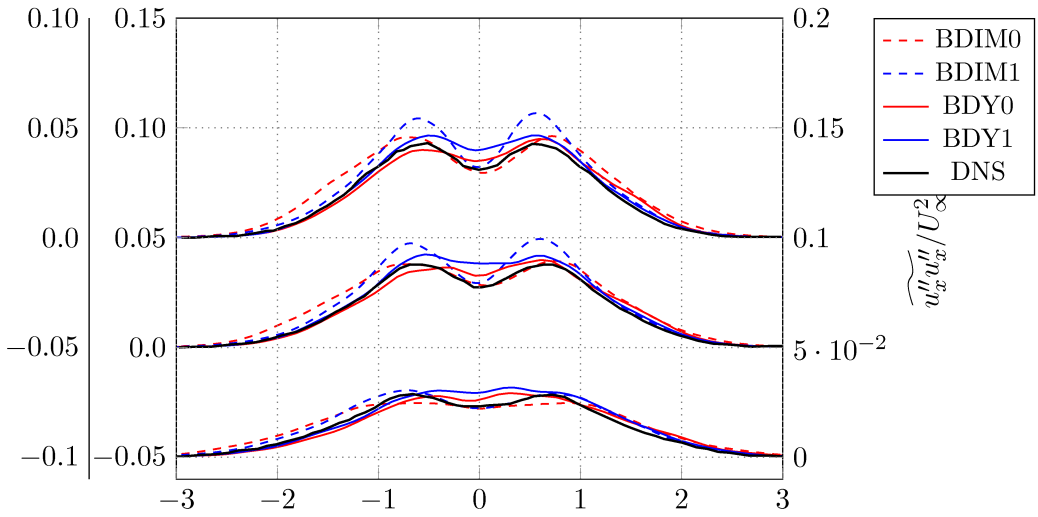

Figure 4.8: Turbulence statistics $\widetilde{u''_x u''_x}/U_\infty^2$ profiles at $x/D = 6$, $x/D = 7$ and $x/D = 10$ from top to bottom respectively with DNS reference data from *Wissink and Rodi* (2008).

and both mesh resolutions. The comparison between the cases is good suggesting that either method coupled with the LES modelling provides good performance with regards to wake deficit. The velocity profile at stream-wise position $x/D = 10$ shown in fig. 4.7 which highlights a slight blockage effect in the immersed boundary cases due to the enlarging of the cylinder by the interpolation kernel. It is seen that all the cases match the peak deficit of the DNS well though there is a tendency to predict a slightly wider wake in the body-fitted and BDIM base cases.

The comparison of the turbulent fluctuations, $\widetilde{u''_x u''_x}/U_\infty^2$ and $\widetilde{u''_x u''_y}/U_\infty^2$, are plotted in fig. 4.8 and fig. 4.9 respectively with the results showing good agreement with the DNS results. Again focusing on $x/D = 10$ only, the turbulent fluctuations are plotted in figs. 4.10a and 4.10b. At

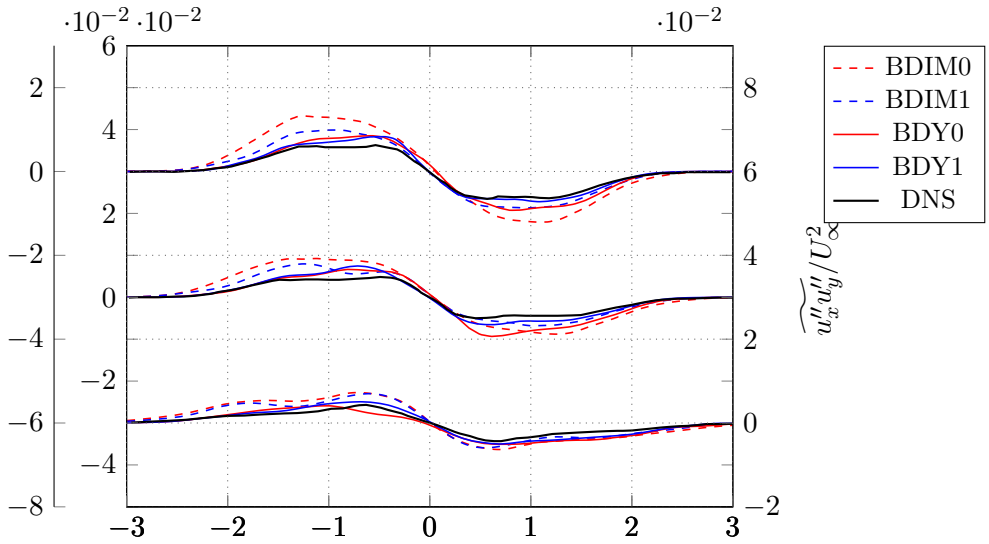

Figure 4.9: Turbulence statistics $\widetilde{u''_x u''_y}/U^2_\infty$ profiles at $x/D = 6$, $x/D = 7$ and $x/D = 10$ from top to bottom respectively with DNS reference data from *Wissink and Rodi* (2008).

this location it is seen that the BDIM refined case compares best with the DNS for the Reynold stresses, $\widetilde{u''_x u''_x}/U^2_\infty$, while the body-fitted cases show better agreement with $\widetilde{u''_x u''_y}/U^2_\infty$ Reynold stresses making both methods acceptable with respect to the turbulent statistics.

The pitch-wise velocity power spectral density of point at 5 diameters down stream of the cylinder is plotted in fig. 4.11 for all cases. The power spectral density is plotted against Strouhal number, based on the cylinder diameter and free-stream velocity. The spectra show that all four cases capture a clear energy cascade and adequately resolve the higher Strouhal numbers.

Overall the comparison of the bar-only cases with the DNS data from Wissink and Rodi show good agreement and adequate resolution for both the fine and course meshes, although there is a slight increase in blockage seen in the BDIM cases due to the immersed boundary interpolation kernel. Despite the slight increase in blockage for the BDIM cases both methods produce satisfactory results at $x/D = 10$ therefore the choice is made on the basis of computational expense.

4.5.2.1 Computational expense

The comparison of computational expense between the two methods for both mesh resolutions is presented in table 4.4. The cpu time per time-step is normalised with the number of cores and number of grid points to account for any miss match in work load distribution. The results are also presented normalised by the body-fitted base case which gave the shortest time per time-step. It is seen in the table that the BDIM method was a factor of 4 slower than the body-fitted method for both cases. This dramatic slow down is attributed to the immersed boundary

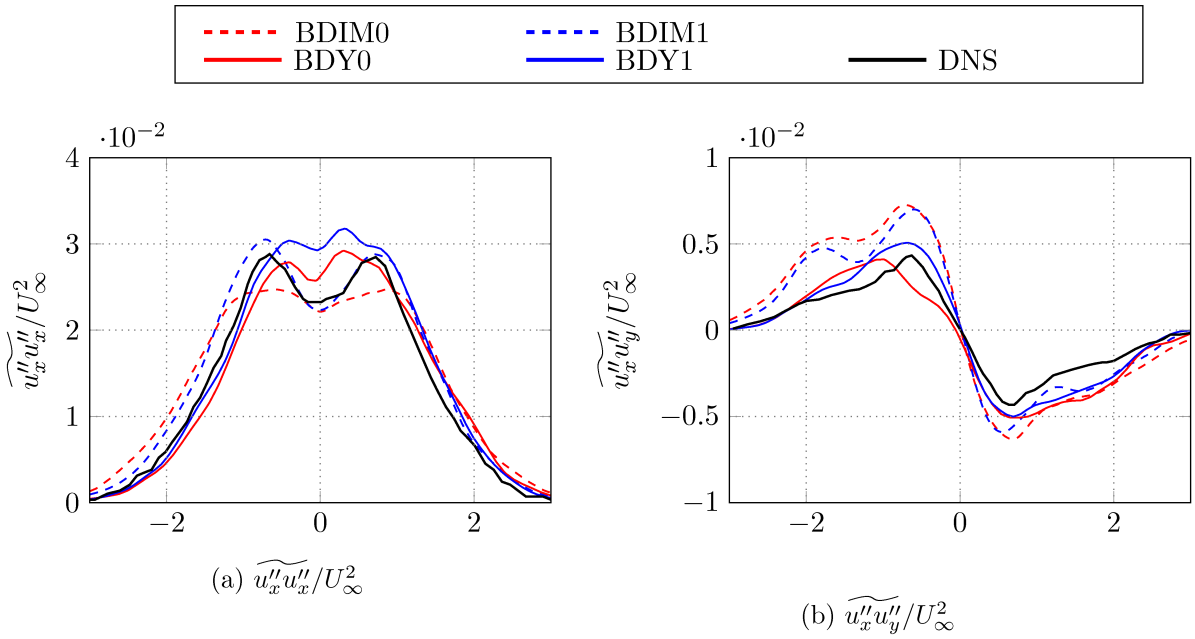

(a) $\widetilde{u''_x u''_x}/U^2_\infty$ (b) $\widetilde{u''_x u''_y}/U^2_\infty$

Figure 4.10: Turbulence statistics for $\widetilde{u''_x u''_x}/U^2_\infty$ and $\widetilde{u''_x u''_y}/U^2_\infty$ profiles at $x/D = 10$ with DNS reference data from *Wissink and Rodi* (2008).

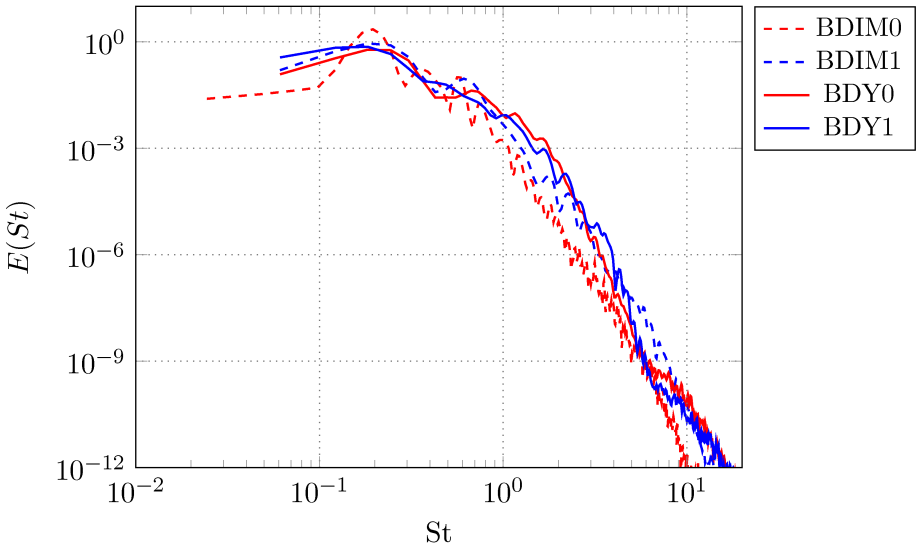

Figure 4.11: u_y velocity power spectral density for all four cases at a point 5 diameters downstream of the cylinder.

Case	$\frac{\text{wall time}}{\#\text{steps}*\#\text{core}*\#\text{grid point}}$	Normalised with BDYF Base
BDIM Base	3.88e-8	4.51
BDIM Fine	3.93e-8	4.56
BDYF Base	8.60e-9	1
BDYF Fine	1.08e-8	1.26

Table 4.4: Bar only mesh resolution for BDIM and Body fitted cases.

implementation which results in poor work load distribution per core as only certain cores have the extra work associated with applying the immersed boundary forcing. Furthermore, with the current implementation of the code it is not possible to allocate a different number of grid points per core within a block, making it difficult to distribute the work more evenly. The slight difference between the two body-fitted cases is also attributed to poor work load distribution, as the increase in mesh resolution of the refined case resulted in blocks that could not be easily divided into equal loading per core for every block.

The BDIM cases however can be run with a larger time step compared with the body-fitted cases, even though both methods have comparable mesh cell sizes. This improved stability of the BDIM method is due to the fact that the body is applied via a forcing rather as well as the mesh being more uniform. The difference in time step however is not beneficial when running the full cascade case as the time step will be determined by the cascade mesh, which is more refined. For the comparison of the simulations here the time step was the same for all of the bar cases.

4.5.3 Findings of Bar Study

From the results of the bar-only study, it is shown that the body-fitted base case provides the best option as all the cases tested matched the DNS results adequately. The body-fitted method proved cheapest although there is added complexity in setting up the mesh for this method. However, the added effort and time is offset by the reduced computational expense and faster computational speed. Therefore the body-fitted approach is adopted in all simulations described below.

4.6 Computational Expense of Full Cascade

The full moving bar simulations were performed on the UK national super computer ARCHER with time granted by the UK turbulence consortium. ARCHER uses the Cray XC30 architecture consisting of compute nodes connected together by the Aries interconnect. Each compute node

contains two 2.7 GHz, 12-core E5-2697 v2 (Ivy Bridge) series processors and within the node, the two processors are connected by two QuickPath Interconnect (QPI) links.

The simulations were performed using 8640 cores run for approximately 40 hours to obtain the statistical convergence. The parallelisation was done using hybrid mpi-openmp with mpi used for in plane parallelisation and openmp for span-wise acceleration. The 3 Bar set-up gave a total running time for statistical convergence of $\approx 345,600$ core hours while the 1 Bar set-up required $\approx 322,500$ core hours due to the slightly smaller mesh required for only one bar.

4.7 Verification

Before looking at the comparison of different disturbance types, the initial three bar simulation is compared with the experimental data available. This case was run for code verification as a compressor cascade with moving bars has not been performed with this code before. However, it is noted that the experiment is not representative of modern compressor flows.

4.7.1 Experimental Comparison

The case is run at a chord Reynolds number of 300,000 and a Mach number of 0.67, the same values used for the off-design cases in chapter 3. The experimental set-up, taken from *Hilgenfeld and Pfitzner* (2004), provides the general case set-up. The final running conditions of the 3 Bar verification case are given in table 4.5

Name	3 Bar
Reynolds	303,700
Mach	0.608
Angle	43.09
Turning	-36.6
%Tu @ LE	0.6
Reduced Frequency	0.7
Flow coefficient	6.8

Table 4.5: Tabulated final running conditions for 3 Bar case. Parameters are calculated at reference planes 15% chord up-stream and 140% chord down-stream of the leading edge.

4.7.1.1 Time traces

Hilgenfeld and Pfitzner provide time traces of velocity and shape factor at several location in the domain. Figure 4.12 shows the trace of velocity down-stream of the moving bars to compare

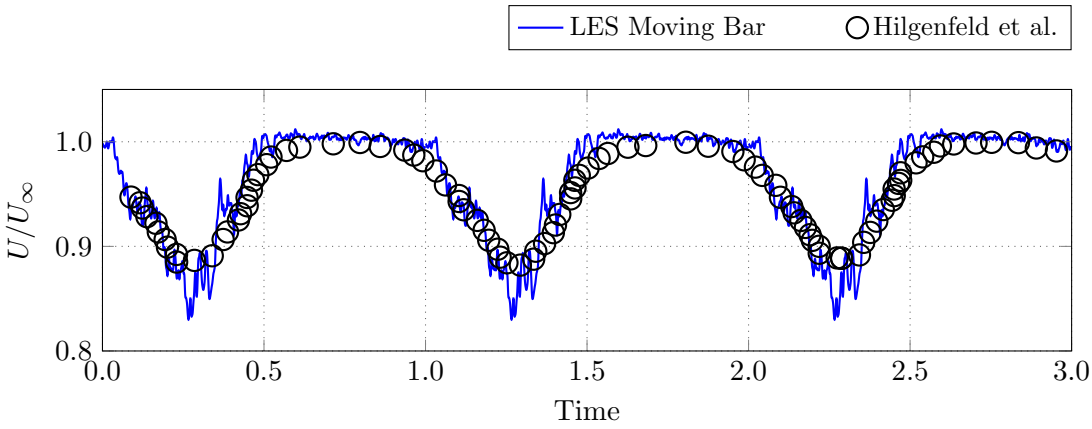

Figure 4.12: Velocity trace at inlet to blade geometry behind the moving bars at 0.15 chord lengths upstream of the leading edge.

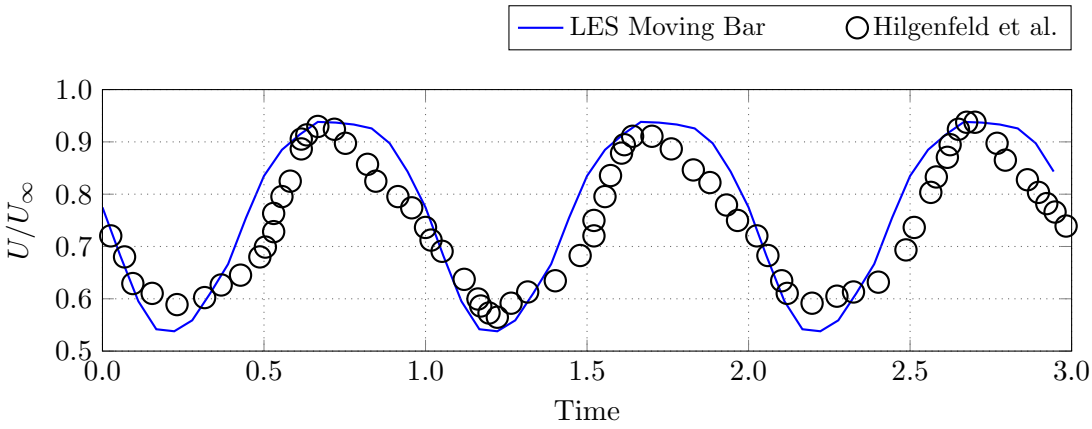

Figure 4.13: Velocity trace at 65% axial chord and 1.14% wall normal chord on the suction surface. Normalised with the free-stream velocity.

the bar wake profiles. A second velocity trace showing the effects of the bar passing on the suction surface boundary layer at an axial position of 65% chord and 1.14% chord above the blade surface is shown in fig. 4.13. Finally a trace of the suction surface shape factor at 99% chord is compared in fig. 4.14.

The agreement of the various traces is good overall. The slight differences in the boundary layer traces are due to the 3 Bar case converging with a blade inflow incidence of 43°. The difference of 1° is due to the blockage affect the bars have that was larger than expected.

4.7.1.2 Profiles

The loading for the 3 bar case and the 44° free-stream turbulence case is compared in fig. 4.15. The bars have a clear effect on the loading seen by the suppression of separation and earlier transition on the suction surface though overall the loading matches well. Showing the same

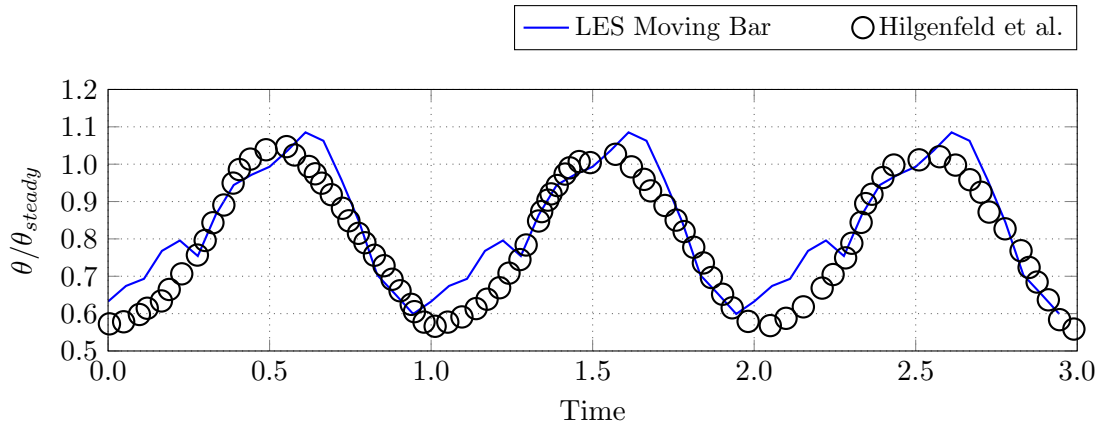

Figure 4.14: Shape factor trace at 99% axial chord for the suction surface. Normalised using the 44° free-stream turbulence case shape factor.

general trends and flow features as the 44° case. The effect of the bars is predominantly on transition as expected, which occurs earlier, and suppresses the distinct transition step seen at $x/l \approx 0.5$ for the 44° free-stream turbulence case in fig. 4.15.

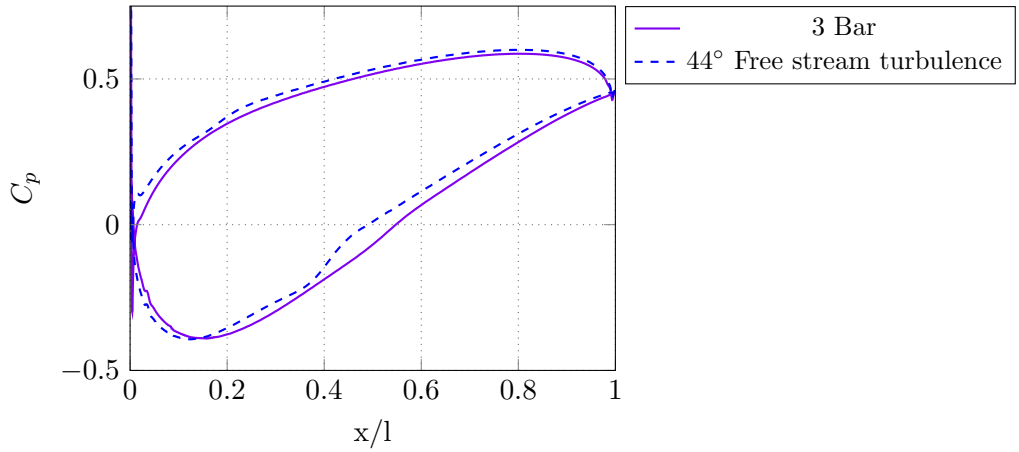

Figure 4.15: Time averaged loading comparison for 3 bar case and 44° free-stream turbulence case.

4.7.2 Verification Conclusions

The simulation results for the three bar case show good agreement with the available experimental data. However, as the comparison is quite limited, due to available data, it is not possible to make strong conclusions. As the code has been verified previously for the loss bucket simulations, as well as showing good performance of the bar-only study, it is deemed that the code and present bar modelling and grid provide a useful basis for further investigation of wake effects at a more representative reduced frequency values.

4.8 Presentation of the Results

The results focus on the comparison between the non turbulent inflow case, the free-stream turbulence case and the one bar case. These three cases are run with similar inlet Mach numbers and incidence angles. The comparison focuses on the effect that discrete wakes and the homogeneous turbulence has on the flow. The case with incident wake has the same average TKE as the turbulent inflow case, however there are large differences in the instantaneous levels. The case without turbulence is used as a reference in order to understand how the different types of inflow disturbance affect the performance of the blade.

The study aims to understand how important it is to capture the variation in turbulence inflow when investigating profile loss. Previous investigations of the effects of wake intensities and free-stream turbulence intensities include *Wissink et al.* (2014) and *Zaki et al.* (2010). These works show that the losses of a blade and the dynamics of the boundary layer are affected by the turbulence levels, as expected, but that the general trends of increased turbulence intensity tend to plateau.

The simulations performed here are at an engine-relevant Reynolds number, making the comparison more relevant to designers. Furthermore, by focusing on the effects of different disturbances types on the flow field it also provides insight for designers into how important it can be to impose representative inflow disturbances in experiments and simulations. This study is slightly contrived in that, generally, wakes and free-stream turbulence will occur together in an engine, but by looking at the effects of each individually it is possible to gain an understanding of how free-stream turbulence and wake structures drive different mechanisms in the boundary layer.

4.8.1 Phase Locked Averaging

Phase averaging is used to understand the periodic changes in the flow as the bars move past the cascade. It is performed by timing the movement of the bars and taking a snap shot of the flow and the same phase angle for each period. For the simulations performed here the bar passing period is dissected into 18 phases giving a phase angle of 20 degrees. For each phase a total of 10 periods are captured and then ensemble averaged.

4.8.2 Final Simulation Parameters

Following the statistical convergence of the simulations the final running conditions are presented here. The parameters of the simulations are calculated on the reference planes, -0.15 chord upstream and 1.4 chord down-stream of the leading edge.

The overall pressure loss for the 44° Base case, 44° free-stream turbulence case (or just turbulence case denoted as 44°Tu) and 44° one bar case (referenced as 1 Bar case) is given in table 4.6. The total pressure loss shows that the effect of turbulence can be quite marked when compared to the Base case without any form of disturbance. It is seen that the the addition of discrete wakes actually results in a decrease in the loss of the blade, while the opposite is true for the effects of homogeneous turbulence. The reasons behind these effects are investigated further in the remainder of the chapter.

Name	44° Base	44°Tu	44° 1 Bar
Reynolds	324,600	322,000	324,800
Mach	0.671	0.665	0.658
Angle	43.97	44.07	43.91
Turning	-38.1	-37.78	-37.57
%Tu @ LE	0.6	4.1	3.5
Reduced Frequency	0.0	0.0	1.897
Flow coefficient	0.0	0.0	0.894
Loss	0.0195	0.0308	0.0108

Table 4.6: Tabulated final running conditions for 44° Base, 44° Tu and 1 Bar cases. Parameters are calculated at reference planes 15% chord up-stream and 140% chord down-stream of the leading edge.

4.9 Blade-to-Blade Flow

Before looking in fine detail at the differences between the cases an overview of the full flow field is given. Starting with the full flow field helps to give an understanding of the changes in flow dynamics and general insight into what might be happening.

Firstly a general view of the flow domain is given in the form of the instantaneous span-wise vorticity. Looking at the span-wise vorticity shows clearly the flow structures and the main changes between each case. The time averaged turbulent kinetic energy (TKE) and phase locked TKE are then presented to show the difference in the boundary layer behaviour in a averaged sense. Then finally the instantaneous wall shear is presented in order to show the dynamics of the difference cases.

4.9.1 Span-wise Vorticity

The span-wise vorticity plots show the change in inflow disturbance as well as the behaviour of the boundary layers. The first figure of the Base case, fig. 4.16a, shows the clean inflow and natural behaviour of the boundary layers. Here it is seen that the boundary layers on both surfaces are initially laminar, undergo transition and then remain turbulent. With the

introduction of free-stream turbulence, fig. 4.16b, the general behaviour of the boundary layers is unchanged though there is slightly earlier transition. The vorticity contour map for the moving bar case, fig. 4.16c, is less clear as to what the boundary layer behaviour is but it shows the direction and relative intensity of the wakes clearly though the boundary layer behaviour outside the region of wake interaction shows behaviour similar to that of the Base case without turbulence, as somewhat expected.

4.9.2 Time-averaged Turbulent Kinetic Energy

The time-averaged turbulent kinetic energy field is presented in fig. 4.17. The comparison between the vorticity and TKE plots allow a simple comparison to be made, removing any short lived phenomena. For the Base case, fig. 4.17a, the TKE shows very similar behaviour to the vorticity plots, with both boundary layers starting as laminar before transition followed by an attached turbulent boundary layer. The turbulent case, fig. 4.17b, has similar suction surface behaviour to the Base case, though the pressure surface transition nearer to the leading edge. The presence of the free-stream turbulence is also shown, with TKE clearly present in the free-stream. Finally the one bar case, fig. 4.17c, shows that the bar wakes result in a similar level of TKE as the turbulent case at the inlet but this dissipates through the domain resulting in a relatively low average level of free-stream TKE through the passage even though the instantaneous vorticity shows the wakes strongly, while the boundary layer TKE behaviour is close to that of the turbulent case.

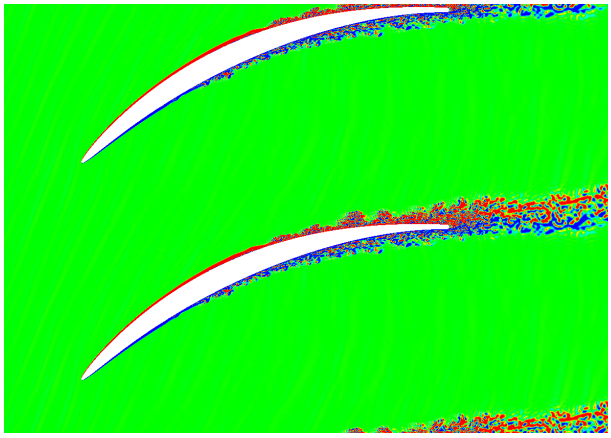

(a) $\alpha = 44°$ Base

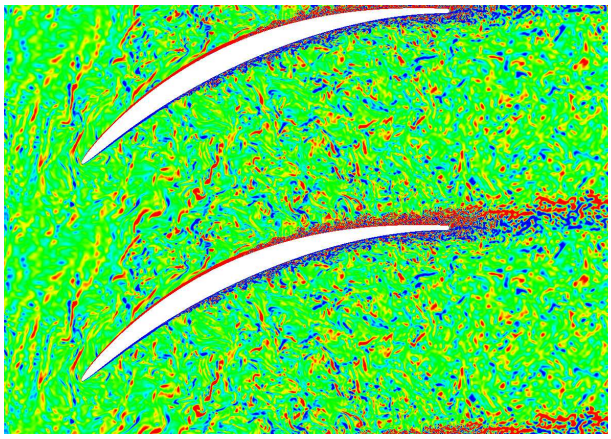

(b) $\alpha = 44°$ Tu

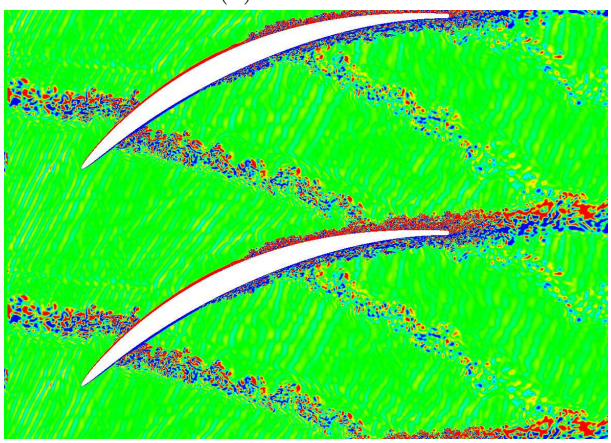

(c) $\alpha = 44°$ 1 Bar wake case

Figure 4.16: Span-wise instantaneous vorticity for Base case (a) free-stream turbulence case (b) and one bar wake case (c). Vorticity contour limits [-10,10]

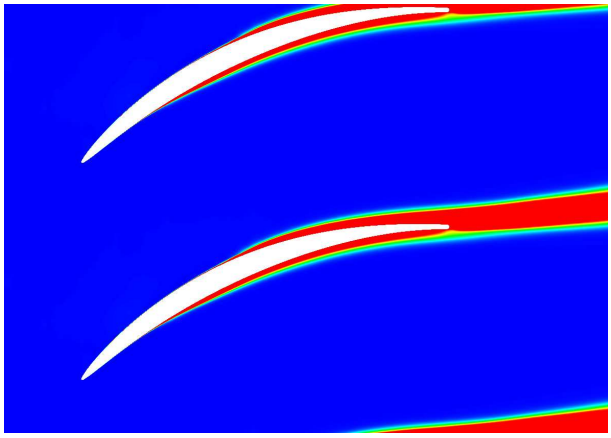

(a) $\alpha = 44°$ Base

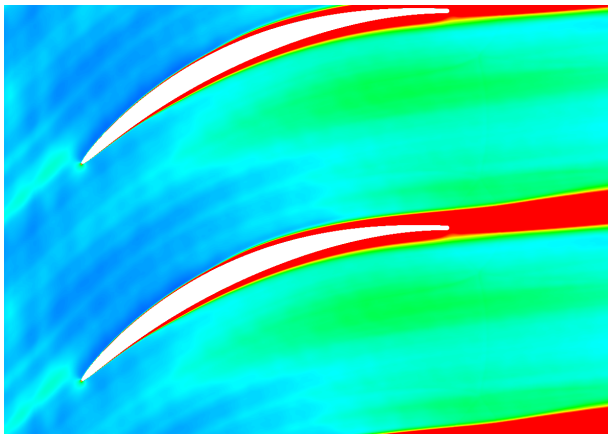

(b) $\alpha = 44°$ Tu

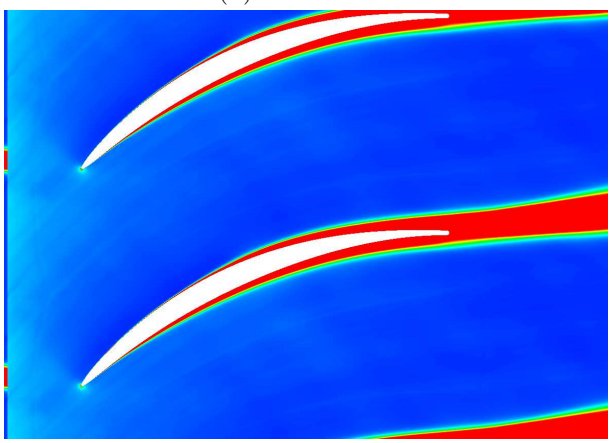

(c) $\alpha = 44°$ 1 Bar wake case

Figure 4.17: Turblent kinetic energy for (a) Base case (b) free-stream turbulence case (c) and one bar wake case. TKE contour limits [0,0.02] normalised with $\frac{1}{2}u_i u_i$.

4.10 Skin Friction

Looking at the instantaneous data of the various simulations provides a good means of understanding what processes are involved. To understand how the two different disturbances affect the boundary layer, it is useful to look at the carpet plots of wall skin friction on the blade surface. These plots, in figs. 4.18 to 4.20, show the variation of the boundary layer and instantaneous skin friction of the suction surface over 1 flow through time unit for the Base and Tu case, and one bar passing period for the bar case.

The carpet plots show that for the Base and Tu cases there is a different transition location but there is little variation in the transition location over time. However, there also increased fluctuations seen up-stream of transition for the 44° Tu case.

It is interesting to see that "waves" are clearly present in the flow domain up-stream of transition. The pressure waves cause fluctuations in the skin friction by periodically changing the local pressure gradient as they pass. It is suggested that these waves originate from the separation bubble, which explains the variation in the structure of the waves between the cases. For the Base case the waves are quite uniform and clear, as the separation and reattachment occurs quite uniformly across the span-wise domain. For the Tu case however the separation and resultant reattachment is not uniform and occurs at different points across the span at any one time, resulting in disorganised waves that propagate up-stream.

For the one bar case the carpet plots are plotted over one bar passing period, which spans ≈ 0.73 time units, showing the effects the wake has on separation and transition. The bar wake is a strong driving force here and results in large perturbation of the boundary layer. For a single passing period it is clearly seen that the boundary layer goes from a large separation bubble, similar to that in the Base case, to a fully suppressed separation bubble, with bypass transition leading to an attached boundary layer as the wake passes the transition region.

This variation is reflected in the waves observed. Over one bar passing period, these waves sometimes show either the same coherent and uniform structure seen in the Base case, produced by the larger natural separation bubble, or the shorter more disorganised waves resulting from the forced transition and non-coherent reattachment of the separation bubble when the wake passes.

The cause and structure of the wave seen in the skin friction is investigated briefly next.

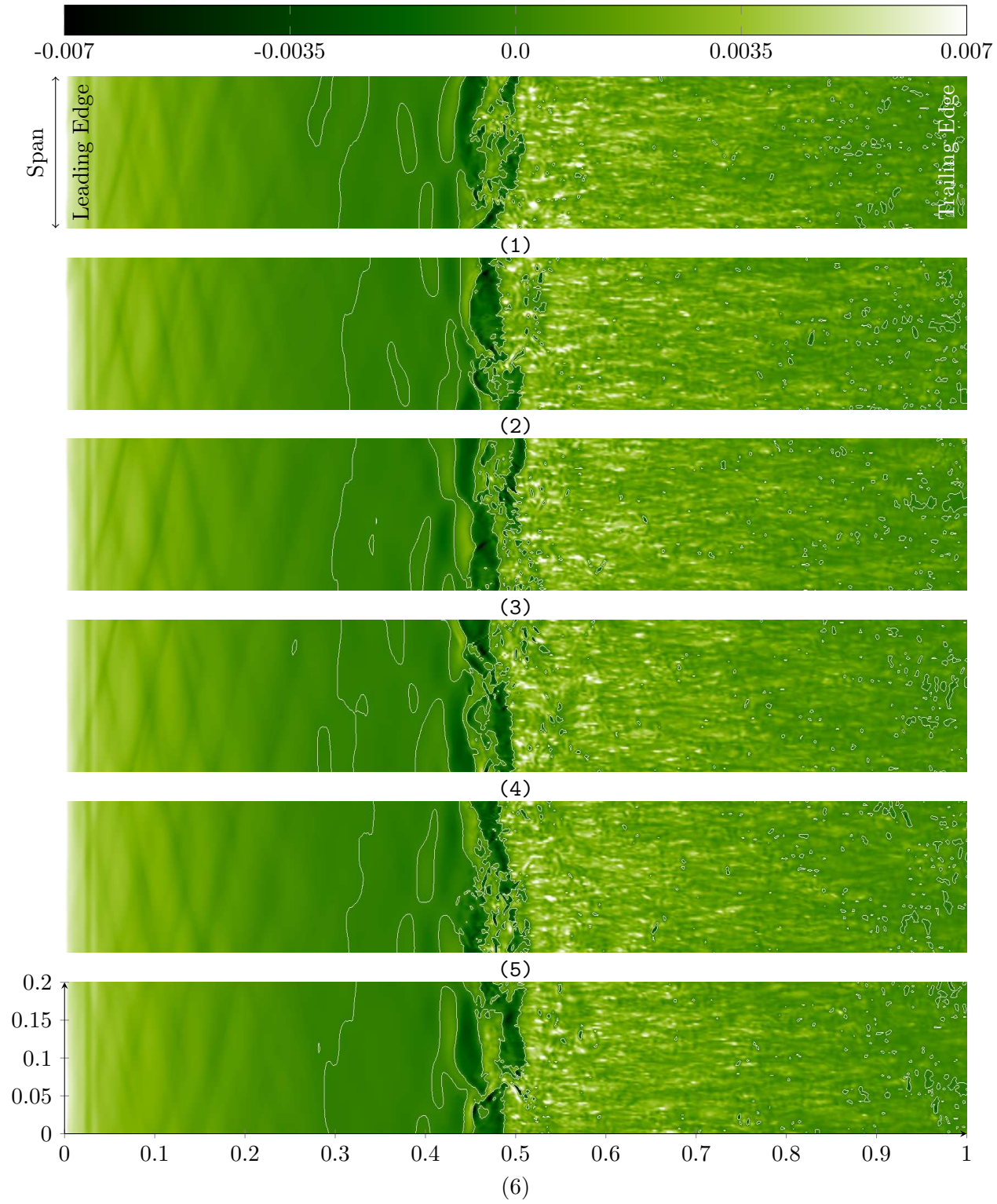

Figure 4.18: Suction surface wall shear carpet plot, showing variation on blade surface over 1 time flow unit for 44° Base case. Zero wall shear shown as a white contour line.

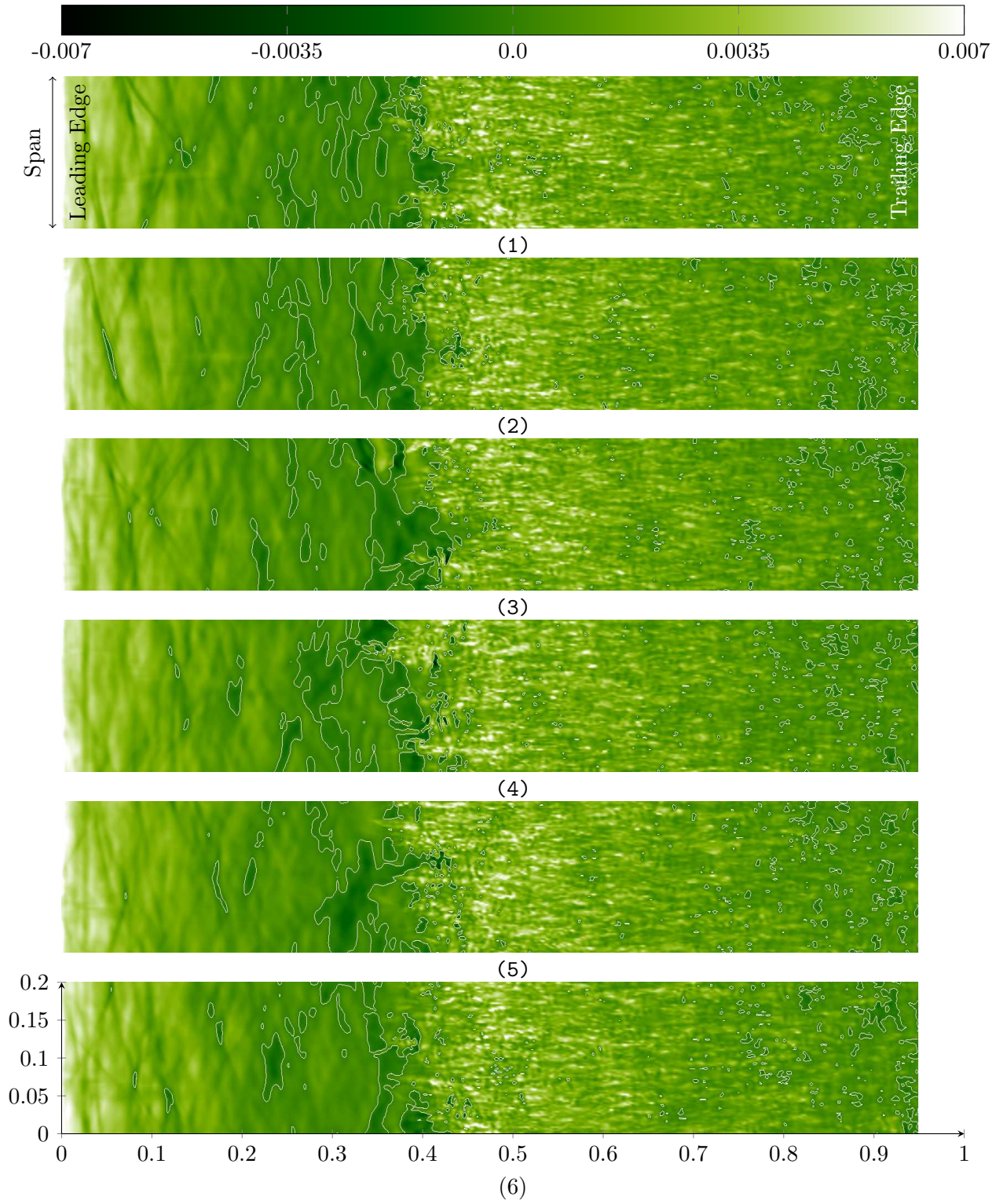

Figure 4.19: Suction surface wall shear carpet plot, showing variation on blade surface over 1 time flow unit for 44° Tu case. Zero wall shear shown as a white contour line.

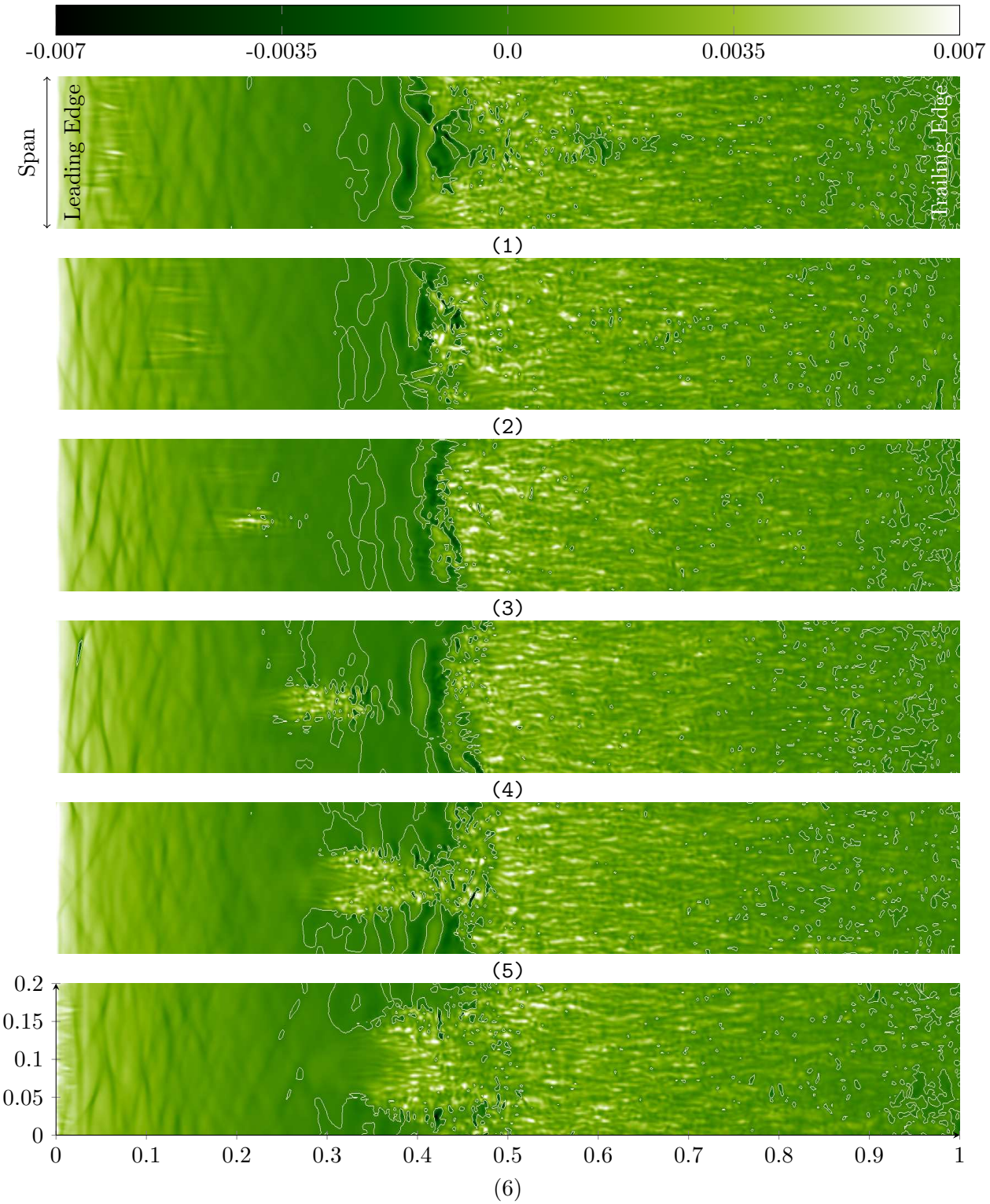

Figure 4.20: Suction surface wall shear carpet plot, showing variation on blade surface over a full bar passing period for the one bar case ($\approx$ 0.73 time units). Zero wall shear shown as a white contour line.

4.10.1 Skin Friction Waves

To try and understand the fluctuations seen in the wall skin friction, the instantaneous wall skin friction time histories are investigated further.

The presences of waves, specifically pressure waves in transonic flows around aerofoils has been noted before. Early work by *Tijdeman* (1977) highlights the presence of up-stream moving waves, termed "Kutta waves", that originate from the trailing edge unsteadiness. Tijdeman studied the waves on an oscillating aerofoil and proposed means of calculating the wave propagation. More recent work by *Lee et al.* (1994) investigated the behaviour of such waves and how they propagate under different flow field conditions. They investigate the feedback mechanisms that sustain the wave propagation and further support Tijdeman's work.

Alshabu and Olivier (2008) also investigated the presence of unsteady waves on supercritical aerofoils and show how supersonic regions of flow over the boundary layer arrest the up-stream travelling waves. For flows without supercritical regions the waves are seen to propagate up to the leading edge, though they become weaker as they do so. The work mentioned here focuses on single aerofoils in flow and suggests that the waves originate from the trailing edge unsteadiness. However, in the investigation performed here it is suggested the waves originate from transition region, though the root cause of the unsteadiness is not known.

4.10.1.1 Power spectral density

The power spectral density (PSD) of the wall skin friction is presented first. Looking at the PSD of the the skin friction highlights the period of most energetic fluctuations in the skin friction and will show clearly if the waves are periodic or random.

For the analysis performed here the PSD is calculated for each point on the surface of the blade. The PSD is then averaged across the span, as the cases are span-wise periodic. As the time history for each point is not truly periodic, the PSD is calculated by windowing the signal. This also allows for further averaging of the PSD by limiting the window length. This is justified as the interest here is in relatively short wave length fluctuations.

Given a signal $G(t_i)$, where t_i are the discrete times at which the signal is captured, the PSD is calculated as follows. Firstly the mean of the signal $\langle G \rangle(t_i)$ is found as

$$\langle G \rangle = \frac{1}{N} \sum_{i=1}^{N} G(t_i)$$

The mean is then subtracted from the signal to normalise it,

$$G'(t_i) = G(t_i) - \langle G \rangle.$$

The discrete signal is then broken down into windows of length M and multiplied with a Hann window of the same length.

$$\langle G \rangle(t_i)_k = W(n)\langle G \rangle(t_i) \qquad i = i_k; i_k + M,$$

where

$$W(n) = 0.5 - 0.5cos\left(\frac{2\pi n}{M-1}\right) \qquad 0 \leq n \leq M-1$$

is the Hann function and i_k is the start index for each of the windows.

Multiplying by a Hann window is necessary to avoid spurious effects from the window not being truly periodic though this does result in a slight reduction of resolution due to signal attenuated. The Hann window is chosen as it results in very low aliasing. Finally the discrete Fourier transformation of the windowed and normalised signal is calculated and the PSD calculated as the square of this.

The averaged PSD is shown in fig. 4.21 for the relative energy over a range of non dimensional frequencies, or Strouhal number (normalised using the chord and inlet velocity), for each axial location for the three cases. The plots show which frequencies have the highest relative energy, shown by the lightest colour (the scale here is slightly arbitrary as it has units of $\frac{\log|\tau^2_{wall}|}{St}$). For the Base case it is clear that there is a periodic fluctuation at $\approx$ 7St that is present from the leading edge up to $x/l \approx 0.45$ and again from $x/l \approx 0.7$ to the trailing edge.

This same fluctuation is present in the Tu case but at a much lower relative energy. For this case it shows strongest from $x/l \approx 0.2$ to 0.4 and again weakly till the trailing edge. The strongest fluctuations are at much lower frequencies and associated with the random fluctuations caused by the free-stream turbulence.

For the one bar case the highest energy fluctuations are again at much lower frequencies, associated with the slow wake passing frequency at $\approx$ 1.4St. However, a second peak is clearly seen though this occurs at a slightly higher frequency than that seen in the Base and Tu cases. Here the fluctuations seen in the skin friction occur at $St \approx 10$. They also appear to be confined to the laminar region up-stream of transition and do not occur down-stream.

The PSD is also shown in fig. 4.22 for six chord-wise locations. These plots are some of the individual plots that make up the spectra in fig. 4.21. Presenting the data as line plots helps to highlight the peaks in energy for the various frequencies. They also show more clearly that the Base and Tu cases show a similar periodic fluctuation at $\approx$ 7St while the 1 Bar case shows a weaker fluctuation at $\approx$ 10St. Furthermore they show more clearly the re-emergence of the periodic fluctuation down-stream of transition in the Base and Tu cases.

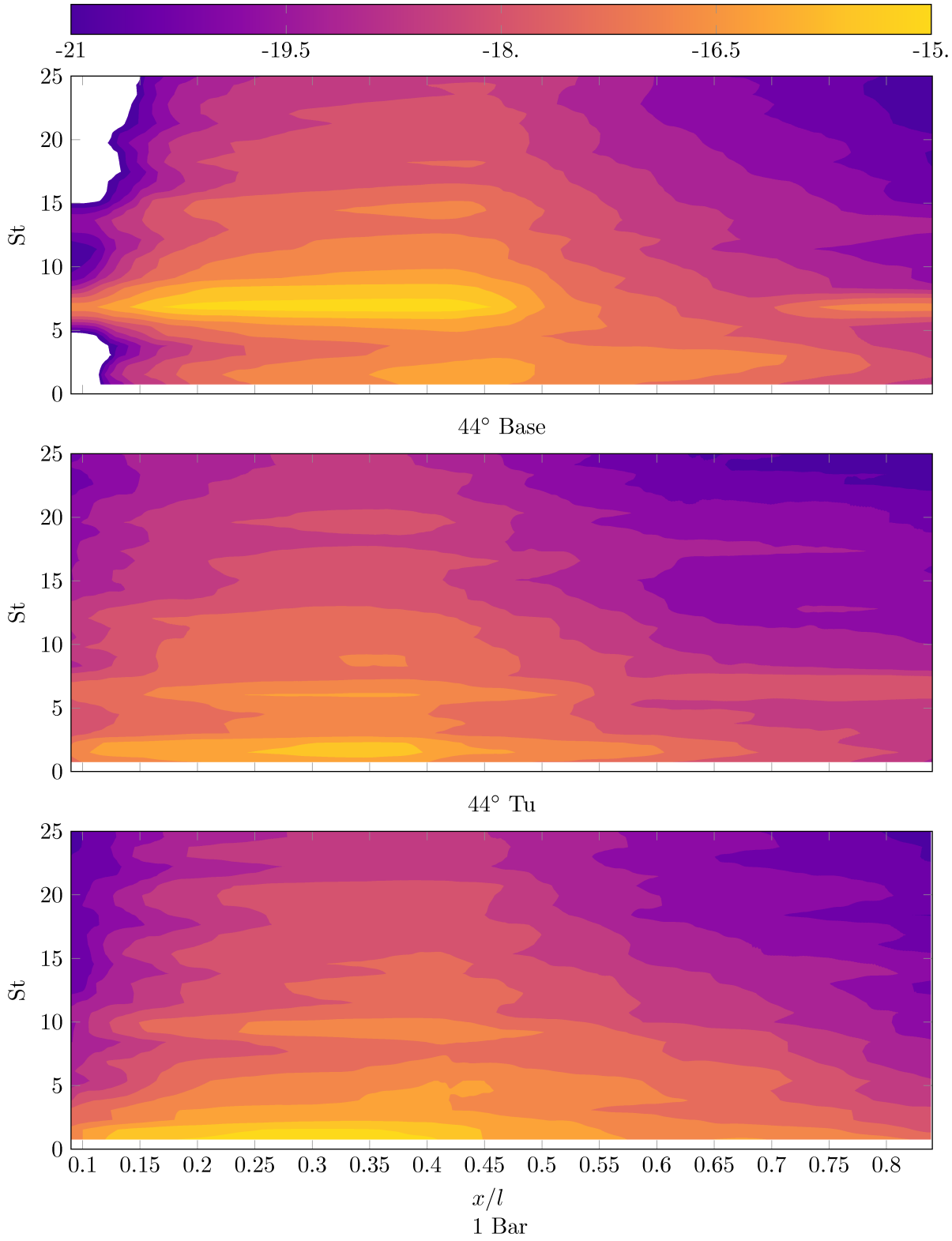

Figure 4.21: Contour plots of suction surface wall skin friction power spectral density ($\frac{\log|\tau^2_{wall}|}{St}$) plotted against frequency of fluctuation and axial chord. Plots are of Base case, Tu case and one bar case from top to bottom.

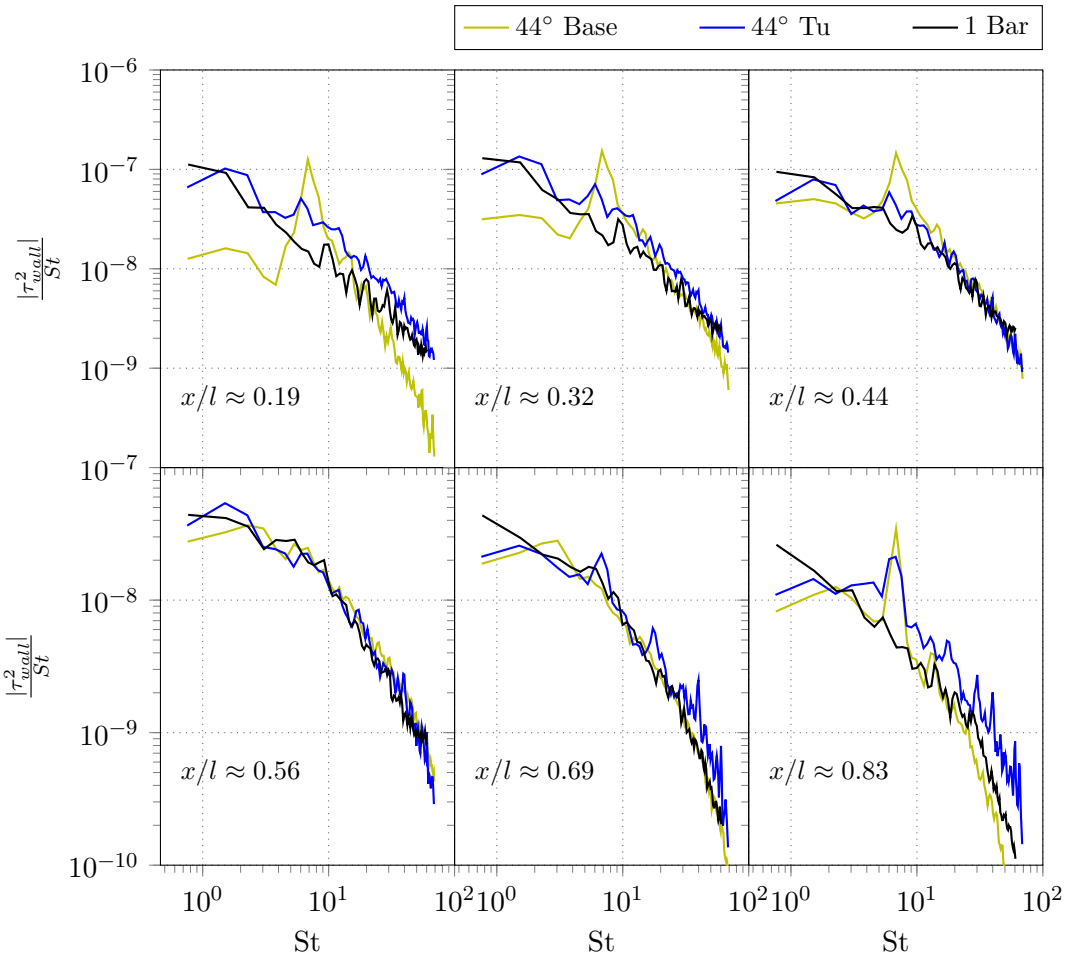

Figure 4.22: Local power spectral density of suction surface skin friction at various chord wise locations. Showing the most energetic frequencies for the Base, Tu and one bar cases.

4.10.1.2 Dilatation Field

Before examining the skin friction fluctuations further the dilatation field for the three cases is presented in fig. 4.23. The figure shows the near wall field around the blade and highlights the presence of weak pressure waves. These waves appear relatively uniform in the Base case, fig. 4.23a , as well as in the 1 Bar case, fig. 4.23c, while those in the Tu case, fig. 4.23b, are somewhat chaotic. These pressure waves coincide with the skin friction variations seen on the suction surface for the three cases. The plot for the 1 Bar case reveals the lack of waves propagating down-stream, which is seen in the PSD plot in fig. 4.21. From the dilatation field plots it can be assumed the skin friction fluctuations are caused by the weak pressure waves seen here.

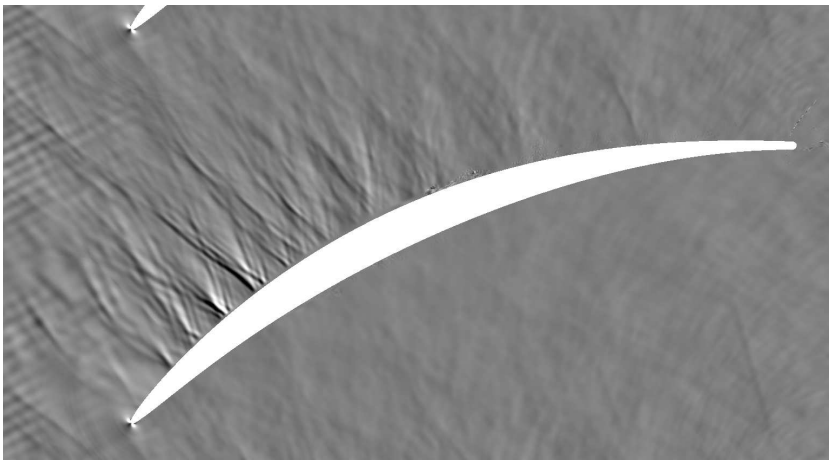

(a) $\alpha = 44°$ Base

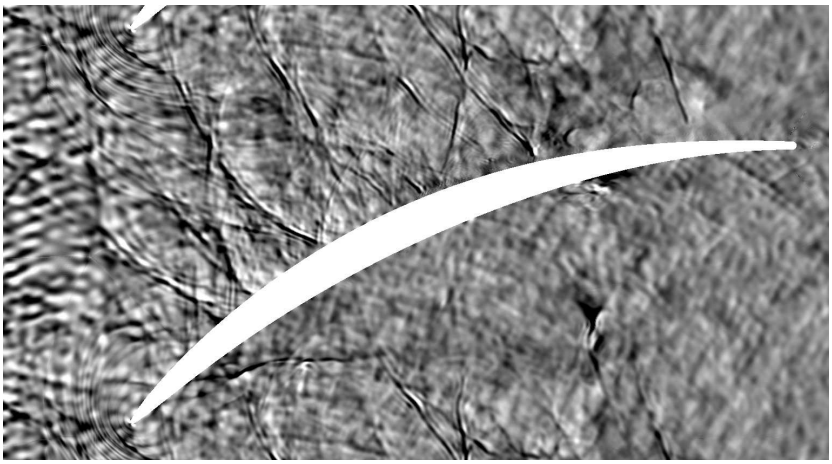

(b) $\alpha = 44°$ Tu

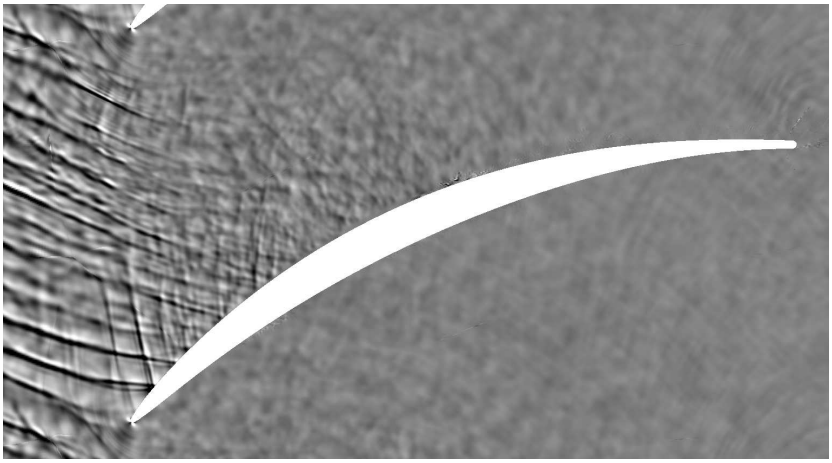

(c) $\alpha = 44°$ 1 Bar

Figure 4.23: Instantaneous dilatation field for the Base, Tu and 1 Bar cases. The field shows the presence of weak shock-like structures along the suction surface. These structures coincide with the wave fluctuations seen in the skin friction. Contours limits are [-10,10]

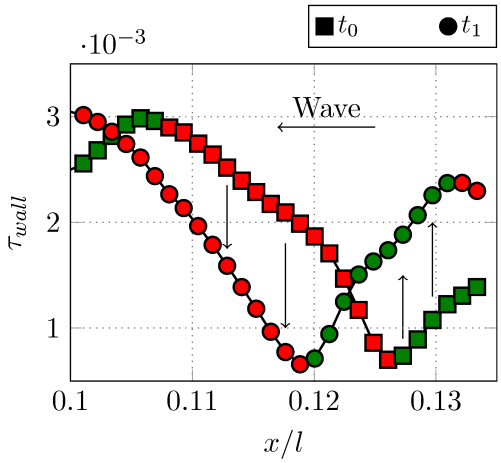

Figure 4.24: Progression of pressure wave, seen in suction surface skin friction from $x/l = 0.1; 0.14$, at two times t_0 and $t_1 = t_0 + 5 * \Delta t$. The plots are coloured with the sign of the local wall shear derivative ($\frac{d(\tau_{wall})}{dt}$). Red indicates a negative derivative and green a positive derivative.

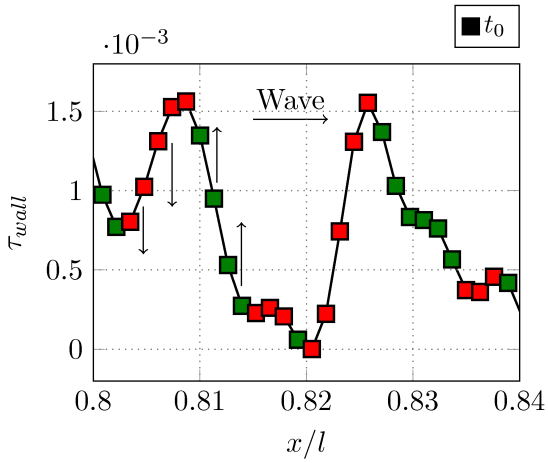

Figure 4.25: Progression of pressure wave, seen in suction surface skin friction from $x/l = 0.79; 0.84$, at time t_0. The plot is coloured with the sign of the local wall shear derivative ($\frac{d(\tau_{wall})}{dt}$). Red indicates a negative derivative and green a positive derivative.

4.10.1.3 Propagation direction

The origin of these fluctuations can be found by calculating the direction the waves are propagating. The propagation of the waves can be shown in two ways. Firstly an instantaneous plot of a single axial plane shows the variation in the local skin friction, and secondly, showing a space-time plot of the instantaneous skin friction for a single axial plane shows the waves propagating in time.

The local instantaneous axial profiles of skin friction are show in figs. 4.24 and 4.25 for sections of blade surface up-stream and down-stream of transition for the Base case. The skin friction is plotted coloured by is derivative with respect to time showing that up-stream the wave is travelling up-stream towards the domain inlet, and down-stream the waves are travelling down-stream to the domain outlet, suggesting that the waves originate around transition.

The space-time plots of skin friction for a single axial plane are shown in fig. 4.26. The space-time plots clearly show structures moving up-stream for the Base and Tu cases. While the 1 Bar case also has structures moving up-stream but they are not as strong or clearly visible. On the other hand all the cases show structures moving down-stream, specifically around the transition/reattachment point. Though further down-stream the turbulent nature of the flow masks any other visible structures which were expected for the Base and Tu cases. The space-time plots show that the origin of this disturbance is near the transition point as the up-stream and down-stream travelling waves appear either side of this location. However, the exact location is hard to determine as the effect of the waves, which occur in the free-stream, must first

travel through the boundary layer to be captured by the skin friction measurements. In regions where the flow is separated the propagation through the boundary layer is interrupted by the separation.

Looking at the space-time plot for the Base case, the speed of the waves can be calculated from the gradient of the disturbance line. This is highlighted on the figure for the Base case by a white dashed line. It is found that the waves in the Base case propagate up-stream at a speed that corresponds to the local characteristic up-stream wave speed. The local wave speed based on the local Mach number and flow velocity, $\lambda_- = U - a$, is shown in fig. 4.27. The average speed calculated from the wall skin friction fluctuations is ≈ -0.34. From this it is clear the fluctuations in the skin friction are the result of pressure waves travelling in the free-stream.

4.10.1.4 Phase locked velocity contours

An initial explanation as to how the introduction of discrete wakes might affect the frequency of the pressure waves, the phase locked average entropy is shown in fig. 4.28. The plot shows the entropy of the flow, showing the bar wakes clearly. The interest in this figure is on the behaviour of the blade wake due to the bar passing. It is clearly seen that blade wake has a periodic forcing of the same frequency as bar wake passing period and disrupts the natural blade wake shedding as a result.

Based on previous works that suggest the presence of pressure waves in the flow are driven by the trailing edge, it is possible that the forcing introduced by the bar wakes disrupts the natural shedding of the blade wake, that may result in a change in the boundary layer instability seen in the spectral plot (fig. 4.22). However, given that the waves appear to originate from the transition region it is unlikely that they are driven directly by the trailing edge though some interference may occur.

4.10.1.5 Wave propagation conclusions

From the flow field review and brief analysis of the skin friction fluctuations it is clear that changing the structure of the incoming disturbances affects the production of pressure waves within the transition region. It is clear when looking at the fluctuations seen in the suction surface skin friction that the introduction of discrete wakes causes a shift in the frequency of the pressure waves. Whereas a comparison between the Base case and the case with free-stream turbulence shows that homogeneous free-stream turbulence does not change the fundamental frequency of the disturbances. However, the free-stream turbulence does appear to influence transition of the boundary layer and reduces the coherence and strength with which the waves are produced. It is argued that the forcing from the free-stream turbulence reduces the likelihood of the instability causing the pressure waves to occur simultaneously across the full span-wise

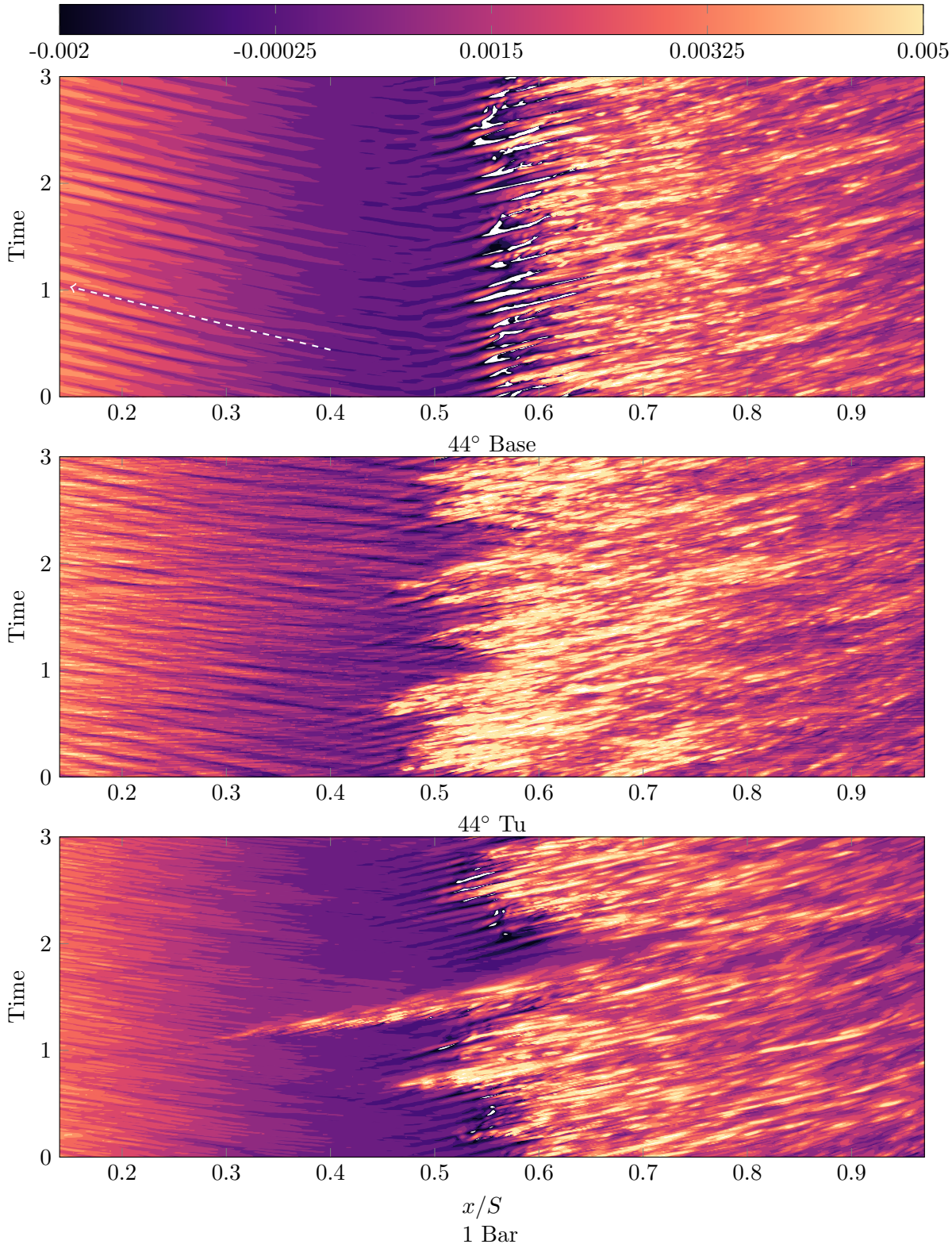

Figure 4.26: Space-time skin friction plot of a single span-wise location along the suction surface. Plots are of the Base case, Tu case and one bar case from top to bottom. Plotted against surface distance from the leading edge (not axial chord). Wave propagation shown as white dashed line on Base case plot.

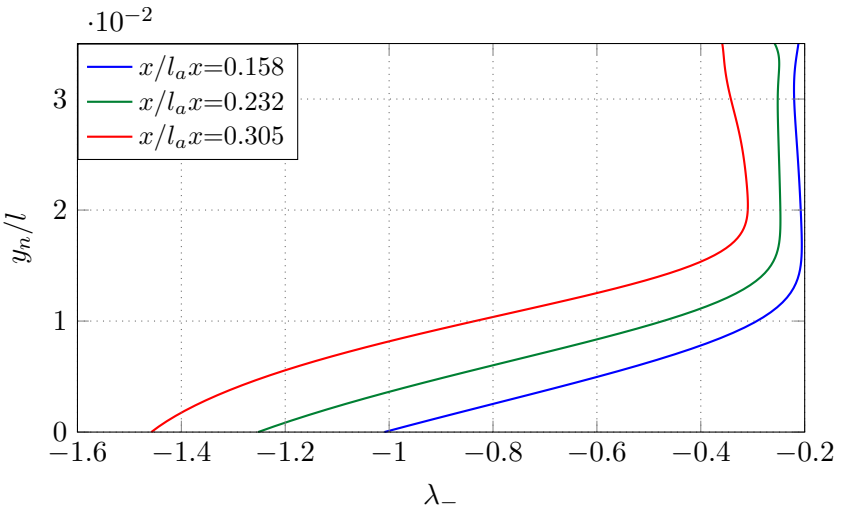

Figure 4.27: Local instantaneous wave speed for the Base case at axial locations, $x/l \approx 0.16, 0.23, 0.31$ plotted against wall normal distance.

domain. Instead, the boundary layer separates and breaks down in a chaotic manner reducing the strength of the waves propagating up-stream. In the Base case this instability appears to occur more uniformly, as seen by the transition resulting in more coherent pressure waves.

Unfortunately the direct cause of these waves has not been identified. However, from the limited work done it is clear that the waves originate from the boundary layer unsteadiness and resemble some form of travelling weak shock, such as the "Kutta waves" described in some of the earlier works reviewed. The waves appear to originate from transition as they are clearly visible in the transitional reattachment in fig. 4.26. Which suggests that they have already been formed and travel down-stream unlike the "Kutta waves" which are theorised to originate from the trailing edge. Finally it is suggested that the introduction of the bar wakes results in a shift in the instability frequency. However, given that the waves originate from the transition region it is unlikely that the trailing edge is the main driver and the shift in frequency is more likely driven by changes in the boundary layer instability.

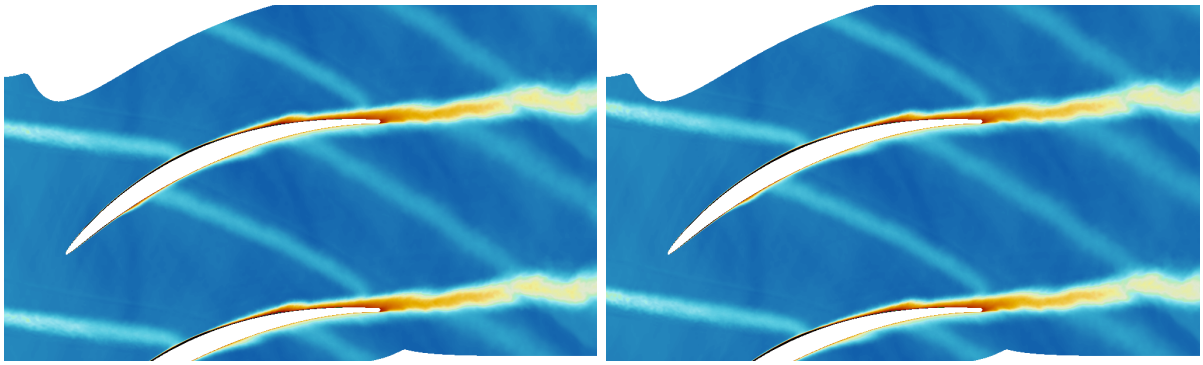

(a) Phase 1

(b) Phase 3

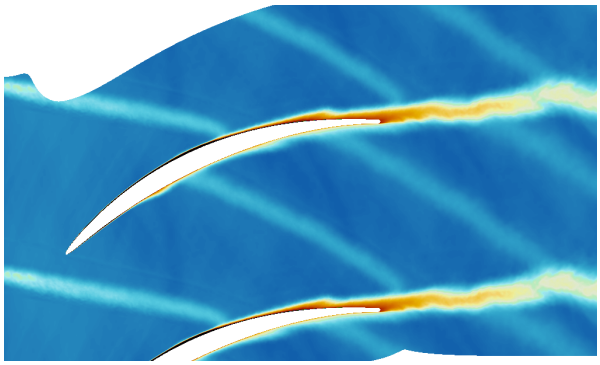

(c) Phase 5

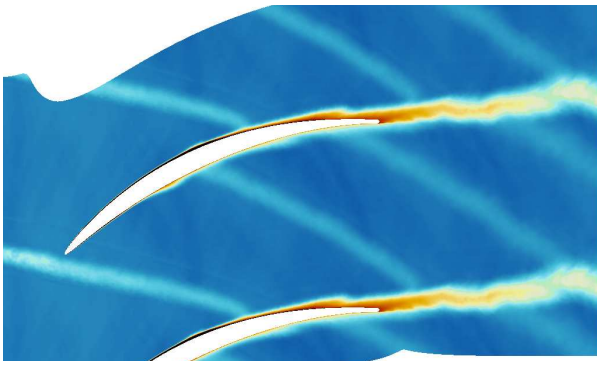

(d) Phase 7

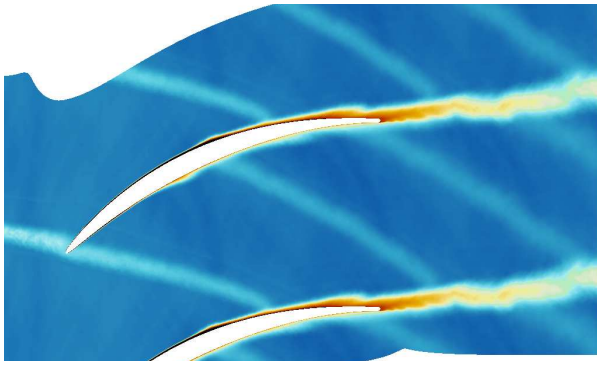

(e) Phase 9

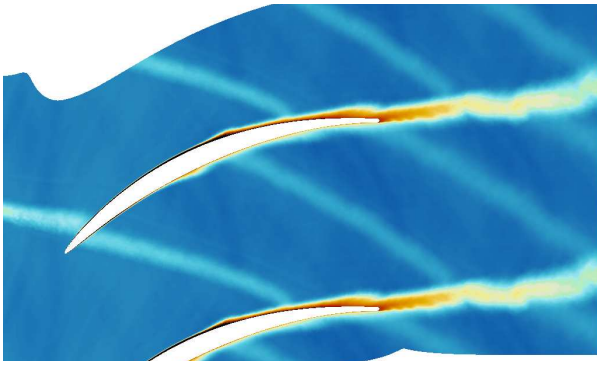

(f) Phase 11

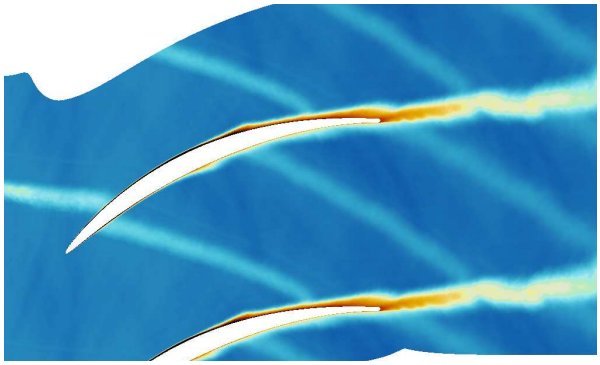

(g) Phase 13

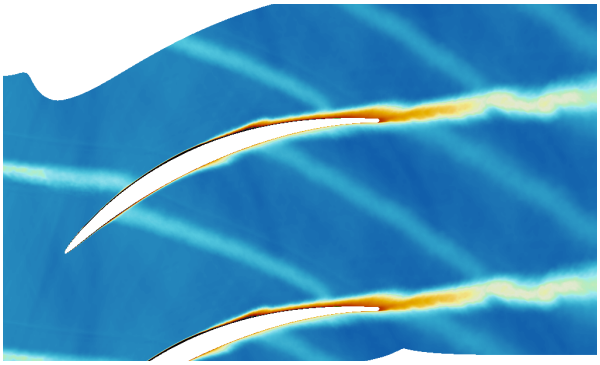

(h) Phase 15

Figure 4.28: Phase locked entropy showing passage of wakes from up-stream bar through the cascade domain. Plots show variation over 15 phases (18 in total). The periodic forcing from the wakes produce variation in the blade wake seen in the wake oscillation.

4.11 Loss Analysis

Looking at the instantaneous and statistical flow field provides good insight into the overall flow dynamics involved. It has also highlighted some of the phenomena that are not captured when investigating statistical results only, such as the effects that different free-stream disturbances can have on the presence of pressure waves in the domain. However, to gain further insight into performance parameters it is necessary to investigate the results in more detail. To do this the time averaged and phase averaged results are examined next.

The comparison focuses on the time averaged statistics for the three cases looking at quantities such as blade loading and skin friction as well as other metrics such as wake profiles and boundary layer quantities. This section of the investigation tries to obtain insight into the differences seen in the total pressure loss for the different cases, which is presented first. It then goes on to apply the Denton loss analysis, as in chapter 3, to try and gain insight into how different free-stream disturbance types may change performance. Following the loss comparison and analysis, the statistical results are reviewed to try and explain the differences seen in the loss results.

The phase averages of the one bar cases are presented along side the time averaged results to show changes in behaviour introduced by the discrete wakes.

4.11.1 Total Pressure Loss

The total pressure loss has already been presented in table 4.6 however it is presented again here in more detail, given in fig. 4.29. The results are presented for the mixed out average pressure loss, mass averaged pressure loss, and total Denton loss, calculated using either the mixed out velocity limit or vorticity limit to define the edge of the blade boundary layer. Two total losses are presented using different averaging techniques as the presence of discrete moving bar wakes may alter the loss measures differently since the bar wakes are not fully mixed out through the cascade. Furthermore, when using a mixed out average the wakes of the bars are assumed completely mixed out before entering the passage of the blade. However, the work by *Smith* (1966a) suggests that under certain conditions a wake travelling through a compressor may result in some form of recovery, which would not be accounted for using mixed out averaging. For this reason the mass averaged pressure loss is also included to show any possible differences that might occur if one assumes all inflow turbulence is mixed out.

The total Denton loss is included in fig. 4.29 but the Denton loss breakdown will be discussed later. One comment will be made though, interestingly the Denton loss prediction does not show the same variation in total loss as that shown by the measured mixed out or mass averaged pressure loss. This is attributed to the fact that the Denton loss focuses on calculating loss based entirely on boundary layer properties and does not take into consideration any effects that may be present in the free-stream.

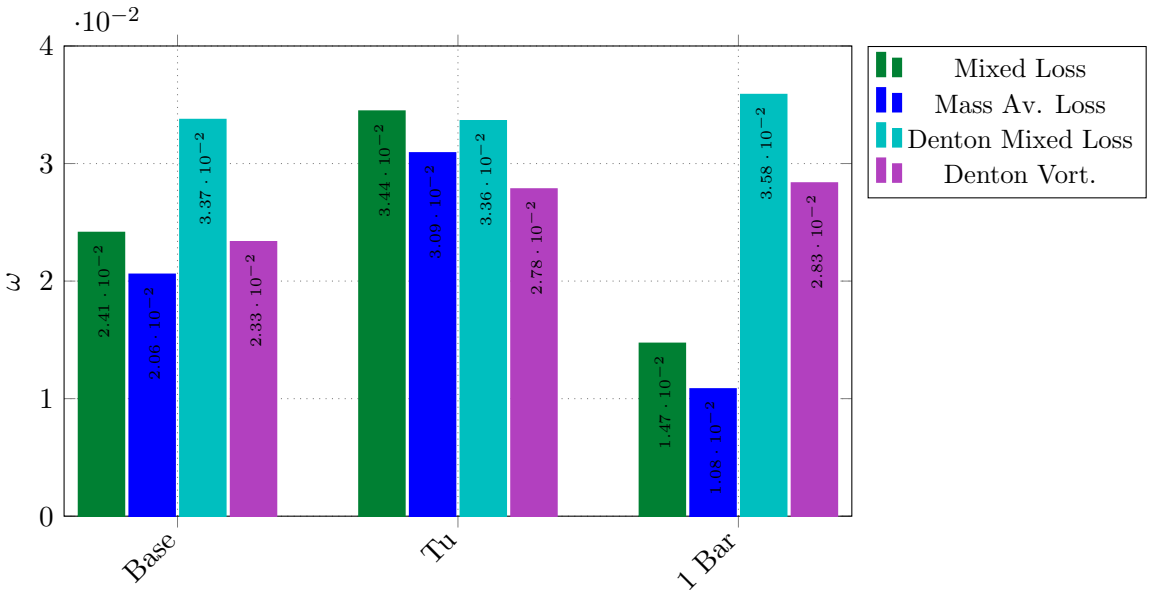

Figure 4.29: Total pressure loss, calculated using mixed out or mass averaged quantities, and Total Denton loss, using mixed out vorticity boundary layer limits, are presented for the one bar, Base 44 and Tu 44 cases.

The comparison of the total pressure loss for the three cases shows that the introduction of homogeneous free-stream turbulence increases the overall loss, while the introduction of a discrete disturbance in the form of a wake of an up-stream moving bar results in an overall reduction in total loss.

4.11.1.1 Total pressure loss breakdown

Before continuing on to the Denton loss breakdown the total loss is investigated a little further. By breaking the loss down into a passage and wake loss the relative difference and behaviour of the three cases can be expanded on. The loss is broken down by first separating the wake from the passage flow. This is done based on the vorticity of the outlet pitch-wise profile. The vorticity profile, and resultant wake and passage breakdown, of the Base case is shown in fig. 4.30. The level of vorticity magnitude specified is done based on visual inspection, and the value is set as constant for all the cases.

The resultant loss contribution was then calculated using a mass-averaged approach. Mass averaging is used here as it provides a simple way of removing the loss contribution from the unwanted section. By setting the local total pressure to that of the inlet reference the local contribution to the mass-averaged loss of that section is zero. In this way the loss attributed to the passage and to the wake can be calculated, as shown in fig. 4.31.

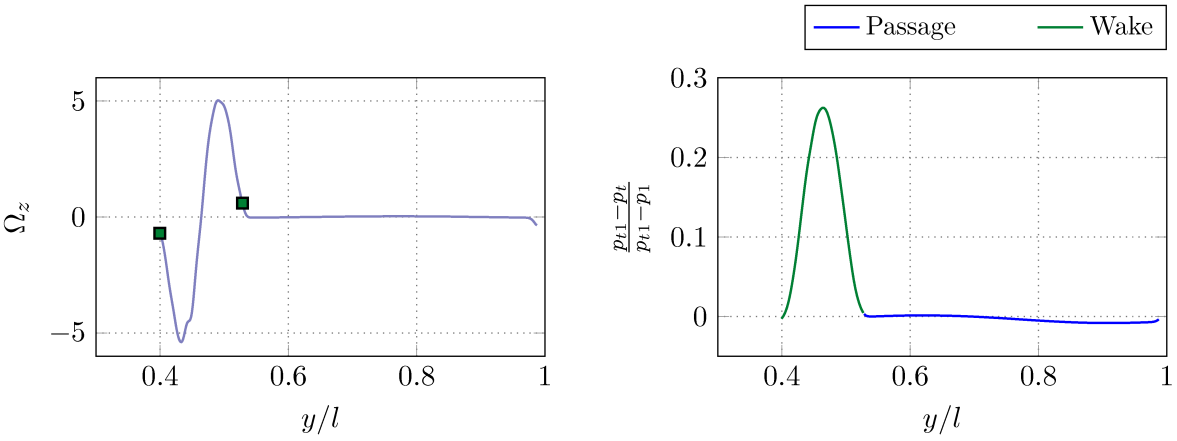

(a) Span wise vorticity

(b) Total pressure loss

Figure 4.30: Local vorticity and total pressure loss for the reference outlet plane. Showing the wake and passage separation, marked by green squares in the vorticity plot.

Figure 4.31 shows that for all three cases the loss contribution from the blade wake is relatively constant. There is a slightly higher wake loss for the Tu case compared with Base case and slightly lower wake loss for the 1 Bar case, compared with the Base case. The changes in wake loss are driven by changes in boundary layer behaviour as highlighted in the instantaneous skin friction plots, figs. 4.18 to 4.20, where the free-stream turbulence and bar wakes resulted in different transition locations as well as wake calming seen in the 1 Bar case. These changes result in slight variation in the overall time averaged statistics as will be discussed.

The difference in the total loss however appears largely due to the differences seen in loss associated with the passage. For the Base case the passage see a slight recovery of mass-averaged total pressure loss while the Tu cases shows a significant additional loss, and finally the 1 Bar case shows substantial recovery, suggesting there is some form of bar wake recovery occurring.

However, the recovery of loss for the Base case is unusual, as no loss or recovery in the passage region is expected for this case. The identification of this recovery effect lead to further investigation of the Base case, highlighting a slight short coming in the simulation set-up. It is found that the limited up-stream domain length of the simulations results in slight variation in stagnation pressure across the up-stream reference plane. The potential-flow disturbance due to the blade and the fixed inlet boundary condition result in a sinusoidal variation in total properties across the pitch.

This variation does not affect the validity of the simulations as the variation is simply convected through the domain. Herein lies some to the confusion though, this variation results in an apparent loss recovery in the passage region when looking at only the passage. However, if a streak line is traced from inlet to outlet this loss is associated with the local maximum in total pressure present in the inflow, biasing the averaged total pressure calculated for the passage region. This effect is shown by the streak lines traced through the time-averaged flow domain,

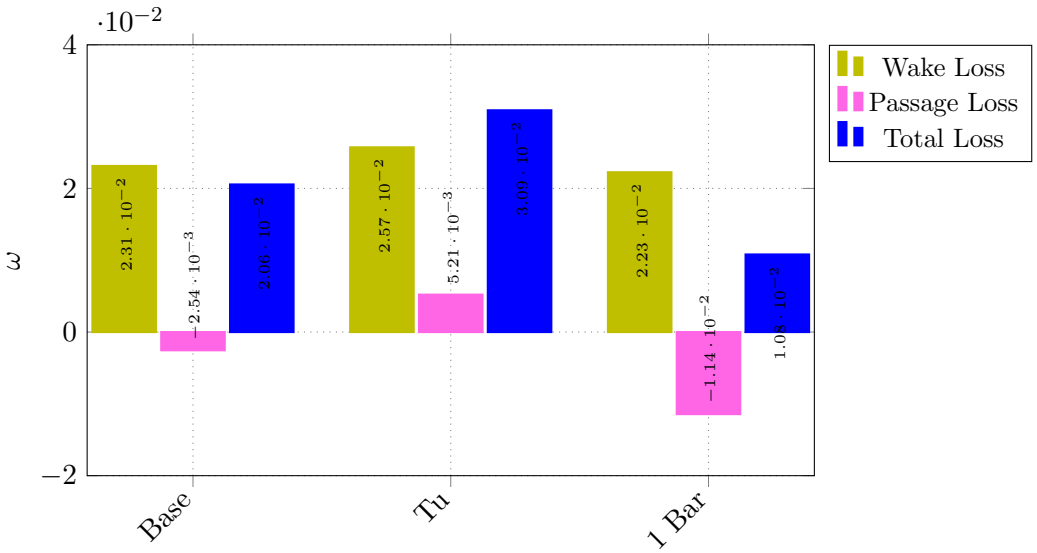

Figure 4.31: Mass-averaged total pressure loss and relative wake and passage loss for one bar, Base 44 and Tu 44 cases. Calculated at a reference 0.15 chord up-stream and 1.4 chord down-stream of the leading edge.

fig. 4.32, and their corresponding total pressure at the inlet and outlet reference planes, fig. 4.33 which also shows the local variation across the inlet. Given that the biasing of the inlet total pressure is seen in all cases a comparison of the loss breakdown can still be performed, assuming the level of biasing is similar.

The results of the total pressure loss breakdown show that despite minor variation in the passage region there is reasonable contribution of loss from the passage for the Tu case and apparent recovery in the Bar case. Assuming that some biasing of the passage loss exists in the bar case as well, to a similar extent as the Base case, then a possible $\omega \approx -8.8 \cdot 10^{-3}$ of loss recovery occurs in the Bar case.

It is suggested that recovery of mass-weighted total pressure can occur through diffusion of turbulent bar wakes, as suggested by *Smith* (1966a). The premise is that the section of wake that is chopped and passes through the passage is deformed in such a manner that the velocity deficit is reduced. The reduction comes from the fact that the velocity deficit is proportional to the wake width, which is increased by the turning and reduction in flow velocity. This is in contrast to the behaviour in lower pressure turbines where *Michelassi et al.* (2014) found that the added wakes increased loss in the passage.

It is suggested that this apparent recovery is associated with a recovery of dynamic head. The total mass-averaged pressure loss is calculated based on time-average of primitive variables, meaning that the total pressure is calculated using variables that do not take into account local fluctuations. However, the calculation of the total pressure is non-linear make the error introduced by calculating it using averaged variables dependant on the size of the fluctuations.

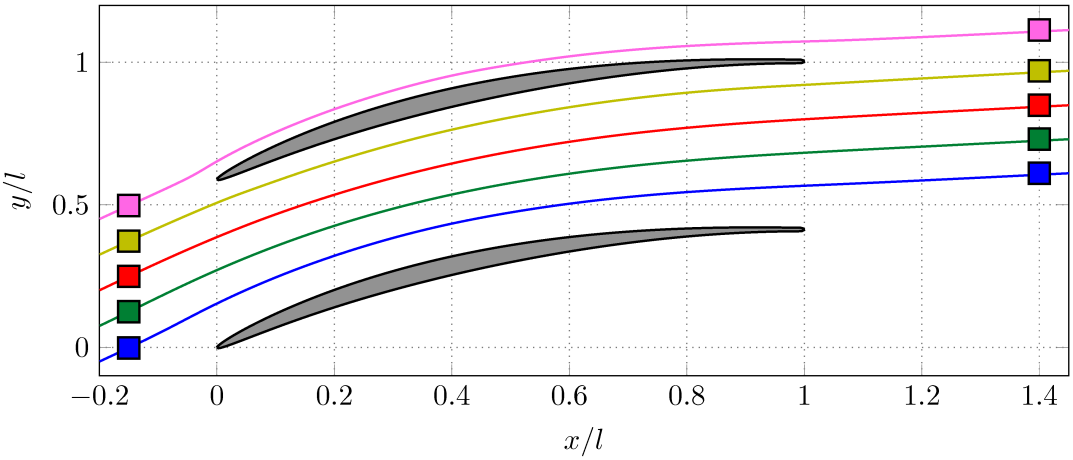

Figure 4.32: Trace of streak lines extracted through the domain for the Base case. Streak lines are coloured with same colour used in fig. 4.33 with markers showing respective position of measurement of inlet and outlet planes.

In a compressor cascade the flow slows as it passes through the domain meaning that any fluctuations in the flow are reduced in magnitude. Furthermore, the turbulent fluctuations introduced in the free-stream dissipate through the domain. This process can be described in a very basic way in fig. 4.34 where a non-uniform inflow is diffused through a domain and the local variation reduces in magnitude.

If we consider the incompressible total pressure equation

$$p_t = p + \frac{1}{2} u_i u_i$$

and focus on the effect of calculating the dynamic head in the example, from averaged velocity,

$$\frac{1}{2}\widetilde{u_i u_i},$$

or by integrating the profile,

$$\frac{1}{2}\int u_i u_i dy,$$

there is a difference in the calculated result. In this simple exaggerated case of a sine wave the difference is 33%. However, in the simulations performed the relative magnitude of the fluctuations is much smaller and as a result the expected error is much smaller.

To estimate the error introduced from the effect of dynamic head "recovery" the average instantaneous total pressure,

$$\overline{p}_t = \frac{1}{t}\int_{t1}^{t2} p\left(1 + \frac{\gamma - 1}{2} M^2\right)^{\frac{(\gamma-1)}{\gamma}},$$

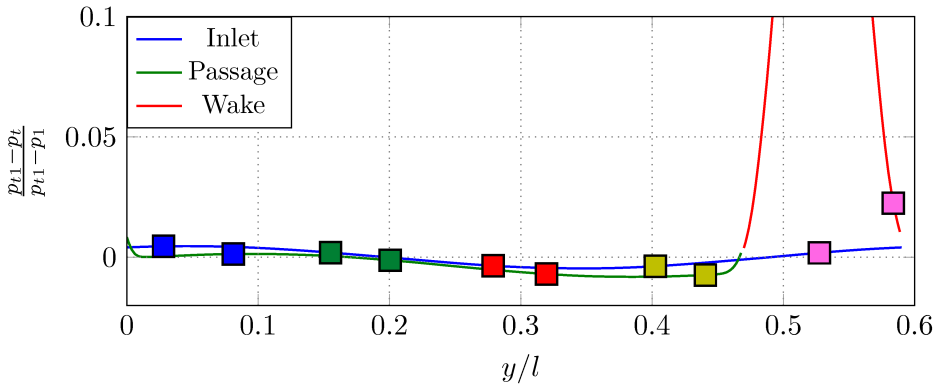

(a) Base Case

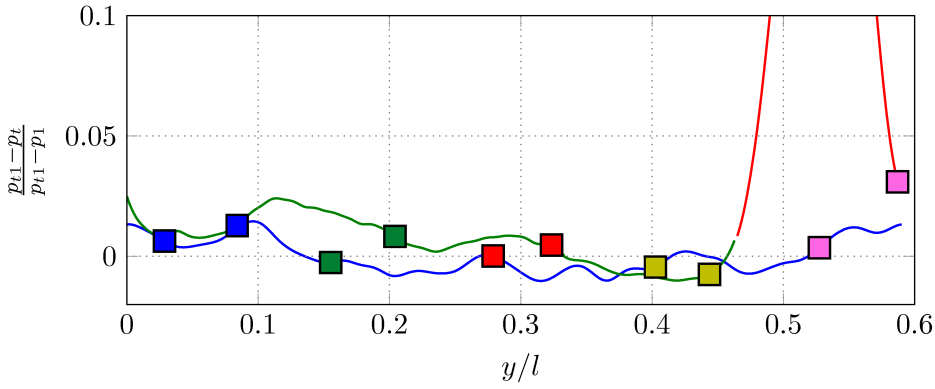

(b) Tu Case

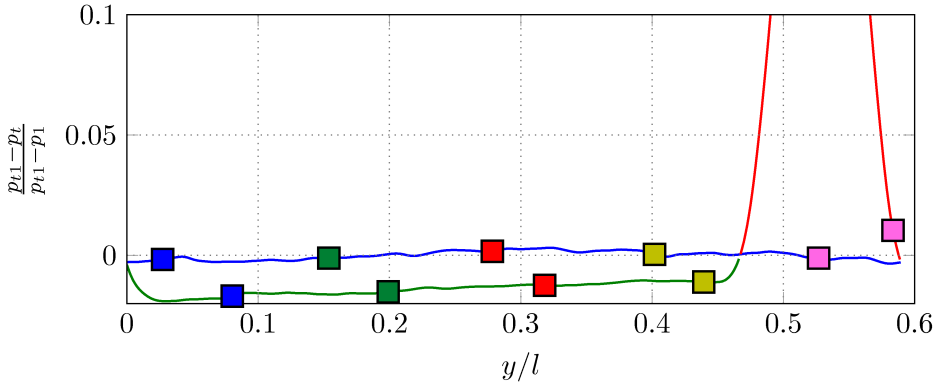

(c) 1 Bar Case

Figure 4.33: Mapping of streak line traces from inlet plane to outlet plane showing relative loss at each station for Base, Tu and 1 Bar case from top to bottom. The outlet plane is represented as passage and wake region.

is calculated for a short time period and compared with the total pressure calculated from the averaged primitive variables, for the same period,

$$\widetilde{p}_t = \overline{p}\left(1 + \frac{\gamma - 1}{2}\widetilde{M}^2\right)^{\frac{(\gamma-1)}{\gamma}},$$

which can be considered a Favre averaged total pressure. This comparison is made for the 44° turbulent case only due to limited computational resources.

The reason that there is recovery is that the effective magnitude of fluctuations in the flow field, that are not captured in the averaged quantities are reduced as the flow slows through the compressor. This reduction in magnitude of the fluctuations results in a smaller error in the total pressure calculated at the exit than at the inlet.

Comparing the two total pressure calculations for the 44° free-stream turbulent case at the inlet reference plan, fig. 4.35, shows that there is a small discrepancy between the values. If it assumed that the difference in total pressure is due to fluctuations then if the flow is brought to rest the relative fluctuations would be zero. The difference between the Favre averaged total pressure and averaged instantaneous total pressure would tend to zero.

The difference in the calculated total pressures at the inlet can be used as an estimate of recovery. By assuming that no loss occurs in the passage, then is it possible for the Favre averaged total pressure to rise to the averaged instantaneous total pressure. This, if given as a loss, would be an estimate of the possible negative loss that could occur in the passage. The recovery loss is give as,

$$\omega = \frac{\widetilde{p}_{t1} - \langle p \rangle_{t1}}{\widetilde{p}_{t1} - \langle p \rangle_1},$$

which gives an estimated recovery loss as $\omega \approx 0.0039$

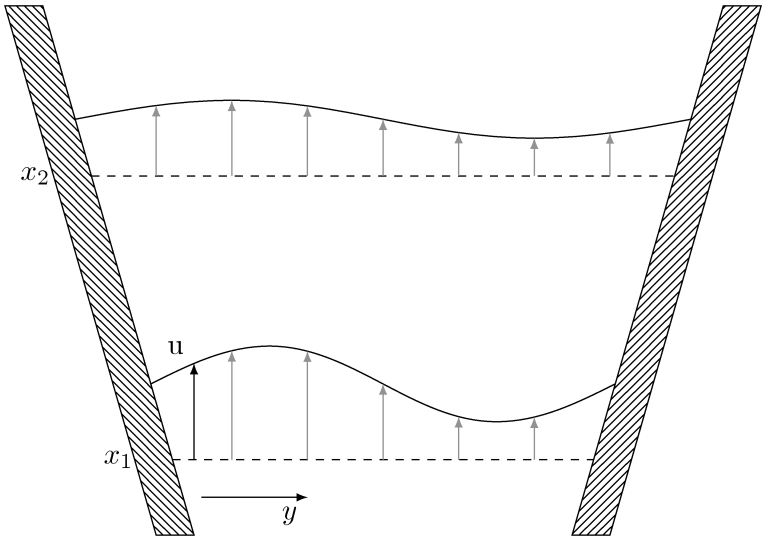

Figure 4.34: Representation of mixing out of velocity variation through a domain. Schematic to highlight how variation results in error in calculation of p_t.

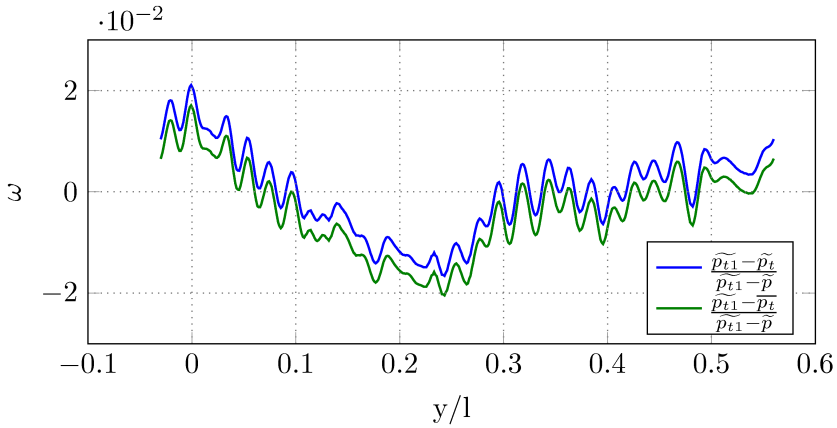

Figure 4.35: Variation in total pressure calculated from averaged primitive variables or averaged instantaneous total pressure for 49° case.

4.11.2 Loss Breakdown

The application of the Denton loss breakdown, introduced and outlined in chapter 3 section 3.4, provides a means of associating blade loss with different processes. It also provides a relatively simple way of showing which blade surface is responsible for the most loss. The application of the loss breakdown analysis in chapter 3 showed that as incidence is varied the main loss production switches blade surfaces. For the incidence considered here, 44°, the loss is predominantly from the suction surface, with most of it coming from momentum loss. This makes the comparison between the different simulations performed here slightly less insightful, as the variation from the different free-stream disturbance types is less pronounced. However, there is variation in the weighting of the different terms that shows how different disturbances force the boundary layer.

For the application of the Denton loss breakdown the vorticity limit has been used instead of the mixed out velocity limit. In chapter 3 it was found that the best practice for the Denton loss breakdown uses a mixed-out velocity limit to define the boundary layer edge. However, for the simulations performed here it proves more useful to match the Denton loss breakdown with the Base case wake loss. By doing this the analysis focuses on the differences in the blade loss, which provides a more detailed comparison, since the variation in wake loss is relatively small as seen in fig. 4.31.

The percentage Denton loss breakdown is shown in fig. 4.36 and a comparison of the total Denton loss and wake loss shown in fig. 4.37. The percentage loss breakdown for the different cases shows almost no variation between the cases, with only minor variation in the suction surface displacement loss for the Base case

The comparison of the loss breakdown with the mass averaged wake loss is shown in fig. 4.37. This shows the contribution of the various terms of the Denton loss breakdown to the total loss. The comparison highlights the poorer performance of the Denton analysis at capturing the loss in the presences of free-stream disturbances. It is seen that increased variation in the free-stream of the 1 Bar case is particularly hard for it to capture, though the comparison with the blade loss alone is more reasonable.

The comparison of relative loss amounts in fig. 4.37 show, that the majority of loss comes from the suction surface momentum loss, as already seen in the percentage breakdown. Interestingly, although the wake loss is relatively constant for the three cases the Denton loss breakdown predicts higher loss for the Tu and 1 Bar cases. This increase in loss is associated with an increase in momentum thickness, as seen in fig. 4.39. The increase in momentum loss is based on the slightly different boundary layer profile for each of the cases. As a constant vorticity limit is used here to determine the boundary layer edge, this results in a slight variation of the boundary layer limit which has a more marked affect on the momentum thickness than other quantities.

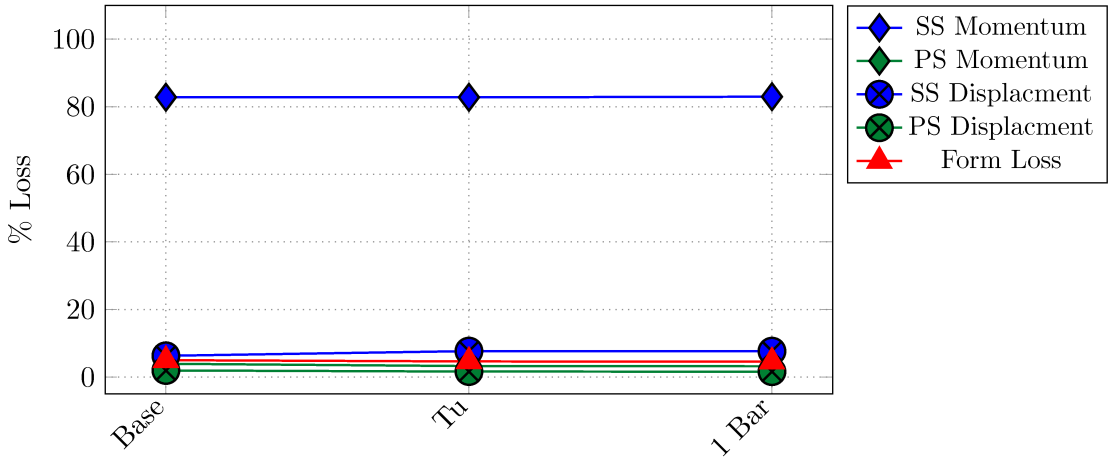

Figure 4.36: Percentage breakdown of terms of Denton loss for Base, Tu and 1 Bar cases. Denton loss calculated using the vorticity limit as this removes some of the ambiguity associated with the passage loss recovery.

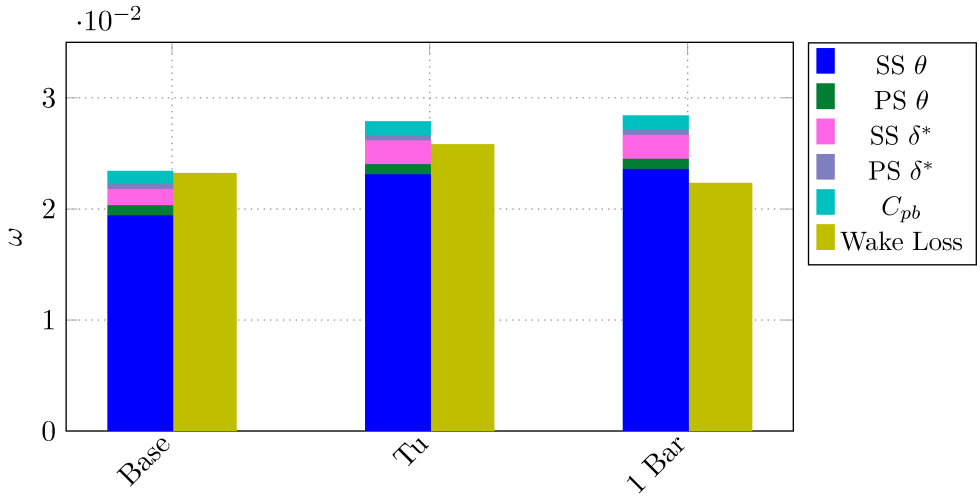

Figure 4.37: Comparison of total from Denton loss breakdown, as sum of relative components, with mass averaged wake only loss for Base, Tu and 1 Bar cases.

The remainder of the Denton loss breakdown, as already shown, is similar in all cases with small contributions to loss from the pressure surface and form loss.

4.11.3 Wake Loss Profiles

The wake profiles are presented for two down-stream locations, one at 1.1 chord from the leading edge, and one at the reference outlet plane 1.4 chord lengths down-stream. The wake loss profiles at 10% chord down-stream show that all three cases produce a similar wake loss profile in the near wake regardless of the free-stream disturbances. However, the profiles change quite dramatically

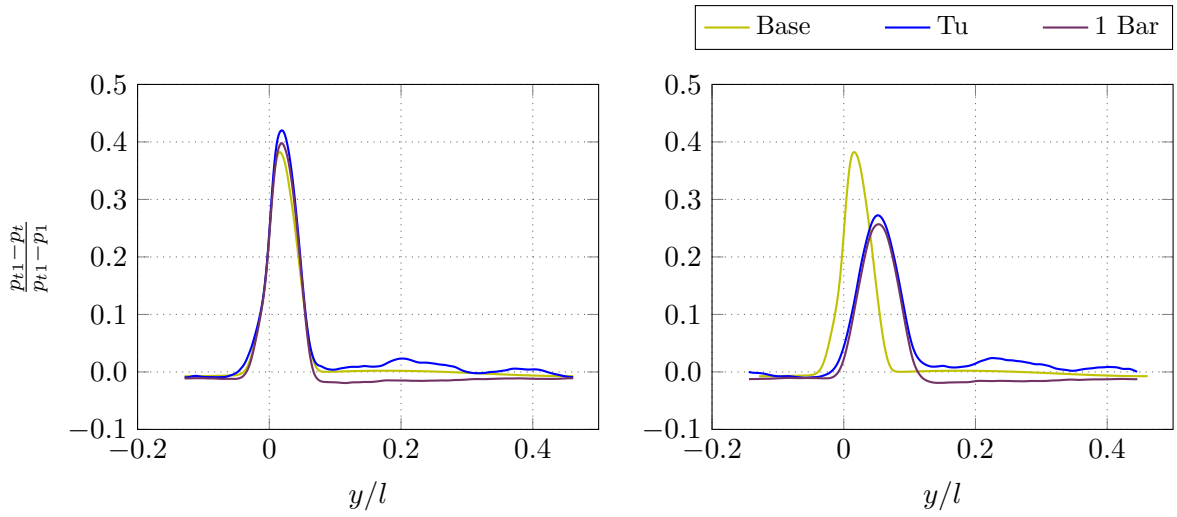

(a) 10% chord.

(b) 40% chord.

Figure 4.38: Wake profiles of local total pressure loss for Base, Tu and 1 Bar cases taken at 10% chord and 40% chord down-stream of the trailing edge. The pressure surface is negative x/l and the trailing edge is at zero.

further down-stream. It is seen that at 40% chord down-stream the Tu and 1 Bar wakes have mixed out substantially more than the Base case.

The mixing out is also accompanied by a migration of the wake, moving toward the suction surface. This migration highlights the increased turning achieved by the Base case where the flow turning at the outlet is up to 0.5° more than the 1 Bar case. The reduction in turning is due to the increased mixing introduced into the free-stream by the added disturbances.

The free-stream turbulence and bar wakes result in a mixing of the local flow, which reduces the over all flow turning due to changes in the transition behaviour.

4.12 Blade Loading

4.12.1 Boundary Layer Quantities

The suction surface boundary layer quantities, plotted in fig. 4.39, show the development of the boundary layer for each case. It is seen in the figures that the difference between the cases is again marginal with the major variation focused on the flow up-stream of transition. The time averaged results show that the Base and 1 Bar cases both predict similar growth rates for the displacement and momentum thickness, figs. 4.39a and 4.39b,up to separation and transition with the 1 Bar case showing a less distinct transition point as expected. The Tu case however shows quite a marked difference up-stream of transition. It appears that the continuous forcing

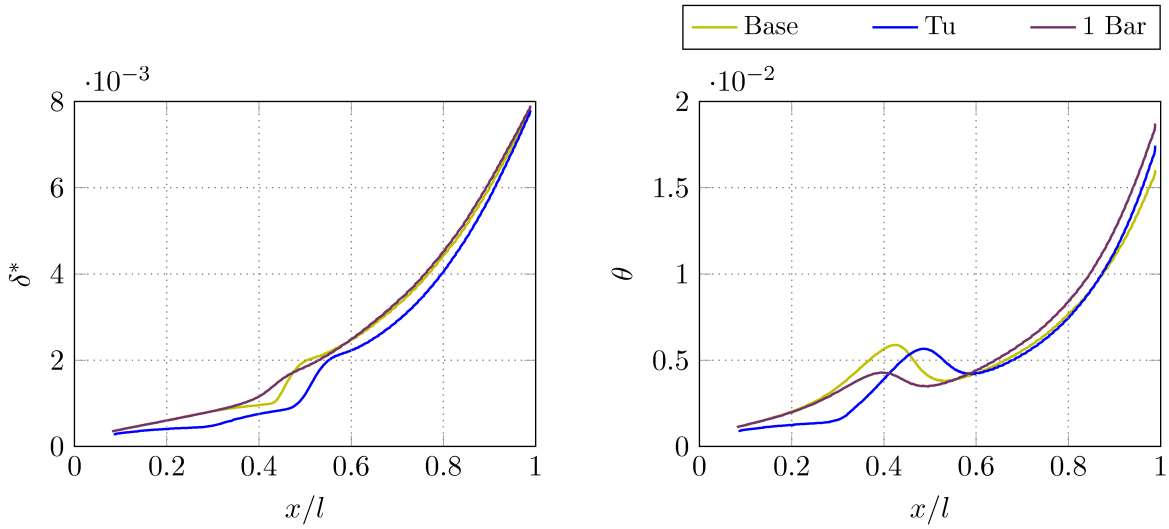

(a) Displacement thickness

(b) Momentum thickness

Figure 4.39: Displacement and Momentum thickness variation along the suction surface for the Base, Tu and 1 Bar cases.

from the free-stream turbulence tends to maintain a thinner boundary layer by forcing a slower more prolonged transitional state. However, after the flow has fully transitioned the boundary layer behaviour quickly catches up to that of the Base and 1 Bar cases.

4.12.2 Profile Loading

The isentropic loading of the blade is presented here. The loading between the three cases is again largely unchanged due to the free-stream disturbances. However, some variation exists around the transition region of the suction surface, as highlighted in the boundary layer quantities previously.

The effects of the free-stream disturbances, either as free-stream turbulence or as a moving bar wake is to suppress the larger separation seen in the Base case. The separation is seen as a peak in the suction surface Mach number at $x/l \approx 0.45$, with the remainder of the loading largely unchanged.

The effects of the bar wake are also shown by the phase averages. The limits of variation of the loading are shown by the shaded area. The phase averages show that the discrete wakes have limited affect on the surface Mach number, effectively reducing the isentropic loading fractionally as the wake passes.

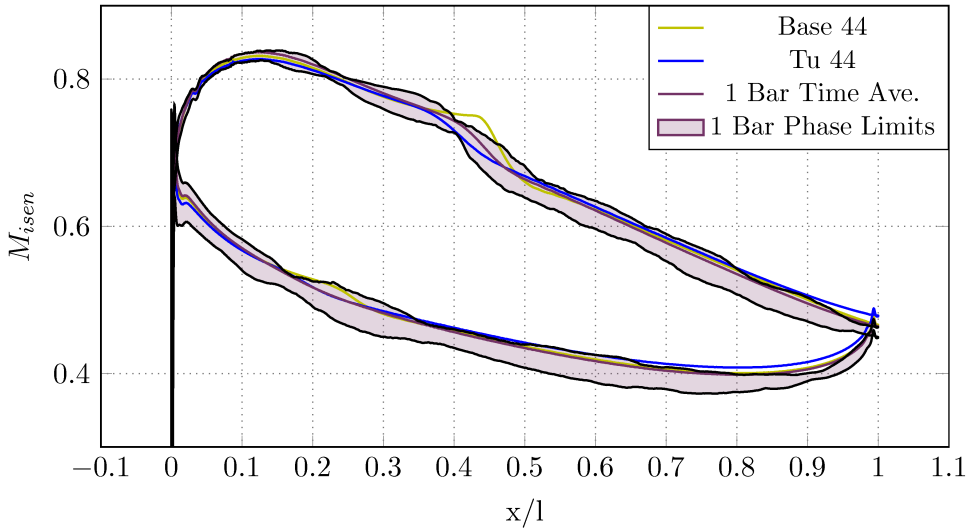

Figure 4.40: Comparison of isentropic Mach number loading for one bar, Base 44 and Tu 44 cases. One bar phase limits shown in grey.

4.12.3 Wall Shear

The wall shear loading plots for the suction and pressure surfaces are show in fig. 4.41a and fig. 4.41b respectively. The wall shear loading shows a more substantial change due to the different free-stream disturbances compared with the blade loading. From the suction surface plot it is seen that the time averaged wall shear shows clear separation for the Base case while this is suppressed for both the Tu and 1 Bar cases. The post transition maximum shear is also different in all three cases. The post transition maximum shear coincides with the respective total losses for each case with the Tu case having the highest followed by the Base case and then the 1 Bar case. Interestingly the Tu and 1 Bar case tend to the same shear value down-stream of the maximum while that of the Base case remains higher, offsetting the loss reduction from a longer laminar boundary layer up-stream of transition. It is suggested that the slight reduction in wall shear for the Tu and 1 Bar cases is driven by further mixing of the turbulent boundary layer by the free-stream disturbances.

Following this, the reasoning for the increase in loss for the Tu case can be attributed to the earlier transition driven by the continual forcing of the boundary layer by the free-stream turbulence. This does not occur in the 1 Bar case highlighted by the phase locked averages which show that the 1 Bar case also undergoes early transition when the wakes pass but then shows separation in between wake passings, similar to that seen in the Base case. The reduced frequency of the bar wakes is such that the flow does not have time to return to the natural, Base case flow.

The comparison on the pressure surface side, fig. 4.41b, is similar to that of the suction surface, although here there is a swap in the transition point between the Tu and 1 Bar case. On the pressure surface the 1 Bar case sees a slower transition but earlier onset, while the Tu case shows

a more rapid slightly later transition. The transition of the Tu case again results in a higher post transition maximum shear with the Base case showing the second highest and finally the 1 Bar case. The peak in maximum shear being attributed to the strong turbulent breakdown that occurs for the Base and Tu cases. Both of these cases have a "stationary" transition point resulting in a strong turbulent wall shear post transition. For the 1 Bar case the transition point oscillates around the mean point resulting in a much lower peak averaged wall shear. This is seen in the phase locked limits, where the peak shear for the 1 Bar case reaches similar levels as the Tu case suggesting that a forced boundary layer undergoes transition more rapidly than the Base case, resulting in a high post transition wall shear due to the energy brought into the boundary layer by mixing.

The transition variation and boundary layer forcing of the 1 Bar case is shown in fig. 4.42. This figure shows the variation in wall shear for several of the phase locked averages. It highlights the transition and forced turbulent spot that originates from the bar wake. This spot can be seen in the sub figures (2) and (3) and again in sub figures (5) and (6) by the bump in the wall shear. The minimum shear stress is highlighted for the sub figures (4) to (6) and can be used to gauge the recovery rate of the boundary layer. The speed of recovery can be estimated based on the rate at which the minimum shear stress propagates down stream, and is found to be $dt/dx \approx 5.87$. From this the reduced frequency required for the boundary layer to fully recover at the same incidence needs to be $\approx 9\%$ less.

Finally the variation of the 1 Bar case is shown in the phase locked space-time plot in fig. 4.43. This plot is included to give an idea of the bar wake passing on both the suction and pressure surfaces as well as the extent of the separation that occurs between bar passing periods.

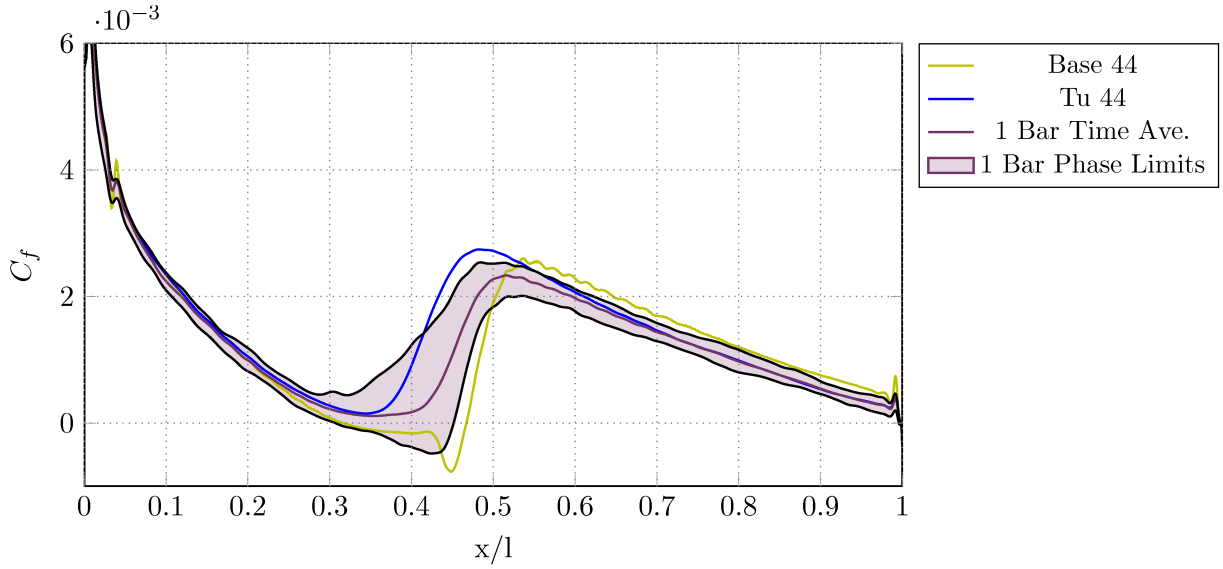

(a) Suction surface

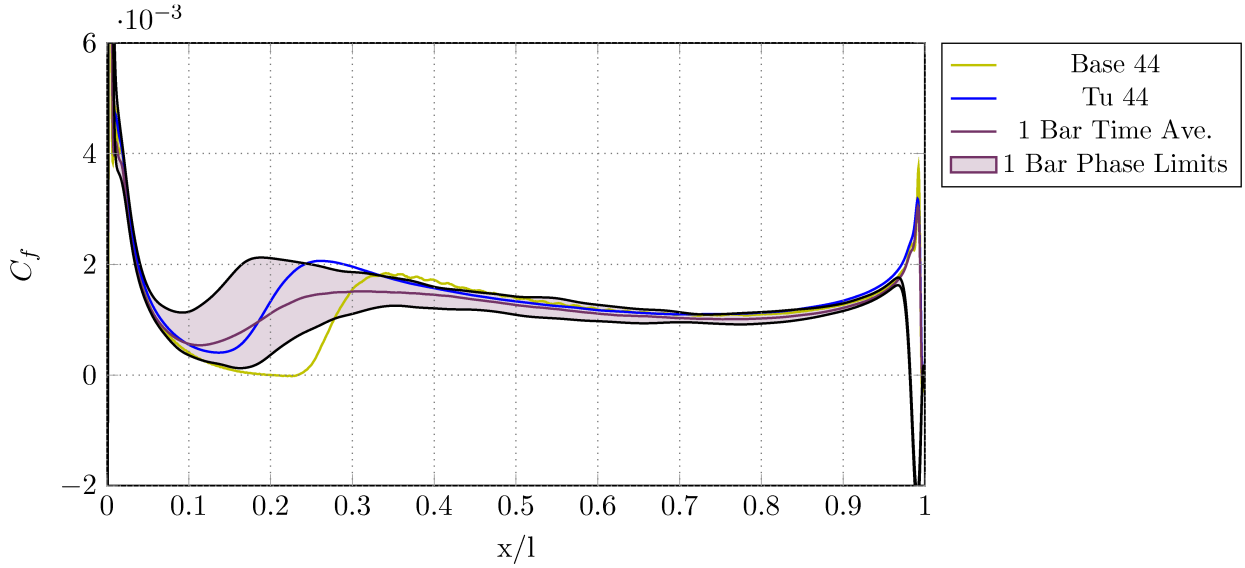

(b) Pressure surface

Figure 4.41: Skin friction plots for suction and pressure surface for one bar, Base 44 and Tu 44 cases.

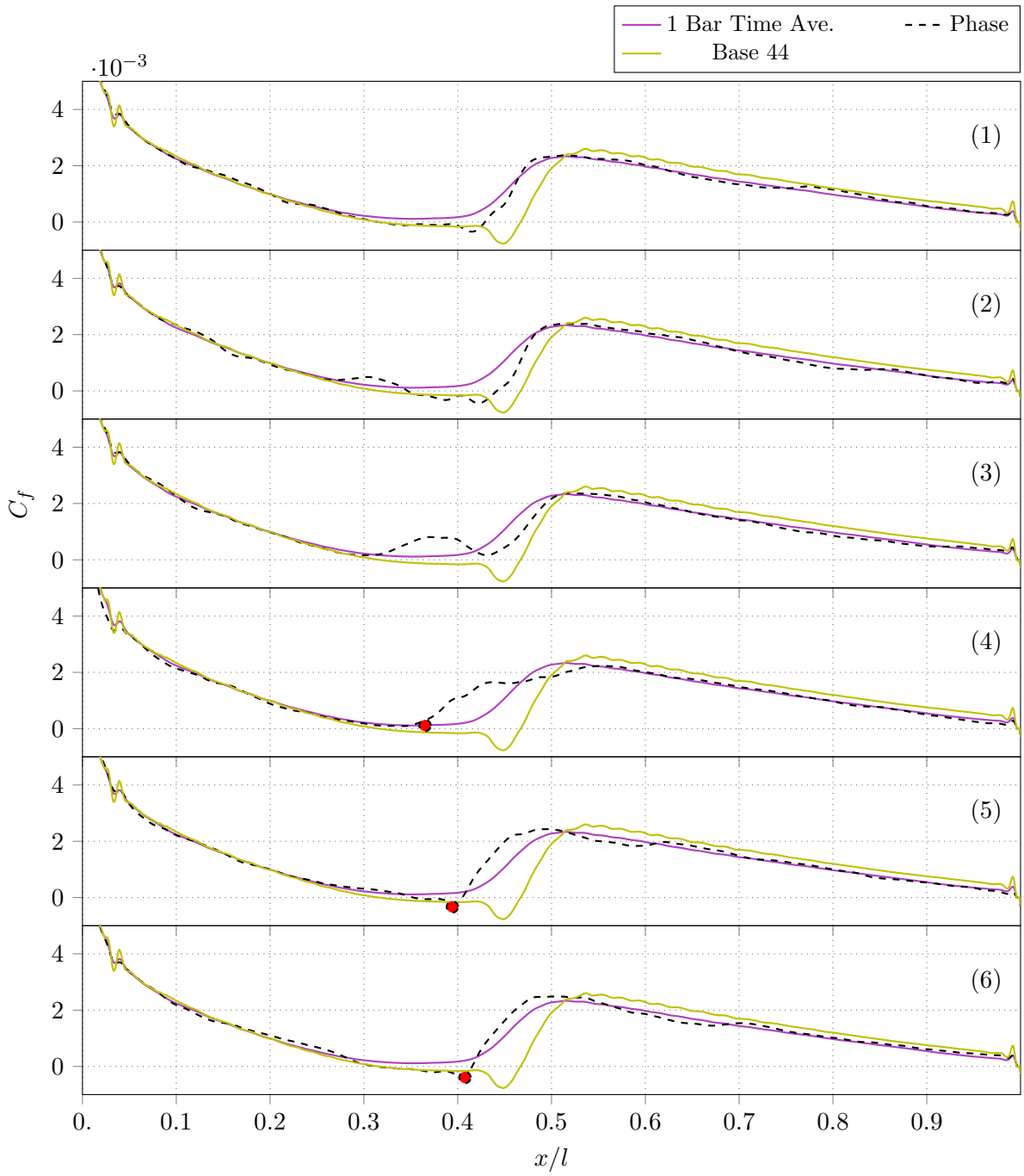

Figure 4.42: Suction surface skin friction variation of one bar case for individual phase locked skin friction plots of phases 1, 4, 7, 10, 13 and 16 for figures (1) top to (6) bottom. Minimum skin friction value is also shown for phases 10, 13 and 16 red circles with the Base case included to show what the full recovered state is.

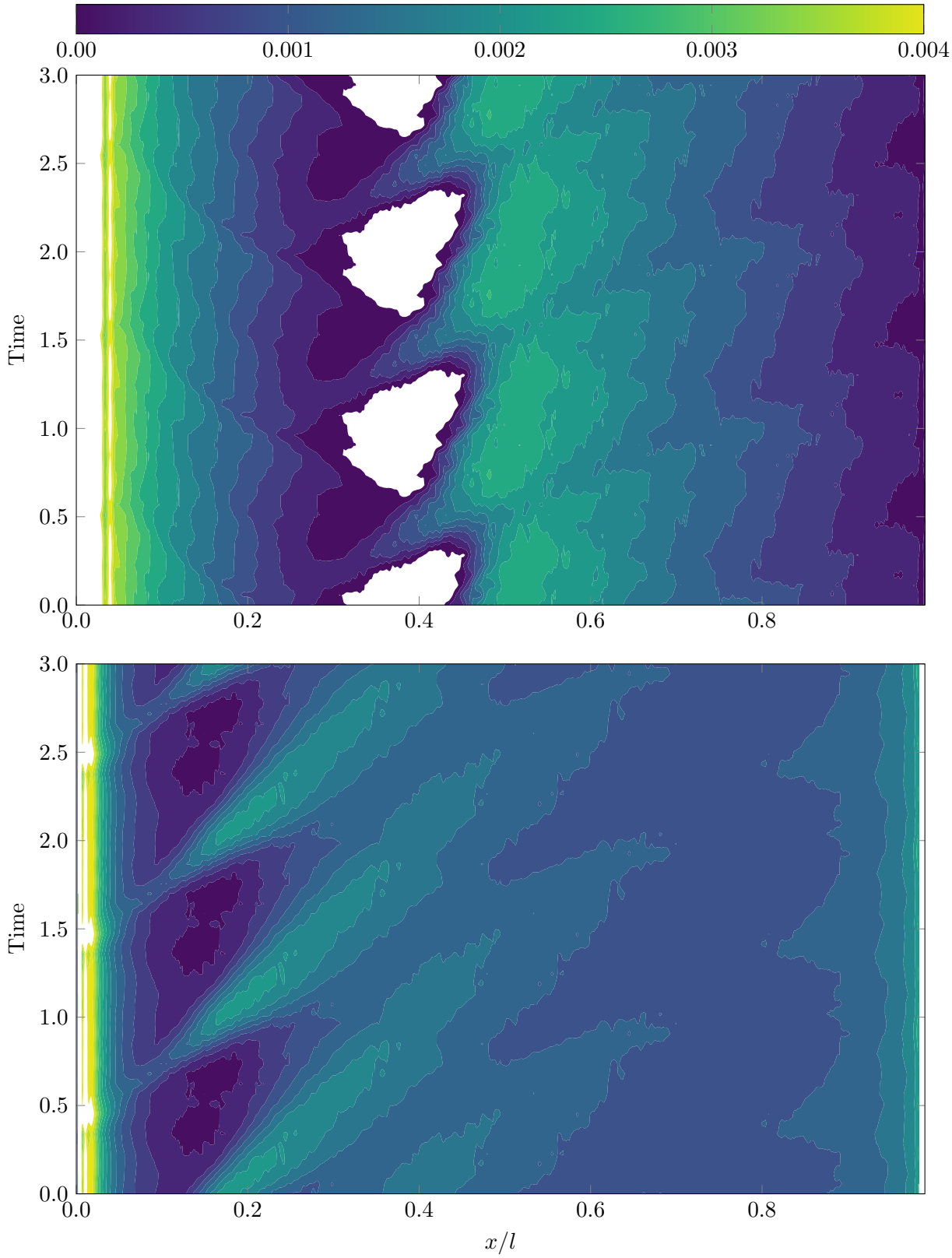

Figure 4.43: Phase locked space-time skin friction plot for suction surface (top) and pressure surfaces (bottom) for the one bar case. Separated flow is shown by white areas.

4.13 Conclusions

The chapter has focused on comparing the performance and flow behaviour in a compressor cascade with three sets of inflow disturbances, a reference case with no incident free-stream disturbances, a turbulent case with a nominal level of incident homogeneous free-stream turbulence and a case with incident discrete wakes without any background homogeneous turbulence. Aside from the differences in the incident disturbances the cases were run with the same Reynolds, Mach and inflow angle.

The three cases allow a clear comparison to be made on how the different structures of free-stream disturbances affect the blade performance and flow field. The initial investigation was aimed at understanding the changes of loss due to the disturbances. However, on looking closer at the instantaneous flow fields an interesting effect of the discrete wakes was highlighted. This led to an additional investigation to understand how the different disturbances affected the presence of pressure waves in the flow domain.

The presence of pressure waves, mentioned in early work such as that by *Tijdeman* (1977), is not a new phenomenon as these have been seen in sub-critical aerofoil flows before. However, the presence of these waves in compressor cascades is not well documented and no mention of the effects of free-stream disturbance type is known of. Further more the investigation of these waves in earlier work is focused on single aerofoils and the origin of the waves is often suggested to be the trailing edge shedding of the blade. In the investigation here it is likely that the pressure waves are driven by some mechanism associated with the trailing edge shedding, though they are clearly originating from the suction surface separation and transition. Unfortunately the direct cause of the pressure waves has not been investigated here as the focus is predominately on loss prediction, but it is suggested that they originate from the roll up and collapse to turbulence of the boundary layer at separation.

The interesting insight gained though is that the pressure waves are strongly affected by the type of free-stream disturbance. In the comparison between the different cases it was found the presence of homogeneous turbulence did little to affect the fundamental frequency of the waves while the addition of discrete wakes resulted in a noticeable increase in the wave frequency. Furthermore, the waves were seen to propagate past transition down-stream becoming visible again near the trailing edge in the Base and homogeneous cases while they appeared confined to the up-stream region in the discrete wake case. This presents an interesting question as to whether they are forced by the trailing edge shedding if they are not see down-stream of transition.

A possible reasoning for this is put forward. It is noted that in the discrete wake case the wake of the bar resulted in a periodic pulling and distorting as it passes the trailing edge. This distortion creates a long wave shedding interval of the blade equal the bar wake passing period.

The effects of this might be to disrupt the natural shedding of the blade trailing edge and force a higher frequency fluctuation that results in the higher frequency pressure waves seen, provided the boundary layer instabilities are forced by the blade trailing edge unsteadiness.

Following the investigation into the instantaneous effects the types of free-stream disturbance have on the flow the statistical data is investigated to understand the effects on loss. The loss is compared and investigated in much the same way as was done for the off-design incidence investigation, starting with the comparison of the total mixed out and mass averaged pressure loss for all the cases. The total loss trends were found to be quite varied for the different cases. Interestingly, it was found that the discrete wake case resulted in the lowest overall loss, something not expected at the onset of the investigation. The turbulent case shows an expected increase in loss compared with the base case.

To understand these differences in loss more the loss was broken down into wake or blade loss and passage loss. This distinction allows a comparison to be made of how the different free-stream disturbances affect the blade boundary layers and how the adverse pressure gradient in a compressor affects the evolution of these disturbances through the domain.

The first and clearest insight from this breakdown is that the blade wake loss is largely unaffected by the different disturbance types investigated here, although looking at the wake loss in more detail does highlight some changes, as there are certainly differences in the flow field that have been shown. The second, and perhaps the more interesting insight, is that the changes in total loss are predominantly caused by variation in the passage loss. It was found that the lower loss of the bar wake case is driven by a substantial "recovery" of loss in the passage. The reason for this apparent "recovery" is not fully understood unfortunately though *Smith* (1966a) suggests that under certain conditions the turbulence in the wakes can be "recovered". It is also suggested that the "recovery" could in part be due to an effective reduction and diffusion of the turbulence in the bar wakes by the deceleration of the flow.

The comparison of the blade boundary layers under the influence of different free-stream disturbances showed largely the same behaviour, as was some what expected due the the fact that the other flow parameters remained constant. However, there were some noticeable differences in the transition behaviour and overall the blade wake loss was lowest for the bar case. As such the difference in total loss are not solely driven by changes in the passage loss. The large changes in transition due to the discrete wakes resulted in an average wall shear with a lower peak post transition wall shear resulting in less loss from the boundary layers. The other cases had quite clear transition points resulting in noticeably higher post transition wall shear.

The investigation also looked at applying the Denton loss breakdown to help explain the changes in the blade loss. However, it is was found that the Denton loss breakdown did not capture the changes in the blade loss as well as expected even when comparing the loss breakdown with the blade wake loss only. It is suggested that the Denton loss breakdown struggles in this case as

it does not take into consideration the changes that might occur in the passage and how these might affect the statistical average of the boundary layers. As such it was deemed less effective in this case at highlighting changes in loss.

Chapter 5

Mechanical Work Potential Analysis

5.1 Introduction

In previous chapters the profile loss has been attributed to different sources using the phenomenological model introduced by *Denton* (1993). That approach does not explicitly account for the unsteady loss contributions associated with wakes passing through the passages between blades and interacting with the blade boundary layers. In order to ascribe losses in an unsteady flow with wakes, a different approach is required. Here, the losses are analysed in terms of flow work potential (*Miller*, 2013). The flow work potential quantifies the maximum possible work output that could be generated by the fluid in a given control volume by expanding that fluid to a reference ambient pressure in a reversible and adiabatic steady flow device such as an isentropic turbine. The work potential is a function of local thermodynamic properties and the reference ambient pressure only, meaning that the processes leading to any change in work potential can be identified unambiguously on an instantaneous and local basis by analysing the governing equations of the underlying thermodynamic variables.

Work potential analysis in a turbomachine is a recent development (*Miller*, 2013), but it is analogous to the longer-established application of exergy analysis in a heat engine (*Horlock*, 1992). The difference is that the maximum work value given by the work potential analysis excludes contributions due to exchanging heat between the working fluid and the environment, which is not usually practical in the context of an aircraft engine. The difference between specific flow work potential m_f and specific flow exergy e_f is illustrated in fig. 5.1 for a fluid at a state denoted by subscript 1 and a reference ambient condition, or dead state, denoted by subscript D. The flow work potential is given by the enthalpy change due to an isentropic expansion from state 1 to the dead state pressure. The state at the end of that isentropic expansion is denoted by subscript se. The maximum work suggested by exergy analysis includes the additional work that could be generated by a series of Carnot engines utilising the heat rejected

reversibly ($\Delta h = \int T.ds$) as the fluid is subsequently cooled from temperature T_{se} to the dead state temperature T_D. For an aircraft engine, in which generally it is not practical to exchange heat with the high-speed propulsion jet, meaning that the thermal flow work potential $e_f - m_f$ is not recoverable and work potential is the more relevant metric for loss analysis in aeroengine applications.

Using mechanical work potential analysis it is possible to distinguish changes in work potential associated with viscous dissipation from those associated with thermal conduction, for example. In the context of an uncooled compressor blade row, the principle loss mechanism is expected to be viscous dissipation, and contributions associated with heat fluxes are expected to be negligible. Even in this relatively simple case mechanical work potential analysis is valuable because it relates the viscous dissipation to the overall reduction in the work output of the engine (or other device), in contrast with some previous analyses that look at entropy production or viscous dissipation in isolation *Wheeler et al.* (2016).

Work potential analysis indicates that viscous dissipation in two dynamically-similar blade rows can make different contributions to the overall loss of work in an engine depending on the pressure in the respective blade rows relative to the reference ambient pressure: viscous dissipation in a high-pressure stage is less deleterious to overall performance than an equivalent amount of viscous dissipation in a low-pressure stage. This difference can be understood by considering the conversion of kinetic energy in to thermal energy associated with viscous dissipation – sometimes called viscous reheat – and noting that increasing the temperature of a gas increases the amount of work that can be recovered when it is expanded, and that the additional work due to a given amount of viscous dissipation then depends on the pressure ratio of the expansion.

Despite the theoretical arguments in favour of the use of mechanical work potential analysis, use of other approaches for measuring, discussing and understanding losses are long-established in industry. Therefore it is important to be able to relate measures of loss based on mechanical work potential analysis to more familiar loss metrics such as stage efficiencies and pressure loss coefficients.

The objectives of this chapter are to explore how mechanical work potential analysis can be applied in a linear compressor cascade in order to quantify the relative magnitude of different contributions to the profile loss, including the unsteady contributions associated with the passage of incoming wakes. In addition, the relationship between the loss measured by mechanical work potential and pressure loss coefficients is explained.

For a compressor this definition is somewhat vague as work is being performed on the fluid, not extracted. In this case the mechanical work potential can be used as a measure of the efficiency of the compressor. If we assume that a compressor is isentropic then the mechanical work potential at the exit of a compressor stage must be equal to the mechanical work potential into the stage plus the work added. If the plane of reference is taken relative to the compressor

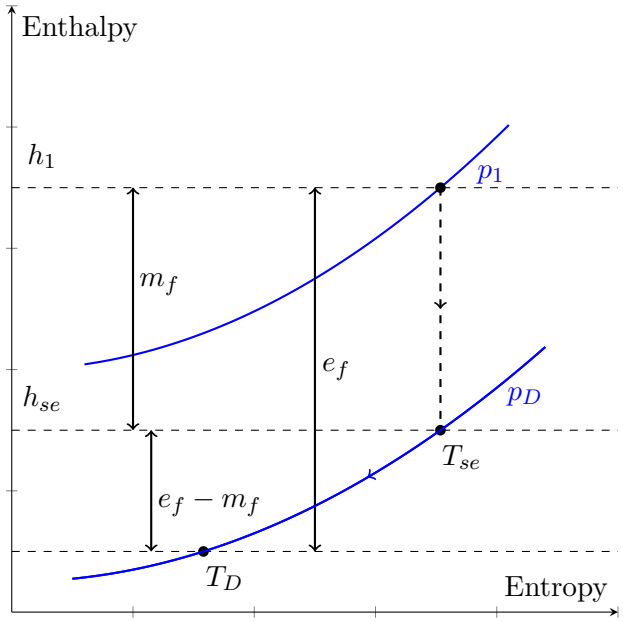

Figure 5.1: Illustration of the difference between flow mechanical work potential and flow exergy marked on an enthalpy-entropy diagram.

stage then no work is performed on the fluid, as the blade is stationary, and the mechanical work potential remains constant for an ideal case. This allows the mechanical work potential of a real non-isentropic cascade to be used as a measure of lost performance in a compressor.

5.2 Formulation

The equation of interest is the budget for the Mechanical work potential that has been introduced in chapter 2. The derivation, given by *Miller* (2013), is also outlined in chapter 2 and assumes the working fluid is a perfect gas and has a uniform composition. The definition and equation governing the mechanical work potential will be given again here for completeness.

The definition of the mechanical work potential in closed and open form systems is given as

$$\mathbf{m} = (e - e_{se}) + p_D(\nu - \nu_{se}) + \frac{1}{2}u_i u_i \tag{5.1}$$

$$\mathbf{m_f} = (e - e_{se}) + p_D(\nu - \nu_{se}) + \frac{1}{2}u_i u_i + (p - p_D)\nu = (h - h_{se}) + \frac{1}{2}u_i u_i \tag{5.2}$$

which can be recast as

$$\mathbf{m} = e\left(1 - \frac{T_{se}}{T}\right) + p_D(v - v_s) + \frac{1}{2}u_i u_i \tag{5.3}$$

$$\mathbf{m_f} = h\left(1 - \frac{T_{se}}{T}\right) + \frac{1}{2}u_i u_i \tag{5.4}$$

using the assumption that the working fluid is a perfect gas such that $T_{se}/T = \left(\frac{p_D}{p}\right)^{\frac{\gamma-1}{\gamma}}$. Here the value T_{se} is the temperature obtained by the fluid when isentropically expanded to the reference pressure.

The govering for the mechanical work potential is given as:

$$\begin{aligned}\frac{d(\rho\mathbf{m})}{dt} + \frac{\partial\left(\rho u_i \mathbf{m_f}\right)}{\partial x_i} =& -\frac{\partial}{\partial x_i}\left[\left(1-\frac{T_{se}}{T}\right)q_i\right] \\ &+\left(\frac{\gamma-1}{\gamma}\right)\frac{1}{p}\frac{\partial p}{\partial x_i}q_i \\ &-(\tau_{ij}\frac{\partial}{\partial x_j})u_i \\ &-\left(1-\frac{T_{se}}{T}\right)\left(\frac{\gamma-1}{\gamma}\right)\frac{1}{p}\frac{\partial p}{\partial x_i}q_i \\ &+\left(1-\frac{T_{se}}{T}\right)(\tau_{ij}\frac{\partial}{\partial x_j})u_i \\ &+\frac{\partial}{\partial x_j}\left[\overline{\overline{\tau}_{ij}}u_i\right] \end{aligned} \tag{5.5}$$

For the LES implementation the equation solved needs to be spatially filtered in the same manner that the Navier-Stokes equations are filtered. The filtering operation results in the following equation.

$$\begin{aligned}\frac{d(\overline{\rho}\widetilde{\mathbf{m}})}{dt} + \frac{\partial}{\partial x_i}(\overline{\rho}\widetilde{\mathbf{m_f}}\widetilde{u_i}) =& -\frac{\partial}{\partial x_i}\left[\left(1-\frac{\widetilde{T_{se}}}{\widetilde{T}}\right)\widetilde{q_i}\right] \\ &+\left(\frac{\gamma-1}{\gamma}\right)\frac{1}{\widetilde{p}}\frac{\partial\widetilde{p}}{\partial x_i}\widetilde{q_i} \\ &-(\widetilde{\tau_{ij}}\frac{\partial}{\partial x_j})\widetilde{u_i} \\ &-\left(1-\frac{\widetilde{T_{se}}}{\widetilde{T}}\right)\left(\frac{\gamma-1}{\gamma}\right)\frac{1}{\widetilde{p}}\frac{\partial p}{\partial x_i}\widetilde{q_i} \\ &+\left(1-\frac{\widetilde{T_{se}}}{\widetilde{T}}\right)(\widetilde{\tau_{ij}}\frac{\partial}{\partial x_i})\widetilde{u_i} \\ &+\frac{\partial}{\partial x_j}\left[\widetilde{\overline{\overline{\tau_{ij}}}}\widetilde{u_i}\right] \\ &+F \end{aligned} \tag{5.6}$$

where F represents a group of residual terms including sub-grid fluxes and sub-grid dissipation. These terms are neglected in the current analysis and their magnitude is assessed from the imbalance of eq. (5.6).

5.2.0.1 Interpretation

The mechanical work potential applied to compressors helps to improve our understanding of loss mechanisms. The mechanical work potential was originally derived for application to turbines, where the interest is in potential work extracted, the application of the mechanical work potential to compressors has a slightly different interpretation. In a compressor the mechanical work potential provides a measure of the work potential gained in the compression process which can be used to measure the efficiency if the work input is known. However, if working in the frame of reference of the blade the mechanical work potential provides a measure of the work potential lost due to irreversibility. It should also be noted that any terms containing the term $(1 - T_{se}/T)$ are affected by the choice of reference pressure or the ratio p/p_D. This means that the choice of reference dead state scales terms that depend the pressure ratio, including $\mathbf{m_f}$, while those without this term remain unaffected, making the relative importance of terms dependant on the dead state.

The interpretations of the terms of eq. (5.5) have been introduced in chapter 2 but are reviewed again here. The various terms and their interpretation are outlined below.

Mechanical work potential due to heat transfer

$$-\frac{\partial}{\partial x_i}\left[\left(1-\frac{T_{se}}{T}\right)q_i\right] \tag{5.7}$$

This term represents the change in mechanical work potential associated with net heat flux.

Thermal creation

$$\left(\frac{\gamma-1}{\gamma}\right)\frac{1}{p}\frac{\partial p}{\partial x_i}q_i \tag{5.8}$$

This term represents the creation of mechanical work potential by heat transfer across a pressure gradient.

Viscous dissipation

$$-(\tau_{ij}\frac{\partial}{\partial x_j})u_i \tag{5.9}$$

This is the rate of viscous dissipation associated with the work done by shear forces in opposing fluid deformation. It is the rate of transfer of kinetic energy to internal energy.

Thermal recool

$$-\left(1-\frac{T_{se}}{T}\right)\left(\frac{\gamma-1}{\gamma}\right)\frac{1}{p}\frac{\partial p}{\partial x_i}q_i \tag{5.10}$$

This term represents the secondary effects thermal creation has on the fluid. In the thermal creation term mechanical work potential is changed based on heat transfer across a pressure gradient. However the thermal recool is the effect the heat transfer has on the local point where the heat is being moved from and is determined by the local pressure. For example if heat is removed from a location where the pressure is higher that the reference then mechanical work potential is lost and visa versa.

Viscous reheat

$$\left(1-\frac{T_{se}}{T}\right)(\tau_{ij}\frac{\partial}{\partial x_j})u_i \tag{5.11}$$

Viscous reheat is similar to the process of thermal recool where secondary effects of one process produce changes in the mechanical work potential. The viscous reheat term captures the effects the viscous dissipations has on mechanical work potential related to the changes in internal energy. It is know that the effects of viscous dissipation result in a local heating as the kinetic energy of the fluid is changed to internal energy. If this local heating from the fluid shearing occurs at a higher pressure compared to the reference pressure then there is a local creation of mechanical work potential. This shows why dissipation at higher pressures within a compressor are less detrimental to the over all efficiency than dissipation at lower pressures.

Shear work

$$\frac{\partial}{\partial x_j}\left[\overline{\overline{\tau}_{ij}u_i}\right] \tag{5.12}$$

This term represents the shear work done on a local fluid element. It is the dissipation resulting from the mean flow resisting shearing by viscous forces.

5.3 Verification

The implementation of the mechanical work potential analysis is verified using a set of simulations performed of a 2D DNS of a cylinder in cross flow and a 3D DNS and 3D LES of a channel flow. The 3D LES is done to check the effect of neglecting the residual terms resulting from spatially filtering the equation. If large errors are present in the balance of the equation then the residual terms cannot be neglected and a model must be used to account for these terms. In the present implementation the unknown terms are neglected.

The 2D DNS is performed at a Reynolds number 100 to ensure the flow is not falsely constrained by the 2D domain. The 2D DNS is performed to allow the implementation of the mechanical work potential to be checked easily and to ensure that the equation balances without great computational expense. Following this the 3D LES and DNS simulations of the channel are performed at a bulk Reynolds number of ≈ 2800. The choice of a channel flow for validation is based on the simple set-up and low computational expense.

5.3.1 Set-up

The cylinder set-up is based on the work by *Wissink and Rodi* (2008) which was used to provide the basic domain parameters. This test case was chosen as it is was also used to test the set-up for the moving bar validation simulations performed in chapter 4, which meant the set-up could be reused. However the flow Reynolds number is greatly reduced making the flow results incomparable. However the results from the moving bar validation showed that both the body fitted mesh and immersed boundary method resulted in good flow agreement at a Reynolds number of ≈ 3000, making the current 2D simulation with the same mesh over resolved. Although the immersed boundary method proved slightly more computationally expensive, the Reynolds number is greatly reduced with the simulations performed only in 2D, making the immersed boundary method a better choice as it further simplifies the set-up and the additional cost is not prohibitive.

The domain size for the cylinder case is set as 10 diameters up-stream 20 down-stream and 10 above and below the cylinder, taken from *Wissink and Rodi* (2008), shown in fig. 5.2.

The boundary conditions are set to a fixed inflow with non-reflective free-stream boundaries for the remaining three boundaries. The free-stream exit boundary has a sponge region applied to further reduce reflections as the wake exits the domain. The cylinder is set as a non slip wall with a constant temperature.

The 3D channel simulations are based on the work by *Kim et al.* (1987) which provided the basic set-up. The simulations are performed at a bulk Reynolds number of ≈ 2800 based on the channel half height. The simulations reported by *Kim et al.* (1987) were incompressible, while the simulations performed here are compressible. To try to match the incompressible behaviour of Kim et al.'s simulations the Mach number is set to 0.2. The channel dimensions and boundary conditions are set as follows; the channel half height is set to 1 with a stream-wise extent of 12 and a span-wise extent of 4. The steam-wise and span-wise boundaries are set as periodic and the channel walls as non slip with a constant wall temperature. In order to drive the channel flow a constant stream-wise pressure gradient is enforced. The channel set-up is shown in fig. 5.3.

The final running conditions for the validation simulations are shown in table 5.1.

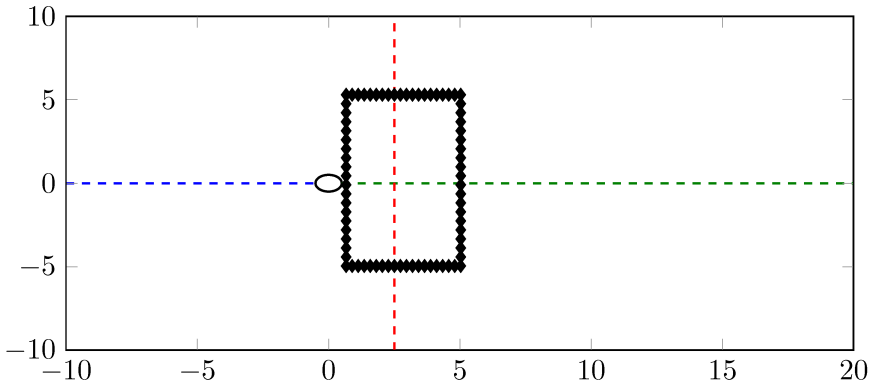

Figure 5.2: Immersed boundary cylinder set-up for mechanical work potential validation. Showing domain extents and lines (dashed) and volume (diamonds) extracted for budget review.

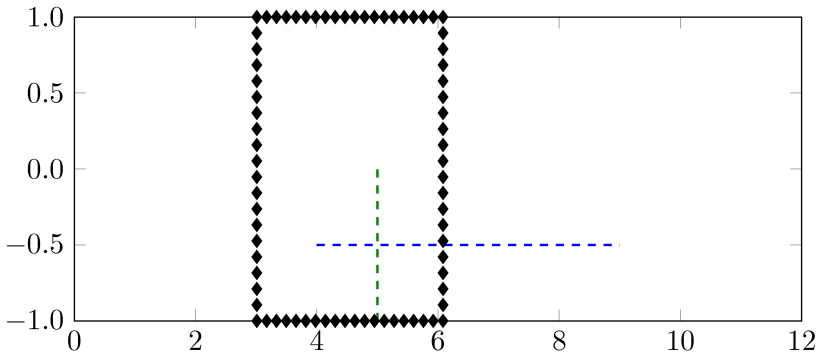

Figure 5.3: Channel set-up for 3D mechanical work potential validation. Showing domain extents and lines (dashed) and volume (diamonds) extracted for budget review.

Table 5.1: Final running conditions for mechanical work potential 3D channel validation simulations

Simulation	DNS Avg.	DNS Instant	LES Avg.	LES Instant
U_b	15.650	15.135	15.658	16.276
U_c	17.460	18.641	17.354	18.823
U_c/U_b	1.116	1.232	1.108	1.156
Re_b	2790	2699	2791	2901
Mach	0.280	0.271	0.280	0.291
Displacement Thickness δ^*	0.148	0.239	0.140	0.107
Momentum Thickness θ	0.092	0.160	0.087	0.047

5.3.2 Budgets

The budgets of the mechanical work potential equation for several locations are presented here. For the 2D cylinder a line up-stream of the bar, a line across the wake and a line down-stream of the bar are extracted for comparison. A volume spanning an area across the wake is extracted for the integral comparison. The lines and volume are outlined in fig. 5.2. It is noted that the immersed boundary method introduces an error where the body forcing is applied meaning the budgets cannot be shown up to the prescribed radius of the cylinder. However, outside of the forcing kernel the solution is correct.

For the 3D channel cases a line across the channel and a line along the channel at a quarter channel height are extracted. The position of the extracted lines are shown in fig. 5.3, as well as a volume spanning the channel domain.

The instantaneous and time averaged results for the 2D DNS are presented first. The budgets for the three locations of instantaneous results are shown in fig. 5.4 and the budgets for the averaged results are shown in fig. 5.5. It is seen in both the instantaneous and statistical results that the shear work and viscous dissipation dominate the process as expected. The budgets also show the implementation balances with negligible error for both the instantaneous and statistical results.

The 3D results for the DNS and LES cases are shown in figures figs. 5.6 and 5.7 for the instantaneous and statistical results respectively. For the 3D channel results an additional term is required to balance the equation, shown as the body forcing. The body forcing is a result of the set-up and is applied in the form of a pressure gradient to maintain the flow. The energy added by the applied pressure gradient is equal to

$$Bodyforcing = \int -\rho u_i \frac{\partial}{\partial x_i} p dV,$$

as it appears in the energy equation, which balances the equation. The body forcing is added to the right hand side to capture the added energy needed to drive the flow. The pressure gradient prescribed to drive the flow was set to 1, making the energy added due to the body forcing equal to the momentum integral.

The instantaneous results in fig. 5.6 do show some local areas of high error, which are attributed to the first order calculation of the time derivative as well as a contribution from the neglected residual terms from the filtering of the equation. The accuracy of the time derivative was not improved as this would require larger memory usage for bigger simulations and the interest in this study was on statistically steady results meaning the time derivative converges to zero.

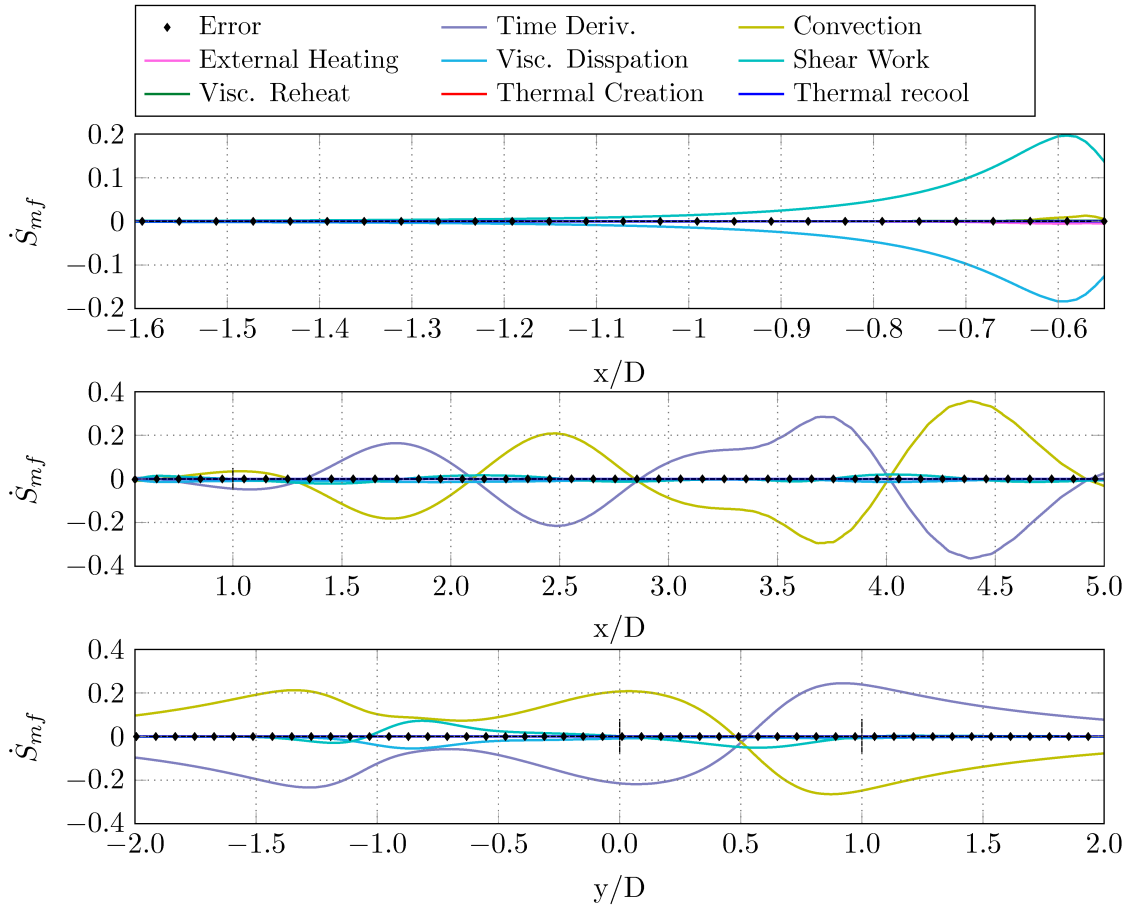

Figure 5.4: Instantaneous mechanical work potential budget for 2D DNS cylinder at Reynolds 100. From top to bottom, up-stream line, down-stream line and cross wake line.

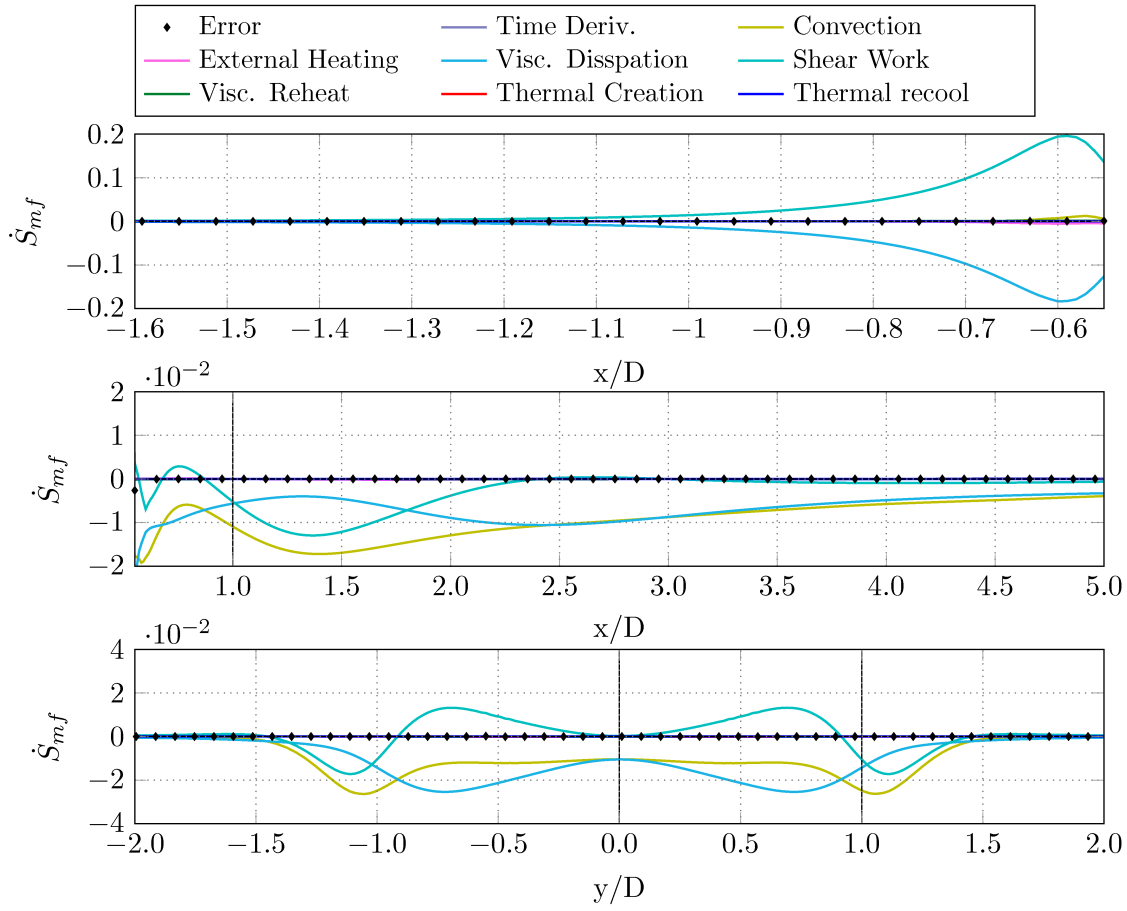

Figure 5.5: Time averaged mechanical work potential budget for 2D DNS cylinder at Reynolds 100. From top to bottom, up-stream line, down-stream line and cross wake line.

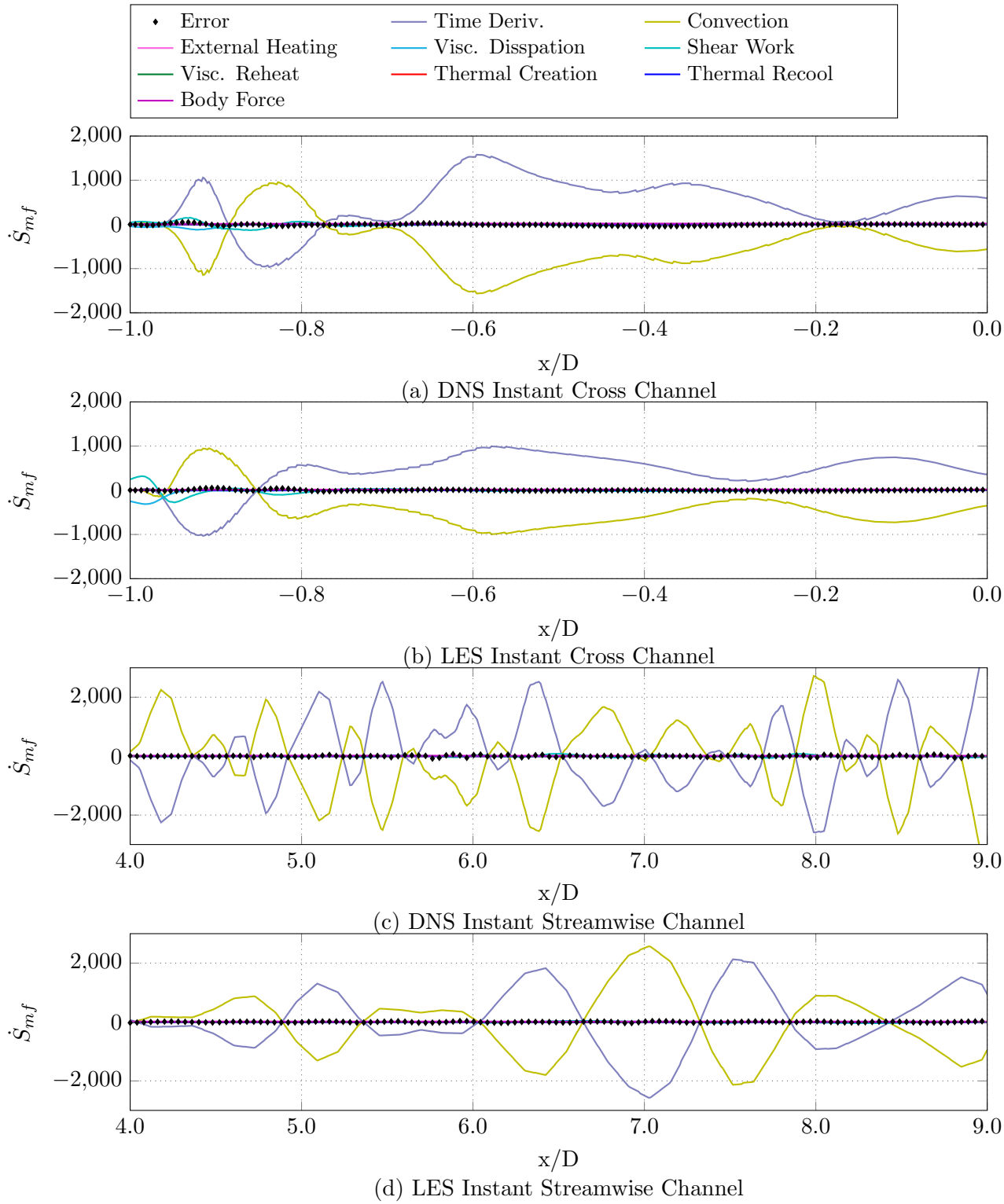

Figure 5.6: Instantaneous mechanical work potential budget for 3D DNS and LES channel flow at Reynolds 2,800. Normal cross channel line (a) DNS (b) LES, Stream-wise 1/4 channel height line (c) DNS (d) LES.

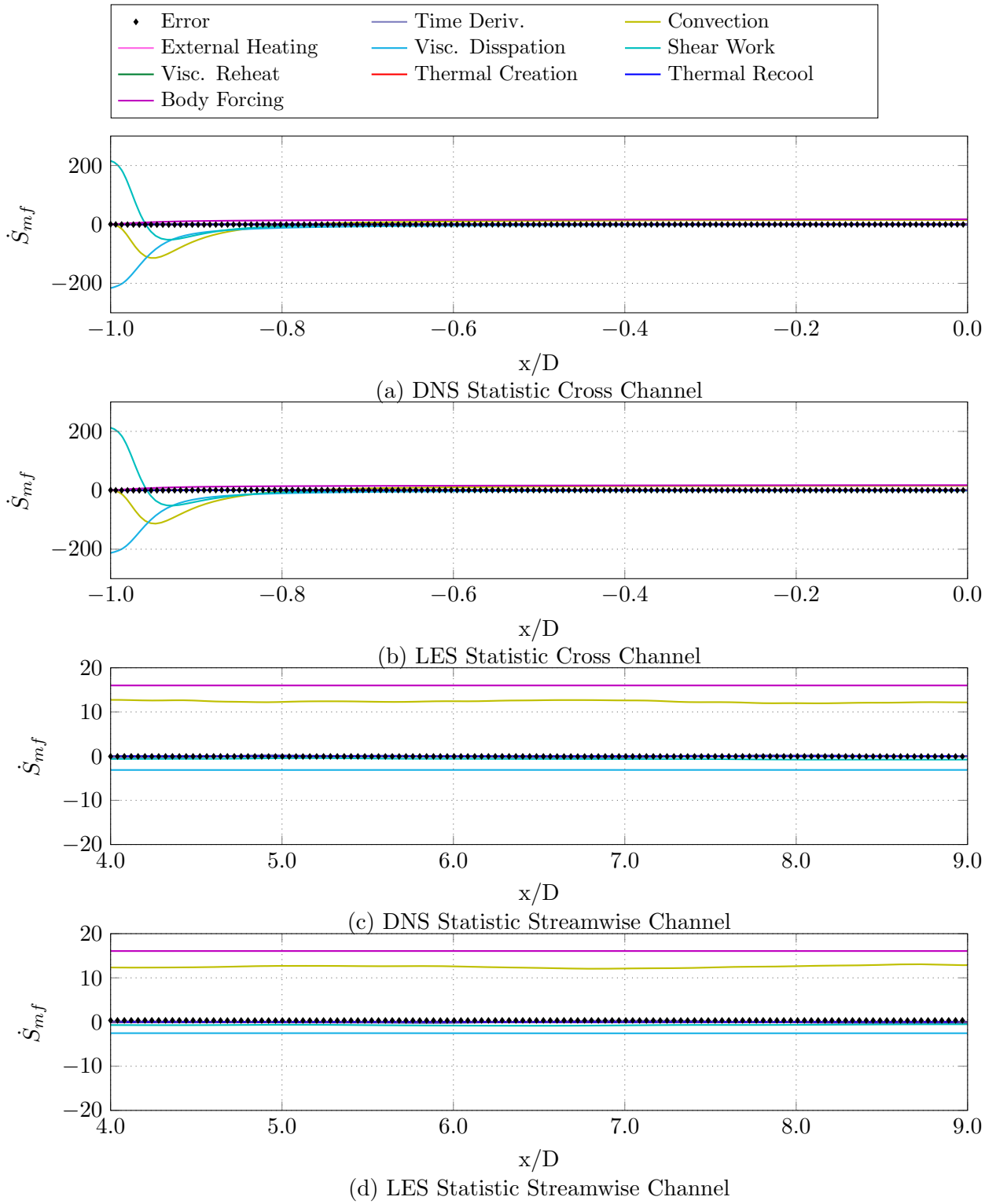

Figure 5.7: Time averaged mechanical work potential budget for 3D DNS and LES channel flow at Reynolds 2,800. Normal cross channel line (a) DNS (b) LES, Stream-wise 1/4 channel height line (c) DNS (d) LES.

5.3.3 Integral Quantities

The total integral changes of the terms of the mechanical work potential equation are calculated for the areas shown in the cylinder and channel schematics, down-stream of the cylinder for the 2D simulation and across the channel for the 3D simulations. The 2D area does not include the cylinder boundary layer due to errors introduced by the immersed boundary method, and is only of the integral area highlighted by black diamonds on fig. 5.2.

The integral analysis for both the 2D and 3D verification simulations are presented as bar graphs. For the 2D DNS the results are presented in fig. 5.8 showing the contributions to the change in the mechanical work potential from the various source terms. The error in balancing the equation for the total integral is also presented, and shown to be minimal for both the instantaneous and statistical results.

The area for the 3D cases is highlighted by the black diamonds on fig. 5.3, and spans the full hight of the channel. The integral results of this area for the LES and DNS are presented in the bar graphs in figures figs. 5.9 and 5.10 showing the contributions from each of the source terms as was done for the 2D case. The error in balancing the equation is also presented and again shows a minimal error, although the error is slightly larger for the fully 3D flow. The Integral for the 3D channel cases also includes the body forcing term necessary to drive the flow. The increase in error is due in part to the increased effect of the neglected turbulent fluctuation terms which are not accounted for in the filtered formulation of the mechanical work potential equation. There is also an error introduced from the time derivative for the instantaneous integral, which is dependent on the choice of time step. For the simulations performed here the time step was chosen to optimise the simulation time not the time derivative, resulting in a large time step and a less accurate time derivative for the mechanical work potential.

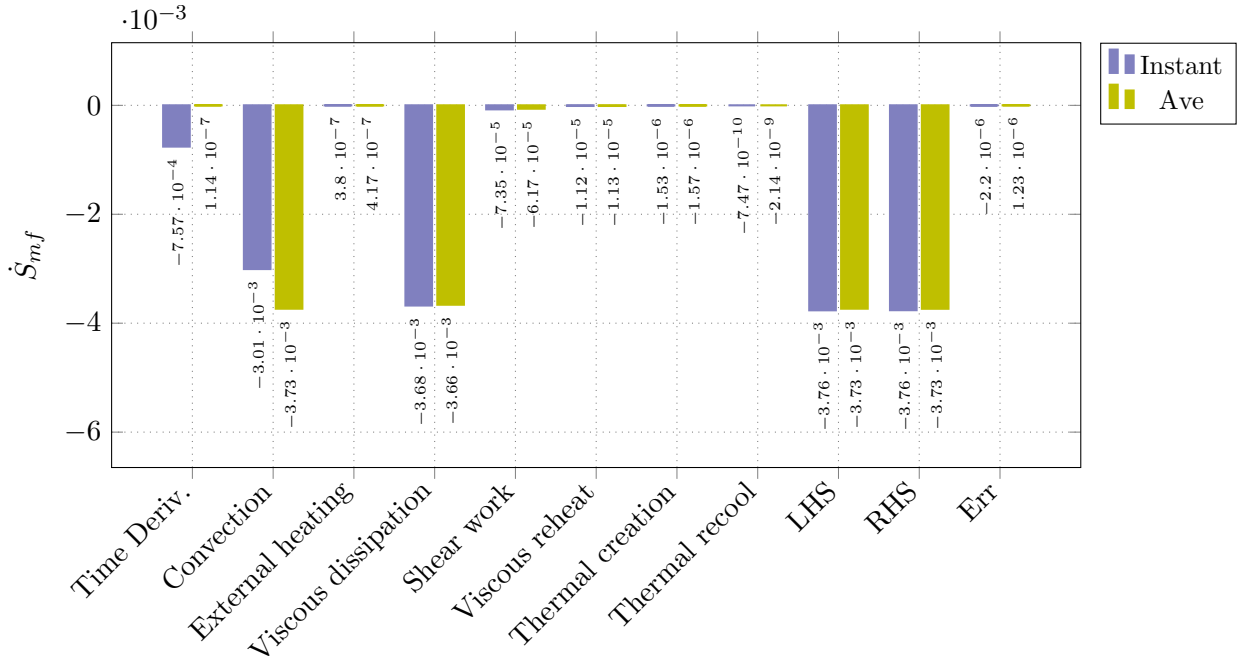

Figure 5.8: Instantaneous and time averaged integral mechanical work potential budget for 2D DNS cylinder at Reynolds 100. Integral is for area shown by diamonds in fig. 5.2. This does not include the bar as the immersed boundary introduce error that cannot be counted for.

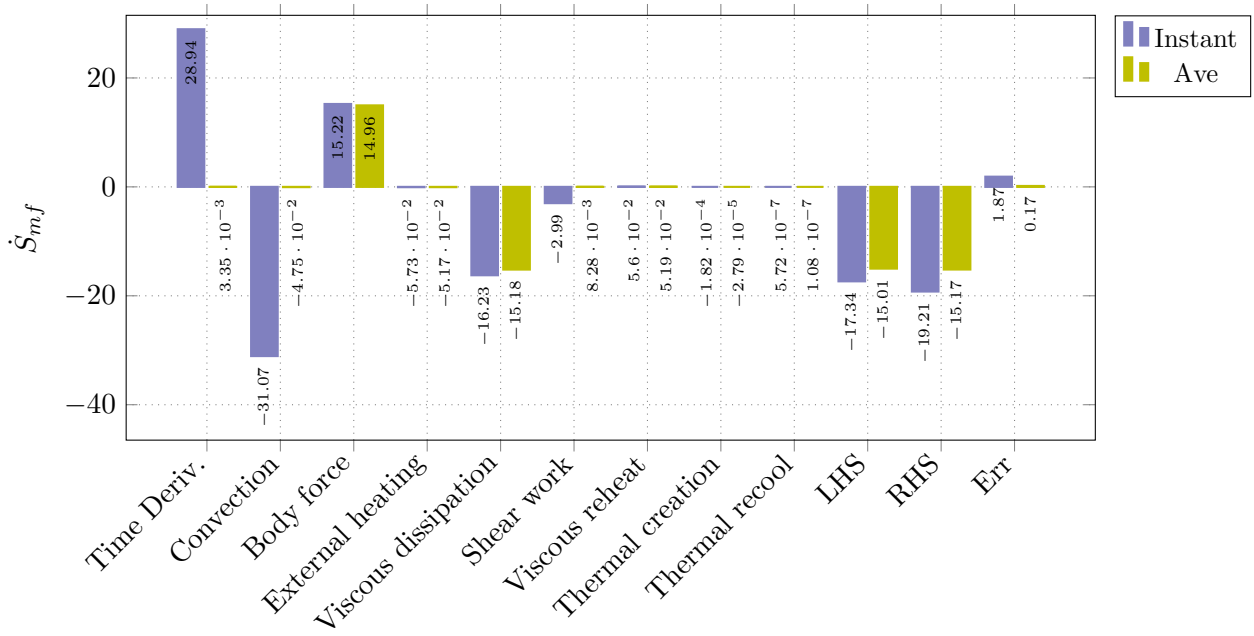

Figure 5.9: Instantaneous and time averaged integral mechanical work potential budget for 3D DNS channel at Reynolds 2,800. Integral is for area shown by diamonds in fig. 5.3.

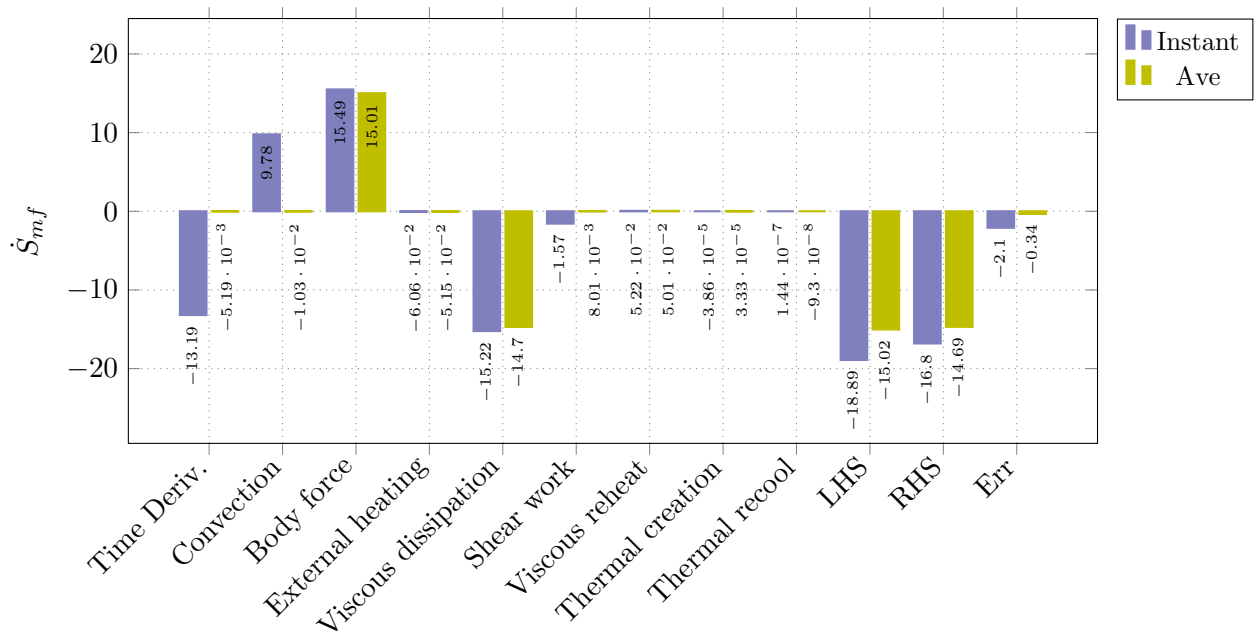

Figure 5.10: Instantaneous and time averaged integral mechanical work potential budget for 3D LES channel at Reynolds 2,800. Integral is for area shown by diamonds in fig. 5.3.

5.3.4 Verification Conclusions

Looking at the comparison of the line budgets and integrated areas the difference seen between the DNS and LES results are minimal. The 2D DNS initially shows the implementation of the mechanical work potential balances for both the instantaneous and statistical results. The results show the expected trend in the budgets with viscous dissipation and shear work accounting for the largest changes in the mechanical work potential. The 3D comparison shows the same trends as the 2D results, with viscous dissipation and shear work being the largest terms. The 3D comparison between DNS and LES shows slight differences in the integrated results though the differences are small. The resulting error in balancing the equation shows the neglected terms do not result in large discrepancies based on the resolution of the LES performed here. It is suggested that should non-wall resolved LES simulations be performed that this be revisited. The comparison of the instantaneous budget plots for the 3D results are less accurate compared to the 2D results which is attributed to the low order calculation of the time derivative term. For the statistical results the comparison is much cleaner. Overall the results of the verification simulations show good comparison and the equation balances with acceptable accuracy to allow neglect of the residual terms.

5.4 Analysis Outline

Following the verification of the mechanical work potential analysis code, the analysis is applied to the compressor cascade simulations, both the incidence loss bucket simulations and the moving bar simulations.

The analysis focuses on changes in the total mechanical work potential and looks at integral changes of the mechanical work potential and various terms of the equation. Before examining the data a mechanical work potential loss coefficient is introduced and a comparison made with the pressure loss coefficient more commonly used. The mechanical work potential loss coefficient is derived in much the same way as the pressure loss and tries to provide a single value for the comparison of loss between different running conditions.

The analysis of the changes in mechanical work potential for the full domain follows, looking at a volume breakdown that tries to improve our understanding of where loss originates and what processes are responsible. The analysis also addresses how this changes as incidence is varied as well as with the addition of discrete wake disturbances.

For the mechanical work potential analysis the statistics are taken for the same non-dimensional interval as the flow statistics used in the analysis in chapters 3 and 4. This is seen to provide adequate statistical convergence to identify the key regions of loss in the flow.

5.5 Flow Field Overview

Before investigating the results in detail an overview of where the processes involved in the mechanical work potential occur in the flow domain is give. Contour plots for each of the terms of the equations are plotted in fig. 5.11 highlighting where the different processes are most prevalent. It is seen in the plots that processes involving heat transfer are most prevalent near the leading edge due to the increase in temperature from stagnation. There is also flow heating at the trailing edge where the strong viscous shear from the boundary layers leaves the blade.

The viscous processes dominate over the remainder of the blade with viscous dissipation and the corresponding viscous reheat focused on the separation and viscous shear layer of the turbulent boundary layer. The final two terms, the shear work and mechanical work potential from heat transfer are concentrated around the boundary layer edge where shear work is done by the free-stream and heat transfer with the bulk of the fluid takes place although changes in mechanical work potential due to heat transfer is also visible in most of the domain where ever a temperature variation exists.

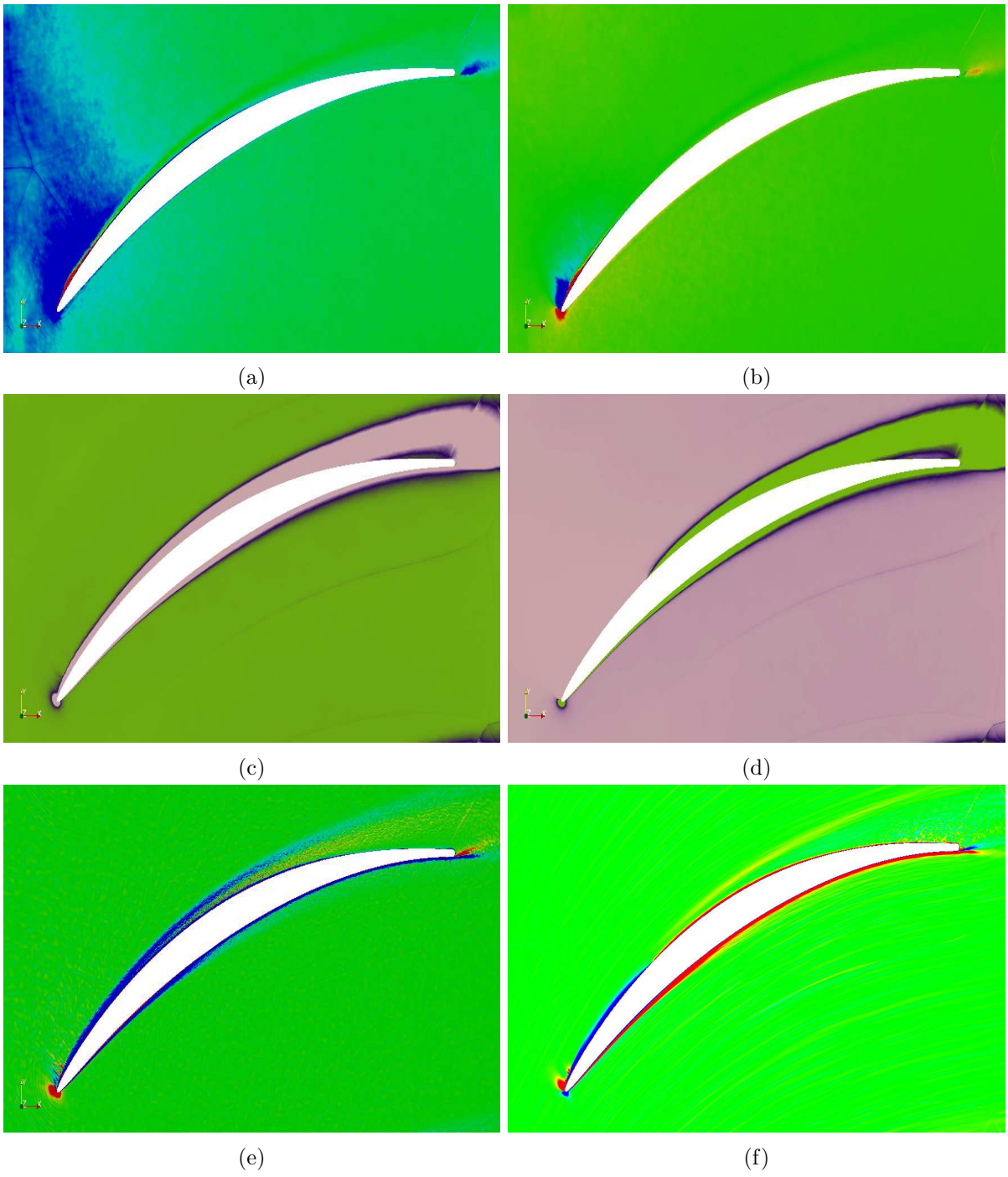

(a) (b)

(c) (d)

(e) (f)

Figure 5.11: Contour plots of terms of mechanical work potential for 49° turbulent case. Contours are for (a) thermal creation $[-10^{-4}, 10^{-4}]$, (b) thermal recool $[-10^{-5}, 10^{-5}]$, (c) viscous dissipation $[-10^{-2}, 0]$, (d) viscous reheat $[-5 \cdot 10^{-4}, 0]$, (e) shear work $[-5 \cdot 10^{-3}, 5 \cdot 10^{-3}]$ and (f) mechanical work potential due to heat transfer$[-3 \cdot 10^{-4}, 3 \cdot 10^{-4}]$. The colour scheme for corresponding processes is same with the limits of the contours given in brackets.

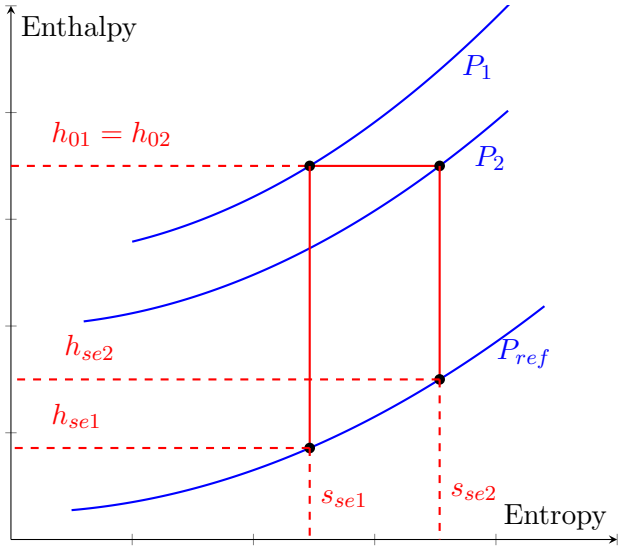

Figure 5.12: Enthalpy entropy relationship showing processes involved in derivation of mechanical work potential loss coefficient.

5.6 Mechanical Work Potential Loss Coefficient

Defining a loss coefficient for the mechanical work potential is useful to compare cases run with different conditions. The loss definition also enables a clear breakdown of the contribution of terms and regions to total loss to be performed and compared across cases. The mechanical work potential loss coefficient is defined in a similar manner to the pressure loss coefficient. Using the mechanical work potential mass flux into and out of a control volume normalized with the dynamic pressure at the inlet. Defining the loss as

$$\omega_{m_f} = \frac{\dot{m_{f1}} - \dot{m_{mf2}}}{(p_{o1} - p_1)/\rho_{o1}} \tag{5.13}$$

for a compressor and

$$\omega_{m_f} = \frac{\dot{m_{f1}} - \dot{m_{mf2}}}{(p_{o2} - p_2)/\rho_{o2}} \tag{5.14}$$

for a turbine with the mechanical work potential flux defined as

$$\dot{m_f} = \int u_i n_i \rho \mathbf{m_f} ds \tag{5.15}$$

The loss is also calculated as the mass averaged integral of the left hand side of eq. (5.5) normalized with the dynamic pressure. An appropriate relationship between the mechanical work potential loss coefficient and the pressure loss coefficient is defined as follows, by assuming the density is constant across the cascade and that the changes in the fluid properties are small. The process can be shown on an entropy enthalpy graph as in fig. 5.12.

Starting with the following definition of entropy

$$Tds = dh - \frac{dP}{\rho}, \tag{5.16}$$

and assuming a small finite change, then

$$T\Delta s = \Delta h - \frac{\Delta p}{\rho} \text{ and } T_t\Delta s = \Delta h_t - \frac{\Delta p_t}{\rho}. \tag{5.17}$$

The total mechanical work potential is

$$\mathbf{m_f} = h_t - h_{se}, \tag{5.18}$$

where h_{se} is the enthalpy following isentropic expansion to the reference pressure P_{se}. Considering a finite change through the stage,

$$\Delta\mathbf{m_f} = \Delta h_t - \Delta h_{se}. \tag{5.19}$$

However for a stator the change in stagnation enthalpy, $\Delta h_t = 0$. The same holds for the relative stagnation enthalpy for a rotor in the reference of the rotor.

$$\therefore \Delta\mathbf{m_f} = -\Delta h_{se} \tag{5.20}$$

From eq. (5.16) we can relate the change in Δh_{se} as

$$\Delta h_{se} = T_{se}\Delta s + \cancelto{0,\text{since } p_{ref} \text{ const.}}{\frac{\Delta p_{ref}}{\rho}}, \tag{5.21}$$

and the change of Δh_t as,

$$\Delta h_t = h_{t1} - h_{t2} = T_t\Delta s + \frac{\Delta p_t}{\rho} = 0, \tag{5.22}$$

Therefore

$$\Delta s = -\frac{\Delta p_t}{\rho T_t} \tag{5.23}$$

and substituting eqs. (5.21) and (5.23) into eq. (5.20) gives

$$\Delta\mathbf{m_f} \approx \frac{T_{se}}{T_t}\frac{\Delta p_t}{\rho}. \tag{5.24}$$

Assuming the working fluid is a perfect gas then

$$\frac{T_{se}}{T_t} = \left(\frac{p_{ref}}{p_t}\right)^{\frac{\gamma-1}{\gamma}}$$

and the relationship can be given in terms of pressures as

$$\Delta \mathbf{m_f} \approx \left(\frac{p_{ref}}{p_{t1}}\right)^{\frac{\gamma-1}{\gamma}} \frac{\Delta p_t}{\rho_1} \tag{5.25}$$

Finally, if we introduce the mechanical work potential loss, $\omega_{mf} = \frac{\dot{m_{f1}} - \dot{m_{mf2}}}{(p_{t1}-p_1)/\rho_{t1}}$, and the pressure loss, $\omega = \frac{p_{t1}-p_{t2}}{p_{t1}-p_1}$, they can be approximately related as

$$\omega_{m_f} \approx \omega \left(\frac{p_{ref}}{p_{t1}}\right)^{\frac{\gamma-1}{\gamma}} \tag{5.26}$$

In a compressor the interest is in converting kinetic energy into static pressure as efficiently as possible. The processes is achieved by slowing down an accelerated flow. In an isentropic flow the loss of the process is zero and the mechanical work potential should remain constant across a blade row in the frame of reference of the blade row. In this sense the mechanical work potential loss coefficient defined here is analogous to the total pressure loss coefficient but additionally takes account of the absolute pressure differences that arise.

Equation (5.26) is derived to show this comparison. Furthermore is allows measurements of the total pressure loss coefficient through a cascade to be interpreted in terms of the loss of potential work from the machine as a whole. The mass averaged mechanical work potential loss and total pressure loss are shown in fig. 5.13. It can be seen in fig. 5.13 that both the pressure loss and mechanical work potential loss show very similar trends ,as expected, although there is a slight quantitative difference. For both loss definitions shown here, the reference planes are taken as 0.3 chord up-stream and 0.1 chord down-stream, further more the reference pressure used for the calculation of the mechanical work potential is taken as the inlet total pressure. This reference pressure is chosen as it removes any ambiguity in comparing different cases which may have pressure ratios very close to unity when the reference pressure is the inlet static pressure.

A further comparison is made by applying eq. (5.26) to the loss coefficients. fig. 5.14 shows the total pressure loss calculated from the statistical data and that calculated from the mechanical work potential loss. While fig. 5.15 shows the mechanical work potential loss calculated from the statistical data and from the pressure loss. It is seen in both cases that the result is essentially the loss calculated from the original metric. This is a result of using the total pressure as the reference for the calculation of the mechanical work potential loss.

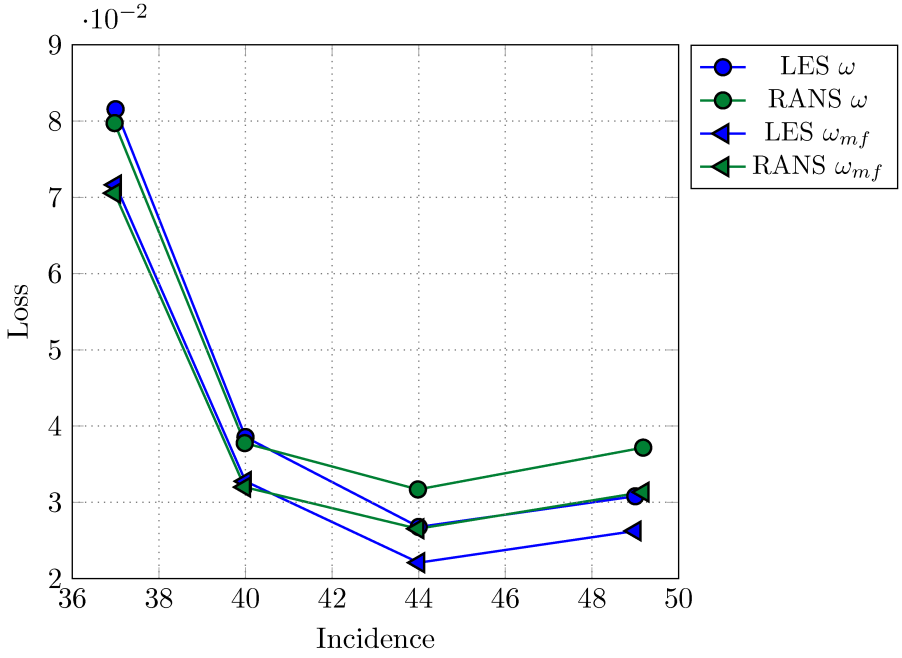

Figure 5.13: Mechanical work potential loss and mass averaged pressure loss for off-design incident cases. Showing RANS and LES.

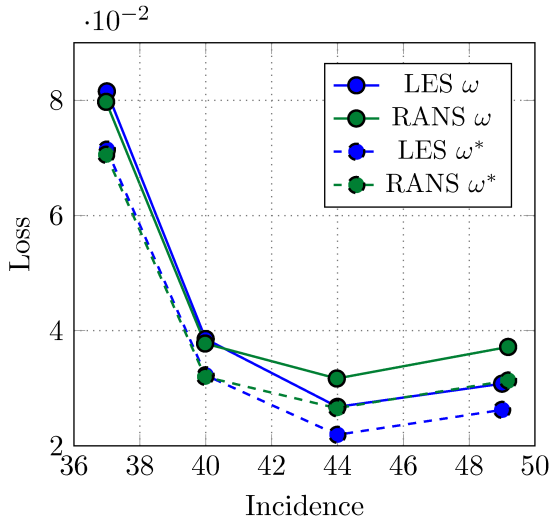

Figure 5.14: Mass averaged pressure loss and pressure loss (*) calculated from mechanical work potential loss using eq. (5.26).

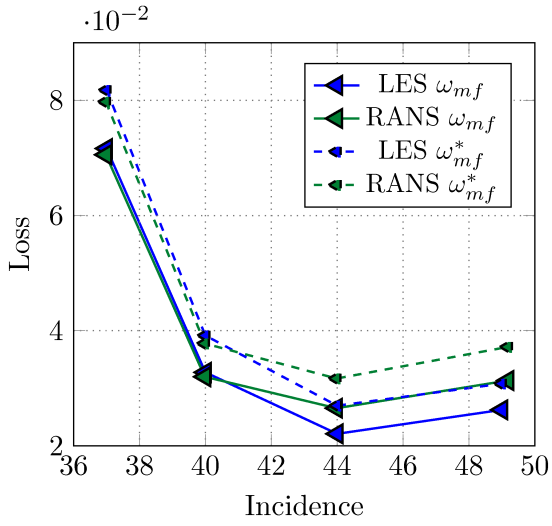

Figure 5.15: Mechanical work potential loss and mechanical work potential loss (*) calculated from pressure loss using eq. (5.26).

5.7 Off-design Incidence Loss Bucket

Applying the mechanical work potential analysis to the incidence loss bucket simulations allows a further breakdown of the loss mechanisms involved. This expands on the analysis performed using the Denton loss breakdown. By applying the mechanical work potential budget the same breakdown between the pressure and suction surfaces as well as the channel can be performed. This allows the loss to be associated with different processes meaning further parallels and deeper understanding of the processes involved can be gained.

The study of the incident loss bucket is performed looking at the integral values. This enables the assigning of loss of mechanical work potential to an area such as the suction surface boundary layer. However, before looking at the integral breakdown the mechanical work potential budgets of three profiles extracted at different locations are presented.

5.7.1 Local Profiles

The profiles show the breakdown of mechanical work potential across the suction surface, pressure surface and the reference wake plane. The suction and pressure surface wall normal profiles are taken at a stream-wise position of 0.8 chord and are shown in fig. 5.16, while the wake profile is taken at 1.1 chord and shown in fig. 5.17.

The budgets clearly show the large viscous dissipation and shear work contribution to changes in mechanical work potential for both the boundary layers and the wake. However, in the boundary layers there is limited viscous reheating which is clearly present in the wake plane, due to the increased pressure at this station. The boundary layers also show the shift in losses from pressure surface to suction surface as incidence is increased though, interestingly there is still substantial viscous dissipation in the near wall region of the suction surface at 37°, generated by the turbulent boundary layer although the maximum is seen to migrate away from the wall at 49° where the boundary layer is near separation at this chord position. The wake profiles are dominated by viscous dissipation though due to the increased pressure at this location in the domain there is a noticeable amount of viscous reheat, clearest at 49° where the viscous reheat is the second largest value concentrated around the shear layer where the two boundary layers meet.

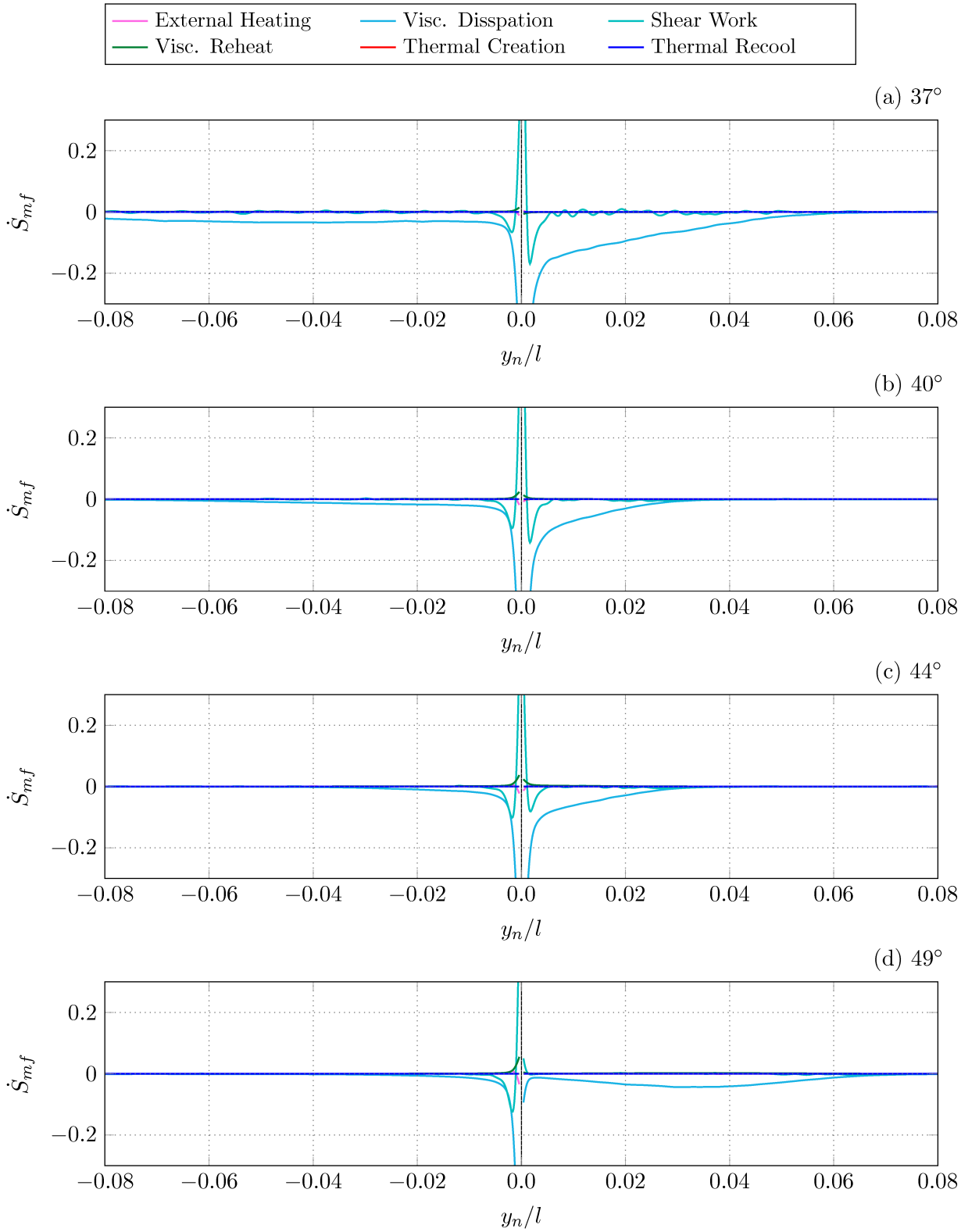

Figure 5.16: Wall normal profiles at 80% chord for the suction surface (+ve) and the pressure surface (-ve) showing the mechanical work potential budget breakdown for the 37°, 40°, 44° and 49° off-design cases from top to bottom respectively.

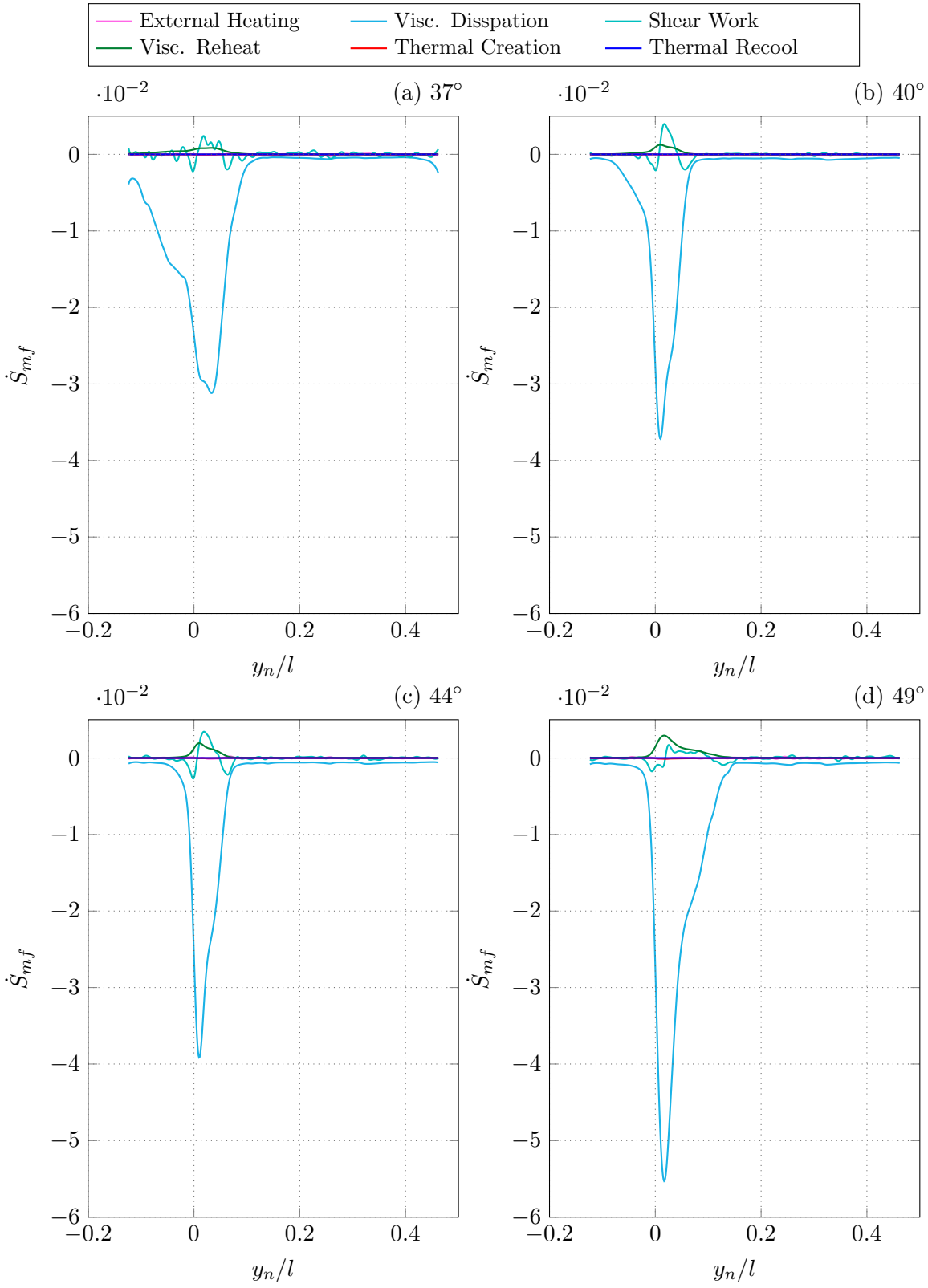

Figure 5.17: Wake profile at 10% chord down-stream showing mechanical work potential budget breakdown for the off-design cases at 37°, 40°, 44° and 49° from top to bottom respectively. Pressure surfaces is negative

5.7.2 Volume Breakdown

By separating the flow domain into several different areas the integral change of various process can be attributed to different areas and different processes. The domain is separated into four different areas. The areas chosen are the two boundary layers, the inlet and blade passage (up to the trailing edge), and exit and wake. The separation is done based on the boundary layer edge using the vorticity limit defined previously. The boundary layers are separated into suction and pressure surfaces and the channel section is defined as the remaining area up to the trailing edge in the stream-wise direction. The wake section is defined by a pitchwise line at the trailing edge to the domain exit. A schematic of the volumes is shown in fig. 5.18.

The vorticity limit to determine the boundary layer edge is defined in chapter 3 section 3.4.

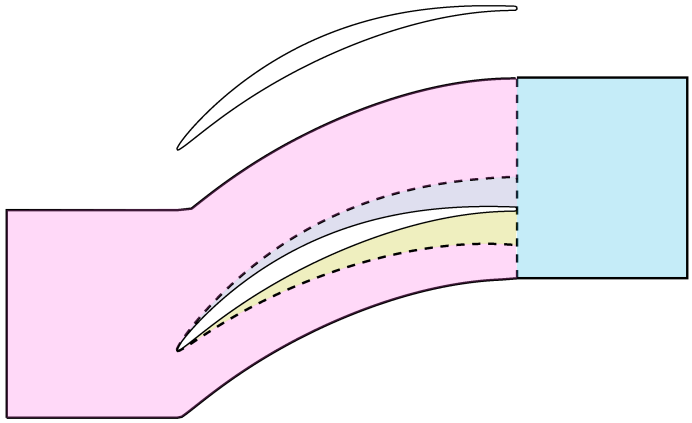

Figure 5.18: Schematic outline showing representative volumes for volume breakdown.

In order to make the integral volumes comparable the mechanical work potential is mass averaged and scaled with the inlet dynamic pressure, as is done with the mechanical work potential loss coefficient definition ω_{m_f}.

A comparison of the calculated boundary layer volumes is shown in fig. 5.19. This shows the outline of the boundary layers for each incidence. It shows how the volume of the boundary layers changes as incidence varies.

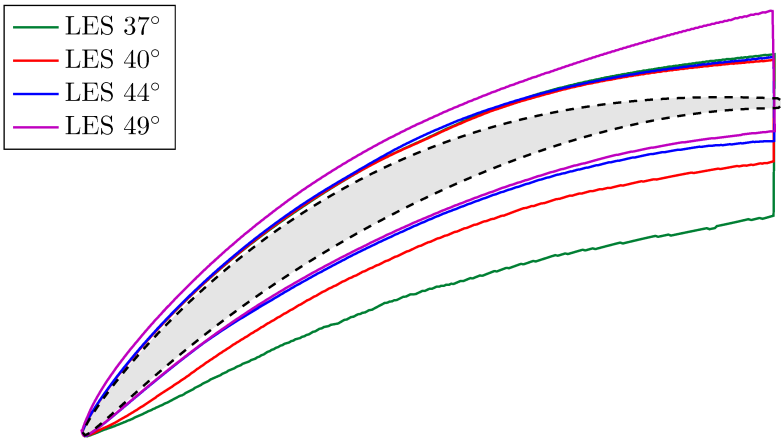

Figure 5.19: Control volume outlines for boundary layer volumes extracted for the mechanical work potential analysis.

5.7.3 Volume Breakdown Results

The areas outlined in fig. 5.18 are integrated and the relative contributions to the mechanical work potential budget compared. The analysis focuses on presenting the changes in mechanical work potential from the various processes described in section 5.2.0.1 and weighing their overall contributions. Each term is normalised by the inlet dynamic pressure, as mentioned, allowing a comparison across the different cases to be made.

The results start with the relative total contributions shown in the bar graphs of figs. 5.20 to 5.24. Followed by the percentage breakdown, similar to that performed for the Denton loss breakdown analysis.

The total loss of mechanical work potential for the full volume outlined in fig. 5.18 is shown in fig. 5.20. Here it is seen that the majority of loss results from viscous dissipation as expected. The full flow field integral also shows the effect of viscous reheat, which is the second most relevant term. It can be seen that the viscous reheat results in further losses at low incidence but starts to result in work potential recovery as the incidence is increased. This is a result of the pressure rise in the higher incidence cases being more substantial. The increase in pressure means that any viscous heating that occurs at this higher pressure (relative to the reference) results in work potential creation.

The remainder of the terms in the work potential budget do not result in any substantial changes in the work potential.

Looking at the breakdown of the various sub volumes gives a better understanding of where the loss processes occur and what might be driving them can be gained. Starting with the suction and pressure surfaces, shown in fig. 5.22 and fig. 5.21 respectively.

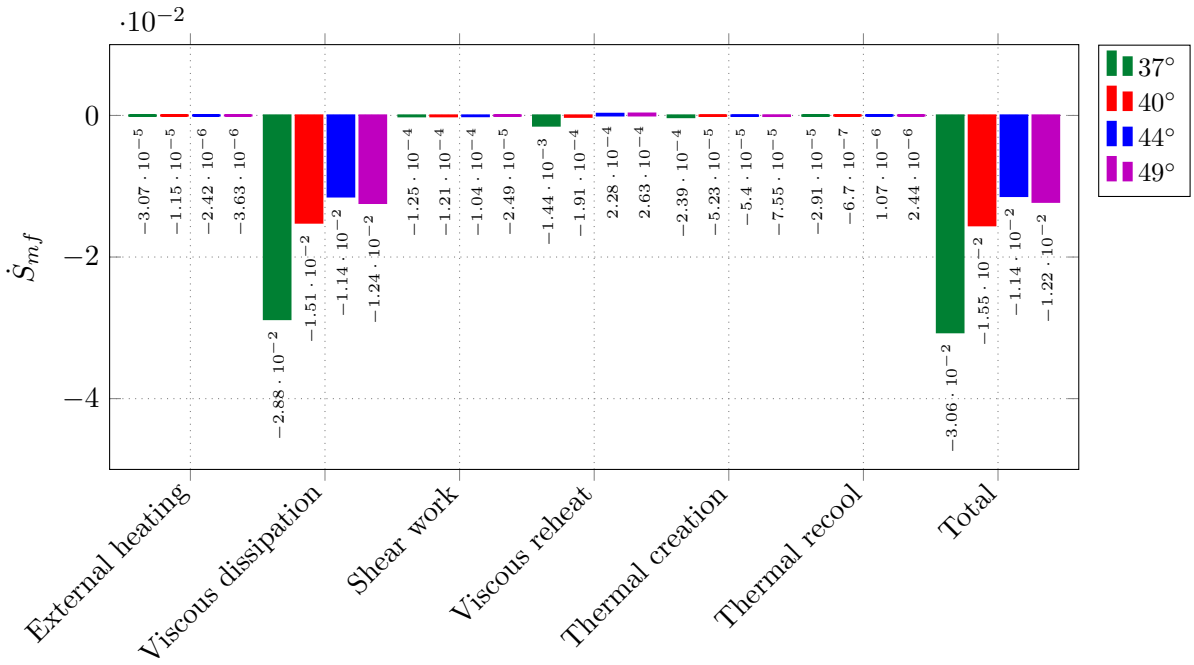

Figure 5.20: Full integral mechanical work potential budget for incident loss bucket cascade at Reynolds 300K and Mach 0.67. Integral is from x/l=-0.15 to x/l = 1.2 from the leading edge.

It can be seen in these two figures that again viscous dissipation is the main factor causing loss, and that it is a relatively large proportion of the total. This is expected from the volumes containing the boundary layers. It is again noted that the viscous reheat plays an interesting role on the pressure surface as the incidence is varied, changing from negative to positive as the incidence is increased. However, on the suction surface the viscous reheat does not result in any recaptured work potential regardless of incidence. In general though the relative size of the viscous reheat for the boundary layer volumes is not as substantial compared with the other terms meaning that the viscus reheat recovery of the total domain occurs more broadly. In fact it is seen that for the suction surface the shear work term is more relevant, and results in more loss of the mechanical work potential.

The volume breakdown of the channel and wake regions account for a much smaller proportion of the total losses. This again is somewhat expected.

For the wake region the viscous dissipation is highest again resulting from the mixing out of the wake. The wake region extends up to the trailing edge of the blade. So the extent of viscous dissipation is understandable given that there is still some forcing of the fluid from the included trailing edge and not just mixing out of the already formed wake. The other terms of the mechanical work potential budget are again very small in comparison though there are now several terms predicting work recovery. This mechanical work potential recovery is not surprising in the wake region as the average pressure for the wake is higher than the reference pressure at the inlet. Because of this there is expected work recovery from a compressor stage

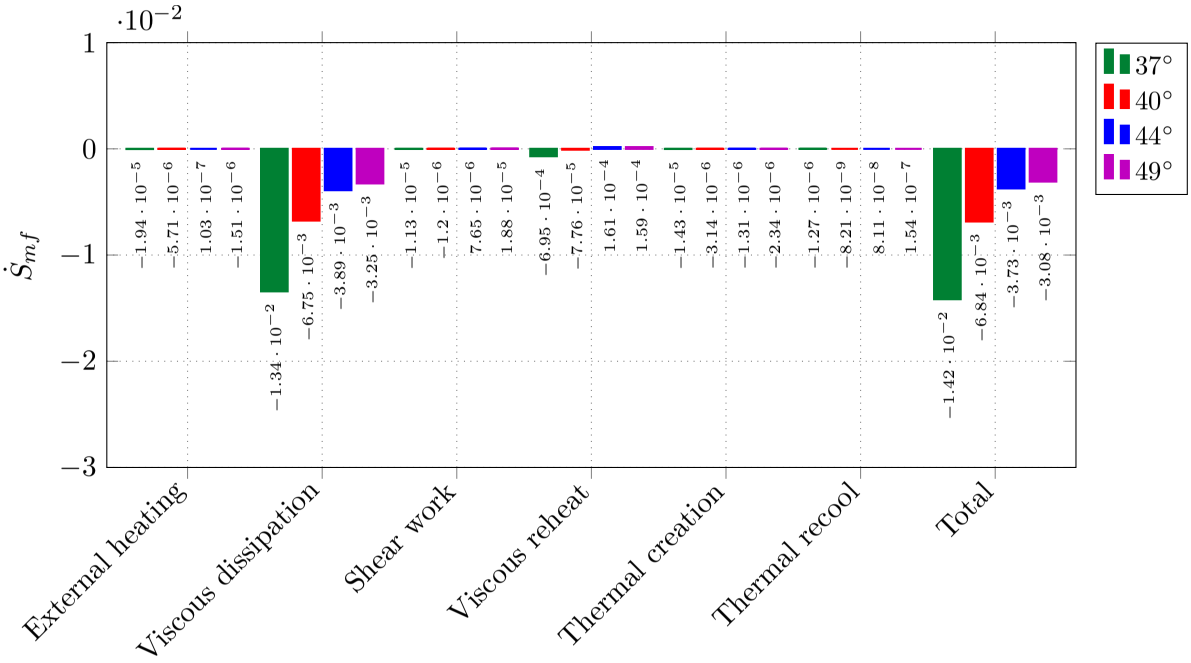

Figure 5.21: Pressure surface boundary layer integral mechanical work potential budget for incident loss bucket cascade at Reynolds 300K and Mach 0.67.

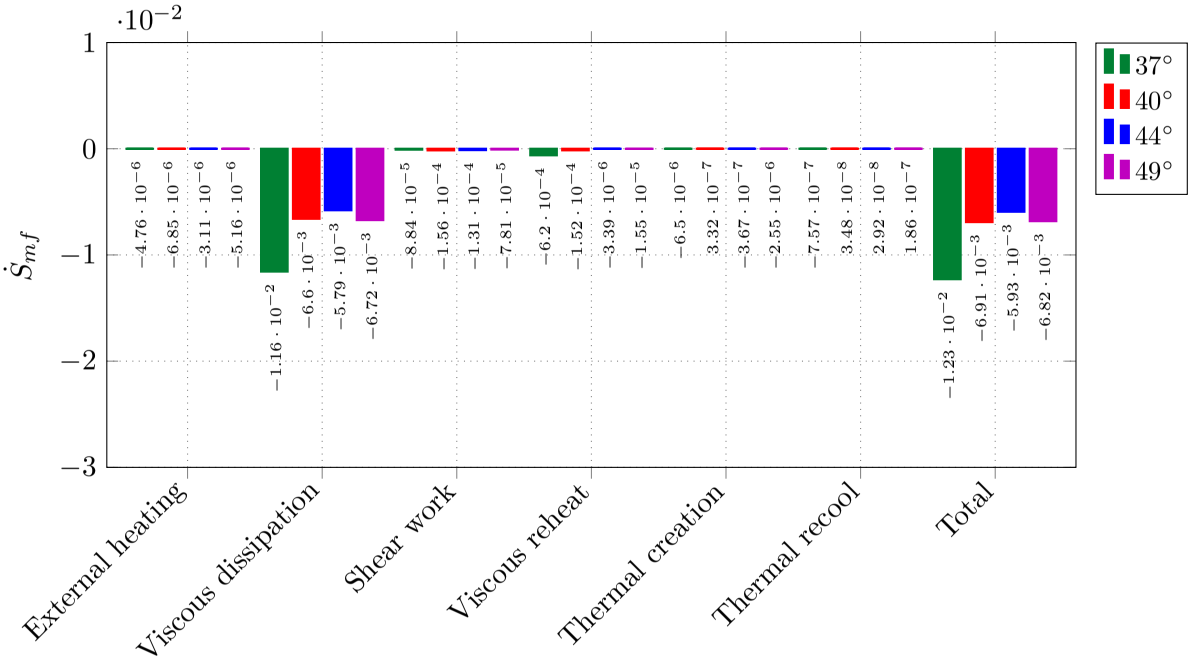

Figure 5.22: Suction surface boundary layer integral mechanical work potential budget for incident loss bucket cascade at Reynolds 300K and Mach 0.67.

with a high pressure ratio, as thermal creation or heat transport in the wake region occurs at a pressure higher than the reference.

In the channel region similar processes occur as in the wake region, though here there is greater viscous dissipation due to the shear work done on the free-stream turbulence. However, the pressure rise seen in the channel is such that the overall volume predicts some slight recovery from the viscous reheat, shear work and thermal re-cool.

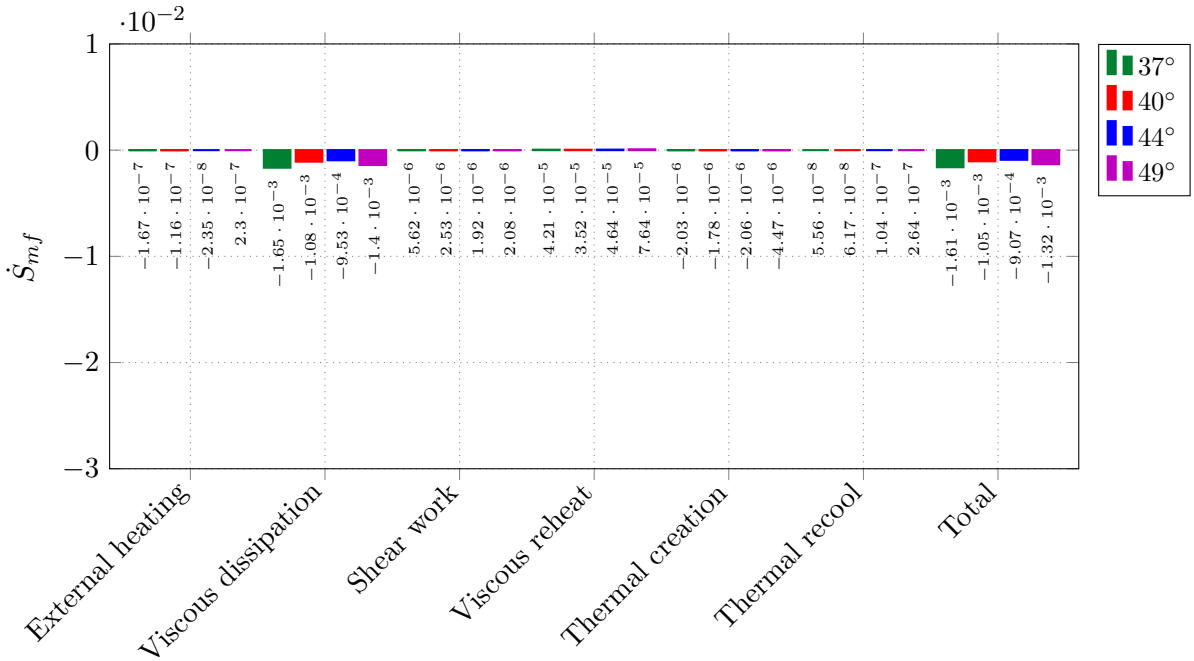

Figure 5.23: Wake region integral mechanical work potential budget for incident loss bucket cascade at Reynolds 300K and Mach 0.67.

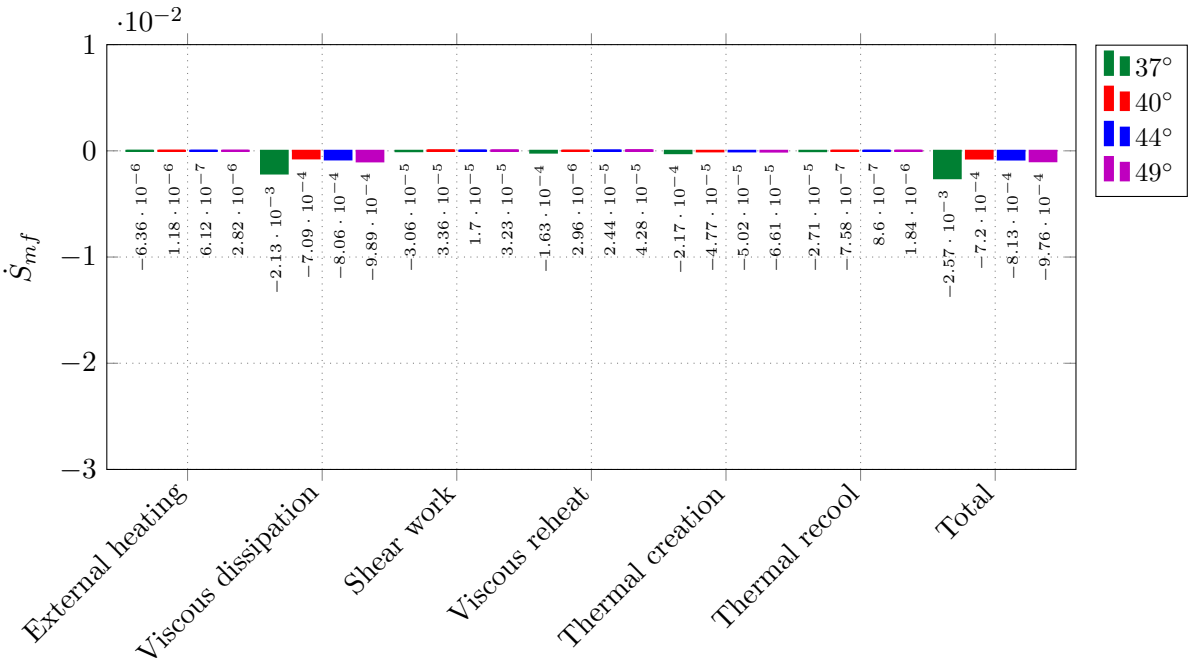

Figure 5.24: Channel and inlet region integral mechanical work potential budget for incident loss bucket cascade at Reynolds 300K and Mach 0.67.

5.7.4 Volume Percentage Breakdown

If the various integral quantities from the volume breakdown are now given as a relative percentage of the full volume, a comparison can be made as to how incidence affects where the majority of loss occurs.

This percentage breakdown is given in fig. 5.25. Here the total change in mechanical work potential for each volume is presented as a percentage of the whole. It can be immediately seen that the suction and pressure surface volumes account for the majority of loss, roughly 80% for all incidences. It is also clear how the main source of loss changes from the pressure surface to the suction surface as incidence is increased. This is something already seen in the Denton loss breakdown and will be discussed shortly. The contribution from the wake and channel regions are substantially lower though the contribution is not negligible. It is seen that there is a slight rise in the relative loss contribution from the wake as the incidence is increased despite there being some work potential recovery seen in the volume breakdown in fig. 5.23. The relative reduction in loss produced by the boundary layers see the wake and channel volumes contribute a slight higher percentage to the over all. Despite their actual contribution being quite constant for the higher incidence cases as seen in the volume breakdowns.

A further thing to note from the percentage breakdown is that the contributions from both the suction and pressure surfaces are equal at the defined nominal incidence of 40°, which also results in a minimum contribution from the channel region. Possibly resulting from the fact

that there is minimal biasing in the loading of either surface of the blade, meaning that the pressure distribution across the channel is the most uniform which also results in less shearing of the free-stream turbulence.

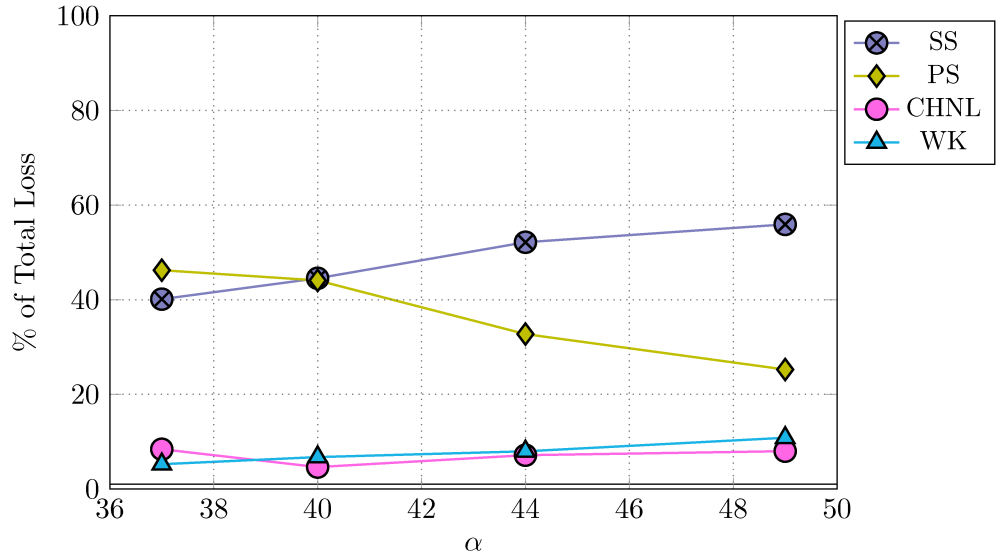

Figure 5.25: Percentage breakdown of total mechanical work potential loss for the various domains defined.

5.7.5 Denton Loss and Mechanical Work Loss Comparison

Following the percentage breakdown of the mechanical work potential analysis it is interesting to look at how this compares with the Denton loss breakdown. In the Denton loss breakdown the analysis tries to associate all the loss with the boundary layers. Which in principle is a logical assumption as the boundary layers will be the main source of loss in a stage. However, following the mechanical work potential analysis it is seen that under certain conditions, such as in the presence of free-stream turbulence or at off-design incidence, the loss contributions from the free-stream can be relevant. Furthermore the assumption that flow at the trailing edge pitchwise plane is uniform, as defined in the Denton breakdown, maybe a further over simplification at off-design conditions. The mechanical work potential analysis shows the general weighting of loss production is captured with both the Denton loss analysis and the mechanical work potential loss but the emphasis put on the boundary layers by the Denton breakdown might be slightly misleading.

The comparison of the percentage breakdown from both the Denton and mechanical work potential analysis is shown in fig. 5.26. Starting with the boundary layers it is seen that both the mechanical work potential and Denton capture the shift in the main source of loss from pressure surface to suction surface as the incidence is increased. The general trend of the change is also captured in both although the Denton breakdown shows a much greater rate of change. What is

seen in this case is that the main loss contribution switches quite dramatically from one surface to another as incidence is varied. At low incidence the pressure surface accounts for $\approx 70\%$ of the loss but this rapidly drops to almost nothing as the incidence is changed to 49°. This increased rate of change suggests that the main contribution of loss can be associated with a single boundary layer at off-design incidence.

However, when comparing this with the mechanical work potential analysis the variation of loss contribution is not quit so pronounced. In this case the shift in the main loss source from pressure surface to suction surface is still seen as the incidence is increased but the pressure surface still contributes a substantial proportion of loss at high incidence not the negligible amount predicted by the Denton breakdown.

It should be noted that the direct comparison between the Denton loss breakdown and the mechanical work potential loss breakdown is not completely rigorous. For example the mechanical work potential channel loss should be included in the boundary layer loss in order to mimic the Denton loss which would increase the rate of change of the boundary layer loss from the mechanical work potential. However, including the channel loss in the boundary layer loss still results in a lower relative boundary layer contributions and a little more would be needed when interpreting the flow physics and reasons for differences.

The comparison of the wake and pressure loss from the mechanical work potential and Denton loss respectively requires a little more care when interpreting the difference as the mechanical work potential includes the mixing out of the wakes while the Denton loss tends to attribute some of that loss to the boundary layers as well. Although the volume from the mechanical work potential and the defined foot print of the Denton analysis try to capture the same region. That being the loss resulting from the trailing edge itself, the Denton loss translates this into an effective pressure drop ignoring the viscous forcing that occurs while the mechanical work potential incorporates all processes that take place at the trailing edge.

This results in a slight difference between the two because the Denton pressure loss is associated with the loss from the low pressure at the trailing edge while the mechanical work potential loss is associated with the loss at the trailing edge from mixing out of the wake. The comparison of the wake and pressure loss is reasonable with both methods showing the same trend, an increase in the trailing edge loss as the incidence is increased. However, it is seen that the Denton loss predicts a lower relative contribution compared with the mechanical work potential. This is likely attributed to the slightly arbitrarily definition of the Denton pressure loss as an average pressure acting over an area defined as the "blunt" section of the trailing edge, making the effective area of the trailing edge hard to define.

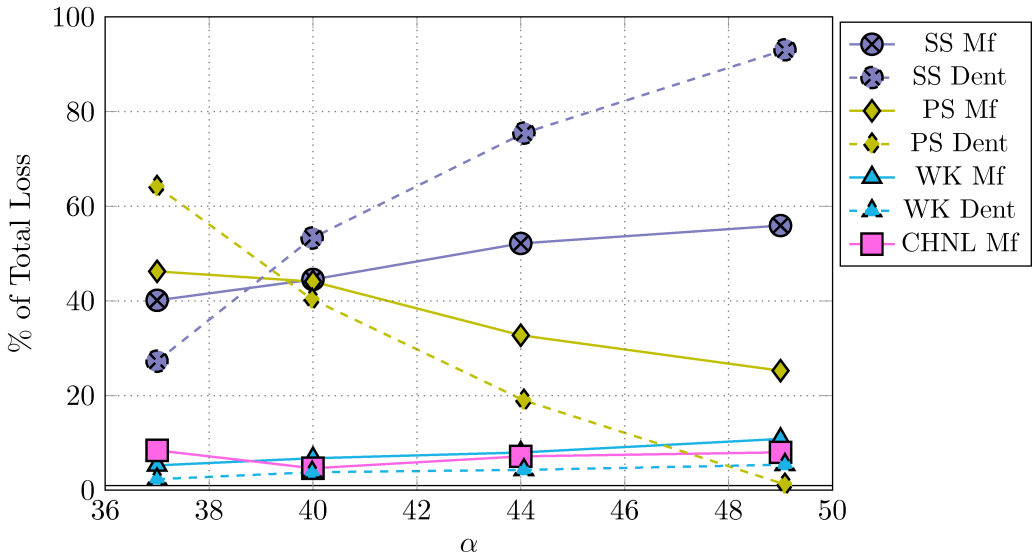

Figure 5.26: Percentage breakdown comparison between the Denton loss analysis and the mechanical work potential. The breakdown shows total loss contribution from each region.

5.7.6 Tabulated Volume Breakdown

The full breakdown of all the source terms in the mechanical work potential are provided in table 5.2. These are included for completeness and to show clearly through which processes loss is generated.

Table 5.2: Tabulated loss breakdown for incidences 37°, 40°, 44° and 49°. Showing percentage loss contribution from suction surface, pressure surface, wake , channel and the full field for each term of the mechanical work potential.

Case	37°				
	Suction Surface	Pressure Surface	Channel	Wake	Full Field
External heating	0.0155	0.0635	0.0208	0.0005	0.1003
Viscous dissipation	37.7698	43.8141	6.9585	5.3949	93.9289
Shear work	0.2886	0.037	0.0998	-0.0183	0.4071
Viscous reheat	2.0239	2.2688	0.532	-0.1374	4.687
Thermal creation	0.0212	0.0467	0.7071	0.0066	0.7817
Thermal recool	0.0025	0.0041	0.0885	-0.0002	0.095
Total	40.1215	46.2342	8.4068	5.2461	100.0
Case	40°				
	Suction Surface	Pressure Surface	Channel	Wake	Full Field
External heating	0.0442	0.0368	-0.0076	0.0007	0.0741
Viscous dissipation	42.5053	43.5155	4.5692	6.9831	97.5742
Shear work	1.0038	0.0077	-0.2165	-0.0163	0.7788
Viscous reheat	0.9773	0.5001	-0.0191	-0.2268	1.2316
Thermal creation	-0.0021	0.0202	0.3074	0.0115	0.337
Thermal recool	-0.0002	0.0001	0.0049	-0.0004	0.0043
Total	44.5282	44.0804	4.6384	6.7519	100.0
Case	44°				
	Suction Surface	Pressure Surface	Channel	Wake	Full Field
External heating	0.0273	-0.0009	-0.0054	0.0002	0.0213
Viscous dissipation	50.9312	34.2124	7.084	8.3757	100.6035
Shear work	1.1513	-0.0672	-0.1493	-0.0169	0.918
Viscous reheat	0.0298	-1.4154	-0.2145	-0.4076	-2.0076
Thermal creation	0.0032	0.0115	0.4414	0.0181	0.4743
Thermal recool	-0.0003	-0.0007	-0.0076	-0.0009	-0.0094
Total	52.1426	32.7398	7.1487	7.9686	100.0
Case	49°				
	Suction Surface	Pressure Surface	Channel	Wake	Full Field
External heating	0.0423	0.0124	-0.0231	-0.0019	0.0297
Viscous dissipation	55.0895	26.68	8.1105	11.4447	101.3244
Shear work	0.64	-0.1545	-0.2648	-0.017	0.2037
Viscous reheat	0.1267	-1.3061	-0.3511	-0.626	-2.1565
Thermal creation	0.0209	0.0192	0.5419	0.0366	0.6187
Thermal recool	-0.0015	-0.0013	-0.0151	-0.0022	-0.02
Total	55.9179	25.2498	7.9984	10.8342	100.0

5.8 Discrete Disturbances

The analysis is now extended to look at the effects of discrete disturbances on the availability of mechanical work potential. The discrete wake disturbances or moving bar cases are a set of cases looking at the influence free-stream wakes have on the blade loading and loss generation. A set of two cases were run with different reduced frequencies one non-representative and one representative of real engine conditions.

The mechanical work potential analysis of the wake cases follows the same outline as the off-design incidence analysis. The mechanical loss budgets at the same three locations are presented first followed with the mechanical work potential loss and then the volume breakdown is applied and the loss of mechanical work potential from the various sections is compared and discussed.

A further case is introduced, this being the base case at 44° with no introduced background turbulence. This case is introduced to aid the comparison between the off-design incidence cases specifically the 44° case, and the bar cases. In the figures the off-design case is labelled as LES 44°. While the base case is referred to as the base case only.

5.8.1 Local Profiles

The budgets for the wall normal profiles at 80% chord are presented in fig. 5.27 and the wake profile budgets in fig. 5.28. Given that the cases are all run at the same angle of 44° apart from the 3 Bar case that was run at a slightly lower incidence of 43°, the boundary layer budgets show very limited difference in the near wall region. There are minor differences further from the wall where the changes in the free-stream affect the boundary layer more, here it can be seen that the viscous dissipation has a slightly different shape on the suction surface for the 1 Bar and LES 44° cases compared with the 3 Bar and Base cases. The difference resulting from the energisation of the boundary layers by the free-stream disturbances. This also occurs in the 3 Bar case but the forcing is large enough that the effect reaches the wall, resulting in a profile similar to that of the Base case.

The wake profiles are shown in fig. 5.28. Again due to the same inflow angle the profiles are very similar though there is a noticeable difference in the magnitude of viscus dissipation in the wake for the difference cases. Furthermore, the free-stream shows substantially larger amounts of viscus dissipation in 3 Bar and LES 44° cases due to the free-stream disturbances. There is also some free-stream viscous dissipation for the 1 Bar case but this is substantially lower in the statistical results. The wake also shows a reasonable amount of viscous reheat similar to the off-design cases, again due to the higher pressure in this region of the domain.

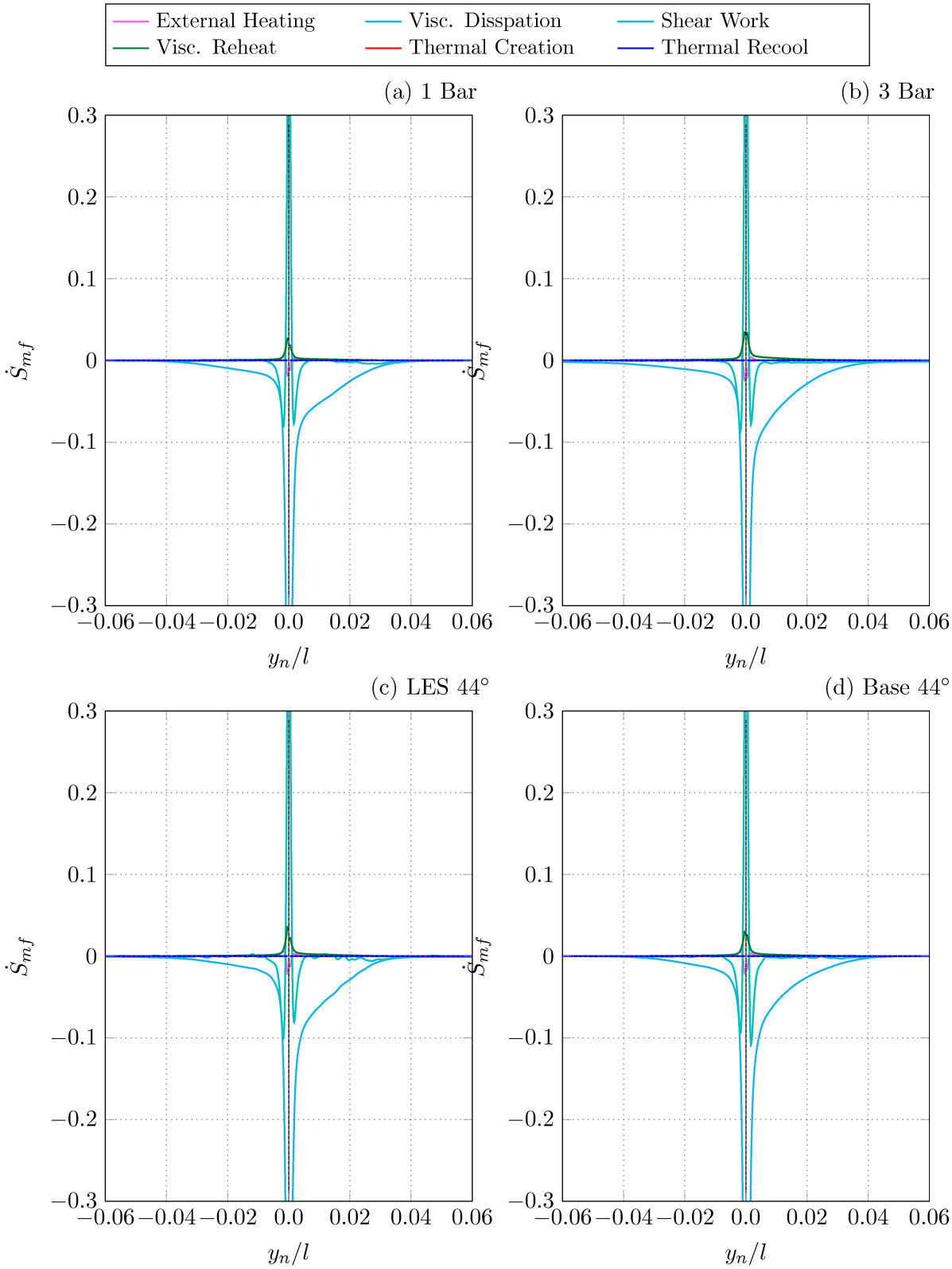

Figure 5.27: Wall normal profiles at 80% chord for the suction surface (+ve) and pressure surface (-ve) showing the mechanical work potential budget breakdown. Profiles are for the 1 Bar, 3 Bar, turbulent 44° case and base case from left to right and top to bottom respectively.

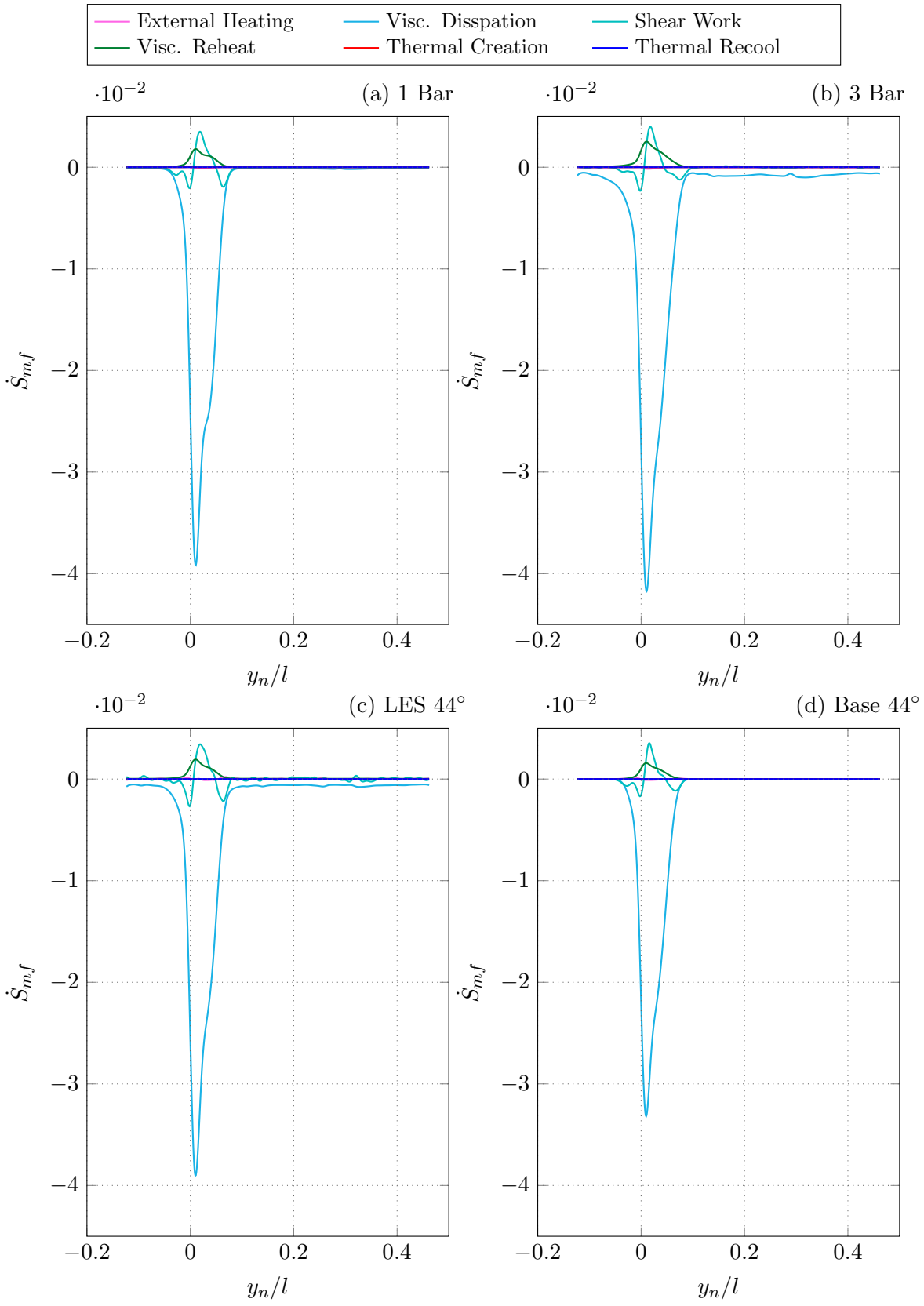

Figure 5.28: Wake profile at 10% chord down-stream for the 1 Bar 3 Bar turbulent 44° case and base case from left to right and top to bottom respectively, showing mechanical work potential budget breakdown. Pressure surfaces is negative

5.8.2 Mechanical Work Loss

The mechanical work potential loss is calculated for the wake cases using eq. (5.13) and is presented in fig. 5.29. It is seen in the figure that loss prediction for the moving bar cases is lower than that for the case with free-stream turbulence. The comparison between the mechanical work potential loss and pressure loss for these cases is also closer. Although the pressure loss is slightly higher again, similar to that seen for the off-design cases.

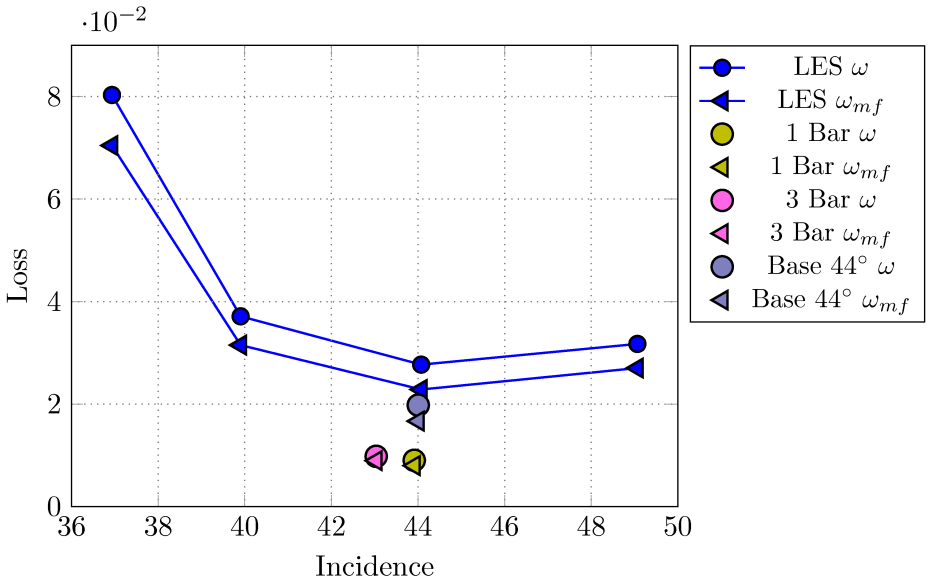

Figure 5.29: Comparison of Mechanical work loss and total pressure loss for wake cases. Including total pressure loss for incidence cases and base 44° case.

5.8.3 Volume Breakdown

For the moving bar cases the domain is broken down into the same areas defined for the off-design cases. These areas are shown in fig. 5.18. The method of defining these volumes is the same as that used for the off-design cases and is outlined in section 5.7.2. The calculated boundary layer edges for the moving bar, 44° off-design and base cases are shown in fig. 5.30.

The domains are broken down into the inlet and channel region (up to the trailing edge), the pressure surface and suction surface boundary layers and the wake region (extending from the tailing edge down-stream). The inlet and wake regions do not extend to the simulation domain boundaries to avoid any unnatural effects from boundary conditions.

From the results of the volume breakdown, the relative contributions of each term and how they affect the mechanical work potential can be examined. The total change of each term in the mechanical work potential budget is presented in fig. 5.31. This shows the most dominant terms and the effects they have. Most obvious is the viscous dissipation, again as expected for a non

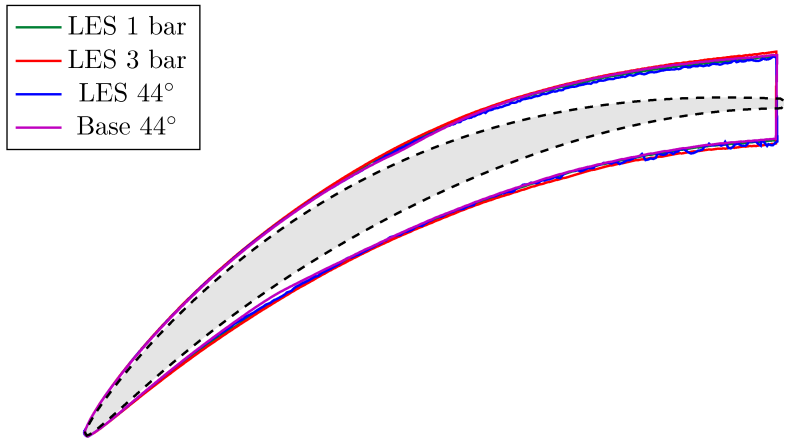

Figure 5.30: Control volume outlines of boundary layer volumes extracted for the mechanical work potential analysis. For 1 bar, 3 bar, 44° Incidence case and 44° Base case.

cooled blade, which accounts for almost all of the loss in mechanical work potential. There is however a slight recovery from the viscous reheat, which is strongest for the 3 bar case. This case produces the most dissipation so it makes sense that it also shows the greatest recovery as the greatest viscous heating occurs. To understand the processes a little more the mechanical work potential budget for each of the defined volumes is given in figs. 5.32 to 5.35 for the pressure surface, suction surface, wake and channel respectively.

The breakdown of the mechanical work potential budget for the different areas shows very similar trend to the full domain, though there is some variation in the relative magnitudes. It is immediately clear that the viscous dissipation is the most predominant process for all the areas, thought the relative viscous reheat recovery changes, as well as some of the other processes. Which also provide some recovery in some areas. The recovery again depends on the relative pressure ratio to the reference pressure. This means that processes nearer the trailing edge and wake region are more likely to create mechanical work potential as the pressure is generally higher.

The breakdown for the pressure and suction boundary layers are shown in figs. 5.32 and 5.33, it is seen that at this incidence the rate of viscous dissipation is roughly similar for both surfaces with the suction surface slightly higher. It is also seen that the moving bar cases result in a lower loss compared with the incidence case with free-stream turbulence. Furthermore it is clearly seen that the 1 bar case has lower boundary layer loss compared with the base case without any free-stream disturbance. It is suggested that the the periodic forcing of the boundary layer results in a decrease in the boundary layer loss due to the wake calming effect following the wake passing. Which is not prevalent on the pressure surface though there is some viscous reheat recovery for all the cases with the three bar case seeing a slight higher return. For the suction surface however this is not the case with only the three bar case having a positive viscous reheat. The change in behaviour of the suction surface for the three bar case is attributed to the very shallow wake

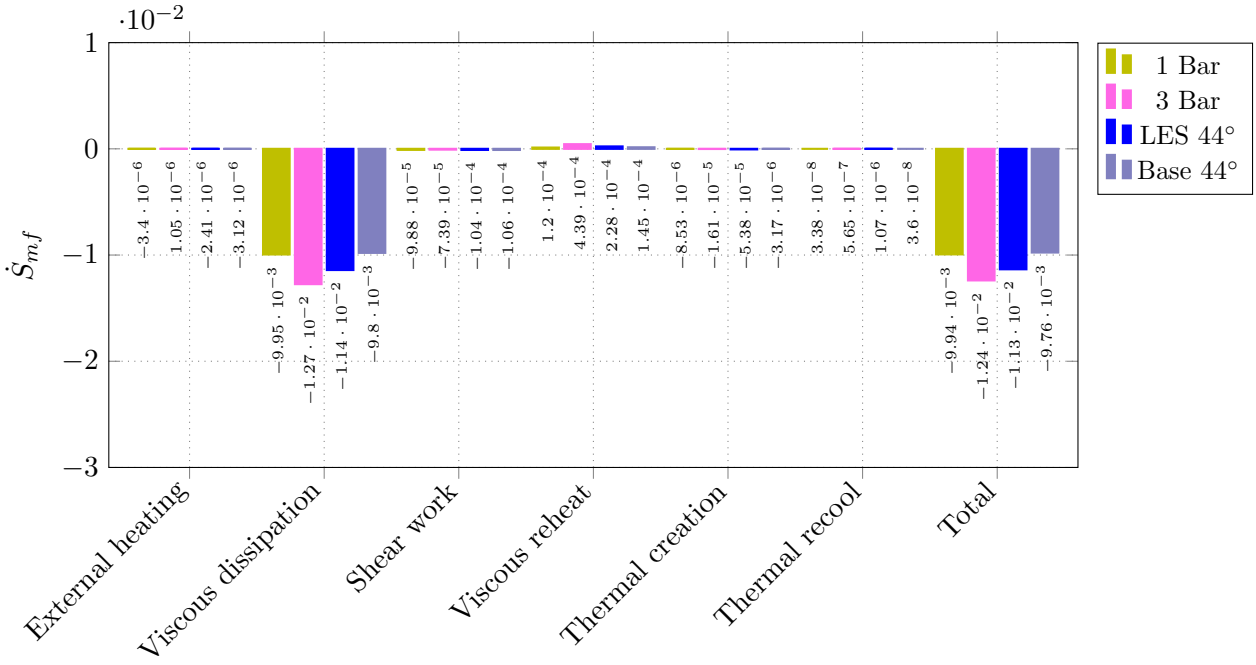

Figure 5.31: Full integral of mechanical work potential budget for moving bar cases, including 44° case from incidence loss bucket and 44° base case at Reynolds 300K and Mach 0.67. Integral is from x/l=-0.15 to x/l = 1.2 from the leading edge.

path. This results in a very large wake foot travelling slower than the free-stream, resulting in a higher pressure on the suction surface and the associated increase in viscous dissipation from the wake boundary layer interaction.

The wake region, shown in fig. 5.34, shows a similar trend to that of the off-design case. With the majority of change attributed to viscous dissipation, again associated with the trailing edge which is included in the volume breakdown. However, the amount of viscous dissipation is small, and in general the wake region sees some mechanical work potential recovery due to the pressure being higher than the reference at the inlet.

The channel volume breakdown, fig. 5.35, is again dominated by viscous dissipation though here there is a strong bias to the three bar case. Where the shallow wake path angle and low reduced frequency result in a very high relative turbulence intensity. The one bar case and off-design case show similar amounts of viscous dissipation while the base case shows nearly none. This correlates well with the relative amounts of turbulence in the channel region for all the cases.

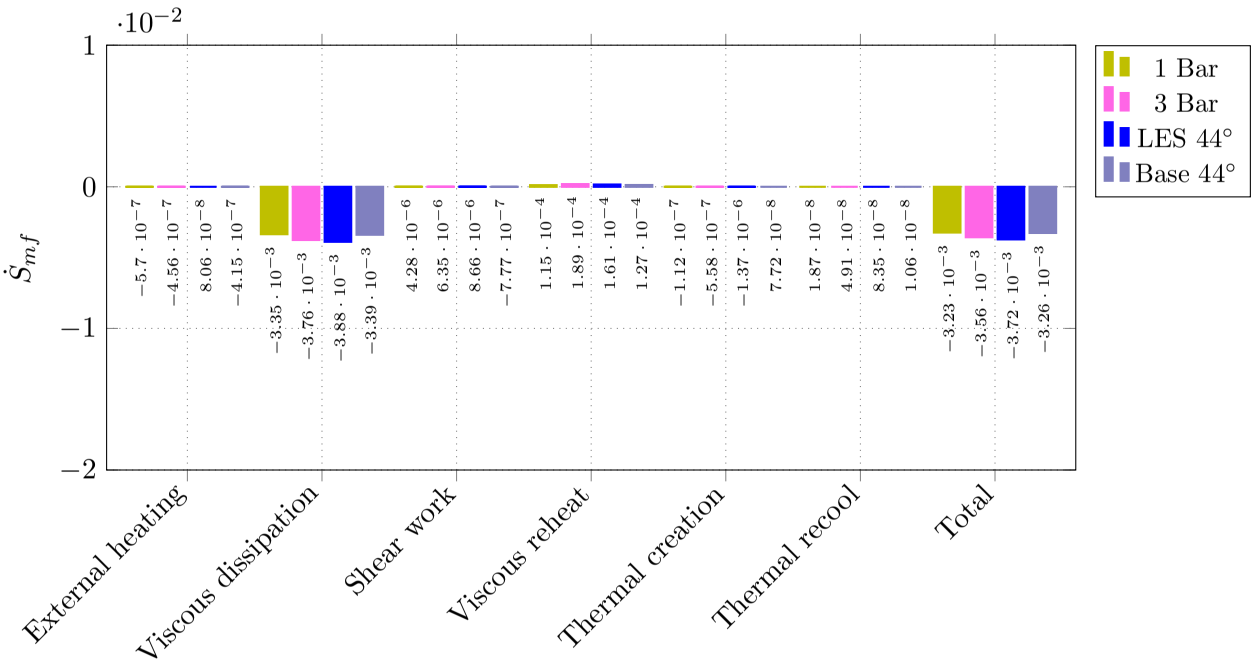

Figure 5.32: Pressure surface integral of mechanical work potential budget for moving bar cases, including 44° case from incidence loss bucket and 44° base case at Reynolds 300K and Mach 0.67.

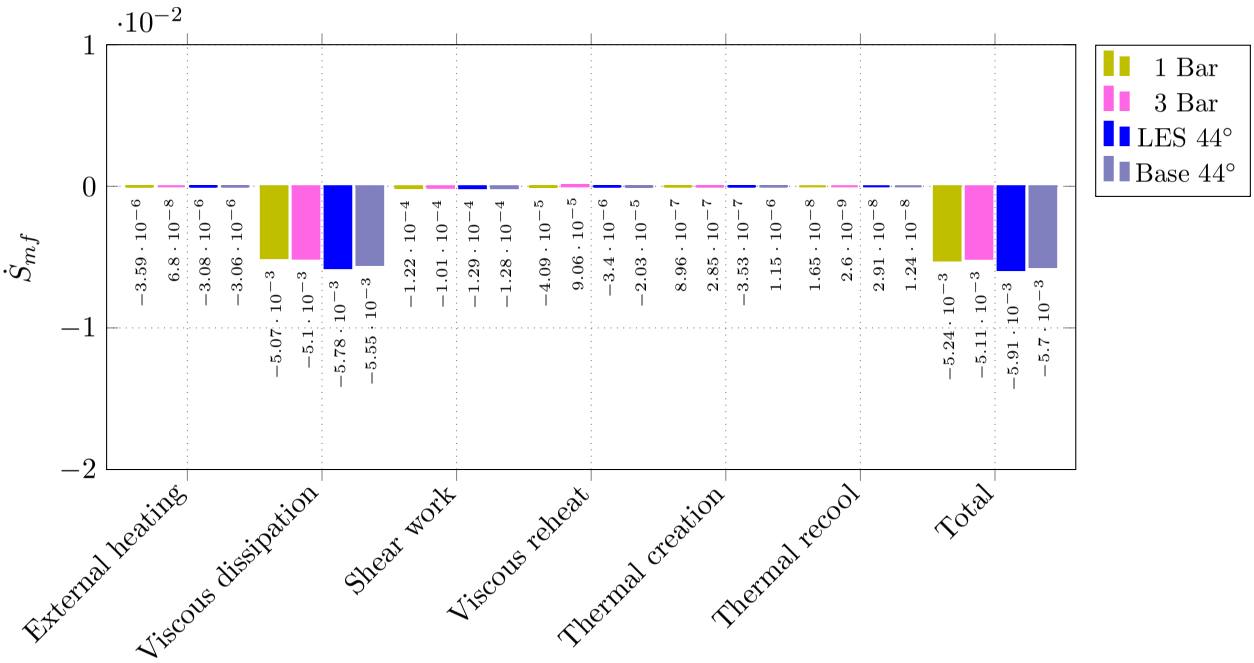

Figure 5.33: Suction surface of integral mechanical work potential budget for moving bar cases, including 44° case from incidence loss bucket and 44° base case at Reynolds 300K and Mach 0.67.

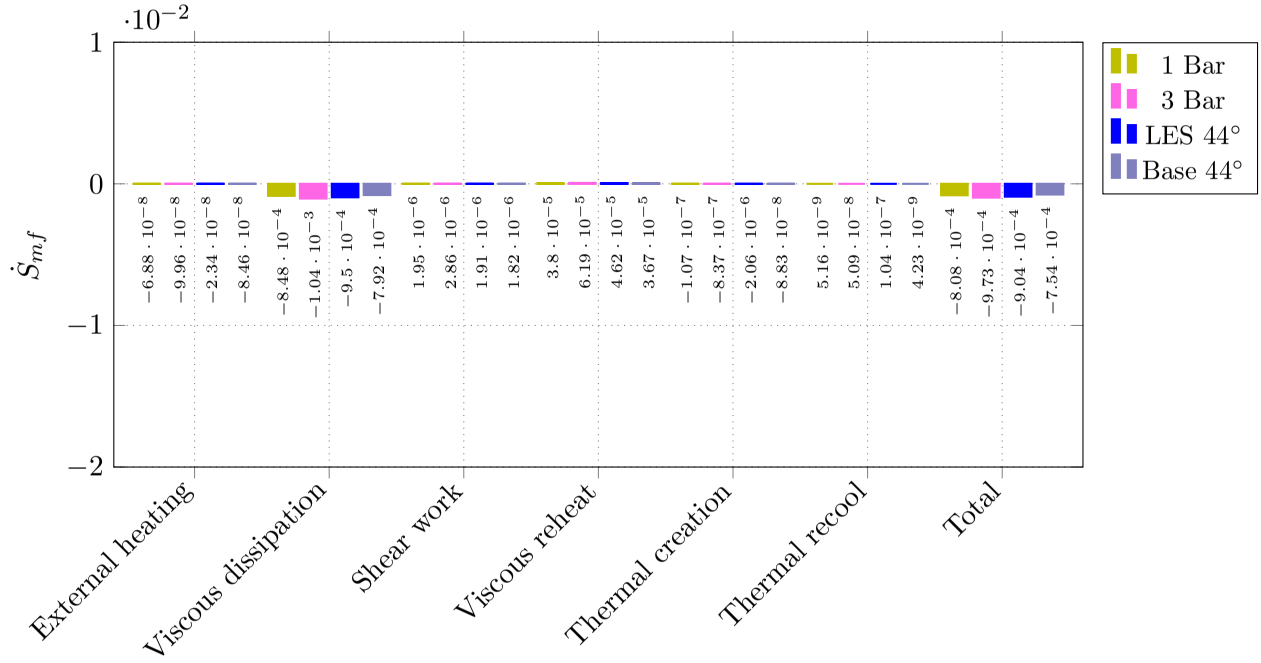

Figure 5.34: Wake integral of mechanical work potential budget for moving bar cases, including 44° case from incidence loss bucket and 44° base case at Reynolds 300K and Mach 0.67.

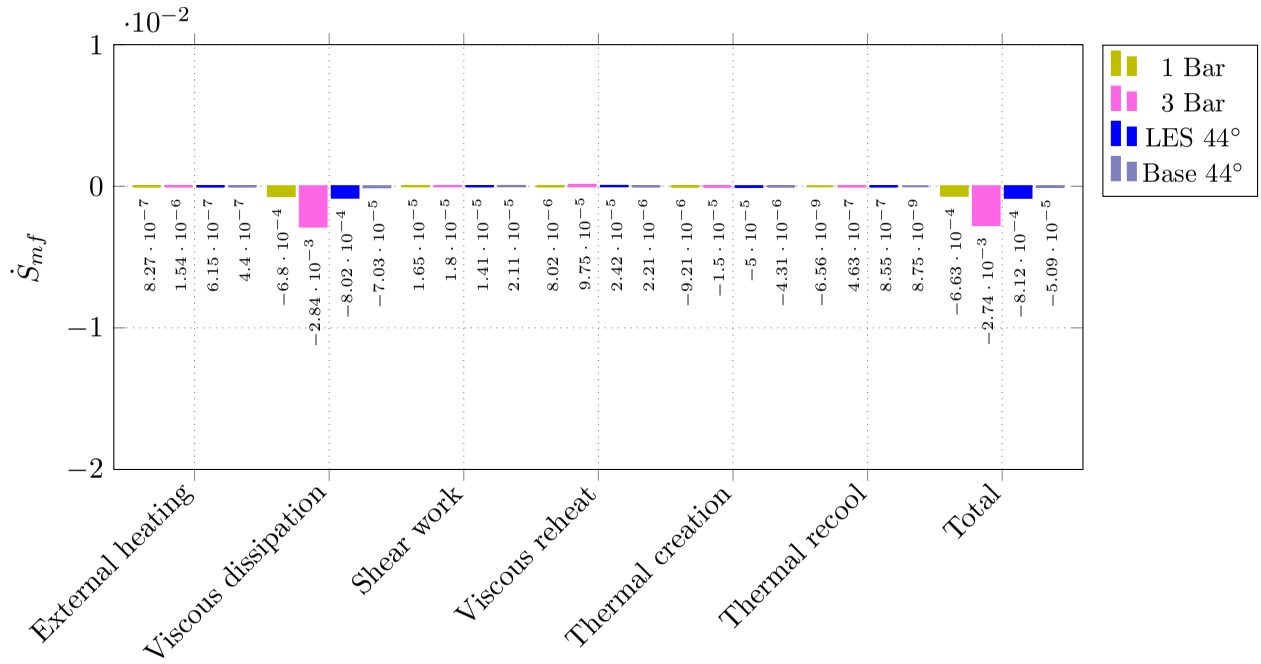

Figure 5.35: Channel integral of mechanical work potential budget for moving bar cases, including 44° case from incidence loss bucket and 44° base case at Reynolds 300K and Mach 0.67.

5.8.4 Loss Trend Discrepancies

It became apparent after the volume breakdown analysis that the cases with discrete disturbances showed different loss trends when measured using the total pressure loss coefficient compared with the volume integral of mechanical work potential. Raising the question of why. The differences are seen in figs. 5.29 and 5.31 and relate to the cases with incoming wakes. Which suggests that the discrepancy seen in the loss trends between the cases with incoming wakes and the cases with homogeneous free-stream turbulence or no free-stream disturbances is due to the unsteady nature of the wake cases. Reigniting the question of "wake recovery".

The idea of "wake recovery" has been suggested by *Smith* (1966b) and later by others such as *Smith* (1958) and *Smith* (1993), as well as *Valkov and Tan* (1999a) and *Van Zante et al.* (2002). More recently work by *Hodson et al.* (2012) proposed a physical interpretation of the mechanism responsible for the wake recovery. Hodson et al., following on from Smith, suggest that if a downstream blade row is in motion relative to the row in which the wake is created wake recovery can occur. This idea is based on the pitch-wise pressure variation as shown in fig. 5.36, and the incident wake passing through. The effects of the wake recovery can also be seen in the reduction of the difference in flow angle of the wake fluid and adjacent free-stream at the exit compared with the inlet.

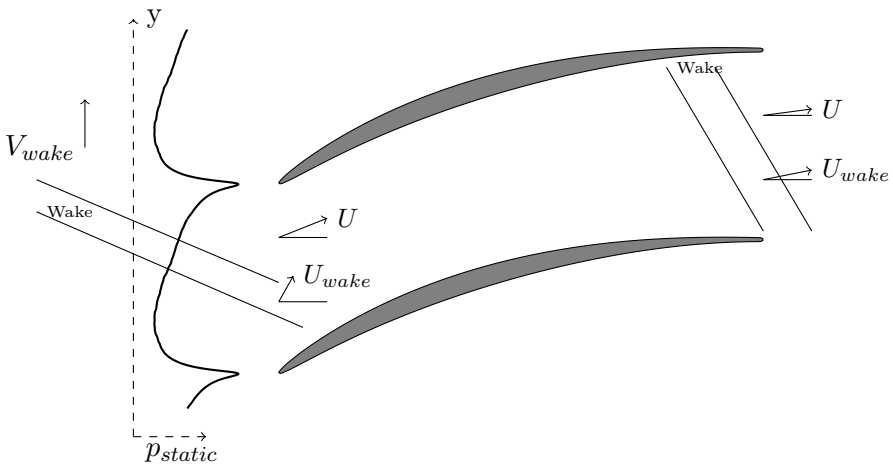

Figure 5.36: Schematic showing pitch-wise pressure variation measured at the leading Edge and change in wake motion through the passage. The difference in flow angle of the wake and free-stream is also shown to highlight wake recovery.

The recovery estimation, as outline by *Hodson et al.* (2012), is based on the different reference frames between the moving and stationary blades and starts with considering the momentum equation of a fluid particle along a streamline, taken from *Horlock* (1968). For an unsteady but reversible compressible adiabatic flow,

$$-\frac{1}{\rho}\frac{\partial p}{\partial s} = \frac{\partial c}{\partial t} + c\frac{\partial c}{\partial s}, \tag{5.27}$$

where, c, is the velocity along streamline, s, and p is the pressure. If the flow is isentropic then

$$-\frac{1}{\rho}\frac{\partial p}{\partial s} = -\frac{\partial h}{\partial s}, \tag{5.28}$$

where h and ρ are the specific enthalpy and density respectively. From equations eq. (5.27) and eq. (5.28) the total enthalpy, h_t, can be introduced,

$$\frac{\partial c}{\partial t} = -\frac{\partial h}{\partial s} - c\frac{\partial c}{\partial s} = -\frac{\partial h_t}{\partial s}. \tag{5.29}$$

Thus the time rate of change of total enthalpy can be given as

$$\begin{aligned}\frac{Dh_t}{Dt} &= \frac{\partial h_t}{\partial t} + c\frac{\partial h_t}{\partial s} \\ &= \frac{\partial h}{\partial t} + c\frac{\partial c}{\partial t} + c\left(-c\frac{\partial c}{\partial t}\right) \\ &= \frac{\partial h}{\partial t} \\ &= \frac{1}{\rho}\frac{\partial p}{\partial t}\end{aligned} \tag{5.30}$$

Similarly for incompressible flow the total pressure can be found to vary with changes in static pressure as

$$\frac{Dp_t}{Dt} = \frac{\partial p}{\partial t}. \tag{5.31}$$

Based on eq. (5.31) Hodson et al. derived an estimate for the changes in total pressure of the wake fluid. Starting with an estimation for the unsteady pressure fluctuations as

$$\left\langle \frac{\partial p}{\partial t} \right\rangle \approx \Omega r \frac{F_y}{wl} = \frac{\Omega r \rho u_x^2 (\tan\alpha_1 - \tan\alpha_2)}{l}, \tag{5.32}$$

where F_y is the blade force in the pitch-wise direction per unit span, w is the pitch, and l the axial chord. The <> denote an average. If the time taken to transit the passage is l/u_x then the average change in total pressure in the passage is

$$\frac{\langle \Delta p_t \rangle}{\rho\,(\Omega r)} \approx (\tan\alpha_1 - \tan\alpha_2)\,\frac{u_x}{\Omega r}. \tag{5.33}$$

From eq. (5.33) an estimate for the additional change in total pressure of the wake can be found as

$$\frac{\delta p_t}{\rho(\Omega r)^2} \approx (\tan\alpha_1 - \tan\alpha_2)\left(\frac{\delta u_x}{\Omega r}\right), \tag{5.34}$$

where δu_x is the wake axial velocity deficit and Ωr is the pitch-wise speed. This can be interpreted as the extra time that the wake fluid is exposed to the average pressure fluctuations due to the unsteady flow. The average pressure fluctuation is estimated by the turning of the flow and the reduced frequency of the incoming wakes as a time scale.

Additionally the changes in total enthalpy can be estimated from eq. (5.30) following the same arguments for the formulation of eq. (5.34), to give an estimation in total enthalpy recovery as

$$\frac{\delta h_t}{(\Omega r)^2} \approx (\tan \alpha_1 - \tan \alpha_2) \left(\frac{\delta u_x}{\Omega r} \right). \tag{5.35}$$

5.8.5 Corrected Pressure Loss Coefficient

To explain the difference in the loss predictions the estimated change in total pressure given by Hodson et al. is applied to the incident wake cases. The fact that the estimation is based on incompressible flow is overcome using numerical integration over the axial length of the blade passage. The estimated recovery is derived for the fluid in the wake. However, in order to find the average total pressure recovery per bar passing period, the wake velocity deficit is averaged across the passage and the estimated change in total pressure calculated. The mass averaged total pressure loss coefficient is then recalculated.

To start with, the bar wakes are extracted from the passage flow at various axial locations, based on a vorticity limit. A selection of the extracted wakes for the 1 Bar case are shown in fig. 5.37. The extraction of the bar wakes is difficult to automate and is done manually at each location in order to ensure that only the wakes are captured. From the extracted wake profiles the wake velocity deficit and wake widths can be measured and a set of polynomials fitted, valid between the leading and trailing edge of the blade. The wake widths are necessary in order to average over the passage width. The measured and curve fitted wake deficit for the two bar cases are shown in fig. 5.38.

Following the extraction of the wake velocity deficit and width the change in total pressure is calculated through the passage. The axial chord is discretised into a number of section and the change in total pressure from each section, based on eq. (5.34), is summed up. Equation 5.34 is rewritten in the following form for the summation,

$$\Delta p_t = \sum_{i=0}^{n} \left(\frac{\rho u_{x,i} u_{y,i} \Delta u_{y,i}}{s} \right) \frac{\Delta x_i}{u_{x,i}},$$

similarly the change in total enthalpy is calculated as

$$\Delta h_t = \sum_{i=0}^{n} \left(\frac{u_{x,i} u_{y,i} \Delta u_{y,ii-1}}{s} \right) \frac{\Delta x_i}{u_{x,i}},$$

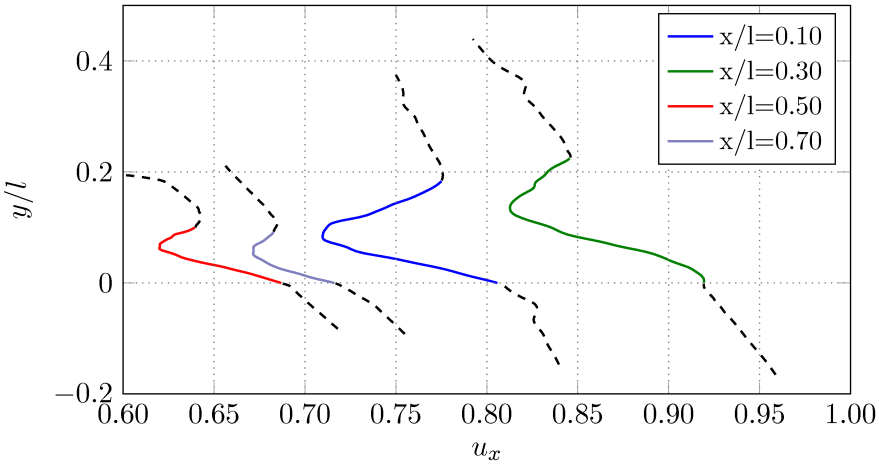

Figure 5.37: Plot of extracted bar wake profiles at four axial locations demonstrating extraction from passage free-stream flow. Wakes are from the 1 Bar case. The pitch-wise location has been normalised such that the start of the wake is zero.

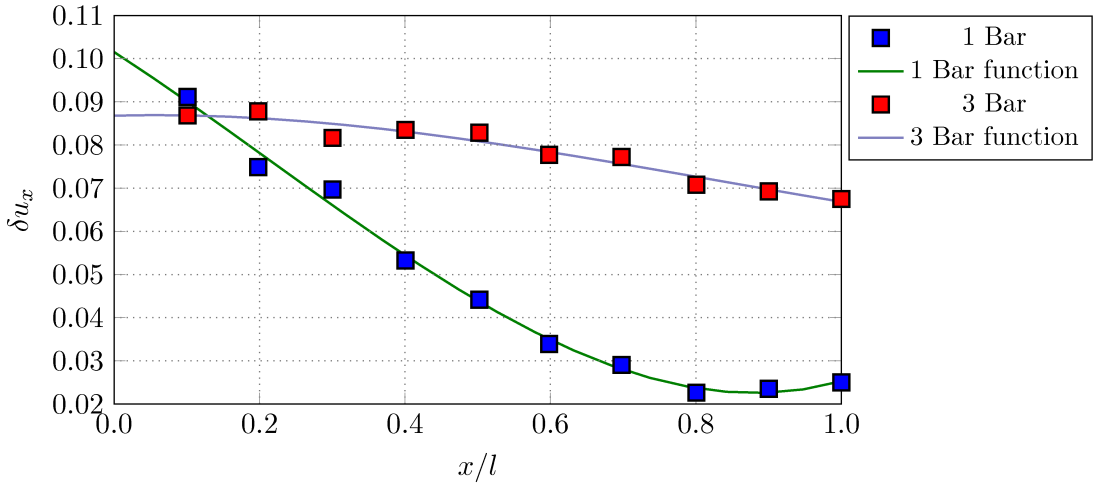

Figure 5.38: Polynomial and measured data for wake velocity deficit with axial distance between leading and trailing edges.

where

$$\Delta u_{y,ii-1} = \frac{(u_{y,i} - u_{y,i-1}) * \Delta w}{s}$$

and Δw is the local wake width.

The average change in total pressure is then added to the local total pressure in the passage at the exit plane and the mass averaged total pressure calculated. The corrected total pressure pressure profile at the exit plane is shown in fig. 5.39. Similarly for the mechanical work potential the average change in total enthalpy is calculated and added to the exit plane and the mass averaged total mechanical work potential recalculated.

Finally the corrected total pressure loss coefficient and mechanical work potential loss coefficient

are compared in fig. 5.40 and table 5.3. The comparison shows that the discrepancy in the loss trends can be accounted for by considering the "wake recovery" due to unsteady effects. This is also supported by the change in flow angle of the wake and adjacent fluid from inlet to exit. At the inlet the difference in flow angle is approximately $\alpha_{wake} - \alpha_{freestream} \approx 4°$ while at the exit $\alpha_{wake} - \alpha_{freestream} \approx 1.25°$. Showing the larger turning experienced by the wake fluid.

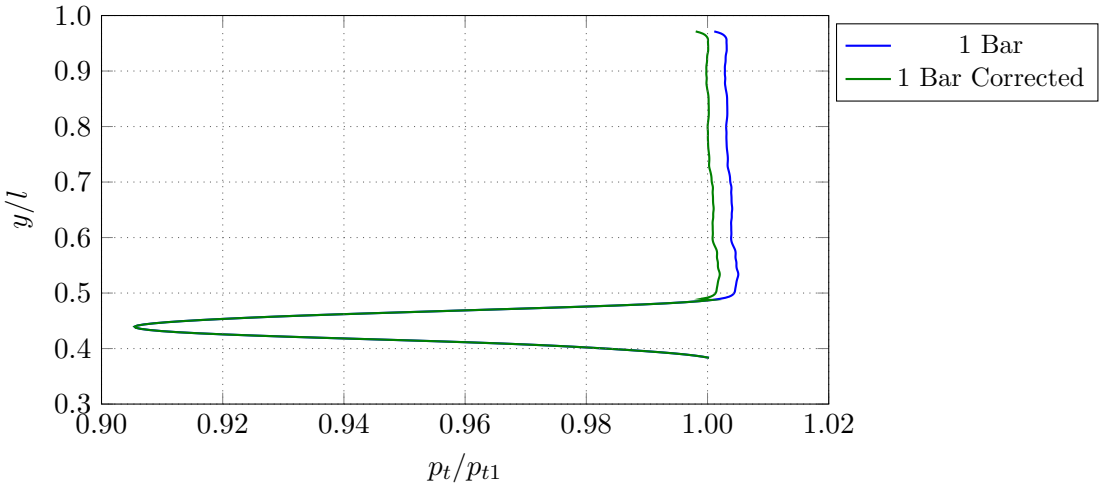

Figure 5.39: Corrected and normal total pressure profile at exit plan for 1 Bar case.

Table 5.3: Comparison of pressure loss and mechanical work potential loss coefficients, corrected and normal, with integral change in mechanical work potential (η), normalised with the corresponding Base case value.

Case		1 Bar	3 Bar	Base
$\eta_{mf}/\eta_{mf:Base}$		1.0059	1.3749	1.0
ω/ω_{Base}		0.4558	0.4950	1.0
ω/ω_{Base}	Corrected	0.9624	1.3476	1.0
$\omega_{mf}/\omega_{mf:Base}$		0.4722	0.5153	1.0
$\omega_{mf}/\omega_{mf:Base}$	Corrected	1.008	1.3764	1.0

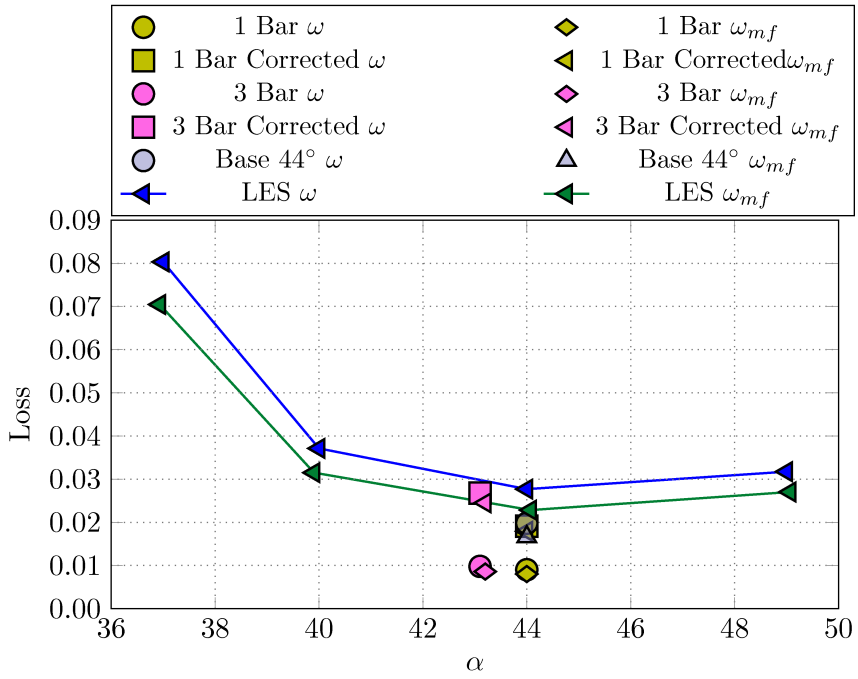

Figure 5.40: Comparison of normal and corrected pressure loss and mechanical work potential loss coefficients for incident wake cases.

5.8.6 Volume Percentage Breakdown

To gain a better understanding of how the addition of discrete disturbances affect the behaviour of the flow and the relative loss the percentage of the total loss for each defined volume is given in fig. 5.41. At the incidence the cases were run at the suction surface is the most predominant loss producer as was seen in the comparison of off-design incidence cases. Similarly the pressure surface follows as the second biggest contributor and then the wake and channel with similar contributions depending on the case. The loss breakdown is reasonably consistent between the cases with the over all trend being that an increase in relative channel losses results in a reduction in the relative suction surface losses. This is seen most clearly between the base case and the three bar case. The change in wake losses seems broadly unaffected by the changes in the inlet conditions, as does the relative pressure surface loss although there is a slight variation with the three bar case showing the lowest contribution from the pressure surface.

Remembering that the total loss from the bar cases is lower than that of the base and off-design cases, seen in fig. 5.29, it is noted that in the three bar case there is a shift of loss from the boundary layers to the channel, not just a relative change in importance. In this case the wakes of the bars are changing the time averaged behaviour of the boundary layers such that they are more efficient. Again this is attributed to the wake calming effect and the fact that this occurs a lot more often for the three bar case compared with the one bar case. Furthermore,

the wake angle and large wake foot print results in a substantial negative jetting slowing down the boundary layer relative to the free-stream.

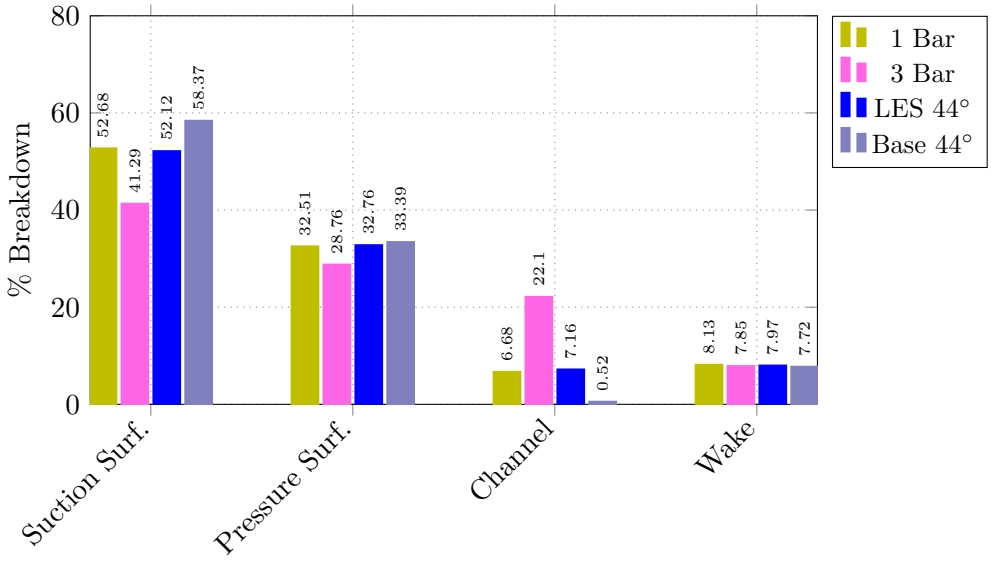

Figure 5.41: Percentage breakdown of mechanical work potential loss for defined volumes for bar cases and 44° incidence and base case.

5.8.7 Denton Loss Comparison

The comparison of the mechanical work potential and Denton breakdown analyses are plotted in fig. 5.42 against the mass averaged inlet TKE, at the leading edge. Using the TKE allows a comparison to be made between the cases without moving bars and those with. The comparisons shows that as the relative TKE is increased the breakdown of loss shifts to the channel, where the free-stream disturbances start to play a roll. It is noted though that the comparison comes with a slight caveat that while the time averaged statistics for the moving bar cases provides a measure of the inlet TKE, the blade actually sees period variation with maximum and minimum TKE values quite removed from the average.

Starting with the one bar and free-stream turbulence cases the relative breakdown is very similar. For the mechanical work potential breakdown the difference is marginal between these cases. With the free-stream turbulence case showing fractionally higher channel losses with an associated drop in the suction surface loss. The pressure surface and wake losses remain almost constant.

If the TKE is increased further as is the case with the three bar simulation the mechanical work potential breakdown changes more significantly. For this case the channel loss increases dramatically with a dramatic corresponding drop in the suction surface loss. Although for this case there is also a slight drop in the relative pressure surface loss, indicating that that wakes

also affect the pressure surface though to a lesser extent. The wake losses again remain constant at this incidence.

Reducing the TKE from the one bar case down to the base case sees a drop to almost zero of the channel losses. This is expected as now there is no turbulence in the channel. The drop in TKE sees a marginal rise in the suction surface loss though not as substantial as the change seen when the TKE is raised to the three bar level. The pressure surface and wake remain essentially constant.

Comparing these trends with the Denton loss prediction shows slightly different behaviour. Firstly the Denton loss breakdown does not show the rise in the channel losses, as this is not accounted for in the analysis. However the lack of channel loss contribution is accounted for by over predicting the relative importance of the suction surface, which accounts for roughly 70-80% of the loss for all cases in the Denton breakdown. The Denton loss breakdown also sees an increase in the suction surface relative loss from the one bar to the free-stream turbulence case, followed by a drop in its relative importance as the TKE increases to the three bar case though not as much as for the mechanical work potential breakdown.

Interestingly the relative pressure surface loss contribution is lower for the Denton breakdown at the lowest TKE value. It remains lower than the mechanical work potential prediction up till the highest TKE value. The Denton loss breakdown in this case is essentially predicting an overloading of the suction surface loss while the pressure surface loss contribution remains relatively constant as the TKE is increased though there is a slight drop for the free-stream turbulence case, counter to the mechanical work potential prediction. Finally the pressure surface contribution rises quite strongly for the three bar case. The rise accounting for some of the increase in channel loss seen in the mechanical work potential breakdown.

The wake loss for the Denton breakdown is essentially constant for all cases the same as the mechanical work potential breakdown although the predicted contribution from the Denton breakdown is lower.

The comparison of the Denton and mechanical work potential loss breakdowns is also given in fig. 5.43 as a bar graph. Showing the breakdown on a case by case bases for completeness.

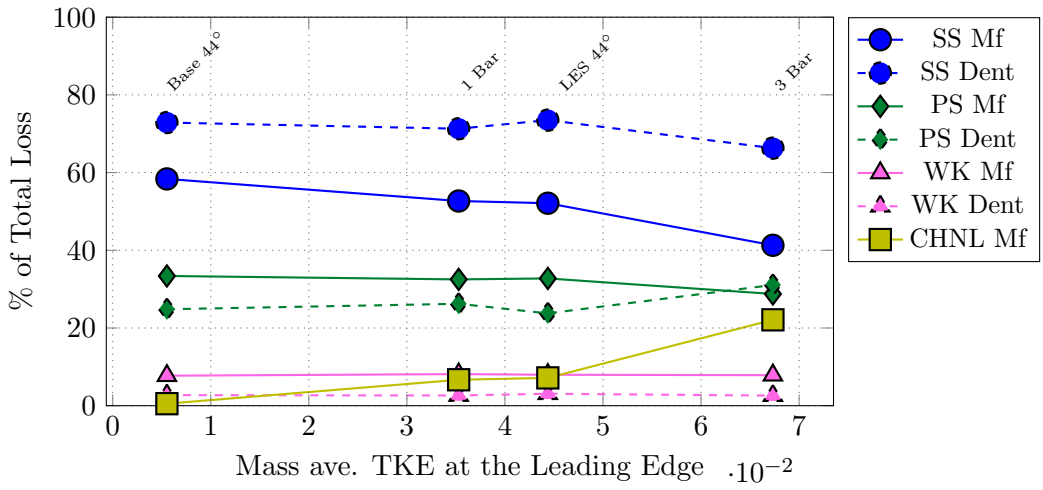

Figure 5.42: Comparison of percentage breakdown of mechanical work potential loss and Denton loss against normalised TKE at the leading.

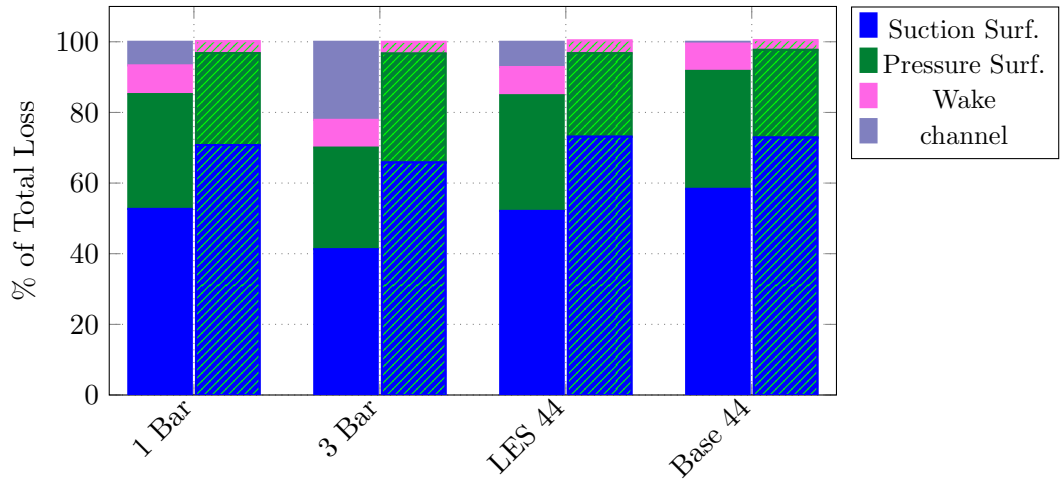

Figure 5.43: Comparison of percentage breakdown of mechanical work potential loss and Denton loss (hatched) for the moving bar cases and 44° incidence and base case. Showing relative importance of each area on a case by case basis.

5.8.8 Tabulated Volume Breakdown

The full breakdown of all the source terms in the mechanical work potential are provided in table 5.4. These are included for completeness and to show clearly through which processes loss is generated.

Table 5.4: Tabulated loss breakdown for base 44° case, 1 bar case and 3 bar case. Showing percentage loss contribution from suction surface, pressure surface, wake , channel and the full field for each term of the mechanical work potential.

Case	44° Base				
	Suction Surface	Pressure Surface	Channel	Wake	Full Field
External heating	0.0313	0.0043	-0.0045	0.0009	0.0319
Viscous dissipation	56.825	34.6772	0.7202	8.1164	100.3358
Shear work	1.3148	0.008	-0.2161	-0.0186	1.0881
Viscous reheat	0.2081	-1.2978	-0.0226	-0.3756	-1.4879
Thermal creation	-0.0118	-0.0008	0.0441	0.0009	0.0324
Thermal recool	-0.0001	-0.0001	-0.0001	-0.0	-0.0004
Total	58.3673	33.3907	0.5211	7.7238	100.0
Case	1 Bar				
	Suction Surface	Pressure Surface	Channel	Wake	Full Field
External heating	0.0362	0.0057	-0.0083	0.0007	0.0343
Viscous dissipation	51.0219	33.6964	6.8386	8.5337	100.091
Shear work	1.2235	-0.0431	-0.1663	-0.0196	0.9945
Viscous reheat	0.4114	-1.1535	-0.0807	-0.3825	-1.2053
Thermal creation	-0.009	0.0011	0.0927	0.0011	0.0859
Thermal recool	-0.0002	-0.0002	0.0001	-0.0001	-0.0003
Total	52.6838	32.5064	6.676	8.1332	100.0
Case	3 Bar				
	Suction Surface	Pressure Surface	Channel	Wake	Full Field
External heating	-0.0005	0.0037	-0.0124	0.0008	-0.0085
Viscous dissipation	41.2039	30.3295	22.9289	8.3691	102.8324
Shear work	0.8159	-0.0512	-0.1449	-0.0231	0.5966
Viscous reheat	-0.731	-1.5281	-0.7867	-0.4999	-3.5457
Thermal creation	-0.0023	0.0045	0.1207	0.0068	0.1297
Thermal recool	-0.0	-0.0004	-0.0037	-0.0004	-0.0046
Total	41.286	28.758	22.1018	7.8532	100.0

5.9 Conclusions

The mechanical work potential analysis introduces a different way to understand the loss processes involved in an axial compressor cascade. The analysis, originally developed as a thermodynamic analysis for turbine stages where heat transfer is more relevant, provides a more rigorous investigation of loss sources compared with the Denton loss breakdown. The mechanical work potential also provides a means of comparing the relative losses of a multi stage set-up as it is based on a single reference pressure. However, in this case this has not been done as the set-up is restricted to a single stage. That being said it does not limit the usefulness of

the analysis in comparing the same stage running under different conditions as has been done. Allowing the analysis to be performed on a single stage or across multiple stages in an engine.

This chapter has introduced a form of loss coefficient for the mechanical work potential which can be used in the same way as the pressure loss coefficient. A relationship has also been introduced to compare the two loss coefficient definitions. In this way the loss coefficients of each stage of a multi stage machine can be compared.

The mechanical work potential analysis has been validated with a set of 2D and 3D simulation and shown to provide a good analysis of the system and processes involved. It has then been applied to a collection of cascade simulations done at off-design incidence and with incident discrete wakes. The analysis of the simulations has provided further insight into loss breakdown and the relative importance of physical processes involved in an axial compressor cascade. Unfortunately the current cascade chosen does not have strong heating effects, such as might be found in the last stages of a high pressure compressor, though it has still provided an understanding of the changes in mechanical work potential and relative weighting of different areas of the domain.

Off-design incidences The mechanical work potential analysis is applied first to the set of simulation run at off-design incidence. The analysis has allowed a more rigorous breakdown of the loss to be carried out and has improved on the Denton loss analysis previously applied. The results show that while the Denton analysis provides a simple and easy way to gage the losses attributed to the different areas of the flow the overall loss breakdown is biased toward the boundary layers. In the mechanical work potential analysis it is shown that the loss from viscous shearing of the free-stream turbulence actually accounts for a small but non-negligible portion. Furthermore the loss from the wake region, albeit a slightly less clear comparison, is higher in the mechanical work potential analysis suggesting that the blade trailing edge design plays a more significant role.

The budget breakdown of the mechanical work potential analysis also provides some understanding of the relevant processes involved. For the cases studied here this is unfortunately predominantly viscus dissipation but it can be seen that some of the other process do play a role and could certainly become significant at different locations in a compressor. In the wake region for example we see that the recovery terms of the mechanical work potential budget are all positive, resulting in mechanical work potential creation. The process of mechanical work potential creation is strongly related to thermal gradients and relative pressures ratios, which in these cases are both quite small, hence the overall recovery is small. However, this changes at different stages in a compressor and can become relevant in the latter stages.

Discrete wakes The effects of discrete disturbances on the performance of an axial compressor are also reviewed. It is found that the breakdown of loss and change in mechanical work potential is relatively unaffected by the type of free-stream disturbance as the results are comparable to that of a cascade with free-stream turbulence. The comparison shows that two cases with similar time averaged inlet TKE values (the one bar case and off-design 44° case) predict similar mechanical work potential breakdown despite the difference in the disturbance type, with only marginal differences in the slightly higher channel loss due to different turbulence in the off-design case. However, when looking at the Denton breakdown of these two cases the changes are more pronounced. It is seen that the Denton loss shows a noticeable shift in the relative loss from the pressure to the suction surface. This is associated with the different dynamics of these two cases and the method of calculating the Denton loss based on the accuracy of calculating the boundary layer properties for an internal flow. Given that this can be ambiguous in these cases the difficulty translates into variation in the predicted loss.

On the other hand the mechanical work potential, which shows different behaviour, is not reliant on boundary layer properties. This allows the analysis to be more robust and dependent on the flow only. However, the breakdown applied here is still dependant on defining a boundary layer volume to compare losses from different areas though the calculation of the loss itself is independent of this.

The mechanical work potential breakdown shows that for cases with similar TKE levels the relative loss breakdown is unaffected by the structure of the disturbance. It is seen that for the one bar case and the 44° off-design case that the loss breakdown is almost the same. However, the total loss calculated is slightly different which suggests that the influence of discrete wakes or free-stream turbulence does not substantially change the overall flow structure but results in a scaling of the magnitudes of loss.

Overall the analysis has provided a means to look more closely at loss production and associating loss with certain defined processes. The analysis also provides a more rigorous breakdown of where loss generation is highest and a means of comparing different operating conditions.

It has also highlighted short comings in the Denton loss breakdown which attempts to associate all loss with the blade boundary layers which is shown not to be the case when there are higher levels of free-stream disturbances.

Chapter 6

Conclusions and Future Work

6.1 Overview

The work presented here focuses on the performance of an axial compressor cascade. Improving our understanding of loss prediction under a variety of different running conditions. To achieve this it utilises highly resolved Large Eddy Simulations at engine relevant Reynolds numbers and Mach numbers, simulations that are not only novel in their resolution and order of accuracy but also in the challenging flow conditions chosen. The simulations are run over a range of off-design incidences as well as with different inflow free-stream disturbances.

6.2 The Effects of Off-Design Incidence

The first study focuses on the prediction of loss over a range of off-design incidences. The study looks at the prediction of loss from both industrial standard RANS and high fidelity LES, allowing a comparison of the performance of the two CFD methods to be investigated, as well as the performance of the axial compressor cascade. The work is further extended to include the application of the loss breakdown proposed by *Denton* (1993). In applying the loss analysis a best practice is put forward with regards to determining necessary flow parameters to calculate the loss breakdown.

The novel application of the Denton loss breakdown to a compressor cascade over a range of off-design incidences has two key results. Firstly, it shows to what processes loss is attributed and how this loss varies over the incidence range, and secondly highlighting the differences in loss attribution of the breakdown between RANS and LES. Furthermore, the study also presents the differences in the flow field results between RANS and LES in an attempt to highlight some of the origins of the differences in the loss breakdown between these two CFD methods.

The Denton loss breakdown applied to the incidence range investigated resulted in the discovery of interesting behaviour in the loss attribution of the flow. It showed that there is a clear shift in the main contribution of loss from the pressure surface to the suction surfaces as the incidence is changed from negative to positive, with the main source of loss produced by viscous momentum loss. However, blockage displacement loss does contribute a significant proportion at positive incidence. Additionally there is a marked change in the make up of the loss breakdown between negative and positive incidence. At negative incidence viscus momentum loss is dominant from both surfaces while at positive incidence an increase in blockage displacement loss from the suction surface sees the relative importance of any loss from the pressure surface tend to zero.

The presence of relevant amounts of blockage displacement loss at positive incidence is interesting because the same does not occur at negative incidence, despite the presence of large turbulent shedding from the leading edge. The work shows that the large pressure surface boundary layer at negative incidence does not result in a reduction of the effective flow area in the same way as a comparatively smaller turbulent suction surface boundary layer.

The study also found that all of the remain terms of the loss breakdown, apart from the form loss, contribute negligible amounts to the total loss. While the form loss contributes a small but measurable amount and is shown to be largely unaffected by changes in incidence. The form loss is also the loss term with the largest discrepancy between RANS and LES with RANS predicting a form loss double that of the LES due to the more coherent wake predicted.

Overall RANS agrees well with the total loss trends shown by the LES over this incidence range. With RANS showing only minor quantitative discrepancy but not to an extent that would be misleading in a design processes. However, when comparing the loss breakdown it is clear that RANS is achieving the total loss via different means. The work presented here shows clearly that RANS predicts a flow field that is not statistically the same as that of the LES. The loss breakdown shows clear variation in the individual loss terms between RANS and LES, suggesting that the RANS and transition models used here are not capturing the true flow. The importance of this finding from a design perspective is that design optimisation can be quite clearly affected depending on the flow parameters chosen, despite the maturity and rigorous testing of tools such as RANS.

6.3 The Effects of Different Free Stream Disturbance Types

The off-design incidence study showed how loss attributed to different areas of the flow changed with incidence highlighting the most important processes at the extremes of the loss bucket. To further this work a second study was performed to investigate how different free-stream disturbances might affect the loss breakdown. The study focussed on the effects of discrete

disturbances at a positive off-design incidence, in order to investigate the effects of flow disturbances on an already unbalanced loss breakdown (i.e. a loss breakdown biased to the suction surface). An LES simulation was performed with the introduction of incoming wakes produced by the addition of upstream pitch-wise moving bars. The moving bar simulation was performed with the same highly resolved mesh and at the same Reynolds number of 300,000 and Mach 0.67.

Before looking in detail at the total loss and loss breakdown it was discovered that local pressure waves were present in the flow domain. The presence of pressure waves around an aerofoil is not new, though previous works have shown these waves to originate from the trailing edge. While in the work presented here it is shown that the pressure wave originate from the separation and transition region of the flow that is not known to have been documented before.

Investigating the pressure waves further showed them to have different fundamental frequencies depending on the type of free-stream disturbances. An interesting results that is not yet fully understood, as the source of the instability causing the waves is not yet know. However, the presence of the waves is unlikely to have any significant effects on the loss performance but may result in tonal noise which is an area of active research and concern for designers.

The initial comparison of the total loss prediction between the cases with different free-stream disturbances displayed slightly confusing results. It is seen that the case with discrete wakes results in the lowest loss. Something unexpected when considering the comparison with the quiescent case without free-stream disturbances. It was shown that this difference in loss is predominantly due to changes in the passage flow. Which was suggested to be due to "wake recovery" as proposed by *Smith* (1966b), though this was initially inconclusive. It was later shown, while working on the mechanical work potential, that an initial application of the recovery process and estimation put forward by *Hodson et al.* (2012) could be used to account for the difference in loss.

The results of the "wake recovery" bring the loss of the incident wake cases in line with the other cases. Which is interesting as it highlights the importance of choosing your frame of reference in what may appear a steady flow. The argument behind the "wake recovery" is that while the frame of reference is fixed and the flow steady for the blade, the wakes see an unsteady flow as they pass through the blade passage. Resulting in a change in the fluid total pressure, as outlined by *Kerrebrock* (1974).

Despite the apparent differences in total loss due to "wake recovery" the application of the loss breakdown analysis is not affected and is still valid. However, the loss breakdown showed little variation between the cases. In fact it is suggested that the loss breakdown fails to capture the loss of the incident wakes in the free-stream, biasing the results by making the loss attributed to the boundary layers larger than it really is.

To further investigate the loss breakdown analysis the total loss was split into passage and wake loss. Given that the Denton loss breakdown is based on the blade boundary layer properties it is argued that the Denton loss breakdown should agree well with the wake loss. However, a comparison made between the Denton loss breakdown and the wake loss showed that the Denton loss breakdown still performed poorly in the presence of free-stream disturbances.

Despite this the loss breakdown still provides insight into changes in the loss trends between cases though its accuracy is shown to decrease in the presence of free-stream disturbances.

6.4 Mechanical Work Potential

Following the inconclusive results of the Denton loss breakdown when applied to cases with different free-stream disturbances. The mechanical work potential analysis was performed to try further explain the breakdown of loss. The mechanical work potential extends the work done by Denton by looking at the flow from an availability point of view providing a means of looking at local changes in loss. It is originally developed as a thermodynamic analysis for turbine stages by *Miller* (2013) where heat transfer is relevant but also provides a tangible means of comparing loss in a compressor. Making it a good candidate for comparison with the Denton loss breakdown.

To start with, a mechanical work potential efficiency has been introduced to allow a comparison between the more standard total pressure loss efficiency. By defining the mechanical work potential efficiency in this way makes it a useful tool for designers already used to the total pressure loss coefficient. The mechanical work potential loss coefficient also allows the variation in reference pressure to be accounted for, making it a powerful tool when comparing the efficiency of different stages through the same engine.

The main interest in the mechanical work potential is the loss breakdown. Done in such a manner as to allow a comparison with the Denton loss breakdown. The breakdown attributes loss to the same areas as the Denton loss breakdown but with one addition. In the mechanical work potential breakdown the loss from the channel is not bundled in with the boundary layers, allowing the loss generated from the free-stream disturbances to be measured.

Although the mechanical work potential loss breakdown does not measure the same metrics, the total loss from each area, such as the total suction surface loss, can be compared. What the mechanical work potential breakdown shows is that while the Denton loss breakdown captures the trends well the suspected behaviour of biasing the boundary layer losses by adding the channel loss is true. This is clearly seen in the off-design incidence cases where the Denton loss breakdown attributes almost all the loss to the boundary layers at the extremes of the loss bucket. Which is not corroborated to the same extend by the mechanical work breakdown. Furthermore, the loss breakdown of the cases with discrete incoming wakes showed relevant

amounts of loss is generated through the channel which directly affects the relative weighting of each of the loss terms, again not captured by the Denton loss breakdown.

Overall, the mechanical work potential loss breakdown, while more involved to apply, provides a more rigorous account of loss production compared with the Denton loss breakdown. Which falls prey to the assumptions made during its' derivation, most notably the assumption that flow is uniform in the passage.

The mechanical work potential also provides a means of looking at local changes in the flow and associating loss with different processes. Although a thorough analysis has not been performed here, the breakdown of loss for the different areas showed that while viscous shearing was the main source of loss, other processes are also involved.

6.5 Future Work

The unexpected behaviour of the discrete disturbance cases and the initial application of the wake recovery processes proposed by *Hodson et al.* (2012) and *Smith* (1966a) has open up many questions. While the estimation of "recovery loss" by *Hodson et al.* (2012) seems to explain the change in loss, its application here is only an estimation which requires a more rigorous examination to properly understand the underlying process. For future work it is suggested that a more rigorous analysis be performed based on a more detailed energy balance approach to understand this process further.

Work on understanding the changes in the upstream travelling pressure waves frequencies is also suggested. This focuses on understand the changes in the boundary layer instabilities and how changing the free-stream disturbances might force their growth. Although this work is not directly related to loss it is an interesting discovery and would be worth investigating as noise pollution becomes and increasing problem.

Appendix A

Navier-Stokes Equations

This appendix gives a detailed breakdown of the Navier-Stokes equations used in the HiPSTAR code, including the transformations from real to computational space, characteristics interface treatment and the non-dimensionalisation employed.

A.0.1 Full Navier-Stokes Equatiosn

The full set of equations are given in flux form as:

$$\frac{\partial \mathbf{Q}}{\partial t} + \frac{\partial \mathbf{F_1}}{\partial x} + \frac{\partial \mathbf{F_2}}{\partial y} + \frac{\partial \mathbf{F_3}}{\partial z} = \mathbf{S} \tag{A.0.1}$$

where

$$\mathbf{Q} = \left\{ \begin{array}{c} \rho \\ \rho u_i \\ \rho E \end{array} \right\} \tag{A.0.2}$$

$$\mathbf{F_k} = \left\{ \begin{array}{c} \rho u_k \\ \rho u_i u_k + \delta_{ik} p - \tau_{ik} \\ u_k(\rho E + p) - q_k - u_j \tau_{kj} \end{array} \right\} \tag{A.0.3}$$

$$\mathbf{S} = \left\{ \begin{array}{c} 0 \\ \rho f_k \\ \rho(u_j f_j) \end{array} \right\} \tag{A.0.4}$$

where f terms are body forcing such as gravitational or buoyancy forces.

The equations are non-dimensionalised using the free stream inflow fluid properties and it is assumed the fluid acts as a perfect gas allowing the pressure to be solved from the perfect gas

law

$$p = \frac{\rho T}{\gamma M^2}$$

The total energy is given as

$$E = \frac{T}{(\gamma(\gamma-1)M^2)} + \frac{u_i u_i}{2}.$$

and the stress and heat flux vectors are calculated as follows.

$$\tau_{ij} = \frac{2\mu}{Re}\left[S_{ij} - \frac{\delta_{ij}}{3}S_{kk}\right] \tag{A.0.5}$$

$$S_{ij} = \frac{1}{2}\left(\frac{\partial u_i}{\partial x_j} + \frac{\partial u_j}{\partial x_i}\right) \tag{A.0.6}$$

$$q_i = \frac{-\mu}{(\gamma-1)M^2 PrRe}\frac{\partial T}{\partial x_i}. \tag{A.0.7}$$

It is assumed here that Stokes hypothesis is used for the bulk modulus.

A.0.2 Transformation to Computational Space

To aid computational efficiency and ensure high-order discretisation of the equations, they are solved on a computational domain. The transformed equations for two dimensions are given by the following, neglecting forcing terms for simplicity:

$$\frac{\partial \widehat{\mathbf{Q}}}{\partial t} + \frac{\partial \widehat{\mathbf{F_1}}}{\partial \xi} + \frac{\partial \widehat{\mathbf{F_2}}}{\partial \eta} = 0. \tag{A.0.8}$$

Where

$$\widehat{\mathbf{Q}} = \mathbf{JQ} \tag{A.0.9}$$

$$\widehat{\mathbf{F_1}} = \mathbf{JF_1}\frac{\partial \xi}{\partial x} + \mathbf{JF_2}\frac{\partial \xi}{\partial y} \tag{A.0.10}$$

$$\widehat{\mathbf{F_2}} = \mathbf{JF_1}\frac{\partial \eta}{\partial x} + \mathbf{JF_2}\frac{\partial \eta}{\partial y}, \tag{A.0.11}$$

$$\tag{A.0.12}$$

and the Jacobian is given as:

$$\mathbf{J} \equiv \begin{vmatrix} \dfrac{\partial x}{\partial \xi} & \dfrac{\partial y}{\partial \xi} \\ \dfrac{\partial x}{\partial \eta} & \dfrac{\partial y}{\partial \eta} \end{vmatrix} \tag{A.0.13}$$

The transformation of derivatives is explained in more detail next. Given two coordinate systems x,y,z and ξ, η, z then the transformation between each system is a function of the others i.e.

$$z = z; x = f(\xi, \eta); y = g(\xi, \eta)$$

$$z = z; \xi = f'(x, y); \eta = g'(x, y)$$

As these these transformation functions are not known we cannot transform between them directly. While this does not affect the variables of the solution directly as these remain constant at each grid point regardless of coordinate system. The derivatives of these variables is dependant on the coordinate system. So if a derivative of a value is needed in the x, y system it must be transformed as only the derivative in the ξ, η system is known. Thus the desired derivatives are as follows, formulated from the chain rule.

$$\frac{\partial}{\partial x} = \frac{\partial \xi}{\partial x}\frac{\partial}{\partial \xi} + \frac{\partial \eta}{\partial x}\frac{\partial}{\partial \eta}$$

$$\frac{\partial}{\partial y} = \frac{\partial \xi}{\partial y}\frac{\partial}{\partial \xi} + \frac{\partial \eta}{\partial y}\frac{\partial}{\partial \eta}$$

the problem is the term $\frac{\partial \xi}{\partial x}$ or any of the other cross derivative of ξ, η with respect to x, y.

However the inverse of this is known because the values of $\partial\xi$ and $\partial\eta$ are set to unity in the computational domain and this is the coordinate system we are working in. This gives the rate of change of x or y with respect to ξ and η but not the other way round. So in order to calculate the value of the derivatives we have to solve the opposite.

$$\frac{\partial}{\partial \xi} = \frac{\partial \xi}{\partial x}\frac{\partial}{\partial x} + \frac{\partial \xi}{\partial y}\frac{\partial}{\partial \xi}$$
$$\frac{\partial}{\partial \eta} = \frac{\partial \eta}{\partial x}\frac{\partial}{\partial x} + \frac{\partial \eta}{\partial y}\frac{\partial}{\partial \eta}$$

which we rearrange and solve as follows.

$$\begin{bmatrix} \frac{\partial x}{\partial \xi} & \frac{\partial y}{\partial \xi} \\ \frac{\partial x}{\partial \eta} & \frac{\partial y}{\partial \eta} \end{bmatrix} \begin{bmatrix} \frac{\partial}{\partial x} \\ \frac{\partial}{\partial x} \end{bmatrix} = \begin{bmatrix} \frac{\partial}{\partial \xi} \\ \frac{\partial}{\partial \eta} \end{bmatrix} \tag{A.0.14}$$

now calculate the inverse of the matrix as

$$\begin{bmatrix} a & b \\ c & d \end{bmatrix}^{-1} = \frac{1}{det\ A} \begin{bmatrix} d & -b \\ -c & a \end{bmatrix}$$

Finally the derivatives are given as

$$\begin{bmatrix} \frac{\partial}{\partial x} \\ \frac{\partial}{\partial y} \end{bmatrix} = \frac{1}{\frac{\partial x}{\partial \xi}\frac{\partial y}{\partial \eta} - \frac{\partial y}{\partial \xi}\frac{\partial x}{\partial \eta}} \begin{bmatrix} \frac{\partial y}{\partial \eta} & -\frac{\partial y}{\partial \xi} \\ -\frac{\partial x}{\partial \eta} & \frac{\partial x}{\partial \xi} \end{bmatrix} \begin{bmatrix} \frac{\partial}{\partial \xi} \\ \frac{\partial}{\partial \eta} \end{bmatrix} \tag{A.0.15}$$

A.0.3 Characteristic Form

In order to treat the metric discontinuities that exist at block interfaces, where grid lines are not higher order continuous, the Navier-Stokes equations are transformed into wave equations and solved. The transformation into wave equations assumes that viscous terms are negligible and as such can be neglected. Finally as the equations are solved in computational space the characteristic waves travel parallel or normal to the boundaries allowing only the normal waves to be treated.

The quasi 1D wave equations normal to the boundary in primitive variables neglecting viscus terms are shown here, which are solved to find the missing terms of the full equations.

$$\frac{\partial \rho}{\partial t} + \frac{1}{c^2}\left[\mathcal{L}_2 + \frac{1}{2}(\mathcal{L}_5 + \mathcal{L}_1)\right] = 0 \tag{A.0.16}$$

$$\frac{\partial p}{\partial t} + \frac{1}{2}(\mathcal{L}_5 + \mathcal{L}_1) = 0 \tag{A.0.17}$$

$$\frac{\partial u_1}{\partial t} + \frac{1}{2\rho c}(\mathcal{L}_5 - \mathcal{L}_1) = 0 \tag{A.0.18}$$

$$\frac{\partial u_2}{\partial t} + \mathcal{L}_3 = 0 \tag{A.0.19}$$

$$\frac{\partial u_3}{\partial t} + \mathcal{L}_4 = 0 \tag{A.0.20}$$

The characteristics wave amplitudes are given by

$$\mathcal{L}_1 = \lambda_1 \left(\frac{\partial p}{\partial x_1} - \rho c \frac{\partial u_1}{\partial x_1}\right) \tag{A.0.21}$$

$$\mathcal{L}_2 = \lambda_2 \left(c^2 \frac{\partial \rho}{\partial x_1} - \frac{\partial p}{\partial x_1}\right) \tag{A.0.22}$$

$$\mathcal{L}_3 = \lambda_3 \frac{\partial u_2}{\partial x_1} \tag{A.0.23}$$

$$\mathcal{L}_4 = \lambda_4 \frac{\partial u_3}{\partial x_1} \tag{A.0.24}$$

$$\mathcal{L}_5 = \lambda_5 \left(\frac{\partial p}{\partial x_1} + \rho c \frac{\partial u_1}{\partial x_1}\right) \tag{A.0.25}$$

and the characteristic velocities by:

$$\lambda_1 = u_1 - c \tag{A.0.26}$$

$$\lambda_2 = \lambda_3 = \lambda_4 = u_1 \tag{A.0.27}$$

$$\lambda_5 = u_1 + c, \tag{A.0.28}$$

$$\tag{A.0.29}$$

Now depending of speed of the flow and direction of travel the characteristic wave amplitudes are set accordingly.

Appendix B

Non-Dimensionalisation

In order to non-dimensionalise the Navier-Stokes equations we need to define a set of reference values to use for the non-dimensionalisation. For a compressor these values are chosen as the inlet free-stream, thought the independent values needed will be determined thought the non-dimensionalisation of the equations.

If we start by introducing a basic non-dimensionalisation of the form

$$\rho^* = \rho\rho_\infty,$$

where the " $*$ " is a dimensional value, and the "∞" is the reference value and finally a value without a script such as ρ is the non-dimensional value. By using this notion and substituting an appropriate form of this for each dimensional quantity into the Navier-Stokes equations we can arrive at a non-dimensional form made of a minimum set of required reference values.

B.0.0.1 Mass Conservation

Starting with the continuity equation the physical equation is given as

$$\frac{\partial \rho^*}{\partial t^*} + \frac{\partial(\rho^* u_i^*)}{\partial x_i^*} = 0 \tag{B.0.1}$$

now replacing all physical quantities with non-dimensional ones,

$$\frac{\partial(\rho\rho_\infty)}{\partial(tt_\infty)} + \frac{\partial(\rho\rho_\infty u_i u_\infty)}{\partial(x_i l_\infty)} = 0. \tag{B.0.2}$$

Given that the reference values are constant the equation can be written as,

$$\frac{\rho_\infty}{t_\infty}\frac{\partial \rho}{\partial t} + \frac{\rho_\infty U_\infty}{l_\infty}\frac{\partial(\rho u_i)}{\partial x_i} = 0, \tag{B.0.3}$$

rearranging,

$$\frac{l_\infty}{t_\infty U_\infty}\frac{\partial \rho}{\partial t} + \frac{\partial(\rho u_i)}{\partial x_i} = 0. \tag{B.0.4}$$

By introducing the relationship $t_\infty = l_\infty/U_\infty$ the equation can be reduced further to give the final non-dimensional form,

$$\frac{\partial \rho}{\partial t} + \frac{\partial(\rho u_i)}{\partial x_i} = 0. \tag{B.0.5}$$

B.0.0.2 Momentum Conservation

Next the momentum equation given as,

$$\frac{\partial(\rho^* u_i^*)}{\partial t^*} + \frac{\partial(\rho^* u_i^* u_j^*)}{\partial x_j^*} = -\frac{\partial p^*}{\partial x_i^*} + \frac{\partial \tau_{ik}^*}{\partial x_k^*} \tag{B.0.6}$$

now replacing all physical quantities as before,

$$\frac{\partial(\rho_\infty U_\infty \rho u_i)}{\partial(t_\infty t)} + \frac{\partial(\rho_\infty U_\infty \rho u_i u_j)}{\partial(l_\infty x_j)} = -\frac{\partial(p_\infty p)}{\partial(l_\infty x_i)} + \frac{\partial(\tau_\infty \tau_{ik})}{\partial(l_\infty x_k)}. \tag{B.0.7}$$

Focusing firstly on the non-dimensionalisation of the shear stress, this can be performed separately to get the form of τ_∞.

$$\tau_{ij}^* = \mu^* \left(\frac{\partial u_i^*}{\partial x_j^*} + \frac{\partial u_j^*}{\partial x_i^*}\right) - \frac{2\mu^*}{3}\left(\frac{\partial u_k^*}{\partial x_k^*}\right)\delta_{ij} \tag{B.0.8}$$

Replacing with non-dimensional values,

$$\tau_\infty \tau_{ij} = \mu_\infty \mu \left(\frac{\partial U_\infty u_i}{\partial l_\infty x_j} + \frac{\partial U_\infty u_j}{\partial l_\infty x_i}\right) - \frac{2\mu_\infty \mu}{3}\left(\frac{\partial U_\infty u_k}{\partial l_\infty x_k}\right)\delta_{ij}, \tag{B.0.9}$$

and rearranging gives

$$\tau_\infty \tau_{ij} = \frac{\mu_\infty U_\infty}{l_\infty}\left(\mu\left(\frac{\partial u_i}{\partial x_j} + \frac{\partial u_j}{\partial x_i}\right) - \frac{2\mu}{3}\left(\frac{\partial u_k}{\partial x_k}\right)\delta_{ij}\right). \tag{B.0.10}$$

From inspection it is seen that $\tau_\infty = \frac{\mu_\infty u_\infty}{l_\infty}$, now replacing this in the momentum equation and rearranging gives,

$$\frac{\partial(\rho u_i)}{\partial t} + \frac{\partial(\rho u_i u_j)}{\partial x_j} = -\frac{p_\infty}{\rho_\infty U_\infty^2}\frac{\partial p}{\partial x_i} + \frac{\mu_\infty}{\rho_\infty l_\infty U_\infty}\frac{\partial \tau_i k}{\partial x_k}. \tag{B.0.11}$$

Defining the non-dimensional Reynolds number as

$$Re = \frac{\rho_\infty U_\infty l_\infty}{\mu_\infty},$$

based on reference values defined here at the inflow, and letting the reference pressure $p_\infty = \rho_\infty U_\infty^2$ then the non-dimensional momentum equation is given as;

$$\frac{\partial(\rho u_i)}{\partial t} + \frac{\partial(\rho u_i u_j)}{\partial x_j} = -\frac{\partial p}{\partial x_i} + \frac{1}{Re}\frac{\partial \tau_i k}{\partial x_k}. \tag{B.0.12}$$

B.0.0.3 Energy Conservation

The energy equation is given as,

$$\frac{\partial(\rho^* E^*)}{\partial t^*} + \frac{\partial(u_j^* \rho^* E^*)}{\partial x_j^*} = -\frac{\partial(u_i^* p^* \delta_{ij})}{\partial x_i^*} + \frac{\partial(u_i^* \tau_{ij}^*)}{\partial x_j^*} - \frac{\partial}{\partial x_j^*}\left(\frac{\partial(k^* T_j^*)}{\partial x_j^*}\right) \tag{B.0.13}$$

where $\rho E = \rho(e + \frac{u_i u_i}{2})$ is the energy density. This can be rearranged to include enthalpy density instead of the convection of internal energy density and pressure, $\rho H = \rho c_p T_t = \rho(E + p/\rho)$, as well as replacing the thermal conductivity with $k = \frac{\mu^* c_p}{Pr_\infty}$ where Pr_∞ is the Prantle number, assumed constant here. The non-dimensionalisation of the energy and enthalpy densities is done using $u_i u_i$.

$$\frac{\partial(\rho^* E^*)}{\partial t^*} + \frac{\partial(u_j^* \rho^* H^*)}{\partial x_j^*} = \frac{\partial(u_i^* \tau_{ij}^*)}{\partial x_j^*} - \frac{\partial}{\partial x_j^*}\left(\frac{\mu^* c_p}{Pr_\infty}\frac{\partial(T_j^*)}{\partial x_j^*}\right). \tag{B.0.14}$$

Now replacing all dimensional value with their non-dimensional counter parts gives;

$$\frac{\rho_\infty u_\infty^3}{l_\infty}\frac{\partial(\rho E)}{\partial t} + \frac{u_\infty^3 \rho_\infty}{l_\infty}\frac{\partial(u_j \rho H)}{\partial x_j} = \frac{u_\infty^2 \mu_\infty}{l_\infty^2}\frac{\partial(u_i \tau_{ij})}{\partial x_j} - \frac{\mu_\infty T_\infty c_p}{Pr_\infty l_\infty^2}\frac{\partial}{\partial x_j}\left(\mu\frac{\partial(T_j)}{\partial x_j}\right). \tag{B.0.15}$$

Rearranging,

$$\frac{\partial(\rho E)}{\partial t} + \frac{\partial(u_j \rho H)}{\partial x_j} = \frac{\mu_\infty}{\rho_\infty U_\infty l_\infty}\frac{\partial(u_i \tau_{ij})}{\partial x_j} - \frac{\mu_\infty T_\infty c_p}{\rho_\infty u_\infty^3 Pr_\infty l_\infty}\frac{\partial}{\partial x_j}\left(\mu\frac{\partial(T_j)}{\partial x_j}\right). \tag{B.0.16}$$

Now introducing the dimensionless numbers Re_∞ and $M_\infty = U_\infty/a_\infty = U_\infty/\sqrt{(\gamma-1)c_p T_\infty}$, where $\gamma = 1.4$ is the isentropic exponent and c_p is the specific heat capacity at constant pressure, both considered constant here.
The equation can finally be formed as

$$\frac{\partial(\rho E)}{\partial t} + \frac{\partial(u_j \rho H)}{\partial x_j} = \frac{1}{Re_\infty}\frac{\partial(u_i \tau_{ij})}{\partial x_j} - \frac{1}{Re_\infty M_\infty^2 Pr_\infty(\gamma-1)}\frac{\partial}{\partial x_j}\left(\mu\frac{\partial(T_j)}{\partial x_j}\right). \tag{B.0.17}$$

B.0.0.4 The Equation of State

Lastly the equation of state is required to close the system of equations given as

$$p^* = \rho^* T^* R \tag{B.0.18}$$

Substituting the dimensional values gives

$$\rho_\infty U_\infty^2 p = \frac{\rho_\infty T_\infty c_p(\gamma - 1)}{\gamma} \rho T \tag{B.0.19}$$

where the specific gas constant has been replaced with

$$R = \frac{c_p(\gamma - 1)}{\gamma}. \tag{B.0.20}$$

It is seen previously in the energy conservation equation that the expression, $(\gamma - 1)c_p T_\infty = a_\infty^2$, is the speed of sound squared. Introducing this into the non-dimensional equation of state gives.

$$p = \frac{\rho T}{\gamma M_\infty^2} \tag{B.0.21}$$

Relating the internal energy, enthalpy and pressure in non-deimensional form is given as follow. The internal energy density is

$$e^* = c_v T^*, \tag{B.0.22}$$

non-dimensionalising and substituting $c_v = c_p/\gamma$

$$e = \frac{c_p T_\infty}{\gamma U_\infty^2} T \tag{B.0.23}$$

Multiplying the LHS with $(\gamma - 1)/(\gamma - 1)$ and noting that this can be rearranged to introduce the speed of sound $c_\infty^2 = (\gamma - 1)c_p T_\infty$ gives

$$e = \frac{T}{\gamma(\gamma - 1)M_\infty^2}. \tag{B.0.24}$$

The enthalpy density can be

B.0.0.5 Reference Values

From this analysis it can be seen that a total of four reference values are necessary to non-dimensionalise the equations given in table B.0.1 with a further three non-dimensional numbers to fully define the non-dimensional Navier-Stokes equations.

Length	L
Velocity	U_∞
Density	ρ_∞
Temperature	T_∞
Isentropic exponent	γ
Reynolds number	Re_∞
Prantle number	Pr_∞

Table B.0.1: Required reference values for non-dimensional equations

Using these reference values all other reference quantities can be derived as follows in table B.0.2.

Time	$t_\infty = l_\infty / U_\infty$
Pressure	$p_\infty = \rho_\infty U_\infty$
Energy density	$e_\infty = U_\infty^2$
Enthalpy density	$H_\infty = U_\infty^2$
Viscosity	$\mu_\infty = f(Re_\infty, T_\infty)$

Table B.0.2: Dependant reference values for non-dimensional equations

Bibliography

Abu-Ghannam BJ and Shaw R. Natural Transition of Boundary Layers—The Effects of Turbulence, Pressure Gradient, and Flow History. *Journal of Mechanical Engineering Science*, **22**(5), 213–228 (1980).

Alshabu a and Olivier H. Unsteady Wave Phenomena on a Supercritical Airfoil. *AIAA Journal*, **46**(8), 2066–2073 (2008). ISSN 0001-1452.

Bhaskaran R and Lele SK. Large eddy simulation of free-stream turbulence effects on heat transfer to a high-pressure turbine cascade. *Journal of Turbulence*, **11**(July 2015), N6 (2010). ISSN 1468-5248.

Bird R. The equations of change and the macroscopic mass, momentum, and energy balances. *Chemical Engineering Science*, **6**(3), 123–131 (1957). ISSN 0009-2509.

Boudet J, Caro J, Shao L and Lévêque E. Numerical studies towards practical large-eddy simulation. *Journal of Thermal Science*, **16**(4), 328–336 (2007). ISSN 10032169.

Bryce JD, Cherrett MA and Lyes PA. Three-Dimensional Flow in a Highly Loaded Single-Stage Transonic Fan. *Journal of Turbomachinery*, **117**(1), 22–28 (1995). ISSN 0889-504X.

Carpenter M, Norstrom J and Gottlieb D. A stable and conservative interface treatment of arbitrary spatial accuracy. *Journal of Computational Physics*, **148**, 341–365. (1999).

Chen WL, Lien FS and Leschziner MA. Computational prediction of flow around highly loaded compressor-cascade blades with non-linear eddy-viscosity models. *International Journal of Heat and Fluid Flow*, **19**(4), 307–319 (1998). ISSN 0142-727X.

Cherrett MA, Bryce JD and Ginder RB. Unsteady Three-Dimensional Flow in a Single-Stage Transonic Fan: Part II—Unsteady Stator Exit Flow Field. *Journal of Turbomachinery*, **117**(4), 514–521 (1995a). ISSN 0889-504X.

Cherrett MA, Bryce JD and Ginder RB. Unsteady Three-Dimensional Flow in a Single-Stage Transonic Fan: Part I—Unsteady Rotor Exit Flow Field. *Journal of Turbomachinery*, **117**(4), 506–513 (1995b). ISSN 0889-504X.

Coull JD and Hodson HP. Unsteady boundary-layer transition in low-pressure turbines. *Journal of Fluid Mechanics*, **681**(1), 370–410 (2011). ISSN 0022-1120.

Cumpsty NA. *Compressor Aerodynamics*. Longman Scientific & Technical (1989).

Cumpsty NA, Dong Y and Li YS. Compressor Blade Boundary Layers in the Presence of Wakes. In *ASME Turbo Expo: Power for Land, Sea, and Air*, volume 1 Turbomac, page V001T01A108. ASME (1995). ISBN 978-0-7918-7878-1. ISSN 04021215.

Denton JD. The 1993 IGTI Scholar Lecture: Loss Mechanisms in Turbomachines. *Journal of Turbomachinery*, **115**(4), 621 (1993). ISSN 0889504X.

Devenport WJ, Wittmer KS, Muthanna C and Wenger CW. Wake of a Compressor Cascade with Tip Gap, Part 1: Mean Flow and Turbulence Structure. *AIAA Journal*, **42**(11), 2341–2346 (2004). ISSN 0001-1452.

Dong Y and Cumpsty NA. Compressor Blade Boundary Layers : Part 1 — Test Facility and Measurements With No Incident Wakes. *Journal of Turbomachinery*, **112(2)**(April 1990), 223–230 (1990a).

Dong Y and Cumpsty NA. Compressor Blade Boundary Layers: Part 2-Measurements With Incident Wakes. *Journal of Turbomachinery*, **112(2)**(April 1990), 231–240. (1990b).

Dong Y, Gallimore SJ and Hodson HP. Three-Dimensional Flows and Loss Reduction in Axial Compressors. *Journal of Turbomachinery*, **109**(3), 354–361 (1987). ISSN 0889-504X.

D'Ovidio A, Harkins JA and Gostelow JP. Turbulent Spots in Strong Adverse Pressure Gradients: Part 2 — Spot Propagation and Spreading Rates. *ASME Paper 2001-GT-0406* (2001).

Drela M. Implementation of Modified Abu-Ghannam Shaw Transition Criterion. In *MISES User's Guide*. Cambridge, MA (1995).

Duchaine F, Corpron A, Pons L, Moureau V, Nicoud F and Poinsot T. Development and assessment of a coupled strategy for conjugate heat transfer with Large Eddy Simulation: Application to a cooled turbine blade. *International Journal of Heat and Fluid Flow*, **30**(6), 1129–1141 (2009). ISSN 0142727X.

Emmons HW. The Laminar-Turbulent Transition in a Boundary Layer-Part I. *Journal of the Aeronautical Sciences*, **18**(7), 490–498 (1951).

Evans S, Hodson H, Hynes T and Wakelam C. Flow Control in a Compressor Cascade at High Incidence. *Journal of Propulsion and Power*, **26**(4), 828–836 (2010). ISSN 0748-4658.

Gostelow JP, Melwani N and Walker GJ. Effects of Streamwise Pressure Gradient on Turbulent Spot Development. *Journal of Turbomachinery*, **118**(4), 737–743 (1996). ISSN 0889-504X.

Gourdain N. Validation of Large-Eddy Simulation For The Prediction of Compressible Flow in an Axial Compressor Stage. *ASME Turbo Expo 2013: Turbine ...*, pages 1–15 (2013).

Gourdain N. Prediction of the unsteady turbulent flow in an axial compressor stage. Part 1: Comparison of unsteady RANS and LES with experiments. *Computers & Fluids*, **106**, 119–129 (2015a). ISSN 00457930.

Gourdain N. Prediction of the unsteady turbulent flow in an axial compressor stage. Part 2: Analysis of unsteady RANS and LES data. *Computers & Fluids*, **106**, 67–78 (2015b). ISSN 00457930.

Greschner B and Thiele F. Wall Modeled LES simulation of Rotor-Stator-Cascade Broadband Noise. *AIAA Conference*, (June), 05 – 08 (2011).

Gross A and Fasel HF. Multi-block Poisson grid generator for cascade simulations. *Mathematics and Computers in Simulation*, **79**(3), 416–428 (2008). ISSN 03784754.

Hah C. Large Eddy Simulation Of Transonic Flow Field In NASA. (January), 1–13 (2009).

Halstead DE, Wisler DC, Okiishi TH, Walker GJ, Hodson HP and Shin HW. Boundary Layer Development in Axial Compressors and Turbines PART 1 OF 4 : Composite Picture. *Journal of Turbomachinery* (1995).

Henderson AD and Walker GJ. Observations of Transition Phenomena on a Controlled Diffusion Compressor Stator With a Circular Arc Leading Edge. *Journal of Turbomachinery*, **132**(3), 031002 (2010). ISSN 0889504X.

Hilgenfeld L and Pfitzner M. Unsteady Boundary Layer Development Due to Wake Passing Effects on a Highly Loaded Linear Compressor Cascade. *Journal of Turbomachinery*, **126**(4), 493 (2004). ISSN 0889504X.

Hobson GV, Hansen DJ, Schnorenberg DG and Grove DV. Effect of Reynolds Number on Separation Bubbles on Compressor Blades in Cascade. *Journal of Propulsion and Power*, **17**, 154–162 (2001). ISSN 07484658.

Hobson GV, Wakefield BE and Roberts WB. Turbulence amplification with incidence at the leading edge of a compressor cascade. *International Journal of ...*, **5**(2), 89–98 (1999).

Hodson HP and Addison JS. Wake–Boundary Layer Interactions in an Axial Flow Turbine Rotor at Off-Design Conditions. *Journal of Turbomachinery*, **111**(2), 181 (1989). ISSN 0889504X.

Hodson HP and Howell RJ. Bladerow Interactions, Transition, and High-Lift Aerofoils in Low-Pressure Turbines. *Annual Review of Fluid Mechanics*, **37**(1), 71–98 (2005). ISSN 0066-4189.

Hodson HP, Hynes TP, Greitzer EM and Tan CS. A Physical Interpretation of Stagnation Pressure and Enthalpy Changes in Unsteady Flow. *Journal of Turbomachinery*, **134**(6), 60902–60908 (2012). ISSN 0889-504X.

Horlock J. *Combined Power Plants: Including Combined Cycle Gas Turbine (CCGT) Plants*. Thermodynamics and fluid mechanics series. Krieger Pub. (1992). ISBN 9781575241975.

Horlock JM. Unsteady Flow in Turbomachines (1968).

Hughes JD and Walker GJ. Natural Transition Phenomena on an Axial Compressor Blade. *Journal of Turbomachinery*, **123**(2), 392 (2001). ISSN 0889504X.

Iseler J, Hilgenfeld L and Pfitzner M. Investigations of the Boundary Layer on a Highly Loaded Compressor Cascade With Wake-Induced Transition. In *ASME Turbo Expo: Power for Land, Sea, and Air*, volume 6 Part A a, pages 1811–1820. ASME (2006). ISBN 0-7918-4241-X.

Johnstone R, Chen L and Sandberg RD. A sliding characteristic interface condition for direct numerical simulations. *Computers and Fluids*, **107**, 165–177 (2015). ISSN 00457930.

Jones WP and Launder BE. On the Preditction of Laminarisation With a Two-Equation Model of Turbulence. *International Journal of Heat and Mass Transfer*, **15**, 301–314 (1972).

Joslyn HD and Dring RP. Axial Compressor Stator Aerodynamics. *Journal of Engineering for Gas Turbines and Power*, **107**(2), 485–492 (1985). ISSN 0742-4795.

Kennedy C and Gruber A. Reduced aliasing formulations of the convective terms within the Navier-Stokes equations for a compressible fluid. *Journal of Computational Physics*, **227**(3), 1676–1700. (2008).

Kennedy Ca, Carpenter MH and Lewis R. Low-storage, explicit Runge–Kutta schemes for the compressible Navier–Stokes equations. *Applied Numerical Mathematics*, **35**(3), 177–219 (2000). ISSN 01689274.

Kerrebrock JL. Unsteady Flows in Jet Engines. In *Project Squid Workshop, United Technologies Research Centre* (1974).

Kim J, Moin P and Moser R. Turbulence statistics in fully developed channel flow at low Reynolds number. *Journal of Fluid Mechanics*, **177**, 133–166 (1987). ISSN 0022-1120.

Kim JJW and Lee DDJ. Characteristic Interface Conditions for Multiblock High-Order Computation on Singular Structured Grid. *AIAA journal*, **41**(12) (2003).

Klein M, Sadiki a and Janicka J. A digital filter based generation of inflow data for spatially developing direct numerical or large eddy simulations. *Journal of Computational Physics*, **186**(2), 652–665 (2003). ISSN 00219991.

Lardeau S and Leschziner MA. Unsteady Reynolds Averaged Navier Stokes Computations of Transitional Wake/Blade Interaction. *AIAA Journal*, **42**(8), 1559–1571 (2004). ISSN 0001-1452.

Lee BHK, Murty H and Jiang H. Role of Kutta waves on oscillatory shock motion on an airfoil. *AIAA Journal*, **32**(4), 789–796 (1994). ISSN 0001-1452.

Leipold R, Boese M and Fottner L. The Influence of technical surface roughness caused by precision forging on the flow around a highly loaded compressor cascade. *Journal of Turbomachinery*, **122**, 416–425 (2000).

Mayle RE. The 1991 IGTI Scholar Lecture: The Role of Laminar-Turbulent Transition in Gas Turbine Engines. *Journal of Turbomachinery*, **113**(4), 509–536 (1991). ISSN 0889-504X.

McMullan WA and Page G. Towards Large Eddy Simulation of gas turbine compressors. *Progress in Aerospace Sciences*, **52**, 30–47 (2012). ISSN 03760421.

McMullan WA and Page GJ. Large Eddy Simulation of a Controlled Diffusion Compressor Cascade. *Flow, Turbulence and Combustion*, **86**(2), 207–230 (2010). ISSN 1386-6184.

Medic G, Zhang V, Wang G, Joo J and Sharma OP. Prediction of Transition and Losses in Compressor Cascades Using Large-Eddy Simulation. *Journal of Turbomachinery*, **138**(12), 121001–121009 (2016). ISSN 0889-504X.

Menter FR. Two-equation eddy-viscosity turbulence models for engineering applications. *AIAA Journal*, **32**(8), 1598–1605 (1994). ISSN 0001-1452.

Michelassi V, Chen LW, Pichler R and Sandberg RD. Compressible Direct Numerical Simulation of Low-Pressure Turbines: Part II — Effect of Inflow Disturbances. In *ASME Turbo Expo: Power for Land, Sea, and Air*, volume 2D, page V02DT44A014. ASME (2014). ISBN 978-0-7918-4563-9.

Miller RJ. Gt2013-95488 Mechanical Work Potential. *ASME Turbo Expo 2013*, **1**, 1–13 (2013).

Mo R. 1999 Turbomachinery Committee Best Paper Award Development of Advanced Compressor Airfoils for Heavy-Duty Gas Turbines — Part I : Design and Optimization. *Journal of Turbomachinery*, **122**(July) (2000).

Mo R, Küsters B, Schreiber HA, Köller U, Mönig R, Mo R and Ag S. 1999 Turbomachinery Committee Best Paper Award Development of Advanced Compressor Airfoils for Heavy-Duty Gas Turbines — Part II : Experimental and Theoretical Analysis. *Journal of Turbomachinery*, **122**(July), 406–415 (2000).

Nicoud F and Ducros F. Subgrid-Scale Stress Modelling Based on the Square of the Velocity Gradient Tensor. *Flow, Turbulence and Combustion*, **62**(3), 183–200 (1999). ISSN 13866184.

Peacock RE. A review of turbomachinery tip gap effects: Part 1: Cascades. *International Journal of Heat and Fluid Flow*, **3**(4), 185–193 (1982). ISSN 0142-727X.

Poensgen C and Gallus HE. Three-Dimensional Wake Decay Inside of a Compressor Cascade and Its Influence on the Downstream Unsteady Flow Field: Part II—Unsteady Flow Field Downstream of the Stator. *Journal of Turbomachinery*, **113**(2), 190–197 (1991a). ISSN 0889-504X.

Poensgen C and Gallus HE. Three-Dimensional Wake Decay Inside of a Compressor Cascade and Its Influence on the Downstream Unsteady Flow Field: Part I—Wake Decay Characteristics in the Flow Passage. *Journal of Turbomachinery*, **113**(2), 180–189 (1991b). ISSN 0889-504X.

Prasad A. Calculation of the Mixed-Out State in Turbomachine Flows. *Journal of Turbomachinery*, **127**(3), 564 (2005). ISSN 0889504X.

Reynolds O. On the Dynamical Theory of Incompressible Viscous Fluids and the Determination of the Criterion. *Philosophical Transactions of the Royal Society of London. (A.)*, **186**, 123 LP – 164 (1895).

Roberts WB. The Effect of Reynolds Number and Laminar Separation on Axial Cascade Performance. *Journal of Engineering for Gas Turbines and Power*, **97**(2), 261–273 (1975). ISSN 0742-4795.

Sandberg R, Suponitsky V and Sandham N. DNS of a canonical compressible nozzle flow. *Direct and Large-Eddy Simulation*, **15**, 291–296 (2011).

Sandberg RD. Numerical investigation of turbulent supersonic axisymmetric wakes. *Journal of Fluid Mechanics*, **702**, 488–520 (2012).

Sandberg RD, Michelassi V, Pichler R, Chen L and Johnstone R. Compressible Direct Numerical Simulation of Low-Pressure Turbines—Part I: Methodology. *Journal of Turbomachinery*, **137**(5), 051011 (2015). ISSN 0889-504X.

Sandberg RD and Sandham ND. Nonreflecting zonal characteristic boundary condition for direct numerical simulation of aerodynamic sound. *AIAA journal*, **44**(2), 3–6 (2006).

Sandberg RD, Sandham ND and Suponitsky V. DNS of compressible pipe flow exiting into a coflow. *International Journal of Heat and Fluid Flow*, **35**, 33–44 (2012). ISSN 0142727X.

Schobeiri MT, Read K and Lewalle J. Effect of Unsteady Wake Passing Frequency on Boundary Layer Transition, Experimental Investigation, and Wavelet Analysis. *Journal of Fluids Engineering*, **125**(2), 251 (2003). ISSN 00982202.

Schreiber HA, Steinert W and Küsters B. Effects of Reynolds number and free-stream turbulence on boundary layer transition in a compressor cascade. *Journal of Turbomachinery*, **124**(1), 1–9 (2002). ISSN 0889504X.

Schreiber HA, Steinert W, Sonoda T and Arima T. Advanced High-Turning Compressor Airfoils for Low Reynolds Number Condition—Part II: Experimental and Numerical Analysis. *Journal of Turbomachinery*, **126**(4), 482 (2004). ISSN 0889504X.

Schubauer BG and Klebanoff SP. Contributions on the Mechanics of Boundary-Layer Transition. Technical Report 1 (1955).

Seymour Lieblein FCS and Broderick RL. Diffusion factor for estimating losses and limiting blade loadings in axial flow compressor blade elements, AD011178 - NACA RM E53DO1. *American Documentation*, **7**(3), 188–200 (1953). ISSN 0096946X.

Smagorinsky J. General circulation experiments with the primitive equations, I, the basic experiment. *Monthly Weather Review*, **91**, 99–165. (1963).

Smith LH. Recovery Ratio-A Measure of the Loss Recovery Potential of Compressor Stages. *ASME Transactions*, **80**, 517–524 (1958).

Smith LH. Wake Dispersion in Turbomachines. *Journal of Basic Engineering*, **88**(3), 688–690 (1966a). ISSN 00219223.

Smith LH. Wake Dispersion in Turbomachines. *Journal of Basic Engineering*, **88**(3), 688–690 (1966b). ISSN 00219223.

Smith LH. Wake ingestion propulsion benefit. *Journal of Propulsion and Power*, **9**(1), 74–82 (1993). ISSN 0748-4658.

Solomon WJ, Walker GJ and Gostelow JP. Transition Length Prediction for Flows With Rapidly Changing Pressure Gradients. *Journal of Turbomachinery*, **118**(4), 744–751 (1996). ISSN 0889-504X.

Sonoda T, Yamaguchi Y, Arima T, Olhofer M, Sendhoff B and Schreiber HA. Advanced High Turning Compressor Airfoils for Low Reynolds Number Condition—Part I: Design and Optimization. *Journal of Turbomachinery*, **126**(3), 350 (2004). ISSN 0889504X.

Spalart PR. Direct simulation of a turbulent boundary layer up to R $\theta = 1410$. *Journal of Fluid Mechanics*, **187**, 61 (1988). ISSN 0022-1120.

Steinert W, Eisenberg B and Starken H. Design and testing of a controlled diffusion airfoil cascade for industrial axial flow compressor application. *Journal of Turbomachinery*, **113** (1991). ISSN 0889504X.

Steinert W and Starken H. Off-Design Transition and Separation Behaviour of a CDA Cascade. *ASME*, **118**, 204–209 (1996).

Storer JA and Cumpsty NA. Tip Leakage Flow in Axial Compressors. *Journal of Turbomachinery*, **113**(2), 252–259 (1991). ISSN 0889-504X.

Storer JA and Cumpsty NA. An Approximate Analysis and Prediction Method for Tip Clearance Loss in Axial Compressors. *Journal of Turbomachinery*, **116**(4), 648–656 (1994). ISSN 0889-504X.

Suryavamshi N, Lakshminarayana B, Prato J and Fagan JR. Unsteady Total Pressure Field Downstream of an Embedded Stator in a Multistage Axial Flow Compressor. *Journal of Fluids Engineering*, **119**(4), 985–994 (1997). ISSN 0098-2202.

Tijdeman H. Investigation of the transonic flow around oscillating airfoils. *National Aerospace Lab. Amsterdam, Netherlands*, **TR-77-090U** (1977).

Valkov TV and Tan CS. Effect of Upstream Rotor Vortical Disturbances on the Time-Averaged Performance of Axial Compressor Stators: Part 1—Framework of Technical Approach and Wake–Stator Blade Interactions. *Journal of Turbomachinery*, **121**(3), 377–386 (1999a). ISSN 0889-504X.

Valkov TV and Tan CS. Effect of Upstream Rotor Vortical Disturbances on the Time-Averaged Performance of Axial Compressor Stators: Part 2—Rotor Tip Vortex/Streamwise Vortex–Stator Blade Interactions. *Journal of Turbomachinery*, **121**(3), 387–397 (1999b). ISSN 0889-504X.

Van Zante DE, Adamczyk JJ, Strazisar AJ and Okiishi TH. Wake Recovery Performance Benefit in a High-Speed Axial Compressor. *Journal of Turbomachinery*, **124**(2), 275–284 (2002). ISSN 0889-504X.

Walker GJ. The Role of Laminar-Turbulent Transition in Gas Turbine Engines: A Discussion. *Journal of Turbomachinery*, **115**(2), 207–216 (1993). ISSN 0889-504X.

Walraevens RE and Cumpsty NA. Leading Edge Separation Bubbles on Turbomachine Blades. *Journal of Turbomachinery*, **117**(1), 115–125 (1995). ISSN 0889-504X.

Wang Y and Devenport W. Wake of a Compressor Cascade with Tip Gap, Part 2: Effects of Endwall Motion (2004).

Weymouth G and Yue DK. Boundary data immersion method for Cartesian-grid simulations of fluid-body interaction problems. *Journal of Computational Physics*, **230**(16), 6233–6247 (2011). ISSN 00219991.

Wheeler APS, Sandberg RD, Sandham ND, Pichler R, Michelassi V and Laskowski G. Direct Numerical Simulations of a High-Pressure Turbine Vane. *Journal of Turbomachinery*, **138**(7), 71003–71009 (2016). ISSN 0889-504X.

White F. *Viscous Fluid Flow.* McGraw-Hill. (1991).

Wilcox DC. *Turbulence Modeling for CFD.* DCW Industries, Inc., 3rd edition (2006). ISBN 978-1928729082.

Wissink J and Rodi W. Numerical study of the near wake of a circular cylinder. *International Journal of Heat and Fluid Flow*, **29**(4), 1060–1070 (2008). ISSN 0142727X.

Wissink JG, Zaki TA, Rodi W and Durbin PA. The Effect of wake Turbulence Intensity on Transition in a Compressor Cascade. *Flow, Turbulence and Combustion*, **93**(4), 555–576 (2014). ISSN 1386-6184.

Wu X, Jacobs RG, Hunt JCR and Durbin Pa. Simulation of boundary layer transition induced by periodically passing wakes. *Journal of Fluid Mechanics*, **398**, 109–153 (1999). ISSN 00221120.

You D, Wang M, Moin P and Mittal R. Large-eddy simulation analysis of mechanisms for viscous losses in a turbomachinery tip-clearance flow. *Journal of Fluid Mechanics*, **586**, 177 (2007). ISSN 0022-1120.

Zaki Ta and Durbin Pa. Separation and transition to turbulence in a compressor passage. In *Proceedings of the Summer Program*, number 1999, pages 1–15 (2006).

Zaki Ta, Wissink JG, Durbin Pa and Rodi W. Direct Computations of Boundary Layers Distorted by Migrating Wakes in a Linear Compressor Cascade. *Flow, Turbulence and Combustion*, **83**(3), 307–322 (2009). ISSN 1386-6184.

Zaki Ta, Wissink JG, Rodi W and Durbin Pa. Direct numerical simulations of transition in a compressor cascade: the influence of free-stream turbulence. *Journal of Fluid Mechanics*, **665**, 57–98 (2010). ISSN 0022-1120.